



**THE ROLE OF miR-140 AND miR-455 IN MURINE
SKELETAL DEVELOPMENT AND OSTEOARTHRITIS
PATHOGENESIS**

Yao Hao

Institute of Genetic Medicine

A thesis submitted for the degree of Doctor of Philosophy

October 2021

Declaration

I, Yao Hao, declare that no portion of the work compiled in this thesis has been submitted in support of another degree or qualification at this or any other University or Institute of learning. This thesis includes nothing which is work of others, nor the outcomes of work done in collaboration, except where otherwise stated.

.....
Yao Hao

Abstract

THE ROLE OF miR-140 AND miR-455 IN MURINE SKELETAL DEVELOPMENT AND OSTEOARTHRITIS PATHOGENESIS

Introduction: Osteoarthritis (OA) is the most common musculoskeletal disorder, which is complex and characterised by degradation of articular cartilage of joint tissue. Epigenetic changes alter transcriptional regulation and disrupt signalling pathways involved in cartilage homeostasis leading to OA, and dysregulation of and by microRNA (miRNA) (e.g. miR-140 and miR-455) correlate with bone and OA development. Bioinformatic analysis of RNA-sequencing (RNA-seq) could reveal the mechanism of the function of miR-140 and miR-455 in murine skeletal development and OA pathogenesis.

Aim: Generation of *Mir140*-null and *Mir455*-null mouse model to understand their role in relation to murine skeletal and OA development.

Material and Methods: By CRISPR/Cas9 technology we generated two mouse lines, for *Mir140* (miR-140^{-/-}) and *Mir455* (miR-455^{-/-}). These mice were interbred to derive mice with deletions of both *Mir140* and *Mir455* (DKO). On the mutant mice, we performed phenotyping of skeletal X-ray, weight growth curve, and tibial growth plate analysis, including histological staining and immunocytochemistry (BrdU labelling to monitor proliferation and TUNEL labelling to monitor apoptosis). Destabilisation of the medial meniscus (DMM) surgery was performed on mutant mice to assess knee articular cartilage integrity following joint trauma. Differential expression of genes within the growth plate of the mutant mice were identified by RNA-seq and potential upregulated miRNA predicted targets validated by 3'UTR luciferase analysis. The expression of two growth plate targets (*Creb3l1* and *Nrf2*) were assessed by western blot analysis in isolated chondrocytes. Transcriptome analysis was also performed on micro-dissected knee articular cartilage (pre- and post-DMM surgery) and on laser micro-dissected growth plates.

Results: Genotyping analysis confirmed the deletion of miRNAs in our mutant mice. Phenotyping of our *Mir140*-null mice matched that of previously published work, including mild short stature, domed skull, and a short tail. Our *Mir455*-null mice were dwarf when compared to control mice, however, *Mir455*-null mice housed at our collaborator were undisguisable from age-matched control mice. Our DKO mice shared a similar phenotype

with *Mir140*-null mice. Histological staining revealed abnormal tibial growth plate morphology and delayed secondary ossification in 1-week and 3-week-old mice. A reduction in tibial growth plate chondrocyte proliferation and increased apoptosis was detected in mutant mouse lines. Mutant mice exhibited different transcriptome profiles of costal chondrocyte by RNA-seq, and three miR-140 growth plate predicted target genes (*Creb3l1*, *Nrf2* and *Zeb1*) were confirmed to be targets and to attenuate chondrocyte proliferation by WST-1 assay analysis.

Following DMM-surgery all mutant mice showed higher OA score with either Glasson scoring system or OARSI scoring system, and all exhibited significant proteoglycan staining loss compared to control mice. Comparison of transcriptome profiles before and after DMM surgery had led to understand the function of miR-140 during OA pathogenesis.

Discussion and conclusion: Our mutant mice showed clear growth phenotypes compared to control mice, however the phenotyping of our *Mir455*-null mouse line was different to recent literature and to similar animals at our collaborator facility. Histological and immunohistochemistry analysis confirmed that mutant mice exhibited abnormal growth plate morphology, with reduced chondrocyte proliferation and increased apoptosis.

Transcriptome profiling from costal chondrocyte and knee cartilage chondrocyte (pre and post-DMM surgery) represents an important tool to identify miRNA target genes and, herein, to gain insights about miR-140 and miR-455 in skeletal developments and OA pathogenesis.

Acknowledgement

I would like to thank my supervisor Professor David Young, for giving this opportunity to do this research for my PhD and for all his help, guidance, patience and encouragement throughout the whole time period of my PhD. He made me move towards the positive side of things and gain more confidence.

I would like to thank Dr Louise Reynard for all her help, guidance, patience and support throughout my PhD.

I would also like to thank Dr Matthew Barter for all his help, patience, guidance and support throughout my PhD.

Thanks to Sarah Charlton for all her help, patience, guidance and support.

Thanks to the Functional Genomics Unit at Newcastle University for help with mouse housing, and special thanks to Steve Smith for all his very kind help.

Thanks to Professor David Young, Dr Colin Miles and Paul Cairns for injection of CRISPR/Cas9 system to generate the mutant mice.

Thanks to Dr Kathleen Cheung for her help to analyse costal chondrocyte RNA-seq data.

Thanks to Dr Jamie Soul for help to analyse knee articular cartilage chondrocyte RNA-seq data with R language method.

Thanks to Hua Lin for her help in mouse housing, DMM surgery, RNA extraction from articular cartilage and her dedication to work.

Thanks to Dr Ralf Kist for his help in histological staining for skulls.

Thanks to Dr Rafiqul Hussain and Dr Jonathan Coxhead for all the help in LMD experiment and RNA sequencing.

Thanks to present and previous members in SRG group for their help and for making me feel that I am not alone.

Thanks to First Hospital of Shanxi Medical University for all the support during my PhD.

Finally, I would like to acknowledge all the mice used in this study. Their sacrifice made this research worked and this thesis finished.

Contents

Declaration	I
Abstract	II
Acknowledgement	IV
List of figures	XII
List of Tables	XVI
Abbreviations	XVII
Chapter 1. Introduction	1
1. 1. <i>MicroRNAs</i>	1
1. 1. 1. The synthesis and the expression of microRNAs	1
1. 1. 2. MicroRNAs in biological processes & diseases	4
1. 2. <i>Bone development & osteoarthritis</i>	6
1. 2. 1. Bone development.....	6
1. 2. 2. Chondrogenesis and articular cartilage development.....	7
1. 2. 2. 1. Chondrocyte proliferation	11
1. 2. 2. 2. Chondrocyte hypertrophy	13
1. 2. 3. Osteoarthritis	15
1. 2. 3. 1. Current opinions on osteoarthritis	15
1. 2. 3. 2. Relationship between OA risk factors and microRNAs	17
1. 3. <i>MicroRNA-140</i>	20
1. 3. 1. Expression of microRNA-140	20
1. 3. 2. The functional role of microRNAs in skeletogenesis	22
1. 3. 3. microRNA-140 in OA pathogenesis	24
1. 4. <i>MicroRNA-455</i>	27
1. 4. 1. microRNA-455 in chondrogenesis and OA pathogenesis	27
1. 5. <i>Project aims</i>	30
Chapter 2. Materials and Methods	31
2. 1. <i>Materials</i>	31
2. 1. 1. Antibodies	31
2. 1. 2. Biochemical assay reagents	31

2.1.3. Cell lines.....	32
2.1.3.1. SW1353.....	32
2.1.3.2. Mouse costal chondrocytes.....	32
2.1.4. Cell and tissue culture reagents.....	32
2.1.5. General molecular biology reagents.....	33
2.1.6. Histological staining immunohistochemistry reagents.....	33
2.1.7. Immunoblotting reagents.....	33
2.1.8. MicroRNA, RNA, and DNA extraction reagents.....	33
2.1.9. siRNA reagents.....	34
2.1.10. 3' untranslated region (UTR) constructs and luciferase reagents.....	34
2.1.11. Whole mouse skeletal staining reagents.....	34
2.2. Methods	34
2.2.1. Cell culture.....	34
2.2.1.1. SW1353 cell culture	34
2.2.1.2. Mouse primary costal chondrocyte culture.....	35
2.2.2. Protein analysis.....	36
2.2.2.1. Whole cell lysis	36
2.2.2.2. Bradford assay.....	36
2.2.2.3. Immunoblotting	37
2.2.3. RNA analysis	38
2.2.3.1. Total RNA extraction from cell culture	38
2.2.3.2. Total RNA extraction from mouse primary rib chondrocyte	38
2.2.3.3. Total RNA extraction from mouse medial knee cartilage.....	39
2.2.3.4. Reverse transcription.....	40
2.2.3.5. Reverse transcription of RNA obtained using Ambion Cells-to-cDNA II kit	40
2.2.3.6. MicroRNA reverse transcription.....	41
2.2.3.7. Primers for real time qRT-PCR	41
2.2.3.8. Real time qRT-PCR	43
2.2.3.9. MicroRNA real-time qRT-PCR.....	44
2.2.3.10. Costal RNA-sequencing (RNA-seq) and data analysis.....	44
2.2.3.11. Short interfering RNAs (siRNAs) transfection	45

2.2.3.12. WST-1 proliferation assay.....	46
2.2.4. Histological analysis.....	47
2.2.4.1. Haematoxylin & Eosin analysis of mice tibia growth plate	47
2.2.4.2. Safranin O analysis of mice tibia growth plate.....	48
2.2.4.3. Whole mount skeletal staining with Alcian Blue/Alizarin Red	49
2.2.4.4. Bromodeoxyuridine (BrdU) labelling analysis	49
2.2.4.5. Terminal deoxynucleotidyl transferase doxyuridine triphosphate (dUTP) nick end labelling (TUNEL) analysis	51
2.2.5. Generation, maintenance and identification of mouse models.....	52
2.2.5.1. Generation of the genetically modified mouse models.....	52
2.2.5.2. Maintenance of the genetically modified mice and non-genetically modified mice	53
2.2.5.3. Genotyping of mice	53
2.2.6. Morphometric analysis of the mice	55
2.2.6.1. Whole body weights	55
2.2.6.2. X-ray measurements	55
2.2.6.3. X-ray micro-computed tomography (μ CT) quantitative analysis of mice skulls.....	55
2.2.6.4. Bone measurements	56
2.2.7. Luciferase assay analysis.....	58
2.2.7.1. Generation of 3'UTR constructs and mutant 3'UTR constructs	58
2.2.7.2. Luciferase assay	60
2.2.8. Destabilisation of the medial meniscus (DMM) surgery model	61
2.2.8.1. DMM surgery.....	61
2.2.8.2. Histological analysis of DMM mice at 8 weeks post-surgery	62
2.2.8.3. Murine medial knee cartilage RNA sequencing	65
2.2.9. Laser microdissection (LMD)	66
2.2.10. Data/statistical analysis	66
<i>Chapter 3. Skeletal development of miR-140-/- mice, miR-455-/- mice, and miR-140: miR-455-/- (Double Knock Out, DKO) mice</i>	68
3.1. <i>Introduction</i>	68
3.2. <i>Results</i>	70
3.2.1. Generation and genotyping of miR-140 ^{-/-} mice, miR-455 ^{-/-} mice, and DKO mice	70
3.2.1.1. Generation of miR-140 ^{-/-} mice	70

3.2.1.2. Generation of miR-455 ^{-/-} mice and DKO mice	73
3.2.1.3. miR-140 ^{-/-} mice, miR-455 ^{-/-} mice, and DKO mice showed defects in endochondral bone growth	76
3.2.1.4. miR-140 ^{-/-} mice, miR-455 ^{-/-} mice, and DKO mice showed altered skeletal growth.....	82
3.2.1.5. Deletion of <i>Mir140</i> , <i>Mir455</i> , and both of <i>Mir140</i> and <i>Mir455</i> result in abnormal growth plate organisation and chondrocyte morphology	86
3.2.1.6. Deletion of <i>Mir140</i> , <i>Mir455</i> , and both of <i>Mir140</i> and <i>Mir455</i> , affects chondrocyte proliferation in the growth plate	93
3.2.1.7. Deletion of <i>Mir140</i> and <i>Mir455</i> alone or in combination affects chondrocyte apoptosis in the growth plate	95
3.3. <i>Discussion</i>	100
3.3.1. <i>Mir140</i> -null mice show defects in skeletal bone development.....	100
3.3.2. <i>Mir455</i> -null mice show defects in endochondral bone growth.....	105
3.3.3. DKO mice show defects in skeletal bone growth.....	107
3.3.4. Knockout of miR-140 and/or miR-455 in chondrocytes reduces proliferation and increases cell death	107
3.3.5. Summary	110
Chapter 4. Identification of the growth plate target genes of <i>Mir140</i> and <i>Mir455</i>	111
4.1. <i>Introduction</i>	111
4.2. <i>Results</i>	113
4.2.1. Validation of genes that highly upregulated in published <i>Mir140</i> -null dataset.....	113
4.2.2. Quality control (QC) check for RNA isolated from primary costal chondrocytes and RNA-seq analysis	115
4.2.3. RNA-seq data analysis of miR-140 ^{-/-} mice P7 costal chondrocytes	115
4.2.4. Confirmation of loss of miR-140-5p effect on genes expression in costal chondrocyte	121
4.2.5. Identification and validation of <i>Mir140</i> in the growth plate	122
4.2.5.1. Identification of <i>Mir140</i> growth plate target genes	122
4.2.5.2. Pathway analysis using GSEA	125
4.2.5.3. Identification and validation of potential novel growth plate targets of miR-140	127
4.2.5.4. Are CREB3L1, NRF2 and ZEB1 increased at protein level in <i>Mir140</i> -null chondrocytes?	135
4.2.5.5. Exploration of the role of <i>Mir-140</i> target genes	140
4.2.6. RNA-seq data analysis on miR-455 ^{-/-} mice	146
4.2.7. Identification and validation of <i>Mir455</i> in the growth plate	152

4.2.7.1. Pathway analysis using GSEA	152
4.2.7.2. Identification of <i>Mir-455</i> growth plate target genes	154
4.2.8. Separation of murine growth plate proliferative zone using laser microdissection (LMD)	157
4.3. <i>Discussion</i>	166
4.3.1. Screening and validation of miR-140 growth plate target genes	166
4.3.2. Exploring the role of selected miR-140 growth plate target genes	170
4.3.3. Screening and validation of miR-455 growth plate target genes	172
4.3.4. An optimised methodology developed to assess the impact of <i>Mir140</i> loss in proliferative zone cartilage using LMD	173
4.3.5. Summary	174
Chapter 5. Identification the role of <i>Mir140</i> and <i>Mir455</i> in murine knee cartilage 176	
5.1. <i>Introduction</i>	176
5.2. <i>Results</i>	179
5.2.1. RNA-seq data analysis of miR-140 ^{-/-} mice 11-week-old medial knee articular cartilage	179
5.2.2. RNA-seq data analysis of miR-455 ^{-/-} mice 11-week-old medial knee articular cartilage	186
5.2.3. RNA-seq data analysis of DKO mice 11-week-old medial knee articular cartilage	192
5.2.4. Selection of murine DMM histological assessment	196
5.2.5. Effect of miR-140 ^{-/-} and/or miR-455 ^{-/-} mutations on murine knee articular cartilage stability	208
5.2.6. RNA-seq data analysis of WT mice pre- and post-DMM surgery at 11-week-old	216
5.2.7. RNA-seq data analysis of <i>Mir140</i> -null medial knee articular cartilage 3-days post-DMM surgery	221
5.2.8. RNA-seq data analysis of <i>Mir140</i> -null medial knee articular cartilage 7-days post DMM surgery at 11-week-old	227
5.2.9. RNA-seq data analysis of <i>Mir140</i> -null medial knee articular cartilage 42-days post DMM surgery at 11-week-old	233
5.3. <i>Discussion</i>	240
5.3.1. Selection of optimal histological assessment	240
5.3.2. Evaluation of articular cartilage damage in the different genotypes	241
5.3.3. Exploration of the role of miR-140 and/or miR-455 in murine articular chondrocytes	243
5.3.4. Identification of the role of miR-140 in murine articular cartilage after DMM treatment	248
5.3.5. Summary	250
Chapter 6. Discussion 252	
Reference	258

List of figures

Figure 1.1 Schematic representing of producing of miRNA.....	3
Figure 1.2 Schematic representing of miRNA-target interactions.....	3
Figure 1.3 Endochondral ossification is the process of long bone development.....	7
Figure 1.4 The structure of growth plate zones in one end of a long bone.....	7
Figure 1.5 Sequence of stages of chondrogenesis during the development of long bones	10
Figure 1.6 Distinct morphologies of chondrocytes in mouse knee articular cartilage development post-natal day 60 (P60) are observed in the different zones with the aid of Safranin O staining.....	11
Figure 1.7 Model of the function of PTHrP/Ihh signalling in regulation in chondrocyte differentiation.....	13
Figure 1.8 Schematic representing the comparison between healthy knee and OA knee	16
Figure 1.9 The role of miRNAs in OA pathogenesis.....	19
Figure 1.10 The role of miR-140 in endochondral bone development and cartilage homeostasis through targeting <i>Dnpep</i> and <i>Adamts5</i> , respectively (Miyaki and Asahara 2012).	24
Figure 1.11 The list on the left are differently expressed miRNAs in OA samples.....	26
Figure 2.1 Conventional scheme of mouse bone measurement used for X-ray analysis of ICD, femur length (FL), tibia length (TL), and pelvis length (PL).	58
Figure 3.1 Generation and genotyping of miR-140 ^{-/-} mice.....	71
Figure 3.2 <i>Wwp2</i> , the <i>Mir140</i> host gene, expression and splicing was unaffected by deletion of <i>Mir140</i>	72
Figure 3.3 Generation and genotyping of miR-455 ^{-/-} and DKO mice.....	74
Figure 3.4 Radiographs of mice at 7 days of age.	78
Figure 3.5 Reconstructed µCT images and radiographs of 7-days skull.	79
Figure 3.6 Weight analysis of mice at 7, 14, 22, and 28 days of age.....	81
Figure 3.7 Skeletal preparation of mice at 7 days of age.....	83
Figure 3.8 Endochondral ossification was affected by deleting <i>Mir140</i> and <i>Mir455</i>	84
Figure 3.9 MicroRNA deletion mice showed shorter body and tail length at 7 days of age....	85
Figure 3.10 MicroRNA knockout mice at P7 showed a disrupted growth plate with abnormal chondrocyte morphology.	88

Figure 3.11 Secondary ossification is disrupted by depletion of <i>Mir140</i> in mice at P7.....	90
Figure 3.12 MicroRNA knockout mice at P22 showed a disrupted growth plate with abnormal chondrocyte morphology.....	91
Figure 3.13 Secondary ossification is disrupted by depletion of <i>Mir140</i> in mice at P22	92
Figure 3.14 Proliferative chondrocytes in growth plate are disrupted by depletion of <i>Mir140</i> and <i>Mir455</i>	94
Figure 3.15 Apoptosis of chondrocytes in growth plate are affected by depletion of <i>Mir140</i> and <i>Mir455</i>	97
Figure 3.16 <i>Mir140</i> and <i>Mir455</i> loss accelerates apoptosis of chondrocytes in tibial hypertrophic and resting growth plate zones, respectively.....	98
Figure 3.17 Lack of <i>Mir140</i> increases apoptosis of chondrocytes in the tibial growth plate... ..	99
Figure 4.1 Validation of the mRNA expression of genes filtered from GSE98306	114
Figure 4.2 An abundance of genes is differentially expressed in <i>Mir140</i> -null mice relative to control mice.....	118
Figure 4.3 MiR-140 targets analysis.....	120
Figure 4.4 Sylamer analysis on miR-140 seed sequence	121
Figure 4.5 Screening <i>Mir140</i> target genes	124
Figure 4.6 GSEA enrichment of miR-140 ^{-/-} gene sets in mouse costal chondrocytes RNA-seq data.....	126
Figure 4.7 Confirmation of <i>Mir140</i> target genes filtered from RNA-seq analysis	132
Figure 4.8 Validation of miR-140-3p growth plate target genes.....	134
Figure 4.9 Protein encoded by <i>Creb3l1</i> is differentially expressed in miR-140 ^{-/-} chondrocytes	137
Figure 4.10 Protein encoded by <i>Nrf2</i> increased in expression in miR-140 ^{-/-} chondrocytes	138
Figure 4.11 Immunoblot analysis of protein encoded by <i>Zeb1</i>	139
Figure 4.12 <i>Mir140</i> regulates chondrocyte proliferation through decreasing the expression of <i>Creb3l1</i> and <i>Nrf2</i>	142
Figure 4.13 <i>Creb3l1</i> and <i>Nrf2</i> play role in regulating proliferation of chondrocytes without <i>Mir140</i>	143
Figure 4.14 <i>Creb3l1</i> and <i>Nrf2</i> affect proliferation of WT rib chondrocyte	144
Figure 4.15 An abundance of genes are differentially expressed in <i>Mir455</i> -null mice relative to control mice.....	148

Figure 4.16 MiR-455 targets analysis	150
Figure 4.17 Screening <i>Mir455</i> target genes	151
Figure 4.18 GSEA enrichment of miR-455 ^{-/-} gene sets in mouse costal chondrocytes RNA-seq data.....	153
Figure 4.19 Identification of miR-455 growth plate target genes.....	156
Figure 4.20 Laser dissected growth plate proliferative zone from 7-d-old murine proximal tibias	160
Figure 4.21 Comparison between our laser captured proliferative samples to published online data.....	162
Figure 4.22 Top 50 gene counts	164
Figure 4.23 Expression of zone markers among the LMD groups.....	165
Figure 5.1 Histological assessment of articular cartilage isolation for RNA-seq analysis.	181
Figure 5.2 The disruption of differentially expressed genes in <i>Mir140</i> -null murine knee cartilage relative to control mice.....	182
Figure 5.3 Profile of significant differentially expressed genes expression in murine knee cartilage between WT and <i>Mir140</i> -null mice.....	184
Figure 5.4 GSEA enrichment of miR-140 ^{-/-} gene sets in mouse knee cartilage RNA-seq data	185
Figure 5.5 The disruption of differentially expressed genes in <i>Mir455</i> -null murine knee cartilage relative to control mice.....	188
Figure 5.6 Profile of significant differentially expressed genes expression in murine knee cartilage between WT and <i>Mir455</i> -null mice.....	190
Figure 5.7 GSEA enrichment of miR-455 ^{-/-} gene sets in mouse knee cartilage RNA-seq data	191
Figure 5.8 The disruption of differentially expressed genes in DKO murine knee cartilage relative to control mice.....	193
Figure 5.9 Profile of significant differentially expressed genes expression in murine knee cartilage between WT and DKO mice	194
Figure 5.10 Profile of significant differentially expressed genes expression in murine knee cartilage between <i>Mir140</i> -null, <i>Mir455</i> -null and DKO mice.....	195
Figure 5.11 Scoring trend of selected 20 test DMM images using system 1.....	201
Figure 5.12 Scoring trend of selected 20 test DMM images using system 2.....	203
Figure 5.13 Scoring trend of selected 20 test DMM images using system 3	205
Figure 5.14 DMM-induced OA in mice	210

Figure 5.15 MiR-140 and miR-455 are involved in GAG metabolism in articular chondrocytes	214
Figure 5.16 OA evaluation using the OARSI (Glasson) scoring system	215
Figure 5.17 GSEA enrichment of pathways in WT mouse knee cartilage RNA-seq data 3 days post-DMM treatment	218
Figure 5.18 GSEA enrichment of pathways in WT mouse knee cartilage RNA-seq data 7 days post-DMM treatment	219
Figure 5.19 GSEA enrichment of pathways in WT mouse knee cartilage RNA-seq data 42 days post-DMM treatment	220
Figure 5.20 The disruption of differentially expressed genes in <i>Mir140</i> -null murine knee cartilage with 3-days post-DMM treatment relative to control mice	223
Figure 5.21 Profile of significant differentially expressed genes expression in murine knee cartilage between WT and <i>Mir140</i> -null mice that are 3-days post DMM surgery	225
Figure 5.22 GSEA enrichment of miR-140 ^{-/-} gene sets in mouse knee cartilage RNA-seq data 3 days post-DMM	226
Figure 5.23 The genes differentially expressed in <i>Mir140</i> -null murine knee cartilage with 7-days post-DMM treatment relative to control mice	229
Figure 5.24 Profile of significant differentially expressed genes expression in murine knee cartilage between WT and <i>Mir140</i> -null mice 7-days post DMM surgery	231
Figure 5.25 GSEA enrichment of pathways in miR-140 ^{-/-} mouse knee cartilage RNA-seq data 7 days post-DMM treatment	232
Figure 5.26 The genes differentially expressed in <i>Mir140</i> -null murine knee cartilage with 42-days post-DMM treatment relative to control mice	235
Figure 5.27 Profile of significant differentially expressed genes in murine knee cartilage between WT and <i>Mir140</i> -null mice 42-days post-DMM surgery	237
Figure 5.28 GSEA enrichment of pathways in miR-140 ^{-/-} mouse knee cartilage RNA-seq data 42 days post-DMM surgery	238
Figure 5.29 ECM proteoglycan pathways gene expression time-course following DMM induction	239

List of Tables

Table 1.1 MiRNAs are implicated to have either protective or destructive role in articular cartilage homeostasis (Endisha, Rockel et al. 2018).	5
Table 2.1 Sequences of primers and probes for probe based real-time qRT-PCR method.....	43
Table 2.2 Primers designed to create miR-140 target gene's 3'UTR constructs.....	59
Table 2.3 Primers designed to create mutant miR-140-5p target gene's 3'UTR constructs....	60
Table 2.4 The recommended semi-quantitative scoring system for assessing cartilage damage on DMM mouse joints. Adapted from (Pritzker et al., 2006).	64
Table 2.5 The recommended semi-quantitative scoring system for assessing cartilage damage on DMM mouse joints. Adapted from (Glasson et al., 2010).	65
Table 4.1 Previously validated miR-140 direct targets	123
Table 4.2 Screening results of predict <i>Mir140</i> target genes.....	129
Table 4.3 Functions of potential miR-140 target genes in cell.....	130
Table 4.4 The effect of miR-140 target genes on chondrocyte proliferative activity	145
Table 4.5 The different sizes of laser dissected sections and treatments used for miRNA sequencing.....	161
Table 4.6 The top 50 ranked genes confirmed that dissected sections contain chondrocytes	163
Table 5.1 The semi-quantitative scoring scheme for system 1.....	200
Table 5.2 The semi-quantitative scoring scheme for system 2.....	202
Table 5.3 The semi-quantitative scoring scheme for system 3.....	204
Table 5.4 Summary of correlation between scorer and the mean (Pearson)	206
Table 5.5 Summary of interscorer correlation (Pearson).....	207
Table 5.6 Enrichr summary of overlapping expression ranked genes and ARCHS4 tissue database	245

Abbreviations

Abca1	ATP binding cassette subfamily A member 1
Acan	Aggrecan
Acvr2b	Activin receptor 2B
Ago	Argonaute
BasO	BasiOccipital
BMD	Bone mineral density
BMG	Bone matrix gelatin
BMP	Bone morphogenetic protein
BMSCs	Bone marrow-derived mesenchymal stem cells
BrdU	5-bromo-2'-deoxyuridine
BSA	Bovine serum albumin
Cdc34	Cell cycle regulators cell division cycle 34
CFA	Craniofacial anomalies
CLEAR	Covalent ligation of endogenous Argonaute-bound RNAs
Col2	Type II collagen
COMP	Cartilage oligomeric protein
Creb3l1	cyclic adenosine monophosphate responsive element binding protein 3-like 1
DA	Dark Agouti
DEGs	Differentially expressed genes
DGCR8	DiGeorge syndrome critical region gene 8
DMM	Destabilization of medial meniscus
Drosha	RNA endonuclease III
ECM	Extracellular matrix
E2F5	E2F transcription factor 5
Fbn1	Fibrillin-1
FDR	False discovery rate values
FGF	Fibroblast growth factor

FGFRs	Fibroblast growth factor receptors
GAG	Glycosaminoglycan
HADSCs	Human adipose-derived stem cells
HCV	Hepatitis C virus
HDAC4	Histone deacetylases 4
H&E	Haematoxylin and Eosin
HH	Hedgehog
HITS	High-throughput sequencing of RNAs
HZ	Hypertrophic zone
ICD	Inter-canthal distance
IHC	Immunohistochemistry
Ihh	Indian hedgehog
IL-1 β	Interleukin 1 β
LMD	Laser microdissection
Med13	Mediator Complex Subunit 13
MFC	Medial femoral condyle
MFS	Marfan syndrome
miRNAs	MicroRNAs
MMPs	Matrix metalloproteinases
mRNAs	Messenger RNAs
MSCs	Mesenchymal stem/stromal cells
MTP	Medial tibial plateau
N-CAM	Neural cell adhesion molecule
Ncstn	Nicastrin
Nrf2	Erythroid-derived 2 p45 related factor 2
Npr3	Natriuretic peptide receptor 3
OA	Osteoarthritis
OARSI	Osteoarthritis Research Society International
OOCHAS	OARSI osteoarthritis Cartilage Histopathology Assessment System

PCA	Principal component analysis
pri-miRNAs	Primary miRNAs
Prx1	Paired-related homeobox gene-1
Prg4	Proteoglycan 4
PTHrP	Parathyroid hormone-related peptide
Pth1r	PTH/PTHrP receptor
PZ	Proliferative zone
RA	Rheumatoid arthritis
RISC	RNA-induced silencing complex
RNA-seq	RNA sequencing
RRHO	Rank-rank Hypergeometric overlap
RZ	Resting zone
Shh	Sonic hedgehog
SphB	Sphenoid Body
sRNA-seq	Small RNA sequencing
TGF- β	Transforming growth factor beta
Tmem123	Transmembrane Protein 123
TUNEL	Terminal deoxynucleotidyl transferase dUTP nick end labelling
μ Ct	Microcomputed tomography
VEGF	Vascular endothelial growth factor
VOI	Volume of interest
WC	Watson-Crick
WT	Wild type
Wwp2	Ubiquitin E3 ligase
Zeb1	Zinc finger E-box binding homeobox 1
3'UTRs	3' untranslated regions

Chapter 1. Introduction

1. 1. MicroRNAs

MicroRNAs (miRNAs) are a class of short (20- to 23- nucleotide long) single-stranded endogenous non-coding RNAs that play an important role at the post-transcriptional level to suppress mRNA expression. They do this by generally targeting the 3' untranslated regions (3'UTRs) of target mRNAs through partial sequence complementary, which leads to suppress translation of the targeted mRNAs and subsequently induces their degradation (Bartel 2004, Lewis, Burge et al. 2005, Bartel 2009), though miRNAs have also been reported to increase target expression (Bluhm, Ehlen et al. 2017). MiRNAs are differentially expressed depending on tissue and cell types, and many miRNAs are evolutionary conserved (Miyaki and Asahara 2012, Miyaki and Asahara 2012). Moreover, miRNAs have been shown to function in fine-tuning the expression of approximately 30% of protein coding genes in mammals, indicating miRNAs have crucial roles in maintaining cellular function (Bartel 2004, Miyaki and Asahara 2012, Miyaki and Asahara 2012).

1. 1. 1. The synthesis and the expression of microRNAs

The synthesis of miRNAs is precisely regulated in the cells (Figure 1). MiRNAs, are usually encoded either within an intron of a host gene or from an intergenic region and are firstly generated as primary miRNAs (pri-miRNAs), transcribed by RNA polymerase II or III. These pri-miRNAs are cleaved by a protein complex comprising RNA endonuclease III (Drosha) and DiGeorge syndrome critical region gene 8 (DGCR8) or processed by splicing to produce the precursor miRNA (pre-miRNA). The pre-miRNA is transferred into cytoplasm with the help of exportin-5, and the 70-100 nucleotide stem-loop structure is subsequently processed by another RNA endonuclease III known as Dicer. The remaining two strands then are then incorporated into the RNA-induced silencing complex (RISC) to bind Argonaute (Ago) proteins which guide the complex to miRNA targets through a short complementary sequence to the 'seed' sequence near the 5'end of the miRNA (Shang, Liu et al. 2013, Fabian 2019). A miRNA sequence can be broken down into 'subdomains' when bound to Ago proteins, the 5' anchor (base 1), the seed sequence (bases 2-8), the centre (bases 9-12), the 3' supplementary (bases 13-16), and the tail sequence (the 3' nucleotides) (Figure 2) (Wee,

Flores-Jasso et al. 2012, Schirle, Sheu-Gruttaduria et al. 2014, Salomon, Jolly et al. 2015, Fabian 2019). The most evolutionary conserved seed sequence-target RNA pairing helps to predict actual targets for specific miRNAs, with the 3' supplementary-target RNA pairing enhancing target recognition (Bartel 2009, Friedman, Farh et al. 2009). Thus, RISC degrades the targets or inhibits the translation of the target mRNA depending on the amount of base pair complementarity.

Previously, microRNAs were named with addition of * to inform that that microRNA arises from the 5' arm of the hairpin, miRNAs named without * arose from the 3' arm of the hairpin. Current nomenclature names these -5p and -3p, respectively. Recently, small RNA sequencing (sRNA-seq) has revealed additional miRNAs that may be shorter or longer at the 5' and/or 3' end than that of the annotated mature miRNA, known as isomiRs (Morin et al., 2008). These miRNAs are not always identical to their genomic DNA origin (non-templated) due to variations at 5' the end, often altering the seed sequence and therefore the miRNA target repertoire. Compared to variations at the 5' end, variants at the 3' end are more common, but miRNA target repertoire is not thought to be as changed (Wyman, Knouf et al. 2011).

Numerous miRNAs have been identified to contribute to many biological processes, but also to phenotypic diversity in mice (Hornstein and Shomron 2006, Park, Choi et al. 2010). Global *Dicer*-null mutant mice arrested at approximately embryonic (E) day 7.5, before the body plan is configured during gastrulation (Bernstein, Kim et al. 2003). In terms of limb development, conditionally removed Dicer from the limb mesenchyme result in much smaller limbs formation (Harfe, McManus et al. 2005). Cartilage specific-*Dicer*-null mice showed severe skeletal growth retardation, a reduced size of the proliferative zone of their growth plate with reduced numbers of proliferative chondrocytes, and accelerated hypertrophic chondrocyte differentiation (Kobayashi, Lu et al. 2008). Growth plate specific-*Drosha*-null mice and *DGCR8*-null mice exhibited similar skeletal phenotype as *Dicer* null mice (Kobayashi, Papaioannou et al. 2015). In addition to mice, inactivation of maternal and zygotic *dicer1* in zebrafish leads to obvious vertebrate development delay (Wienholds, Koudijs et al. 2003). This therefore proves that global miRNA deficiency plays a critical role in skeletal development and tissue morphogenesis. However, there are several hundred miRNAs expressed in chondrocytes, thus it remains to be fully determined which specific

miRNAs are responsible for the skeletal development defects observed in mice lacking *Dicer* in cartilage.

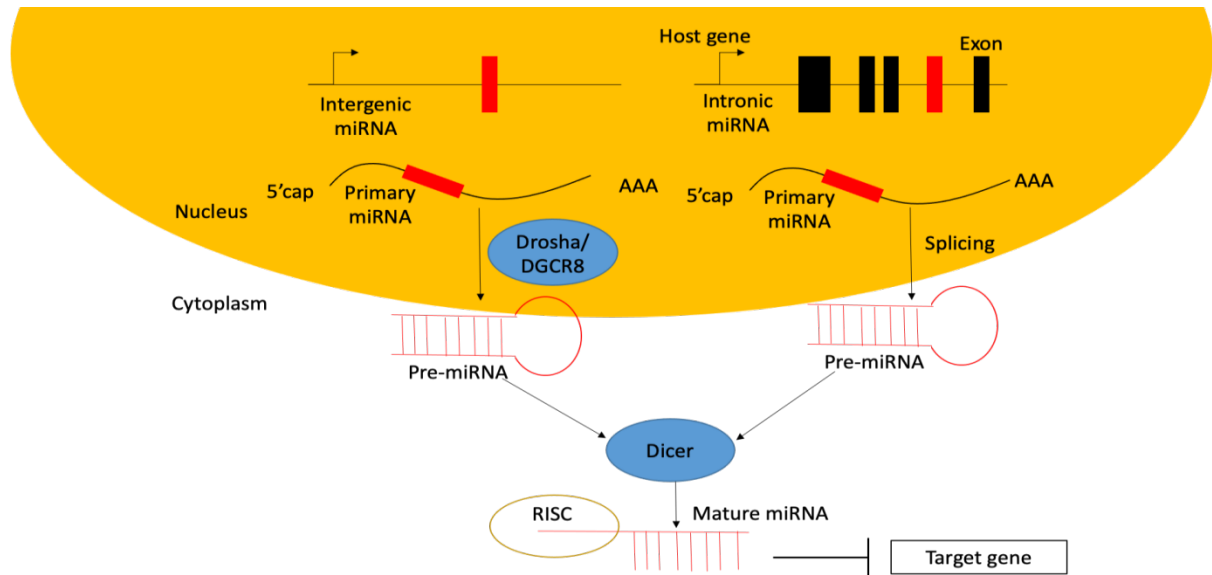


Figure 1.1 Schematic representing of producing of miRNA. Normally, miRNA (red) is encoded within an intron of a host gene or may also be encoded from an intergenic region. A stem loop (pre-miRNA) is either cleaved by Drosha/DGCR8 from pri-miRNA or is generated from splicing (intronic miRNA) of a primary transcript in the nucleus. This is then exported to the cytoplasm, where Dicer cleaves pre-miRNA into mature miRNA. MiRNA further regulates the expression of target mRNA through either translation repression or degradation of mRNAs (Miyaki and Asahara 2012).

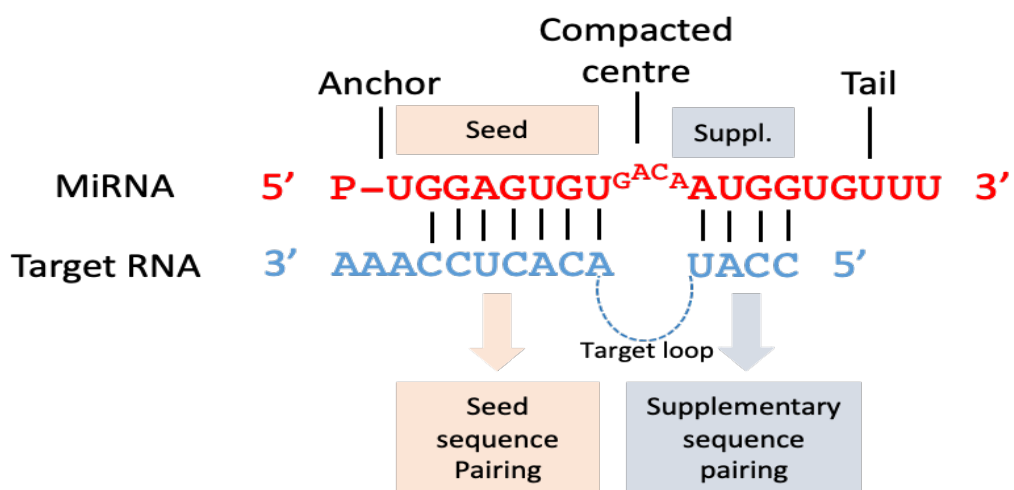


Figure 1.2 Schematic representing of miRNA-target interactions. MiRNA sequence was broken down within Ago proteins into subdomains: the 5' anchor, the seed sequence, the compacted centre, the 3' supplementary sequence, and the tail (Fabian 2019).

1. 1. 2. MicroRNAs in biological processes & diseases

Studies have demonstrated that specific expression patterns of miRNAs are associated with disease pathogenesis including cardiovascular disorders and cancers (Volinia, Calin et al. 2006, Small and Olson 2011). Tissue specific expression of miRNAs can have both protective and pathogenic functions in mice through controlling expression of numerous protein encoding genes in the tissue (Park, Choi et al. 2010). These findings indicate that miRNAs can have a potential therapeutic role for treating human diseases, in particular through the use of antisense miRNAs or double stranded miRNA mimics. For example, a study on primates with chronic hepatitis C virus (HCV) infection revealed that a synthetic antisense miRNA improved HCV-induced liver pathology through inhibition of a specific miRNA, miR-122, that contributes to accumulation of HCV RNA in hepatocytes (Lanford, Hildebrandt-Eriksen et al. 2010). Moreover, miRNAs could act as biomarkers for various diseases (Volinia, Calin et al. 2006, Park, Choi et al. 2010, Small and Olson 2011). Serum miRNAs including hsa-miR-140-3p, hsa-miR-671-3p, and hsa-miR-33-3p have been proposed as Osteoarthritis (OA) biomarker based on a comparison of human primary OA serum samples with serum samples obtained from healthy individuals (Ntoumou, Tzetis et al. 2017, Jones, Esa et al. 2021).

Given the above, there is therefore the promise of improved clinical treatments of some intractable diseases using miRNA-based drugs or antisense of miRNAs in the near future. Such potential is based on fully understanding the mechanisms of action of miRNAs in these diseases. Of particular interest and relevance to this thesis, several miRNAs have been implicated in maintaining cartilage homeostasis and in OA development (Miyaki and Asahara 2012, Bluhm, Ehlen et al. 2017, Endisha, Rockel et al. 2018). Currently, the mechanisms to deliver miRNA therapeutically to damaged cartilage and the joint are still developing. Different miRNAs play various roles as protectors or destructors of articular cartilage through targeting different genes (Table 1.1). Further, the expression levels of miRNAs are different at the different stages of OA. Thus, it remains elusive what roles individual miRNAs play in OA pathogenesis, with a better understanding of the mechanism of miRNAs for treating OA required.

miRNA	Target gene(s)	Role of miRNA	Involve in cartilage protective/destructive mechanisms	Reference(s)
miR-140	<i>ADMATS5, IGFBP5, DNPEP, SP1, BMP2, HDAC4</i>	Cartilage development and homeostasis	Protective	(Tuddenham, Wheeler et al. 2006, Nicolas, Pais et al. 2008, Miyaki, Nakasa et al. 2009, Tardif, Hum et al. 2009, Miyaki, Sato et al. 2010, Nakamura, Inloes et al. 2011, Yang, Qin et al. 2011)
miR-455	<i>SMAD2, ACVR2B, CHRDL1, HOTTIP, CCL3, PTEN, HDAC2, HDAC4, HDAC8, DNMT3A, EPAS1</i>	Chondrocyte differentiation, cartilage homeostasis	Protective	(Swingler, Wheeler et al. 2012, Sun, Zhao et al. 2018, Mao, Kang et al. 2019, Wen, Li et al. 2020, Ito, Matsuzaki et al. 2021)
miR-33	<i>CCL2</i>	Regulates monocyte chemotaxis	Protective	(Wei, Xie et al. 2016)
miR-105	Runx2	Inhibits Runx2 activation and ADAMTS5 expression	Protective	(Ji, Xu et al. 2016)
miR-125b	<i>ADAMTS4</i>	Prevent aggrecan loss	Protective	(Matsukawa, Sakai et al. 2013)
miR-101	<i>SOX9</i>	Cartilage degradation	Destructive	(Dai, Zhang et al. 2012)
miR-16-5p	<i>SMAD3</i>	Cartilage degradation	Destructive	(Li, Jia et al. 2015)
miR-146a	<i>SMAD4</i>	Activation of early OA	Destructive	(Yamasaki, Nakasa et al. 2009)
miR-138-5p	<i>FOXC1</i>	Promotes cartilage degradation	Destructive	(Yuan, Zhang et al. 2016)
miR-15a-5p	<i>VEGFA</i>	Apoptosis, matrix degradation	Destructive	(Chen and Tian 2017)

Table 1.1 MiRNAs are implicated to have either protective or destructive role in articular cartilage homeostasis (Endisha, Rockel et al. 2018).

1. 2. Bone development & osteoarthritis

1. 2. 1. Bone development

For long bone development, skeletogenesis initiates with the migration of mesenchymal stem/stromal cells (MSCs) from the embryonic lineages which accumulate at a high cellular density to outline the shape of future bones, and thus pre-determine the anatomic identity of the bone (Hall and Miyake 1992, Berendsen and Olsen 2015). A series of processes happen after condensation of MSCs, the cells either differentiate into chondrocytes and form cartilage and bones in the future (endochondral bone formation), or differentiate into osteoblasts to directly form bone (intramembranous bone formation). Endochondral ossification is a complex process that proceeds through differentiation of proliferative chondrocytes to hypertrophic chondrocytes, a process that is completed with extracellular matrix (ECM) calcification and vascular invasion.

The primary ossification centre mostly occurs during foetal development, then expands and the second ossification centre is formed at both ends of the developing long bones, which results in the development of epiphyseal growth plate cartilage and longitudinal bone growth (Figure 3) (Karsenty and Wagner 2002, Kronenberg 2003). Chondrocytes located in the growth plate are well organised into structural and functional zones (Mundlos 1994). Inactive chondrocytes are present in the resting zone close to the secondary ossification centre, the proliferative chondrocytes undergo clonal expansion and align themselves into columns parallel to the direction of longitudinal bone growth. When the proliferative chondrocytes enter hypertrophy, the cells stop proliferating and either undergo apoptosis or are differentiated into osteoblasts (Figure 4) (Yang, Tsang et al. 2014, Berendsen and Olsen 2015).

Many factors contribute to regulate chondrocyte proliferation, differentiation, and apoptosis. Probably the most studied example is that of Indian hedgehog (*Ihh*) / parathyroid hormone-related peptide (*PTHRP*) signalling pathways which regulates the differentiate rate of proliferative chondrocytes into hypertrophic chondrocytes through a negative feedback loop.

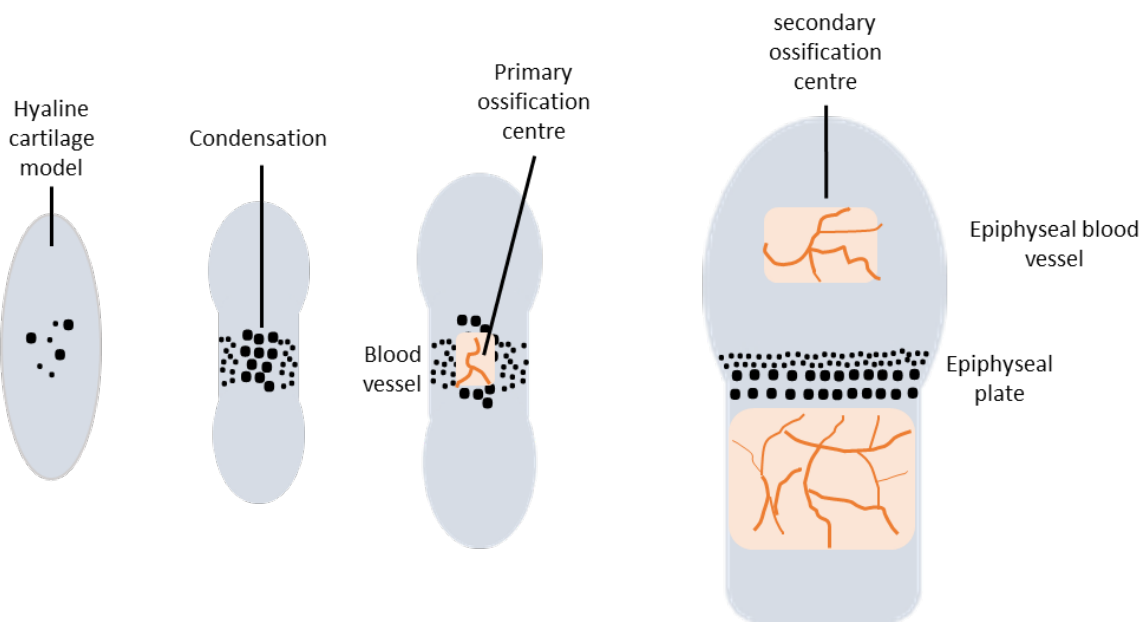


Figure 1.3 Endochondral ossification is the process of long bone development. Bone development involves the formation of primary ossification centre, secondary ossification centre and eventually compact bone.

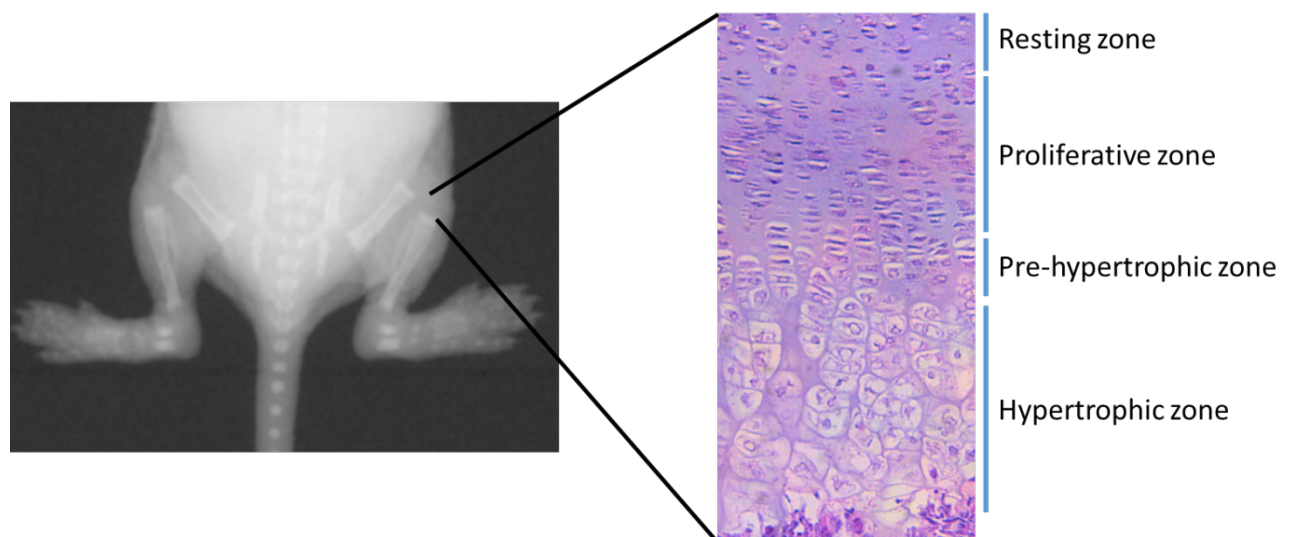


Figure 1.4 The structure of growth plate zones in one end of a long bone. The growth plate consists of a reserve zone (resting zone), proliferative zone, pre-hypertrophic zone, and hypertrophic zone.

1. 2. 2. Chondrogenesis and articular cartilage development

Growth plate and articular chondrocytes arise from distinct progenitor populations. For growth plate development, the cartilaginous nodules first appear in the middle of the densely accumulated precursor mesenchymal cells (also termed skeletal blastemal), at the same time peripheral cells flatten and elongate, giving rise to the perichondrium.

Development of the growth plate is elaborately controlled by cellular interaction with its surrounding matrix, and as described growth factors, and other environmental factors involving signalling pathways that regulate differentiation of chondrocytes. Cell-cell contacts and cell-matrix interactions produce signals that contribute to the MSC condensation and differentiation. This ECM is rich in type I and type II collagen, and hyaluronan. The activity of hyaluronidase and the appearance of cell adhesion molecules like neural cell adhesion molecule (N-CAM) are considered to trigger MSC condensation (Sandell, Nalin et al. 1994, Goldring, Tsuchimochi et al. 2006). Many signals are important for cells condensation, transforming growth factor beta (TGF β), stimulates the synthesis of fibronectin. ECM molecules such as cartilage oligomeric protein (COMP) bind cell adhesion molecules to trigger intracellular signalling pathways to help chondroprogenitor cells transition and differentiate into chondrocytes (DeLise, Fischer et al. 2000). Different factors and interactions among them determine a dynamic balance during chondrogenesis, involving positive and negative transcription factors, such as Sox9 and Runx2. During chondrogenesis (Figure 5), Wnt, Bone morphogenetic protein (BMP), Hedgehog (HH), Fibroblast growth factor (FGF), and TGF- β signals are involved in chondroprogenitor cell proliferation and differentiation (Hall and Miyake 1992, DeLise, Fischer et al. 2000, Olsen, Reginato et al. 2000). Wnt signals, such as Wnt2a and Wnt2c, are necessary to induce FGF-8 and FGF-10, which are required during both limb initiation and limb bud outgrowth (Tickle and Munsterberg 2001, Niswander 2003, Tickle 2003). Sonic hedgehog (Shh) is required for early limb patterning (Liu, Sun et al. 2005). BMPs are important for bone morphogenesis through initiating chondroprogenitor cell differentiation and also regulating chondrocyte maturation and terminal differentiation into hypertrophic chondrocytes at the later stages (Goldring, Tsuchimochi et al. 2006).

In contrast to growth plate chondrocytes, less know is about development of articular chondrocytes. Two growth mechanisms of articular chondrocytes are plausible, including interstitial and appositional. Human articular cartilage comprises of 4 zones (superficial zone, middle zone, deep zone, and mineralized zone) according to histological features. For interstitial growth, distinct articular chondrocytes arise from a precursor cell population, and then populate the different layers. For appositional growth, similar to growth plate development, a precursor cell population firstly give rise to articular chondrocytes in the

superficial zone, which then undergo a maturation process to form distinct cells that populate the other zones (Kozhemyakina, Zhang et al. 2015).

Articular cartilage is a complex tissue consisting of many matrix proteins, the composition and order of which vary from the superficial layer to the deep layer and between load and non-load bearing regions (Kozhemyakina, Zhang et al. 2015). Further, the morphology of chondrocytes in articular cartilage varies from a flattened shape at the surface to rounder and larger in the deep zones (Figure 6) (Goldring, Tsuchimochi et al. 2006, Goldring 2012). In contrast to growth plate chondrocytes, lineage tracing experiments reveal that articular cartilage originates from common progenitor populations with synovial cells that surround the joint cavity (Hyde, Dover et al. 2007, Koyama, Shibukawa et al. 2008).

Chondrocytes in the growth plate and in the articular cartilage go through different mechanisms during long bone development, which might result from the role of different transcription factors, cytokines, and loading, etc. MiRNAs can influence long bone development through affecting the expression level of transcription factors that are involved in the development of growth plate and articular cartilage. To reveal the role of specific miRNAs, such as miR-140 and miR-455, in mouse long bone development an understanding of the different mechanisms of chondrogenesis and articular cartilage homeostasis are required.

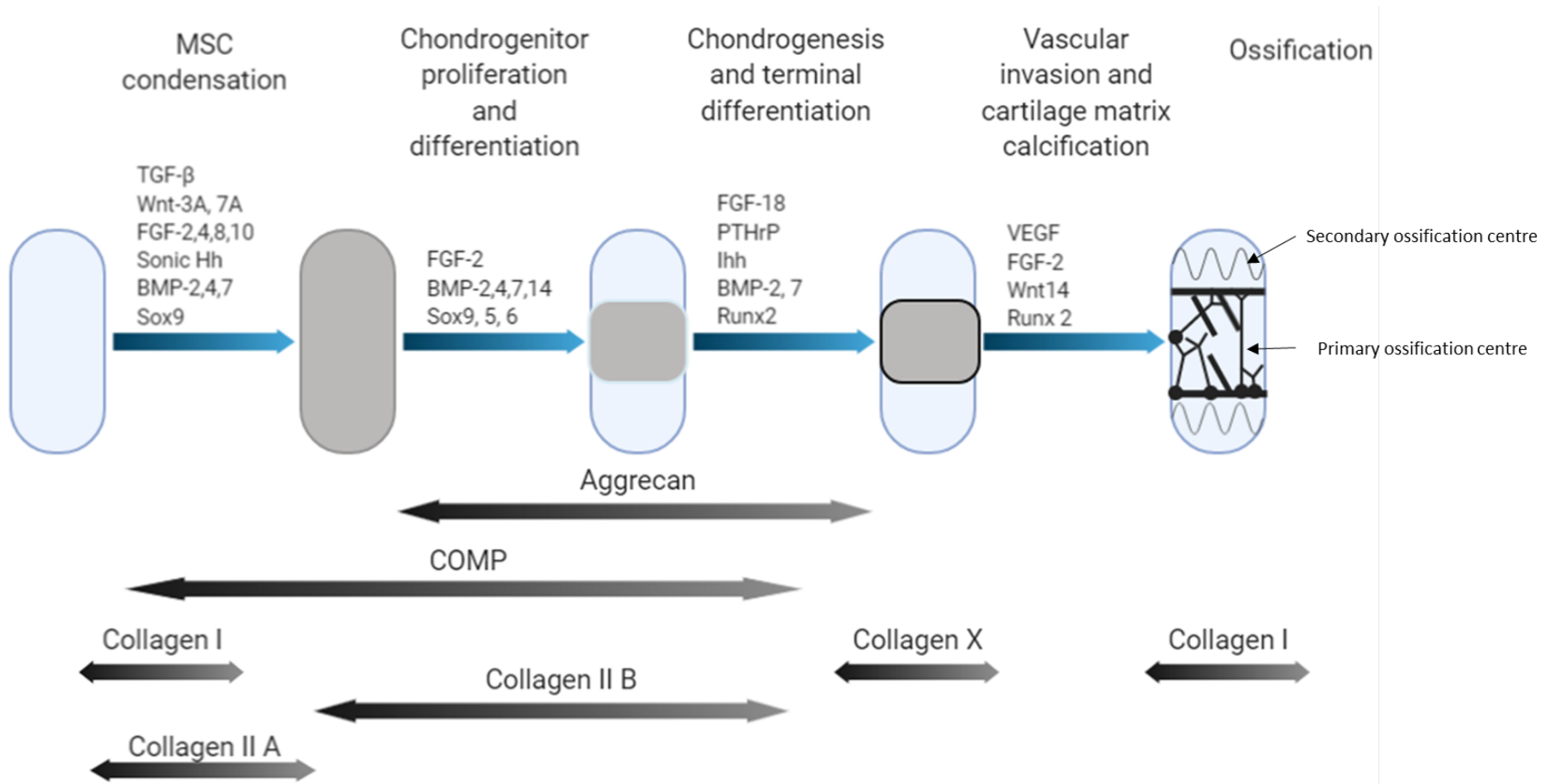


Figure 1.5 Sequence of stages of chondrogenesis during the development of long bones. The different stages of chondrogenesis above are presented to show the temporal patterns of growth factors, differentiation factors, and transcription factors involved in development of long bones. Below this are listed the main extracellular proteins synthesised at different stages of chondrogenesis (Goldring, Tsuchimochi et al. 2006).

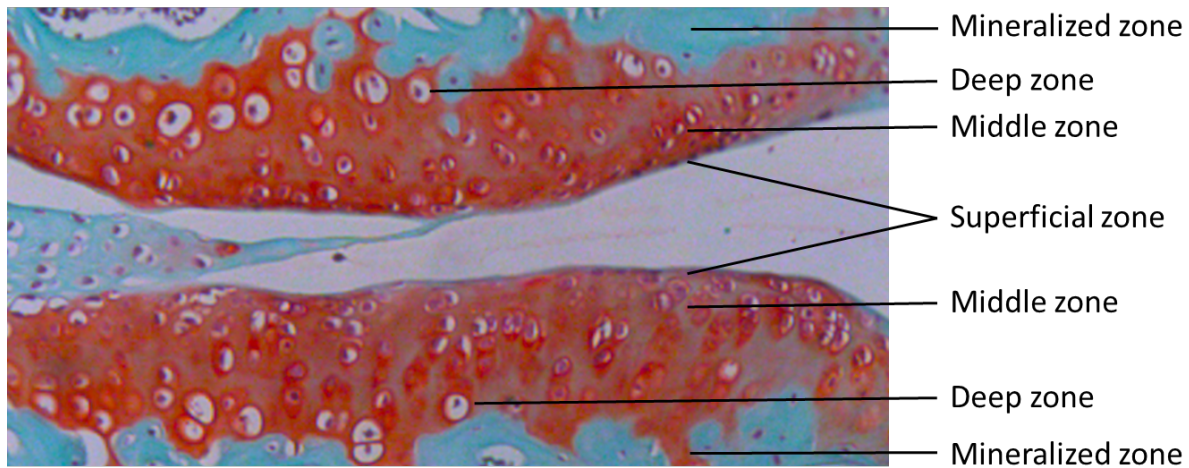


Figure 1.6 Distinct morphologies of chondrocytes in mouse knee articular cartilage development post-natal day 60 (P60) are observed in the different zones with the aid of Safranin O staining. The four different zones from the surface to the deep also termed the superficial zone, middle zone, deep zone, and mineralized zone, respectively.

1. 2. 2. 1. Chondrocyte proliferation

As mentioned above, BMPs and FGFs are important throughout chondrogenesis, and in part determine the rate of proliferation of chondrocytes and the velocity of the chondrocyte differentiation. Among the BMPs, BMP-3 is found primarily expressed in resting zone, BMP-7 is expressed in the proliferating chondrocytes of long bone development, with Bmp-1, BMP-2 (Bmp-2), and BMP-6 (Bmp-6) found in hypertrophic chondrocytes (Minina, Kreschel et al. 2002). Fibroblast growth factor receptors (FGFRs) are upregulated during chondrogenesis, FGFR2 is upregulated in MSC condensation, FGFR1 is found in surrounding loose mesenchyme, while FGFR3 is associated with proliferation of chondrocytes in the central core of mesenchymal condensation. Furthermore, dominant mutations in FGFR1 and FGFR2 cause bone syndromes which result from defects in intramembranous ossification; mutations in FGFR3 indicate a role in endochondral ossification. *Fgfr3* deficient mice have an expanded proliferating zone of the growth plate, a phenotype similar to that of *Fgf18* deficient mice, indicating FGF18 is the major ligand of FGFR3 in growth plate chondrocytes. FGFR3-mediated signalling, by the phosphorylation and activation of Stat1, acts as an inhibitor of chondrocyte proliferation by increasing the expression of the cell cycle inhibitor p21 (Sahni, Ambrosetti et al. 1999, Liu, Xu et al. 2002).

Studies have also shown that the interaction between FGF18 and FGFR1 regulates vascular invasion in the pre-hypertrophic zone and hypertrophic zone of growth plate through

inducing the expression of vascular endothelial growth factor (VEGF). The increase in FGFR1 expression in these zones suggests FGF signalling plays a role in the regulation of chondrocytes differentiation and cell death (Ornitz 2005).

The mechanism that regulates the proliferation of chondrocytes in the lower proliferative and pre-hypertrophic zones is in part due to the PTHrP/Ihh negative feedback loop (Figure 7). The expression of Ihh is restricted to the pre-hypertrophic zone while the *PTHrP* receptor is expressed in periarticular chondrocytes, which are located at the distal zone of long bones. Ihh induces the expression of *PTHrP* in the perichondrium, and *PTHrP* signalling stimulates chondrocyte proliferation (Lanske, Karaplis et al. 1996, Vortkamp, Lee et al. 1996). The above mechanism is further modulated by the balance between BMP and FGF signalling that determines the rate of chondrocyte terminal differentiation into proliferating chondrocytes (Minina, Kreschel et al. 2002). Studies show that Ihh acts in a PTHrP-dependent manner that stimulates periarticular chondrocytes into columnar chondrocytes located in the proliferative zone, whereas PTHrP plays a role in preventing premature differentiation of chondrocytes into pre-hypertrophic and hypertrophic chondrocytes to maintain the length of columns, and indeed suppressing premature expression of Ihh (Kronenberg 2006, Ohba 2016). Others showed that Ihh promotes chondrocyte hypertrophy independently of PTHrP but mediated by Bmp/Wnt signalling (Kobayashi, Soegiarto et al. 2005, Mak, Kronenberg et al. 2008). Post-natal deletion of either *Ihh* or PTH/PTHrP receptor (*Pth1r*) in mice result in premature fusion of epiphyseal growth plate (Maeda, Nakamura et al. 2007, Hirai, Chagin et al. 2011). In humans, inactivating mutations in *IHH* or in the *PTH1R* cause premature closure of the growth plate (acrocapitofemoral dysplasia) and Blomstrand dysplasia (skeletal abnormalities similar to *Pth1r* deficient mice), respectively (Jobert, Zhang et al. 1998, Karaplis, He et al. 1998, Zhang, Jobert et al. 1998, Hellemans, Coucke et al. 2003).

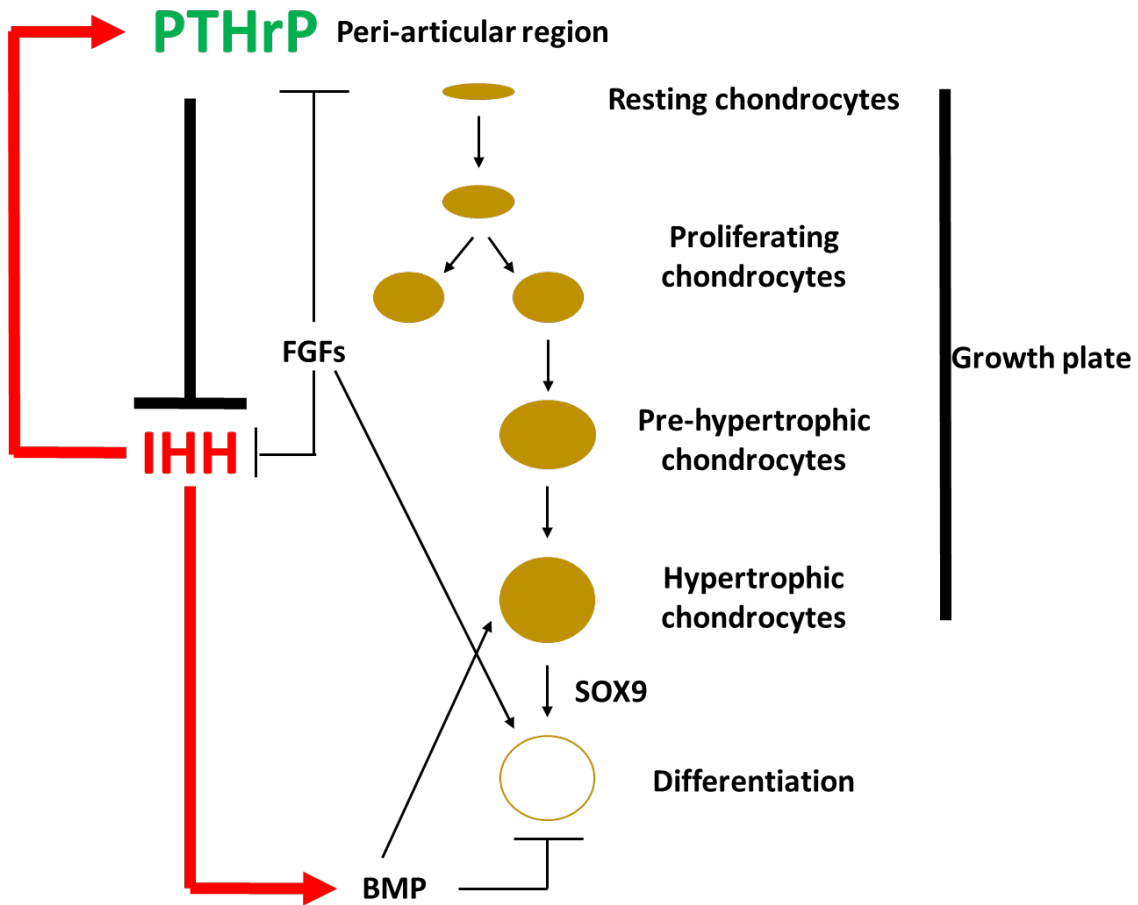


Figure 1.7 Model of the function of PTHrP/Ihh signalling in regulation in chondrocyte differentiation. Chondrocyte proliferation and differentiation follows along the longitudinal axis. The length of the proliferative zone is determined by the rate of periarticular chondrocyte differentiation, columnar chondrocyte proliferation and hypertrophy. BMP signalling promotes chondrocyte differentiation into hypertrophic chondrocyte through Ihh.

1. 2. 2. 2. Chondrocyte hypertrophy

Endochondral ossification includes the differentiation of chondrocytes to the hypertrophic chondrocytes, ECM calcification, vascular invasion, and eventually the formation of bone tissue (Ferguson, Miclau et al. 1998, Colnot and Helms 2001, Ballock and O'Keefe 2003, Provot and Schipani 2005). The main physical difference between a proliferative chondrocyte and hypertrophic chondrocyte is that the cellular fluid volume increases by almost 20 times in hypertrophic cells. *Ihh* as mentioned above, is expressed in pre-hypertrophic chondrocytes and regulates the expression of hypertrophic markers include Type X collagen (*COL10A1*) and alkaline phosphatase. *Ihh* is crucial for endochondral bone formation, skeletal angiogenesis and perichondral maturation. Runx2 acts as a positive

regulator in chondrocyte maturation into hypertrophic chondrocytes. It is expressed in the adjacent perichondrium, pre-hypertrophic chondrocytes, and less in late hypertrophic chondrocytes, overlapping with the expression of *Ihh*, *Col10a1*, and *Bmp-6* (Ferguson, Miclau et al. 1998, Kim, Otto et al. 1999, Enomoto, Enomoto-Iwamoto et al. 2000, Takeda, Bonnamy et al. 2001, Colnot 2005). *Runx2* deficient mice show blocked differentiation of chondrocytes into hypertrophic chondrocytes, demonstrating that *Runx2* is important for the hypertrophic differentiation of chondrocytes (Komori, Yagi et al. 1997, Otto, Thornell et al. 1997). *Mmp13* is a downstream target of *Runx2* and is expressed in hypertrophic chondrocytes. *Mmp13* deficient mice show abnormal endochondral bone development in the growth plate, which is partially a consequence of imperfect ECM remodelling. Extracellular proteins such as osteopontin, have restricted expression in terminally differentiated hypertrophic chondrocytes, but its expression is expanded in the hypertrophic zone of the growth plate of *Mmp13* deficient mice, indicating the exit of late differentiated chondrocytes from the growth plate is delayed (Inada, Wang et al. 2004, Stickens, Behonick et al. 2004). In addition, *Col10a1* deficient mice showed a shorter proliferative and hypertrophic zone and also abnormal mineral deposition (Gress and Jacenko 2000, Jacenko, Chan et al. 2001). ECM remodelling and terminal differentiation of chondrocytes contributes to hypertrophic chondrocytes eventually undergoing apoptosis, which is the dominant rate-limiting step for angiogenesis and osteoblast recruitment during endochondral ossification (Ferguson, Miclau et al. 1998, Vu, Shipley et al. 1998, Gerber, Vu et al. 1999, Jacenko, Chan et al. 2001, Ortega, Behonick et al. 2004).

Angiogenesis in endochondral ossification is a process where blood vessels invade the perichondrium and hypertrophic zone, eventually replacing the tissue with bone (Colnot, Lu et al. 2004, Colnot 2005). A longer length of the hypertrophic zone was observed after removal of *Vegf* and VEGF receptors (Gerber, Vu et al. 1999, Maes, Carmeliet et al. 2002). VEGF plays roles in vascular invasion through its receptors on the cells of the perichondrium and hypertrophic chondrocytes (Colnot and Helms 2001). VEGF can be released from the ECM by MMPs, such as MMP-9, which may explain why *Mmp-9* deficient mice have a similar growth plate phenotypes as those that lack either VEGF or VEGF receptors (Vu, Shipley et al. 1998). MMP-14 is more widely expressed than MMP-9 and *Mmp14* deficient mice showed severe skeletal development defects and impaired vascularisation of chondroepiphyses,

which result in delayed secondary ossification, indicating MMP14 is important for chondrocyte differentiation and secondary ossification (Zhou, Apte et al. 2000).

AP-1 transcription factor members also function during endochondral ossification and skeletal development; for example, one of the AP-1 family member, c-Fos is a key regulator of osteoclasts and osteoblast differentiation (Grigoriadis, Schellander et al. 1993, Reimold, Grusby et al. 1996, Jochum, Passegue et al. 2001, Hess, Hartenstein et al. 2003, Karreth, Hoebertz et al. 2004). Mengshol et al. identified that Runx2 interacts with AP-1 family members to regulate PTHrP-dependent *Mmp-13* expression (Mengshol, Vincenti et al. 2001). *Mmp-13* is a target of c-Maf, which is expressed in hypertrophic chondrocyte at E14.5-E18.5 and is required for normal chondrocyte differentiation during endochondral ossification. *c-Maf* deficient mice showed shorter bone length, abnormal hypertrophic chondrocyte differentiation, and an accumulation of hypertrophic chondrocytes at 4-week-old age, which are similar to mice lacking *Mmp13* (MacLean, Kim et al. 2003).

1. 2. 3. **Osteoarthritis**

1. 2. 3. 1. **Current opinions on osteoarthritis**

Osteoarthritis (OA) is a chronic degenerative joint disease that is characterised by gradual loss of cartilage, expansion of subchondral bone, formation of osteophytes, thickened and inflamed synovium, and thickened joint capsule and ligaments (Figure 9) (Goldring and Goldring 2007). Half of the world's population over the age of 65 are predicted to suffer from OA (Bijlsma, Berenbaum et al. 2011). OA is the most common reason for pain and disability in the elderly (Arden and Nevitt 2006). The disease mainly occurs in joints of knee, hip, and hands. The pathophysiology of OA is complicated and currently unclear. Many factors are involved in the development of OA such as ageing, biomechanical stimulation, and chronic inflammation along with genetic factors (Miyaki and Asahara 2012).

Articular cartilage is composed of a cellular element, chondrocytes, and ECM. Chondrocytes are responsible for the synthesis and secretion of specialised proteins (particular type II collagen and aggrecan) to form the ECM. They also play a crucial role in maintaining a balance between anabolism and catabolism for cartilage homeostasis. In OA, the phenotype of chondrocytes changes, with a shift from cartilage homeostasis to excessive ECM

degradation (Blanco, Rego et al. 2011). Proteolytic enzymes like MMP-13 and ADAMTS5 are responsible for ECM degradation by targeting type II collagen and aggrecan, respectively (van den Berg 2011).

The number of chondrocytes are reduced during the progress of OA, which results in poor responsiveness to growth factors, such as insulin-like factor-1, bone morphogenetic protein-7, and transforming growth factor-beta (TGF- β) (Li, Wei et al. 2013). Moreover, degradation of type II collagen and aggrecan are observed during this process (Huang, Lai et al. 2011). It is also reported that epigenetic alternations, including miRNAs, contribute to OA pathogenesis (Reynard and Loughlin 2012, Barter, Tselepi et al. 2015). Several individual miRNAs have been reported to play important roles in cartilage homeostasis and OA pathogenesis (Table 1).

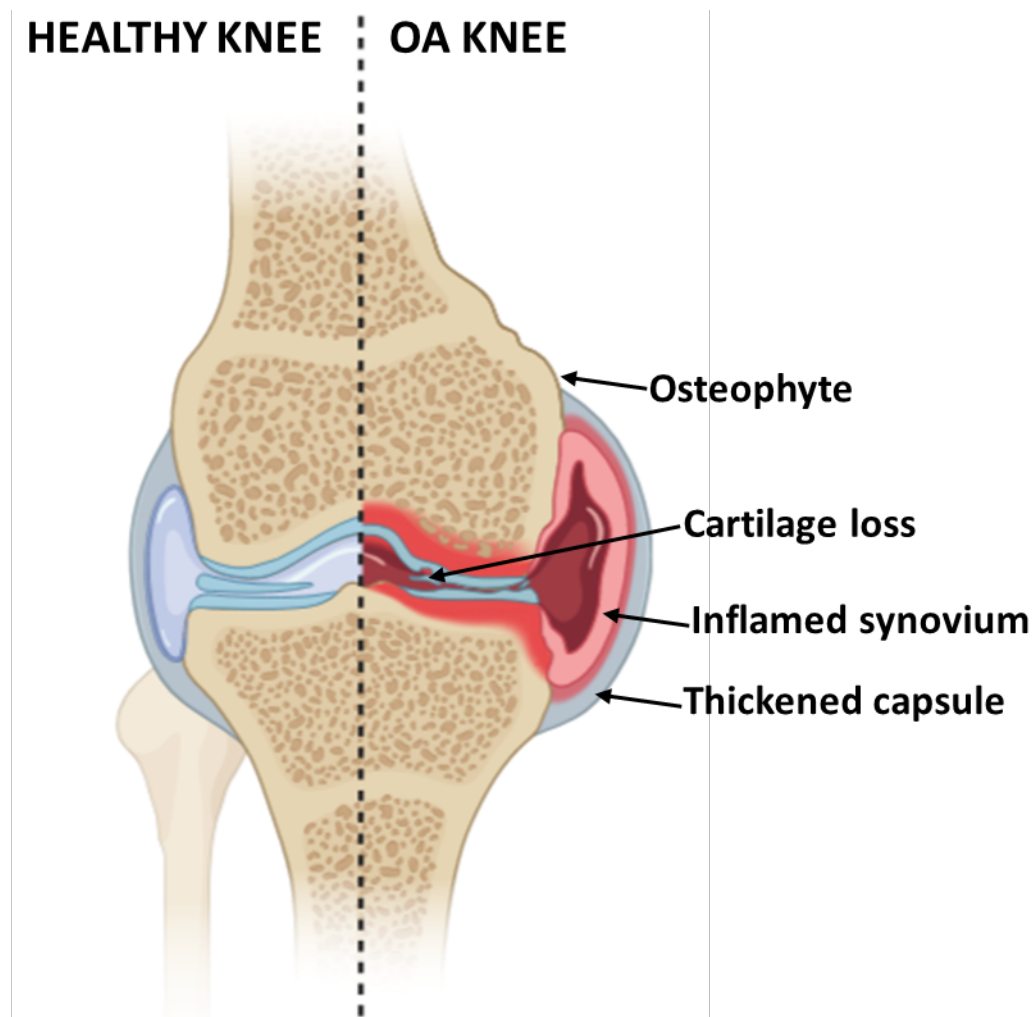


Figure 1.8 Schematic representing the comparison between healthy knee and OA knee, which is characterised by cartilage loss, thickened capsule, inflamed synovium, and formation of osteophyte.

1.2.3.2. Relationship between OA risk factors and microRNAs

Several factors have been identified as OA risk factors such as ageing, mechanical stress, obesity, genetics, and inflammation. OA risk factors altered the homeostatic balance between degradation and repair mechanisms in joint tissue (Hashimoto, Nakasa et al. 2008, Goldring and Marcu 2009, Lotz and Kraus 2010, Miyaki and Asahara 2012). The loss of homeostatic balance in articular cartilage induces differentiation, proliferation, senescence, and cell death through a switching from anabolism to catabolism (Figure 10) (Miyaki and Asahara 2012).

Chen et al. showed that miRNAs are involved in pathways that are tightly associated with the ageing process, including DNA repair, apoptosis, oxidative defence, intermediate metabolism, and mitochondrial oxidative phosphorylation (Chen, Chiou et al. 2010). In principle, stress accumulation within cells induced by abnormal miRNA expression which may, in turn, be involved in OA development (Miyaki and Asahara 2012). A miRNA expression profile generated from the comparison of human OA femoral head cartilage with human non-OA cartilage from femoral neck fracture patients revealed that several miRNAs are significantly dysregulated in expression and thus may play a role in OA pathogenesis (Swingler, Wheeler et al. 2012). Another comparison between human knee OA cartilage and non-OA cartilage from fracture patients characterized 16 miRNAs differentially expressed in OA cartilage (Iliopoulos, Malizos et al. 2008). By overlapping RNA-seq data of miRNA and mRNA using preserved and lesioned human OA cartilage that are obtained from the same patient, a miRNA-mRNA interactome in the OA cartilage has been described which contains 142 miRNAs and 2387 genes as significantly differential expressed between the cartilage states, and a regulatory network of 62 miRNAs targeting their 238 potential target mRNAs were further created (Coutinho de Almeida, Ramos et al. 2019).

The appropriate mechanical load is required to maintain articular cartilage homeostasis through regulating ECM synthesis, with reduced mechanical load blocking nutritional intake for cartilage. Excessive mechanical load inhibits ECM production. Imbalanced loading for example caused by joint injury, gives rise to long term pain for individuals and even worse leads to post-traumatic arthritis (Lotz and Kraus 2010). When comparing bovine non-and-weight-bearing articular cartilage, miR-222 expression is elevated, an indication the miRNA

is a regulator of mechanotransduction. In addition, in human articular chondrocytes that were pre-cultivated under chondrogenic conditions before treating with dynamic compression loading, miR-222 expression was upregulated, further evidence that this miRNA is mechanosensitive in cartilage chondrocytes (Dunn, DuRaine et al. 2009, Stadnik, Gilbert et al. 2021). Altered miRNA expression in articular cartilage is associated with OA pathogenesis (Araldi and Schipani 2010, Swingler, Wheeler et al. 2012) with a small number of miRNAs previously identified as being mechanosensitive in cartilage chondrocytes (Dunn, DuRaine et al. 2009, Guan, Yang et al. 2011, Jin, Zhao et al. 2014, Cheleschi, De Palma et al. 2017). A discrete subset of miRNAs have been shown to be differentially regulated in response to ‘non-beneficial’ loading in tissue-engineered human cartilage and bovine articular cartilage (Hecht, Johnstone et al. 2019, Stadnik, Gilbert et al. 2021). Since abnormal mechanical loads is a primary risk factor for OA development, non-physiological loading will influence *in situ* cartilage ECM homeostasis via miRNA regulation.

Inflammatory cytokines such as interleukin 1 β (IL-1 β) and tumour necrosis factor α (TNF- α) are expressed in response to joint trauma, OA development and cartilage damage, and lead to a disruption in cartilage homeostasis (Hashimoto, Nakasa et al. 2008, Goldring and Marcu 2009). Akhtar et al. showed that 42 miRNAs were down-regulated in human OA chondrocytes when treated with IL-1 β , while miR-146 and miR-491 were up-regulated. (Akhtar, Rasheed et al. 2010). The expression of miR-146a was increased in early OA cartilage, and decreased in severe OA cartilage, and also plays a role in down-regulating IL-1 β induced TNF- α production (Jones, Watkins et al. 2009, Yamasaki, Nakasa et al. 2009). Together, these results demonstrated that miRNAs are connected closely with OA risk factors, and are involved in maintaining cartilage homeostasis.

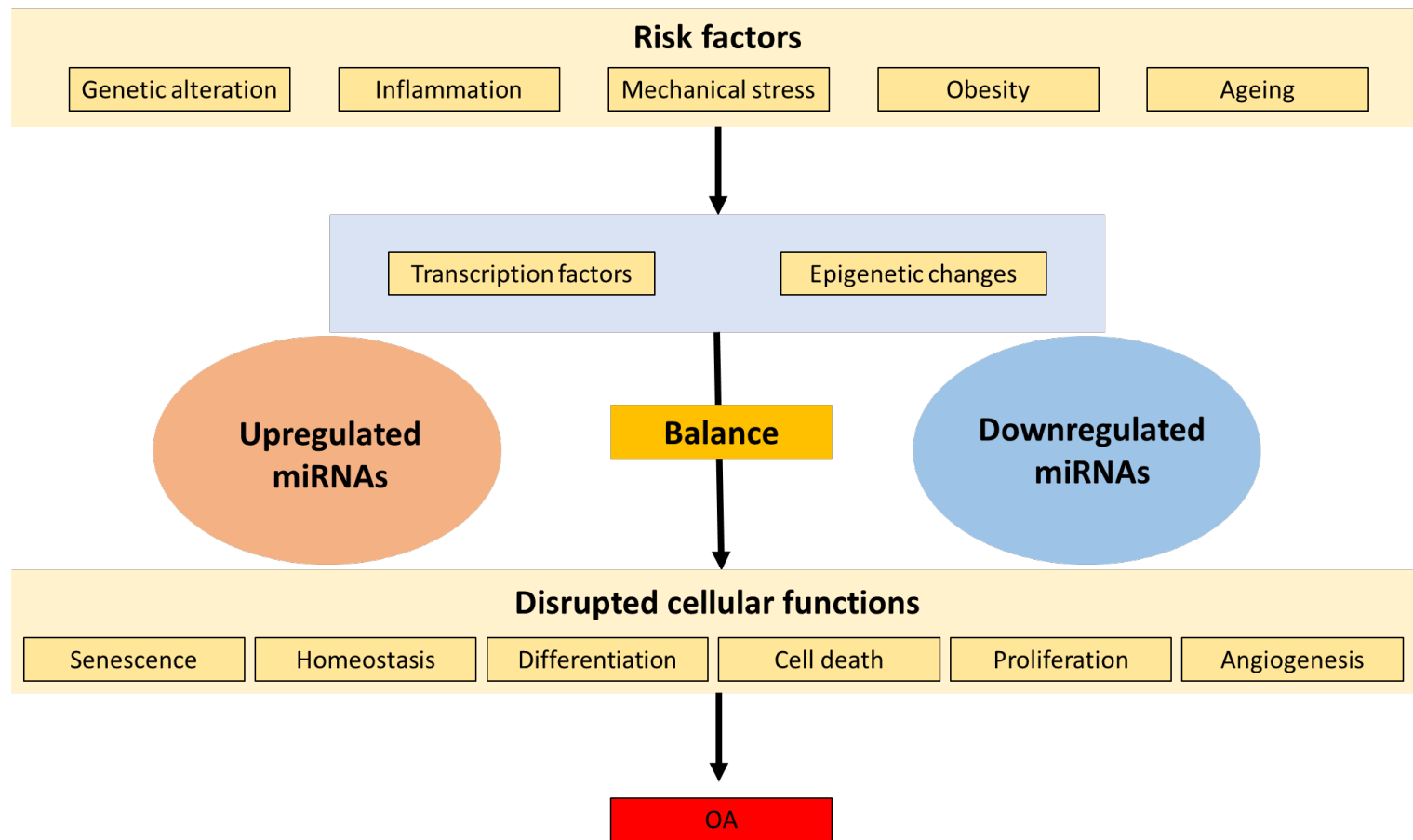


Figure 1.9 The role of miRNAs in OA pathogenesis. OA is the outcome following the loss of articular homeostasis (the balance between degradation and repair mechanisms in articular cartilage). Multiple risk factors contribute to change transcription factor regulation and the epigenetic status in cells, which in turn affect the expression of miRNAs. However, either upregulation of miRNAs or downregulation of miRNAs are partially responsible for OA pathogenesis (Miyaki and Asahara 2012).

1. 3. MicroRNA-140

Weinholds et al. reported that the expression of most miRNAs exhibits a tissue-specific pattern and are important for tissue differentiation and/or maintenance of tissue identity (Wienholds, Kloosterman et al. 2005). Among known miRNAs, microRNA-140 (miR-140) has been widely studied and is selectively expressed in cartilage tissue of zebrafish and mice. As a result of this tissue-selectivity, miR-140 was the first miRNA studied in cartilage and osteoarthritis (Wienholds, Kloosterman et al. 2005, Tuddenham, Wheeler et al. 2006, Nakamura, Inloes et al. 2011, Gabay and Clouse 2016). MiR-140 is generated from the *Mir140* gene, a highly conserved gene in vertebrates, which is located between exons 16 and 17 of the ubiquitin E3 ligase (*Wwp2*), on chromosome 8 in mouse and chromosome 16 in humans (Araldi and Schipani 2010). Expression of miR-140 seems to be regulated in both a *Wwp2* transcription-dependent and independent manner (Nakamura, He et al. 2008, Yang, Qin et al. 2011, Yamashita, Miyaki et al. 2012, Inui, Mokuda et al. 2018, Shvedova and Kobayashi 2020). However, in zebrafish *Wwp2* knock-down results in a phenotype which includes palate and trabeculae fusion, a different phenotype from that observed in *Mir-140* deficient zebrafish. These data, indicate that *Mir-140* and its host gene have different biological roles in bone development of zebrafish (Nakamura, He et al. 2008).

1. 3. 1. Expression of microRNA-140

MiRNA expression is tightly regulated by several mechanisms include DNA methylation, and histone deacetylation - general mechanisms involved in the regulation of gene expression in mammalian development and disease (Bandres, Agirre et al. 2009, Li, Marin-Muller et al. 2009, Liu, Chen et al. 2013).

In zebrafish, Nakamura et al. identified that miR-140 was exclusively expressed in cartilage using *in situ* hybridization. The first evidence that miR-140 was essential for cartilage development again came from zebrafish where smaller pharyngeal cartilage was observed after depleting *Mir-140* expression using anti-sense oligonucleotides, with the phenotype rescued after injection of a miR-140 duplex (Nakamura, He et al. 2008). In mouse, *Mir-140* is also exclusively expressed in cartilage, starting during embryogenesis during long and flat bone development (Tuddenham, Wheeler et al. 2006). Confirming miR-140 expression is

highly conserved, Miyaki et al. compared the miR-140 expression between human primary articular chondrocytes and undifferentiated human bone marrow-derived mesenchymal stem cells (BMSCs) and confirmed that miR-140 is abundantly expressed in primary human articular chondrocytes (Miyaki, Nakasa et al. 2009).

As with all microRNAs, miR-140 gives rise to two transcripts, miR-140-5p and miR-140-3p, yet unlike many microRNAs both appear expressed. When comparing hip cartilage from patients with femoral neck fractures to OA hip cartilage, expression of miR-140-5p is significantly higher in the OA tissue, but a significant reduction of its expression is observed in OA knee cartilage compared to normal knee cartilage (Miyaki, Nakasa et al. 2009, Swingler, Wheeler et al. 2012). MiR-140 was found to negatively correlate with *ADAMTS5* expression in OA chondrocytes stimulated with IL-1 β , with the increase in *ADAMTS5* expression reversed by miR-140 over-expression. Moreover, in *Mir-140* deficient mice spontaneous proteoglycan loss and fibrillation of articular cartilage was observed, with these OA-like changes associated with an increase in *Adamts5* expression. Using a 3'UTR luciferase reporter assay, *Adamts5* was identified as a direct target of *Mir-140-5p* (Miyaki, Nakasa et al. 2009, Miyaki, Sato et al. 2010). In addition to *Adamts5*, *Dnpep* was identified as *Mir-140* target gene in chondrocytes. *Dnpep* is antagonistic to BMP signalling (Nakamura, Inloes et al. 2011).

During chondrogenesis of human bone marrow-derived mesenchymal stem cells (BM-MSCs) in pellet cultures, miR-140 expression level was increased, positively correlating with the expression of *SOX9* and *COL2A1* (Miyaki, Nakasa et al. 2009). Again, during BM-MSC chondrogenesis, the removal of *SOX9* expression, TGF β , or high-density pellet culture all negatively impacted miR-140 (Barter, Tselepi et al. 2015). Interestingly, an unbiased gene expression analysis demonstrates that during chondrogenesis only predicted targets of miR-140-5p, as opposed to other miRNAs, are enriched in down-regulated genes, the implication being that this is the most important of all induced microRNAs for chondrogenesis.

A number of other MiR-140 target genes are implicated in chondrocyte differentiation, such as *Cscl2* and *Smad3* (Nicolas, Pais et al. 2008, Pais, Nicolas et al. 2010). miR-140 is also proposed to regulate chondrocyte differentiation through regulating the PTHrP-HDAC4 pathway, and *Mir140*^{-/-} *PTHrP*^{+/+} and *Mir140*^{-/-} *Hdac4*^{+/+} compound mutant mice showed more severe skeletal development when compared to miR-140^{-/-} mice (Papaioannou,

Mirzamohammadi et al. 2015); MiR-140 also negatively regulates the expression of *MMP13*, an important collagenase in OA pathology (Miyaki, Nakasa et al. 2009, Liang, Zhuang et al. 2012, Zhang, Ma et al. 2013). In addition, expression of *IGFBP-5* is negatively regulated by miR-140 (Tardif, Hum et al. 2009). Together, these findings lead to a conclusion that miR-140 expression is tightly associated with genes that are important in chondrocyte development or pathogenesis of OA.

1. 3. 2. The functional role of microRNAs in skeletogenesis

Two mechanisms contribute to skeletal development including intramembranous ossification and endochondral ossification (Karsenty and Wagner 2002). As described above (Section 1.1.1), conditionally removal of *Dicer* in limb bud mesenchyme of early mouse embryo (E7.5) using a paired-related homeobox gene-1 (*Prx1*) enhancer-driven CRE results in a much smaller limb formed with an increase in cell death, initially suggested miRNAs are essential for limb development (Harfe, McManus et al. 2005). Following on, Kobayashi et al. reported that specific later stage depletion of *Dicer*, using a type II collagen (*Col2*) promoter-driven CRE in chondrocytes reduced chondrocyte proliferation and accelerated the differentiate of proliferative chondrocytes into hypertrophic chondrocytes, observations which would account for the smaller size of long bones in these mice (Kobayashi, Lu et al. 2008). Kobayashi et al. also created a chondrocyte-specific deletion of *Drosha* and articular cartilage specific *Drosha*-null mice using *Col2*-CRE and Lubricin/Proteoglycan 4 (*Prg4*) promoter-driven CRE, respectively. Conditional deletion of *Drosha* in the growth plate chondrocytes (*Col2*-expressing cells) of mice showed similar skeletal defects as that of *Dicer* deletion mice, such as a lethal skeletal dysplasia, and reduced chondrocyte proliferation. Conditional deletion of *Drosha* in the articular chondrocytes (*Prg4*-expressing cells) caused cell death and reduced proteoglycan staining in the tissue. OA-like changes such as surface erosion and cleft formation were found in the articular cartilage of these mice, indicating that microRNAs that are important for chondrocyte development in the growth plate can also be involved in maintaining structure integrity of the articular cartilage (Kobayashi, Papaioannou et al. 2015).

Miyaki et al. were the first to demonstrate that the lack of a single microRNA, in this case *Mir-140*, results in a mouse of short stature, low body weight, and domed skull (Miyaki, Sato

et al. 2010). This phenotype is potentially due to impaired proliferation of chondrocytes in growth plate. Papaioannou et al. also showed acceleration of proliferating chondrocyte differentiate into hypertrophic chondrocytes in mouse tibia growth plate in the absence of *Mir-140*, along with inhibition of differentiation from resting chondrocytes into columnar proliferating chondrocytes. Furthermore, deletion/inhibition of *let-7* miRNA, through overexpression of *Lin28a*, combined with *Mir140* deletion caused a more severe skeletal growth defect than removal either *Mir-140* or overexpression of *Lin28a* alone (Papaioannou, Inloes et al. 2013). During chondrogenesis, miR-140 is predominately expressed in the proliferative zone and is proposed to play a role in maintaining PTHrP/Ihh regulatory activity by suppressing MEF2C, a well-known transcription regulator to drive hypertrophy, through negatively regulating p38 mitogen-activated protein kinase (MAPK) signalling (Papaioannou, Mirzamohammadi et al. 2015). As described above, miR-140 also negatively regulates the expression of HDAC4, which in turn repress the expression of Runx2 and MEF2C (Tuddenham, Wheeler et al. 2006). A second *Mir-140* targeted mouse confirmed the phenotype of the original line developed by Miyaki *et al.* Through the analysis of growth plate gene expression, *Dnpep* was identified as a miR-140 target gene. Overexpression of *Dnpep* showed a weak effect on BMP signalling, and thus *Mir140* is posited to also play a role in BMP signalling. Supporting this, knockdown of *Mir140* in limb bud micromass cultures arrests chondrogenic proliferation via regulating Sp1, which is downstream of BMP signalling (Figure 11) (Nakamura, Inloes et al. 2011, Yang, Qin et al. 2011). Transgenic mice overexpressing MiR-140 in a cartilage specific manner did not influence cartilage development, however, this overexpression did protect animals against antigen-induced arthritis (Miyaki, Sato et al. 2010). Grigelioniene et al. reported that gain-of-function mutations in *MIR140* locus in human results in abundant mutant miR-140-5p expression, which derepress wild type miR-140-5p targets and repress mutant miR-140-5p targets, and in turn causes a novel autosomal dominant human skeletal dysplasia (Grigelioniene, Suzuki et al. 2019).

Given that the phenotypes of the different *Mir140* deficient mice are not as severe as conditional Dicer depletion mice, the implication is that other microRNAs (such as *Let-7*) are also important for limb development. Apart from miR-140, another microRNA cluster has been reported to be tightly associate with mouse skeletal development, miR-17~92, which is

encoded by *Mirc1*. The embryos of *Mir17~92* deletion mice have severe skeletal development defects and general delayed membranous and endochondral ossification, leading to the phenotype of short stature, craniofacial abnormalities, limb and digit malformations, similar to patients with Feigold syndrome type 2. This reveals *Mir17~92* is essential for normal growth and skeletal development in both human and mouse (de Pontual, Yao et al. 2011, Han, Vidigal et al. 2015, Mirzamohammadi, Kozlova et al. 2018).

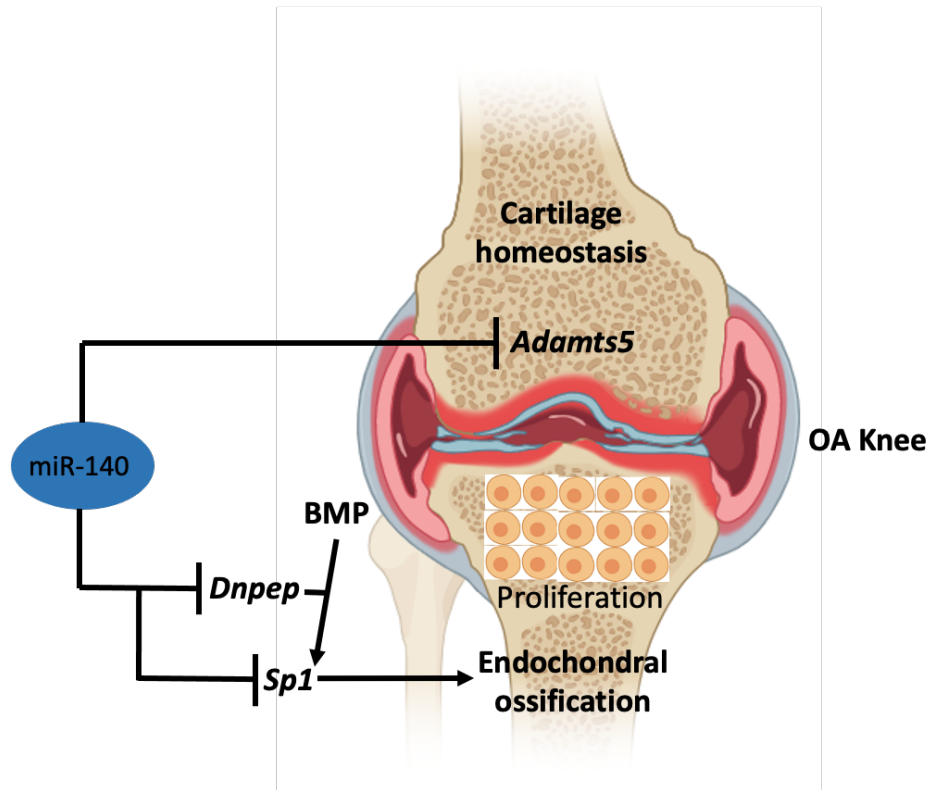


Figure 1.10 The role of miR-140 in endochondral bone development and cartilage homeostasis through targeting *Dnpep* and *Adamts5*, respectively (Miyaki and Asahara 2012).

1. 3. 3. microRNA-140 in OA pathogenesis

Numerous publications have illustrated that miRNAs are abnormally expressed during the degradation of articular cartilage in OA (Gibson and Asahara 2013), though results are often contradictory. There are probably a number of reasons for this inconsistency, variations in the comparator groups (e.g. normal vs. OA, or damaged vs. intact cartilage), joint site examined and technology platforms for miRNA profiling. Of the many differentially expressed miRNAs identified, miR-140 is reportedly approximately fourfold decreased in OA

knee cartilage, yet increased in OA hip (Miyaki, Nakasa et al. 2009, Tardif, Hum et al. 2009, Swingler, Wheeler et al. 2012), indicating the miRNA has a complex role OA pathogenesis.

The articular cartilage of *Mir140*-null mice shows spontaneous age-related OA-like cartilage damage (Miyaki, Sato et al. 2010). The decreased expression level of miR-140 reported in OA cartilage may affect gene expression that is conducive to OA development (Miyaki, Nakasa et al. 2009). In a surgical model to induce abnormal mechanical loading on the mice knee joint, resection of the medial meniscotibial (MMTL), miR-140 deficient mice showed accelerated proteoglycan loss and fibrillation of articular cartilage as compared with wild type animals, indicative of an OA-like pathology. As described above, this could be ascribed to an increase in *Adamts5* expression, an identified target gene of *Mir-140* (Figure 12) (Miyaki, Sato et al. 2010). However, the repression of *Adamts5* by *Mir-140* is modest, which means in order to investigate the role of miR-140 in OA pathogenesis, other targets of miR-140 need to be confirmed. Databases like TargetsScan predicted 1690 genes as human miR-140 target genes through searching for predict binding sites of 3'UTR that match the seed region of each miRNA. However, in addition to binding to 3'UTR region of mRNAs, miRNAs can, less commonly, also interact with coding region of mRNAs or bind to 5'UTR (Lytle, Yario et al. 2007, Tay, Zhang et al. 2008, Lee, Ajay et al. 2009, Kumar, Wong et al. 2012).

Taken together, these studies confirm miR-140 is an important regulator in OA pathogenesis, regulating target genes normally important for cartilage homeostasis. Those findings strongly imply that miRNA dysregulation as a mechanism for OA pathogenesis, modulation of which could influence disease progression.

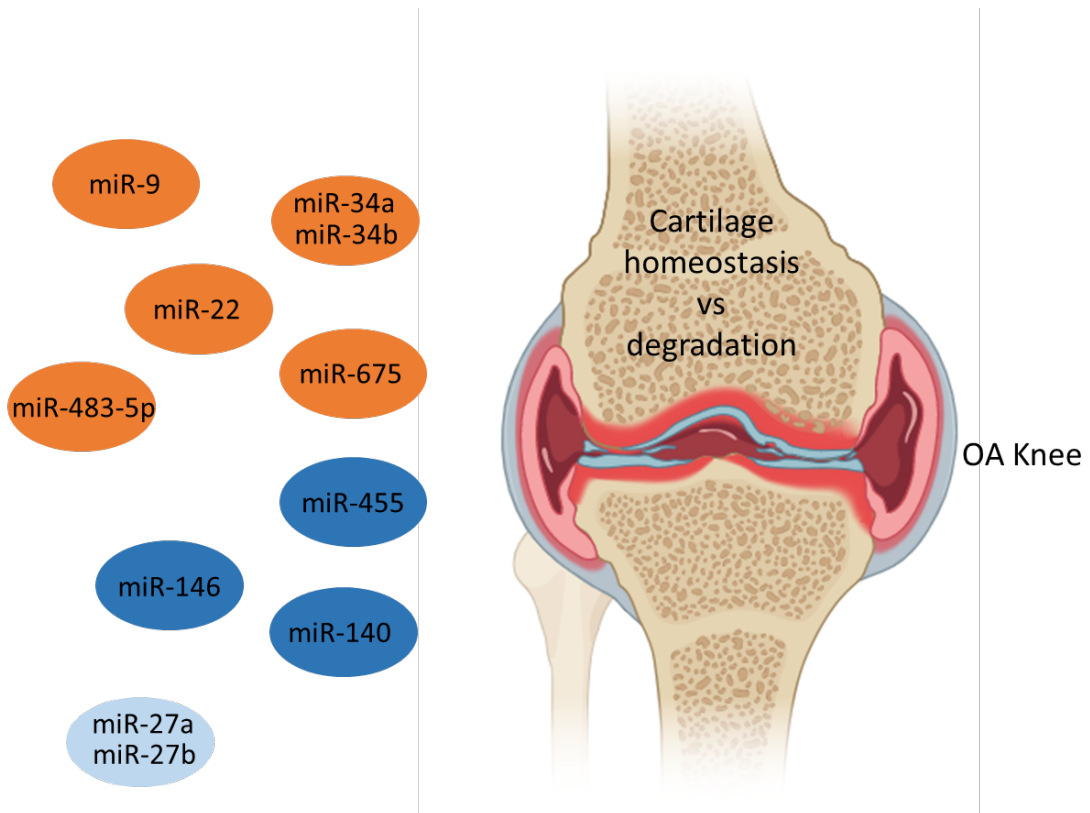


Figure 1.11 The list on the left are differently expressed miRNAs in OA samples. Orange circle represents increased miRNAs in OA, and light blue circle stand for decreased miRNAs in knee OA, whereas dark blue indicates the miRNAs that are expressed variously in OA pathogenesis (Miyaki and Asahara 2012, Endisha, Rockel et al. 2018).

1. 4. MicroRNA-455

Both mature miR-455-5p and miR-455-3p are derived from gene *Mir455*, which is located in intron 10 of the host gene *Col27a1* that encodes a fibrillar collagen (Pace, Corrado et al. 2003). Expression of *COL27A1* is regulated by *SOX9*, and miR-455 is co-ordinately expressed with the host gene, thus it is assumed that miR-455 potentially uses the same promoter as *COL27A1* (Jenkins, Moss et al. 2005, Swingler, Wheeler et al. 2012, Lalevee, Lapaire et al. 2014, Barter, Tselepi et al. 2015). Human *COL27A1* is approximately 156kbp long and consists of 61 exons that locate at chromosome 9q32-33, whereas the homologous mouse *Col27a1* locates at chromosome 4 (Pace, Corrado et al. 2003). Human *COL27A1* is expressed selectively in cartilage, with an expression pattern similar to *COL2A1* and *COL13A1*. The *COL27A1* protein, pro α 1 (XXVII), is an important component of cartilage ECM. Similarly, mouse *col27a1* is highly expressed in adult cartilage and in cartilage development (from E14.5). *COL27A1* mutation is thought to underlie Steel syndrome, a rare Mendelian disorder of the skeleton which amongst other phenotypes results in short stature and hip pathology (Gonzaga-Jauregui, Gamble et al. 2015, Kotabagi, Shah et al. 2017). Similarly, mice with a large coding deletion in *Col27a1* exhibit severe chondrodysplasia (Plumb, Ferrara et al. 2011).

The expression level of miR-455-3p increases during stem cell-derived chondrogenesis (Swingler, Wheeler et al. 2012, Zhang, Kang et al. 2012). Other studies evidenced that miR-455-3p acts as an important transcription regulator in chondrogenesis and in cartilage degradation through inhibiting *RUNX2*, *HDAC2*, *HDAC8*, and/or *DNMT3A*, indicating that miR-455-3p is the dominant arm (Zhang, Hou et al. 2015, Chen, Chen et al. 2016, Sun, Zhao et al. 2018). Thus, taking these data into account the hypothesis is that in addition to miR-140, miR-455 will act as another important regulator in chondrogenesis and OA pathogenesis.

1. 4. 1. microRNA-455 in chondrogenesis and OA pathogenesis

Swingler et al. demonstrated the upregulation of both miR-455-3p and miR-455-5p during chondrogenic differentiation and hypertrophy in the murine ATDC5 cell model, an expression pattern similar to miR-140. Whole-mount *in situ* hybridisation revealed miR-455

expression in developing long bones in chicks, with expression restricted to developing joints, cartilage and perichondrium with age. Furthermore, *in situ* hybridisation in mouse embryos showed a similar expression of miR-455 in long bones and joints, but additionally observed miR-455 expression in the sutural of the developing skull and in the interdigital region of the developing paw, indicating miR-455 expression may regulate apoptosis during development (Swingler, Wheeler et al. 2012).

Many factors are implicated to the regulation of postnatal chondrogenesis, such as transcription factors, growth factors, ECM, and miRNAs (Shang, Liu et al. 2013). Profiling of miRNA expression during human BM-MSCs chondrogenic differentiation also identified significant upregulation of miR-455-3p and miR-455-5p, concomitant with an increase in miR-140 expression. Removal of SOX9, TGF β , or cell condensation prior to or during chondrogenesis prevented the increase in miR-455-5p and miR-455-3p expression (Barter, Tselepi et al. 2015). Similarly, Zhang et al. identified miR-455-3p amongst 12 miRNAs that are upregulated during chondrogenic differentiation of human adipose-derived stem cells (HADSCs), suggesting that miR-455-3p may play a crucial regulatory role in chondrogenesis (Zhang, Kang et al. 2012).

Using *in situ* hybridisation to detect miR-455-3p, Chen *et al.* showed expression of the miR-455-3p mainly in proliferative and pre-hypertrophic chondrocytes of E16.5 mouse limbs, similar to findings by Swingler et al (Swingler, Wheeler et al. 2012, Chen, Chen et al. 2016). A similar expression pattern of *Sox9* was observed from *in situ* hybridisation (Chen, Chen et al. 2016). The expression pattern of miR-455-3p during chondrogenesis in ATDC5 cells mirrored that of *Hdac2* and *Hdac8*, which were subsequently verified as direct targets of miR-455-3p by 3'UTR luciferase analysis. Meanwhile, throughout the whole ATDC chondrogenic differentiation time-course, *Sox9* expression mirrors that of miR-455-3p, as with the *in vivo* *in situ* hybridisation data (Chen, Chen et al. 2016). Sun *et al.* also reported the upregulation of miR-455-3p during human BMSCs chondrogenic differentiation with the expression decreasing at later stages (Sun, Zhao et al. 2018).

The bone matrix gelatin (BMG) rat model can be used to demonstrate different development stages of cartilage formation *in vivo*. Min et al. implanted BMG in supraspinatus and rhomboid muscles of Dark Agouti (DA) rats, collected the generated cartilaginous tissue at 1, 2, 3, and 4 weeks after implantation, and found that miR-455-3p

was highly expressed at 1 week and 2 weeks but dropped from 3 weeks onwards, suggesting that miR-455-3p expression is correlated with cartilage development (Min, Zhang et al. 2015).

MiR-455 appears to be regulated by TGF- β , with the miRNA then targeting several factors involved in TGF- β signalling, including *Smad2*, activin receptor 2B (*Acvr2b*), and chordin-like 1 (*Chrdl1*). The proposal is that miR-455 represses *Smad2/3* (TGF- β) and promotes *Smad1/5/8*-dependent BMP signalling through competition for the co-Smad, Smad4. Thus miR-455-3p overexpression decreases TGF β signalling and promotes chondrocyte terminal differentiation (Swingler, Wheeler et al. 2012). TGF β signalling is very important for maintaining homeostasis of articular cartilage, and decreased TGF β signalling through the SMAD2/3 pathway induced by miR-455 expression could contribute to the progression of OA. Mutant Smad3 mice show degenerative knee joints with an increase in the number of hypertrophic chondrocytes in the articular cartilage, similar to human OA (Yang, Chen et al. 2001). Others also confirmed that miR-455-3p expression strikingly increased during chondrogenic differentiation of mouse ATDC5 cells, human adipose-derived stem cells (hADSCs), and human bone mesenchymal stem cells (hBMSCs) (Swingler, Wheeler et al. 2012, Zhang, Kang et al. 2012, Zhang, Hou et al. 2015, Sun, Zhao et al. 2018, Hu, Zhao et al. 2019, Mao, Kang et al. 2019, Wen, Li et al. 2020, Ito, Matsuzaki et al. 2021). Published work also showed that miR-455 deficient mice have a spontaneous OA phenotype (Hu, Zhao et al. 2019, Mao, Kang et al. 2019, Wen, Li et al. 2020, Ito, Matsuzaki et al. 2021). Recently published work showed that *Mir455*-null mice had a similar skull length, trabecular bone volume fraction of femur, volumetric BMD of cancellous bone of femur, and body weight when compared to control mice. Further, *Epas1*, a central transactivator that targets several crucial catabolic genes, was confirmed as a target gene of miR-455, which may help us to get a deeper understanding of the mechanisms of miR-455 in chondrogenesis and OA pathogenesis (Ito, Matsuzaki et al. 2021). As with miR-140, miR-455 expression is increased in human hip OA cartilage as compared to NOF cartilage. Fully understanding the relationship between miR-455 expression and SMAD pathway and/or TGF β signalling could provide new insight into understanding the potential mechanistic link between microRNAs, chondrogenesis, and OA (Swingler, Wheeler et al. 2012).

1. 5. Project aims

Significant *in vitro* and *in vivo* evidence has confirmed the involvement of miR-140 in skeletal development and with the initiation and progression of OA. *In vitro* data indicates a similar potential importance for miR-455, though *in vivo* data is limited.

In this thesis our aim was to further characterise the function of miR-140 and miR-455, using newly generated transgenic miRNA-null mice developed using CRISPR/Cas9. To this end, we successfully generated miR-140^{-/-}, miR-455^{-/-}, and miR-140: miR-455^{-/-} (DKO, double knockout) mice. Phenotypic analysis of these novel lines is a major focus of this thesis.

To understand the molecular mechanisms and pathways that microRNAs regulate it is necessary to identify gene targets of the selected miRNAs. Though progress has been made on the identification of relevant targets for skeletogenesis and OA of miR-140, with *Dnpep* and *Adamts5*, respectively, target prediction tools suggest many more targets exist.

Moreover, the effect of miR-140 expression manipulation on *Adamts5* and *Dnpep* expression are modest, again suggesting other miR-140 target genes are likely important in cartilage. Information on the targets of miR-455 remain limited. The mechanism of action of miR-140, and potentially miR-455, may provide new insights to understand the roles of miRNAs in skeletal development and OA.

To further characterise the impact of miR-140 and miR-455 on knee articular cartilage homeostasis OA-like disease will be induced in wild-type and miRNA-null mice using the destabilization of the medial meniscus (DMM) model. Surgery will be performed at 11 week of age and then subject to histological staining (Safranin-O and Fast green staining) 8 weeks later to compare damage on knee articular cartilage between different genotypes. In addition, RNA will be extracted from the medial part of tibia plateau of all different genotypes 1 day prior to surgery and, for wild-type and *Mir140*-null mice during the time-course of disease. These RNA, along with RNA from 7-day old costal chondrocytes, will be subjected to RNA-sequencing, with the overall aim of identifying miR-140 and miR-455 cartilage targets in development and during OA pathogenesis.

Chapter 2. Materials and Methods

2. 1. Materials

2. 1. 1. Antibodies

All primary antibodies used for identifying *Mir140* growth plate target genes were rabbit polyclonal unless otherwise stated. Anti-CREB3L1/OASIS antibody (ab33051) and anti-Nrf2 antibody (ab137550) were purchased from Abcam (Cambridge, UK), Anti-Zeb1 antibody (Cat. No: #PA5-40350) was obtained from Invitrogen/Thermo Fisher Scientific (Oxford, UK). Anti-Collagen X rabbit monoclonal antibody was a kind gift from Professor Michael Briggs (Newcastle University). Anti-Ki67 rabbit monoclonal antibody (ab16667) came from Abcam. Alexa Fluro 594 goat anti-rabbit IgG (heavy and light chains (H+L)), Alexa Fluro 594 goat anti-mouse (H+L), Alexa Fluro 594 rabbit anti-goat IgG (H+L), and Alexa Fluro 488 goat anti-mouse IgG (H+L), were obtained from Thermo Fisher Scientific (Cramlington, UK). Agilent Dako (Manchester, UK) supplied Polyclonal rabbit anti-goat immunoglobulins/HRP, Polyclonal goat anti-rabbit immunoglobulins/HRP, and Polyclonal goat anti-mouse immunoglobulins/HRP. Cell proliferation labelling reagent (Bromodeoxyuridine (BrdU)) was purchased from GE Healthcare (Little Chalfont, UK). DeadEnd Fluorometric TUNEL system kit was obtained from Promega (Southampton, UK). Merck Millipore (Livingston, UK) supplied polyclonal anti-GAPDH antibody (AB2302, 1:40,000 dilution in (BSA) solution) used as an internal control to normalise sample differences.

2. 1. 2. Biochemical assay reagents

Tissue culture plates (96-well-plate, 6-well-plate), T75 culture flask (75cm²), and T25 culture flask (25cm²) were purchased from Corning/Costar (Sunderland, UK). BSA came from Fisher Scientific (Cambridge, UK). Bradford Ultra reagent were purchased from Expedeon_ (Cambridge, UK). Tissue culture dishes (100mm) were supplied by VWR (East Grinstead, UK). Disposable polystyrene serological aspirating pipettes (5ml, 10ml, 25ml) were bought from Corning/Falcon (Sunderland, UK). Natural flat cap microcentrifuge tubes (1.5mL) came from Star Lab (Blakelands, UK). Non skirted PCR 96-well plates were purchased from Cell Projects (Kent, UK). Thin-walled individual PCR tubes with flat cap (0.2 ml) came from Thermo Fisher

Scientific. Fast optical 96-well reaction real-time PCR plates with barcode (0.1 mL) were obtained from Thermo Fisher Scientific. Combitips plus (0.1ml, 0.5ml, 1.0ml) were supplied by Eppendorf Combitips Advanced (Stevenage, UK). Flat-bottomed and V-bottomed non-sterile 96-well-plates, universals (5ml, 20ml) were acquired from Barloworld Scientific (Stone, UK). Phire tissue direct PCR matrix mix, TaqMan microRNA cells-to-C_TTM kit, Cells-to-cDNA // kit and TaqMan Advanced master mix used for PCR were purchased from Thermo Fisher Scientific.

2. 1. 3. Cell lines

2. 1. 3. 1. SW1353

The SW1353 cell line derived from a primary grade II chondrosarcoma in the right humerus of 72-year-old Caucasian female. Full details of this cell line are listed on the ATCC company website (www.atcc.org), which supplied the cell line (catalogue HTB-94). For the experiment, cells were cultured in Dulbecco's modified Eagle's medium (DMEM)/F12 culture medium by the method outlined in section 2.2.1.1.

2. 1. 3. 2. Mouse costal chondrocytes

Primary mouse costal chondrocytes were isolated from 7-day-old miR-140^{-/-}, miR-455^{-/-}, DKO and WT mice that were housed at Functional Genomics Unit (FGU), Newcastle University, UK (section 2.2.5.2). The cells were cultured in DEME/F12 medium by the method outlined in section 2.2.1.2.

2. 1. 4. Cell and tissue culture reagents

DMEM, DMEM/F12, foetal bovine serum (FBS), and Dulbecco's Phosphate Buffered Saline (DPBS), non-essential amino acids, L-glutamine and penicillin-streptomycin, and Trypsin-EDTA (0.05%) phenol red were purchased from Thermo Fisher Scientific/Gibco. Dimethyl sulphoxide (DMSO) and were purchased from Sigma-Aldrich (Poole, UK). Syringe filters (0.2 µm) and syringe came from Pall Life Sciences (Portsmouth, UK). Bacto-tryptone, yeast extract and bacto-agar were purchased from Difco Laboratories (Detroit, MI, USA).

2. 1. 5. General molecular biology reagents

Triton X-100 and β -mercaptoethanol came from Sigma-Aldrich. Agarose (electrophoretic grade) was obtained from Invitrogen (Paisley, UK). RNase- and DNase-free H₂O came from Sigma-Aldrich. All reagents used for RNA work were molecular biology grade. All the other chemicals were obtained from Sigma-Aldrich, Thermo Fisher Scientific, Invitrogen Life Technologies/Thermo Fisher Scientific or BDH Chemicals (Poole, UK) unless otherwise stated.

2. 1. 6. Histological staining immunohistochemistry reagents

Mayer's hemalum solution, Haematoxylin solution and Fast-green solution were purchased from Sigma-Aldrich. Eosin Y Staining (1%, Alcoholic) came from CellPath (Powys, UK). Ethanol absolute solution came from VWR (East Grinstead, UK). Vectorshield with DAPI mounting medium used for immunohistochemistry was supplied by 2BScientific (Oxford, UK). Proteinase K powder, hydrochloric acid (HCl) solution, borate buffer powder, and formaldehyde powder came from Sigma-Aldrich.

2. 1. 7. Immunoblotting reagents

N,N,N',N'-Tetramethylethylenediamine (TEMED) and polyoxyethylene sorbitan monolaurate (Tween-20) were obtained from Sigma-Aldrich. Ammonium persulphate (APS) came from BDH Chemicals. Acrylamide Bis-Acrylamide stock solution (40% w/v Acrylamide ratio: 37.5:1 Bis-Acrylamide) was obtained from Severn Biotech (Worcestershire, UK). Immobilon-P polyvinylidene difluoride (PVDF) was purchased from Millipore (Watford, UK). ECL select western blotting detection reagent and ECL western blotting detection reagent were obtained from Amersham Biosciences (Little Chalfont, UK). Immobilon Western Chemiluminescent substrate used for developing western blot membrane came from MERCK. Non-fat dry milk powder came from Tesco (Newcastle, UK).

2. 1. 8. MicroRNA, RNA, and DNA extraction reagents

mirVana miRNA isolation kit with Acid Phenol:ChCl₃ were obtained from Thermo Fisher Scientific. Collagenase type II powder came from Sigma-Aldrich. Cell strainers (100 μ m,

Nylon) came from Corning/Falcon. QIAGEN supplied QIAzol lysis reagent. Chloroform came from Sigma-Aldrich. Isopropanol and ethanol were supplied by VWR (East Grinstead, UK).

2. 1. 9. siRNA reagents

The Creb3l1 siRNA (5 nmol), Nrf2 siRNA (5 nmol), Zeb1 siRNA (5 nmol) and control siRNA were obtained from Horizon/Dharmacon (Cambridge, UK). The transfection reagent (Dharmafect 1) and siRNA dilution buffer were purchased from Horizon/Dharmacon.

2. 1. 10. 3'untranslated region (UTR) constructs and luciferase reagents

All PCR primer sequences for 3' UTR of candidate target genes and mutated 3'UTR constructs were designed using Primer3 (Untergasser et al., 2012). Primers were purchased from IDT (Integrated DNA technologies) (Belgium, EU). In-Fusion HD cloning kit came from TAKARA Clontech (Mountain view, USA). QuikChange lightning site-directed mutagenesis kit was obtained from Agilent Technologies (Manchester, UK). PureYield Plasmid miniprep system (A1223), Dual-Luciferase reporter assay system and transfection reagent FuGENE HD were obtained from Promega.

2. 1. 11. Whole mouse skeletal staining reagents

Alcian Blue 8GX powder, Alizarin Red S powder, Potassium hydroxide powder and Glycerol solution were purchased from Sigma-Aldrich.

2. 2. Methods

2. 2. 1. Cell culture

2. 2. 1. 1. SW1353 cell culture

Reagents:

SW1353 cell line: DMEM/F12 cell culture medium containing 10% (v/v) FBS, 2mM L-glutamine, 1% (v/v) non-essential amino acid, 100U/ml penicillin, and 100µg/ml streptomycin.

Method:

SW1353 cells were seeded into T75cm² flasks and maintained at 37°C in an incubator with an atmosphere of 5% (v/v) CO₂/humidified air to reach approximately 90% confluence. Trypsin-EDTA was used to detach the cells, which were subsequently seeded at an appropriate amount for the given experiment (96-well-plates) or into further T75cm² flasks for continuation of the cell line every 3 days. For long term storage in liquid nitrogen, cells were detached with trypsin-EDTA, centrifuged cells at 500 x g for 5 minutes to pellet the cells and resuspended in cryo-freezing medium before being frozen slowly and stored under liquid nitrogen.

2. 2. 1. 2. Mouse primary costal chondrocyte culture

Reagent:

DMEM/F12 cell culture medium (for mouse primary rib chondrocyte) containing 10% (v/v) FBS, 2mM L-glutamine, 1% (v/v) non-essential amino acid, 100U/ml penicillin, and 100µg/ml streptomycin.

Collagenase solution containing Dulbecco modified Eagle medium (DMEM F-12), 2% (v/v) fetal bovine serum (FBS), 100U/ml penicillin, 100µg/ml streptomycin, and 2mg/ml collagenase type II.

Method:

Prior to mouse costal chondrocyte culture, mice at P7 were sacrificed by dislocation of neck, skins and internal organs were carefully removed from rib cage. Once the sternum was removed, rib cage was cut and separated along the spine, and placed in warm DPBS to keep moist. The rib cage was then digested with 2mg/m collagenase type II in DMEM/F12 medium at 37°C for 75 minutes, vortexing every 15 minutes. Then single ribs were separated from muscle and fibrous tissue in a petri dish with DPBS under microscope. Cartilage was harvested after a collagenase digestion with 2mg/m collagenase type II in DMEM/F12 medium at 37°C for 4 hours, vortexing every 30 minutes. After incubation, cartilage was mechanically disaggregated by pipetting and chondrocytes were then separated through a cell strainer (100µm, Corning), washed in DPBS, and pelleted. Costal

chondrocytes were plated into 6-well-plates (100,000 cells per well) and maintained at 37°C in an incubator with an atmosphere of 5% (v/v) CO₂/humidified air to reach approximately 90% confluence. The cells were detached using trypsin-EDTA and seeded into appropriate amount for further experiments (6-well-plate: 100,000 cells per well, for maintaining or western blot experiment; 96-well-plate: 5,000 cells per well, for transfection of siRNA and miR-140-5p mimic, and WST-1 proliferation assay) or passaged into a further 6-well-plates for continuation.

2. 2. 2. Protein analysis

2. 2. 2. 1. Whole cell lysis

Reagents:

Lysis buffer containing 50mM Tris-HCl, pH 7.5, 1mM EGTA, 1mM EDTA, 1mM Na₃VO₄, 10mM glycerol phosphate, 50mM NaF, 10% (v/v) glycerol, 1% (v/v) Triton X-100, 5mM Na₄P₂O₇, 1µM microcystin-LF, 0.1% (v/v) β-mercaptoethanol, and 1x complete protease inhibitor mini tablet from (Roche Diagnostics, Burgess Hill, UK) for 10ml of buffer.

Method:

Cells were plated in 6-well-plates at a density of 25,000 cells/cm². Prior to protein extraction, the 6-well-plate was placed on ice, medium was aspirated, and cells washed twice with cold DPBS to remove the residual medium. To each well, 150µl of lysis buffer was added. The cells were scraped and the cell lysis transferred to a cooled Eppendorf on ice, incubated for 20 minutes, followed by centrifugation at 13,000 x g for 3 minutes at 4°C. The supernatant was collected in a new cooled Eppendorf and stored at -80°C.

2. 2. 2. 2. Bradford assay

Reagents:

Bovine serum albumin (BSA) and Bradford Ultra reagent.

Method:

4mg of BSA powder was dissolved in 1ml of distilled H₂O, and further diluted to 0.4mg/ml. A range from 0-4mg/ml BSA was added to flat-bottomed 96-well-plate and the volume increased to 10μl with H₂O. 3μl of cell lysates or lysis buffer (used as blanks) were added to each well with 7μl of H₂O. 150μl of Bradford reagents was then added to each well. Samples were gently mixed up by pipetting, incubated for 5 minutes at room temperature before reading absorbance at 595nm using Thermo Varioskan LUX microplate reader.

2. 2. 2. 3. Immunoblotting

Reagents:

Laemmli sample buffer: 0.1M Tris HCl, pH 6.8, 0.35M SDS, 20% (v/v) glycerol, 0.01% bromophenol blue and 5% (v/v) β-mercaptoethanol.

Running buffer: 25mM Tris base, 192mM Glycine, and 0.1% (v/v) SDS.

TBS-Tween: 10mM Tris-HCl, pH 7.4, 150mM NaCl, 0.1% (v/v) Tween-20 (v/v).

Transfer buffer: 39mM Glycine, 48mM Tris base, 0.0325% (v/v) SDS, and 20% (v/v) methanol.

Method:

Cell lysates were thawed on ice and 0.2 volumes of Laemmli sample buffer added to the cell lysates. The mixture was heated to 100°C for 5 minutes, briefly centrifuged and electrophoresed on 10% SDS-polyacrylamide gels. The gel was then transferred to PVDF membrane by semi-dry electroblotting for 1.5 hours at 1mA/cm² in transfer buffer.

The PVDF membrane was then submerged in blocking buffer (5% (w/v) non-fat dry milk powder in 10ml TBS-T) for 1 hour at room temperature on a rocker, washed three times for 5 minutes with TBS-T before Incubation with diluted primary antibody (1:1000 dilution in 5% (w/v) milk or BAS in 10ml TBS-T) at 4°C overnight. The membrane was then washed three times for 5 minutes in TBS-T before incubation with an appropriate horseradish peroxidase (HRP)-conjugated secondary antibody (1:2000 dilution in 10ml 5% (w/v) milk/TBS-T) for 1 hour at room temperature on a rocker. Following incubation, the membrane was again washed three times for 5 minutes with TBS-T. Blots were visualised with Millipore detection reagents using a C600 Azure Biosystems.

In order to measure the reference protein expression (GAPDH), the membrane was incubated with diluted primary antibody solution (1:40,000 dilution in 5% (w/v) BSA/ TBS-T) for 1 hour at room temperature on a rocker before washing and processing as described above. The blots were visualised with ECL detection reagents using C600 Azure Biosystems.

2. 2. 3. RNA analysis

2. 2. 3. 1. Total RNA extraction from cell culture

Reagents:

Cells-to-cDNA II kit (Ambion).

Method:

Cells were plated in 96-well-plates at a density of 25,000 cells/cm². Following appropriate treatments (siRNA transfection, mimic transfection, or plasmid transfection) for the desired time-point, cell culture medium was aspirated and cells washed in ice-cold DPBS. 30µl of Cells-to-cDNA II lysis buffer was added to the cells and then incubated on a rocker at room temperature for 15 minutes. The cell lysates were then transferred to 96-well PCR plate and heated to 75°C for 15 minutes. The lysates were stored frozen at -80°C or used immediately for reverse transcription and PCR.

2. 2. 3. 2. Total RNA extraction from mouse primary rib chondrocyte

Reagents:

mirVana microRNA isolation kit (Invitrogen).

Acid-Phenol:Chloroform reagent (Invitrogen).

Method:

Mouse primary costal chondrocyte pellets (approximately equal to 30µl) in Eppendorfs were formed after centrifugation of freshly isolated mouse costal chondrocytes at 350 x g for 5 minutes. The cells were treated with 400µl of Lysis/Binding buffer and mixed vigorously by vortexing. MiRNA homogenate additive were added at 1/10 of the volume and the mixture incubated on ice for 10 minutes. A volume of Acid-Phenol:Chloroform equal to that of the

lysate, was added to the mixture, and mixed by vortexing for 30-60 seconds before centrifugation at 10,000 x g for 5 minutes to separate the aqueous phase and organic phase. The upper aqueous phase was carefully collected into a new Eppendorf and 1.25 volumes of 100% (v/v) ethanol was added. The lysate/ethanol mixture (~700µl) was added to a filter cartridge, placed in a collection tube and centrifuged at 10,000 x g for 15 seconds. The filter was washed with 700µl miRNA wash solution 1 and centrifuged for 5-10 seconds at 10,000 x g. The filter was washed twice with 500µl wash solution 2/3 before eluting RNA with an elution solution or nuclease-free water heated to 95°C. The RNA was used immediately for reverse transcription and PCR or stored -80°C. The concentration of RNA was measured through the absorbance at 260 and 280nm using a NanoDrop-1000 spectrophotometer (Thermo Scientific, UK).

2. 2. 3. 3. Total RNA extraction from mouse medial knee cartilage

Reagents:

mirVana microRNA isolation kit (Invitrogen).

Chloroform reagent (Sigma-Aldrich).

QIAzol lysis reagent (QIAGEN).

Method:

Medial knee cartilage caps were dissected from mice prior to or at 3-, 7- and 42-days post-DMM surgery at 11-week-old, washed three times with sterile DPBS and placed in cryogenic vials (Corning, UK) and immediately frozen in liquid nitrogen. All tissue was kept in sterile cryovial and snap freeze in liquid nitrogen and ready for the RNA extraction. Tissue grinding chambers, balls and tools were autoclaved before collecting the tissue and then kept in the oven at 160°C overnight or 5-6 hours. For grinding, the tissue was placed in a chamber with a ball inside and 250µl QIAzol lysis reagent was added under fume hood. The Chambers were transferred to Retsch MM200 mixer mill, which was secured by clamps and then run at 25.0 frequents per second for 90 seconds. To the ground tissue/QIAzol mixture was added an additional 250µl QIAzol lysis reagent to make the volume up to 500µl. Transfer the ground tissue/QIAzol mixture to a RNase free tube and Incubated at room temperature for 5

minutes. To this was added 100 μ l chloroform and the mixture vortexed for 15 seconds. The sample was incubated at room temperature for 10 minutes then centrifuged at 12,500 x g at 4°C for 5 minutes. The upper aqueous phase was transferred into a new Eppendorf and processed as in section 2.2.3.2.

2. 2. 3. 4. Reverse transcription

Reagents:

M-MLV reverse transcription kit (Invitrogen).

Method:

Random hexamers (p(dN)₆) (1 μ g) (IDT DNA) and 3 μ l of 10mM dNTPs (Bioline) were added to RNA (either 1 μ g, 500ng, 200ng depending on the experiment – with the concentration consistent within an experiment) in a total volume of 8 μ l. This was heated to 70°C for 5 minutes, to denature the RNA secondary structures and then chilled to allow the hexamer to anneal. To the RNA samples were added a reaction mix containing 4 μ l of 1st 5x RT buffer, 2 μ l of 0.1 M DTT, 0.5 μ l (200U/ μ l) MMLV, and 1.5 μ l H₂O, which was then heated to 37°C for 50 minutes followed by 70°C for 15 minutes. The mixture was finally diluted 1/100 in H₂O for target gene quantification with a further 1/10 dilution for 18S housekeeping gene quantification. Samples were routinely frozen at -20°C for future use.

2. 2. 3. 5. Reverse transcription of RNA obtained using Ambion Cells-to-cDNA II kit

Reagents:

Cells-to-cDNA II kit (Ambion).

M-MLV reverse transcription kit (Invitrogen).

Method:

After processing cell line samples described in section 2.2.3.1, 8 μ l of 'RNA' samples were transferred to a fresh 96-well plate, and 3 μ l of dNTPs (2.5mM) and random hexamers p(dN)₆ (0.2 μ g) added to each well. The plate was heated at 70°C for 5 minutes and then chilled down followed by the addition of the reaction mix described in section 2.2.3.4. The plate

was heated to 37°C for 50 minutes and then 70°C for 15 minutes. The samples were diluted by adding 30µl of H₂O for target gene quantification with a further 1/10 dilution for 18S housekeeping gene quantification (Table 2.1). Samples were routinely frozen at -20°C for future use.

2. 2. 3. 6. MicroRNA reverse transcription

Reagents:

TaqMan microRNA reverse transcription kit (ThermoFisher).

TaqMan microRNA reverse transcription assay (ThermoFisher).

Method:

For reverse transcription to 5µl of RNA samples in a 96-well plate were added 0.15µl of dNTPs (100mM), 50U MultiScribe™ reverse transcriptase, 1.5µl of RT buffer (10x), 0.188µl of RNase inhibitor, 4.16µl of nuclease free water, and 3µl assay-specific RT primer (5x). The plate was then incubated at 16°C for 30 minutes, 43°C for 30 minutes, and 85°C for 5 minutes before chilling on ice. The samples were diluted 1/6 for target miRNA or housekeeping small non-coding RNA (*U6*) quantification or immediately frozen at -20°C for future use.

2. 2. 3. 7. Primers for real time qRT-PCR

Pre-Developed TaqMan assay reagent Eukaryotic 18S endogenous control (20X, FAM™/MGB probe, non-primer limited) (Life technologies).

Pre-Developed TaqMan assay reagent Mouse *Gapd*(*Gapdh*) endogenous control (20X, FAM™/MGB probe, non-primer limited) (Life technologies).

Forward and reverse primers and Universal probe

Method:

Forward and reverse primers were designed using Universal ProbeLibrary (UPL, Roche). Primers were designed within different exons close to, or spanning, an intron/exon

boundary to avoid amplification of any residual genomic DNA. Pre-designed assay to the house keeping genes glyceraldehyde 3-phosphate dehydrogenase (*Gapdh*) and *18S* were diluted to 5X and then used as endogenous control to normalise for differences in the amount of input RNA/cDNA conversion efficiency. All the primers were designed for mouse species unless otherwise stated.

Table 2.1 Sequences of primers and probes for probe based real-time qRT-PCR method

Genes	Forward primer	Reverse primer	UPL probe
<i>Creb3l1</i>	gatggaggacaccactcaaga	ttcaccatgtggagcacag	81
<i>Lmnb1</i>	gggaagtttattcgcttgaaga	atctcccagcctccatt	15
<i>Ank2</i>	caaggaatcgagtcagatca	tgctcatctggggatttt	69
<i>Adam10</i>	caaagatgattgctgctcg	ctgtacagcagggtcctgac	20
<i>Aplp2</i>	cacgggattgtggagggtt	acacgctgtccttaatctgc	1
<i>Ece1</i>	ggttttccgtcactca	gaggcgaaacccatttaga	11
<i>Hyou1</i>	gaggcgaaacccatttaga	gactgcttctgttcaggc	1
<i>Hr</i>	catcaactgaccgggtgct	cgcagcaggacactctgat	60
<i>Faim</i>	gacgtatggtcaatggtca	aagtgcgtctcagtccatc	94
<i>Gm20388</i>	aaggcagtggcgagtggac	ggcttcattgtggaatgtga	83
<i>Dnpep</i>	cccaactggctatgcactct	aagggaacagctcaaagaagc	94
<i>Adamts5</i>	cctggatgtggatggta	agttcctcgggaccaaaa	38
<i>Col10a1</i>	gcatctccagcaccaga	ccatgaaccagggtcaagaa	84
<i>Col2a1</i>	cacgaagggagttatgattg	cccctcagaggcaaggag	1
<i>Npr3</i>	ctttcaacagttctcctacgg	gcttgtagttcagactcg	55
<i>Zeb1</i>	actgccagcagaccagaca	tcacactcggtcttcacg	16
<i>Med13</i>	agtttcaatcccaacaatga	tgtacaggagatgcagttgg	4
<i>Nrf2 (Nfe2l2)</i>	catgtggactggagttgc	cctccaaaggatgtcaatcaa	3
<i>Tmem123</i>	ccatctgcatacaggtgagg	cactcaagtgtttatgtgagca	89
<i>Ncstn</i>	gtgggtgtgaccgatgg	ccattacatctgtggtaagagc	67
<i>Fbn1</i>	tggtttatgttctgtggatt	aaccaggagactttatccacc	19
<i>Golt1b</i>	ttatggattcttctgttcagg	tttaggaggatccgaggac	48
<i>Abca1</i>	gcggatcaagcatccaaact	gcaggaatccagagaatattc	1

2. 2. 3. 8. Real time qRT-PCR

Reagents:

2x TaqMan gene expression master mix (TGE) (ThermoFisher).

Method:

Real-time qRT-PCR was performed using 2x TaqMan Gene Expression Master Mix for potential target genes and *18S/Gapdh*. For target gene quantification, 5 μ l 2x TGE reagent, 0.2 μ l of forward primer (10 μ M) and reverse primer (10 μ M), 0.1 μ l of correspondent probe, and 0.5 μ l of nuclease free water were added to 4 μ l of diluted cDNA in a 96-well plate. The plate was incubated at 95°C for 10 minutes and then subjected to 40 PCR cycles consisting of 95°C for 15 seconds and 60°C for 1 minute (QuantStudio 3). For housekeeping gene quantification 4.7 μ l TGE reagent, 0.1 μ l of forward primer (30 μ M) and reverse primer (30 μ M), and 0.1 μ l (15 μ M) of the appropriate FAM-TAMRA probe were added to 5 μ l of diluted cDNA in a 96-well plate. The PCR protocol was the same as above. The primers and probes are given in Table 2.1.

2. 2. 3. 9. MicroRNA real-time qRT-PCR

Reagents:

TaqMan gene expression master mix (TGE) (ThermoFisher).

TaqMan microRNA real time assay (ThermoFisher).

Method:

Real-time qRT-PCR for miR-140 (5p and 3p) and *U6* were performed using microRNA PCR assays (ThermoFisher) according to the manufacturer's protocol. For a 10 μ l reaction, 5 μ l 2x TGE reagent, 0.5 μ l of microRNA TM assay (20x), and 0.5 μ l of nuclease free water were added to 4 μ l of diluted cDNA in a 96-well plate. The plate was heated at 95°C for 10 minutes and then subjected to 40 PCR cycles consisting of 95°C for 15 seconds and 60°C for 1 minute. All qRT-PCR results were analysed using the Thermo Fisher Connect™ software (<https://www.thermofisher.com/uk/en/home/digital-science.html>).

2. 2. 3. 10. Costal RNA-sequencing (RNA-seq) and data analysis

Method:

RNA (200ng/mouse) was extracted from costal chondrocytes isolated from mice at P7 as described in sections 2.2.1.2 and 2.2.3.2. Then RNA underwent RNA sequencing to identify

potential miR-140 target genes in the growth plate. RNA from the costal chondrocytes of 4 mice per genotype was sequenced and all samples had an RNA-integrity number (RIN) ≥ 9 determined using an Agilent Tapestation.

After sequencing, between 15.4-22.5 million of 75bp single end reads were generated per sample (average 19.0 million). The quality control (QC) and bioinformatic analysis of the ata was performed by Dr Kathleen Cheung from Newcastle University Bioinformatics support unit. The data underwent QC, using FastQC and summarised using MultiQC, and transcripts were quantified using Salmon (Patro et al., 2017) in quasi-mapping mode to mm10 and summarised to gene level using the tximport package, batch correction and normalisation followed by differential gene expression using DESeq2analysis. Statistical *p*-value attained by the Wald test and were corrected for multiple testing using the Benjamini and Hochberg method to provide the false discovery rate (FDR). Data were filtered using an FDR threshold of 0.05 and fold-change threshold ≥ 4 (log2).

2. 2. 3. 11. Short interfering RNAs (siRNAs) transfection

Reagents:

DharmaFECT 1 transfection reagent (Dharmacon).

DharmaFECT buffer (Dharmacon).

Method:

Pre-designed ONTARGETplus siRNAs (5nmol) (for *Creb3l1*, *Zeb1*, and *Nrf2*) were obtained from Dharmacon. Primary costal chondrocytes were isolated from 7-day old C57BL/6 wild-type or miR-140^{-/-} mice, then plated into 6-well plates to reach 90% confluence. Following cell passage, 6,000 cells were plated in a 96-well plate (for qRT-PCR) and 150,000 cells were plated in a 6-well plate (for western blotting) to attain ~50% of confluence after culture overnight at 37°C. Transfection was performed following the manufacturer's instruction with the concentration of siRNA at 100nM. Briefly, siRNA was diluted to 20 μ M in 1x DharmaFECT buffer. For a well of a 6-well plate, 10 μ l of diluted siRNA were mixed with serum free DMEM F12 and Dharmafect 1 (4 μ l) transfection reagent to reach the volume of 400 μ l and left for 20 minutes at room temperature to form siRNA containing liposomes. For

a well of a 96-well plate, a 20th of all the reagents used for 6-well plate experiment were mixed and left at room temperature for 20 minutes. Sufficient volume of serum containing DMEM F12 were added to the mix to reach the desired volume of transfection medium (2ml for each well of a 6-well plate, 100µl for a 96-well plate). The previous culture media were removed from well and appropriate amount of media containing respective siRNA/transfection reagent complex were added into each well, the cells were incubated at 37°C for 48 hours. RNA or protein were then extracted from cells for further experiments.

2. 2. 3. 12. WST-1 proliferation assay

Reagents:

Cell Proliferation Reagent WST-1 (Sigma-Aldrich).

Method:

WST-1 is a stable tetrazolium salt that can be cleaved by dehydrogenases that exist in mitochondria, to form a soluble formazan. The formazan formed is largely dependent on the glycolytic production NAD(P)H generally produced in viable cells. Thus, the amount of formazan dye formed is highly correlated to the number of metabolically active cells in the culture.

The experiment was carried out according to the manufacturer's instruction using untransfected or cells transfected (section 2.2.3.11) with siRNA and/or miR-140 mimic as indicated and described in section 2.2.3.11, to identify the role of miR-140 target genes in cell proliferation. Primary costal chondrocytes were isolated from mice and seeded expanded as previously described above or five thousand P0 cells were plated directly into 96-well-plate after isolation, cultured in complete DMEM/F12 at 37°C for 24 hours, and then transfected with desired siRNA, miR-140-5p mimic, miCon2 control mimic (Dharmacon), and control siRNA (Dharmacon) and incubated at 37°C for 24 hours. 10µl of cell proliferation reagent WST-1 were added in culture medium and placed in a 37°C incubator for 2.5 hours, followed by measurement of the absorbance of the samples against a background control as blank (DMEM medium + WST-1 reagent) using a Varioskan LUX plate reader. The wavelength for measuring the absorbance of the formazan product was set as 450nm (recommended range is between 420nm to 480nm). When using cells at P1, once the

primary costal chondrocytes cultured in a 6-well plate reached 90% confluence the cells were treated with trypsin + EDTA and 5,000 cells were seeded into each test well of a 96-well plate and treated as above.

A student's unpaired t-test was used for statistical analysis between treatment groups and the subsequent mean and standard deviation (SD) was carried out to analyse the data obtained from the absorbance values.

2. 2. 4. Histological analysis

2. 2. 4. 1. Haematoxylin & Eosin analysis of mice tibia growth plate

Reagents:

Filtered Haematoxylin & Eosin (H&E) solution.

Absolute ethanol solution (VWR).

Xylene solution (VWR).

DPX Phthalate-free mounting medium (CellPath).

Method:

Mouse legs were collected at 7-day-old and 3-week-old. The legs were fixed in 10% (w/v) neutral buffered formalin solution (Sigma-Aldrich) and were decalcified in pH7.4 20% (w/v) EDTA solution at room temperature for 1 week to perform H&E staining and Safranin O staining (section 2.2.4.2). Following decalcification, the legs were washed with running tap water before being processed overnight in a Thermo Scientific™ STP 120 Spin Tissue Processor, and then embedded in paraffin blocks in patella left/right orientation and allowed to set overnight.

A Thermo Scientific HM3555 Automatic Microtome was used to cut six μm of paraffin-embedded sections through from lateral side to medial side of knee joint were collected on slides. Slides were dewaxed at room temperature in xylene twice for 5 minutes and then rehydrated through a series of decreasing concentration of ethanol (100% (v/v), 95% (v/v), 75% (v/v), and 50% (v/v), each for 5 minutes), followed by a final tap water wash. Slides were rinsed in haematoxylin for 1 minute before being washed with tap water. To remove

excess staining, slides were incubated in 0.5% (v/v) acid alcohol for 10 seconds and washed with tap water. Slides were then rinsed in Scott's tap water for 1 minutes to retain nuclear staining, followed by a tap water wash for 2 minutes. Following incubation with eosin for 1 minute, slides were rinsed in tap water for 2 minutes until the slides were clear. Slides were then dehydrated through a series of increasing ethanol concentration (50% (v/v), 75% (v/v), 95% (v/v), 100% (v/v), each for 2 minutes) and rinsed in xylene for 10 minutes before mounting in DPX Phthalate-free mounting medium. Slides were incubated at room temperature overnight before imaging. Under the microscope, nuclei appear blue, extracellular matrix and cytoplasm appear stained pink.

2. 2. 4. 2. Safranin O analysis of mice tibia growth plate

Reagents:

Weigert's Iron Haematoxylin working solution (Sigma-Aldrich).

0.06% Fast Green (FCF) solution.

Absolute ethanol solution (VWR).

Xylene solution (VWR).

DPX mounting medium (CellPath).

Method:

The preparation of paraffin-embedded sections was as described above in section 2.2.4.1. Slides were dewaxed in xylene (twice for 5 minutes) and then rehydrated through a series of decreasing concentrations of ethanol (100% (v/v), 95% (v/v), 75% (v/v), and 50% (v/v), each for 5 minutes), followed by a tap water wash. Slides were stained with Weigert's Iron Haematoxylin working solution for 10 minutes. Briefly, slides were washed with distilled water and dipped in 0.5% acid alcohol, washed in tap water to stop the reaction, then rinsed with running tap water for 10 minutes before submerging in 0.06% fast green (FCF) solution for 5 minutes (with agitation). Slides were quickly rinsed in 1% (v/v) acetic acid solution for 10 seconds and stained with 0.1% Safranin O solution for 5 minutes, before dehydration through increasing concentrations of ethanol (95% (v/v) for 1 minute, 100% (v/v) twice for 1 minute), rinsing in xylene for 10 minutes and finally mounting in DPX (Phthalate-free)

mounting medium. Slides were incubated at room temperature overnight before imaging. Under the microscope, nuclei appear black, cartilage extracellular matrix (glycosaminoglycans, GAG) appears orange/red in colour.

2. 2. 4. 3. Whole mount skeletal staining with Alcian Blue/Alizarin Red

Reagents:

Alcian Blue powder (Sigma-Aldrich).

Alizarin Red S powder (Sigma-Aldrich).

Method:

C57BL/6 wild-type mice and genetically modified mice were sacrificed at 7-days of age, skin and internal organs were then removed and the samples were fixed in 95% (v/v) ethanol for 5 days and then stained with Alcian Blue solution (45mg of Alcian Blue powder were dissolved in 240ml of 95% ethanol and 60ml of acetic acid) for 24 hours. Samples were rinsed in 95% (v/v) ethanol twice and incubated in 95% ethanol for 24 hours. Following staining in 1% (w/v) potassium hydroxide (KOH) solution for 6 hours, samples were rinsed in Alizarin Red solution (25mg of Alizarin Red S powder dissolved in 500ml of 2% (w/v) KOH solution) for 12 hours, followed by an incubation in 2% KOH (w/v) solution for 48 hours until all the flesh disintegrated. Samples were then rinsed through a series of decreasing concentrations of KOH in glycerol solution (80% (w/v), 60% (w/v), 40% (w/v), and 20% (w/v); 24 hours per step) before imaging.

2. 2. 4. 4. Bromodeoxyuridine (BrdU) labelling analysis

Reagents:

BrdU cell proliferation labelling kit (GE healthcare).

Fluoroshield Mounting Media with DAPI (Abcam).

Donkey anti-rat 488 Alexa Fluor secondary antibody (Life Technologies).

Method:

BrdU reagent is an analogue of the nucleotide thymidine, which can be incorporated into DNA during S-phase of DNA replication. BrdU positive cells are visualised using a specific antibody to BrdU by immunocytochemistry (ICC).

Twenty two-day-old mice were subcutaneously injected with BrdU labelling reagents according to the weight of mice (0.1ml of BrdU reagent per 10g of mouse weight) 2 hours before harvest by CO₂ euthanasia according to Schedule 1 of The Animals (Scientific Procedure) Act (ASPA) 1986. One hindlimb/mouse was fixed in 5% acetic acid in ethanol for 2 days at 4°C, decalcified in 20% EDTA on a shaker for 2 weeks, processed, paraffin embedded, and sectioned (as described in section 2.2.4.1) for detecting BrdU labelled cells.

6μm of sections were prepared for IHC. Slides were dewaxed in xylene and rehydrated through decreasing ethanol concentration solutions as described in section 2.2.4.1.

Following a PBS wash, slides were rinsed in 4M HCl for 15 minutes to expose antigen. Slides were then incubated in 0.1M borate buffer (0.5M borate buffer containing 30.9g boric acid dissolved in 13.5ml 10M sodium hydroxide, to this distilled water added up to 1 litre, and then diluted to 0.1M borate buffer with distilled water) for 5 minutes to stop the reaction, followed by three washes with PBS. Slides were then blocked with 4% (v/v) donkey serum (AbD Serotec, diluted in PBS) overnight at 4°C.

Slides were treated with BrdU primary antibody (dilution 1:100 in PBS) for 1 hour at room temperature, followed by two PBS washes. The secondary antibody (dilution 1:200 in PBS) was added onto slides for 1 hour at room temperature. Slides were then washed twice with PBS before mounting the slides with Fluoroshield Mounting Media with DAPI. Slides were imaged after incubation in a dark box at room temperature overnight.

Nine matched sections per mouse and three mice per genotype were used for analysis. Slides were imaged on a Zeiss AxioImager with Apotome at 20x magnification using the DAPI and AlexaFluor 488 channels. Images were tiled and stitched using Zen software.

For analysis, images were opened in ImageJ software, colour channels were separated, and images were converted to compatible format (grayscale). BrdU positive cells were counted using Watershed segmentation and Overlaid Dams, and finally expressed as a ratio of positive cells against the total cells within the proliferative zone.

2. 2. 4. 5. Terminal deoxynucleotidyl transferase doxuryidine triphosphate (dTTP) nick end labelling (TUNEL) analysis

Reagents:

DeadEnd Fluorometric TUNEL system kit (Promega).

Proteinase K powder (Sigma-Aldrich).

Fluoroshield Mounting Media with DAPI (Abcam).

Method:

The DeadEnd Fluorometric TUNEL system was designed to label apoptotic cells on formaldehyde fixed samples. The method detects DNA fragmentation by labelling the 3' hydroxyl termini of double-strand DNA breaks generated during cell apoptosis.

The contralateral hindlimb of the same mice subjected to BrdU labelling (section 2.2.4.4) were used for TUNEL staining, with this limb fixed in 10% formalin (the equivalent of 4% PFA) for 48 hours at 4°C. Limbs were decalcified, processed, embedded, and sectioned as the same as described in section 2.2.4.4.

Slides were washed twice in xylene (5 minutes per wash), followed by a wash in 100% ethanol for 5 minutes. Slides were then rehydrated through decreasing concentrations of ethanol (100%, 95%, 75%, 50%; 3minutes each wash) before a wash in 0.85% sodium chloride (NaCl) for 5 minutes and in PBS for 5 minutes. Slides were fixed in 4% formaldehyde in PBS for 15 minutes and then rinsed in PBS twice. 100µl of a 20µg/ml Proteinase K solution were added on slides to unmask antigens. Slides were incubated at room temperature for 9 minutes. Following a PBS wash, slides were fixed in 4% formaldehyde in PBS again for 5 minutes and subsequently washed with PBS. Slides were incubated in equilibration buffer for 10 minutes at room temperature. For labelling positive cells, 50µl of TdT reaction mix were added on slides, covered by plastic membrane, and incubated in a humid chamber at 37°C for 60 minutes. Slides were then washed in 2X saline sodium citrate (SSC) for 15 minutes to stop the reaction, followed by a PBS wash for 3 times before mounting with Fluoroshield Mounting Media with DAPI.

Once dry, slides were imaged with a Zeiss AxioImager with Apotome confocal fluorescence microscopy at 200 times magnification using DAPI and AlexaFluor 488 channels. 3 matched sections per mouse from 3 mice per genotype were used for analysis. For analysis, images were opened in ImageJ software and analysed essentially as above.,

2. 2. 5. Generation, maintenance and identification of mouse models

2. 2. 5. 1. Generation of the genetically modified mouse models

Method:

All animal experiments were conducted according to The Animals (Scientific Procedure) Act (ASPA) 1986 at the Functional of Genetics Unit (FGU) of Newcastle University (UK). We generated C57BL/6 background maintained *Mir140* knockout (KO) mouse model using CRISPR/Cas9. Two guide RNAs (gRNAs) (5'-GTTTCGGTGTGACCTCTCCAGG-3' and 3'-CCCTATGGTAGGTTACGTCATGC-5') designed using the web tool CHOPCHOP (<http://chopchop.cbu.uib.no/>) to target the murine miR-140 locus, gRNAs were directly linked to the TRACR from the pLKO.1 vector (Addgene #52628), which also contained an upstream T7 promoter for subsequent *in vitro* transcription, using the MegaShot kit (Ambion). The two guide RNAs and linked TRACR were microinjected into zygotes (produced from B6D2F1 mice) with recombinant Cas9 protein (ToolGen), which were then implanted into the ovary of pseudopregnant mice (Albino mouse). The resulting offspring were crossed (5 times) with wild-type C57BL/6 mice to get heterozygous animals on the desired background, and the genotype was confirmed by PCR and agarose electrophoresis. Homozygous mice were obtained from the cross between heterozygous and heterozygous animals. DNA isolated from ear notches was analysed by PCR using mouse miR-140 primers (forward primer, 5'- TTGCTGGTGGTAGTCTTCTGT -3'; reverse primer, 5'-TCACCCTAGAACCCATTAGCAT -3'). Sanger sequencing was conducted to visualise and confirm the position of deletion of *Mir140*.

Generation of miR-455 null mice was conducted at the University of Manchester, and we obtained miR-455^{-/-} mice from our collaborator Prof Ian Clark (University of East Anglia, UEA). Briefly, the generation of miR-455^{-/-} mice were achieved again using CRISPR/Cas9 and two gRNAs (5'-GGTGTGAGCGTATGTGCCTTGG-3' and 3'-CCATGCAGTCCACGGGCATATAC-5')

that were designed to target *Mir455* locus, using a similar strategy as described for *Mir140*. Genomic DNA was extracted from the resulting offspring (F_0) and genotyped to confirm the deletion. An 18bp deletion around the *Mir-455-3p* hairpin was detected and used to make the miR-455^{-/-} mouse line, and genotype was confirmed using PCR and agarose electrophoresis. Homozygous mice were obtained from the cross between heterozygous and heterozygous mice. DNA isolated from ear notches was analysed by PCR using mouse miR-455 primers (forward primer, 5'-AATTGGCATCATCTCTAGCCTC-3'; reverse primer, 5'-AGGTGGGGATCAGAGAGGTAA-3').

Generation of miR-140: miR-455^{-/-} mice (DKO mice) was achieved from the cross between miR-140^{-/-} mice and miR-455^{-/-} mice, and genotype was confirmed by PCR and agarose electrophoresis.

2. 2. 5. 2. Maintenance of the genetically modified mice and non-genetically modified mice

Method:

Mice were housed at the FGU in the Institute of Genetic Medicine at Newcastle University, in compliance with the Animals (Scientific Procedures) Act 1986 and its associated Codes of Practice. Up to 5 mice were housed together in independently ventilated cages (300cm², 12cm height) to allow enough space for physical activities/exercise. All animals had access to food and drinking water *ad libitum* and were subjected to a 12-hour light-dark cycle. When breedings were ended, re-introduction of the male breeders to already populated cages was avoided in order to avoid social incompatibility issues. The FGU technical staff performed the check and cleaning rota of the cages twice a week. Detailed records about each animal used in this study was recorded using the AniBio and Softmouse (<http://softmouse.net>) software system and returns of procedures including severity limits and protocols performed annually.

2. 2. 5. 3. Genotyping of mice

Reagents:

Phire tissue direct PCR matrix mix (Thermo Fisher Scientific).

Agarose powder (Invitrogen).

Tris-borate-EDTA (TBE) buffer (Thermo Fisher Scientific).

Ethidium Bromide (EtBr) Dye for DNA and RNA detection kit (Thermo Fisher Scientific).

HyperLadder 100bp DNA ladder (BIOLINE).

Method:

A small piece of tissue from an individual mouse's ear or tail was collected in 1.5ml Eppendorf tube to which 20 μ l dilution buffer and 0.5 μ l DNA release Additive, provided within kit, were added. Samples were briefly vortexed and centrifuged to ensure the added solution submerged the sample. Samples were heated at 98°C for 2 minutes after an incubation at room temperature for 2 minutes, followed by a brief vortex and centrifugation.

A Phire PCR reaction contained 2x master mix buffer (10 μ l), 10 μ M forward primer (0.5 μ l), 10 μ M reverse primer (0.5 μ l), 8 μ l of DNase free water, and 1 μ l of DNA from the step above was added to make the volume up to 20 μ l. Mice were genotyped using primers that were designed to analyse the presence of the *Mir140* and *Mir455* genes, and to amplify a region of the genes spanning the deletions. Primers for *Mir-140* and *Mir-455* are listed in the section 2.2.5.1. For PCR cycling conditions, annealing temperatures of *Mir140* and *Mir455* were 58°C and 65°C, respectively. The plate was incubated at 98°C for 30 seconds and then subjected to 35 PCR cycles consisting of 95°C for 5 seconds, annealing temperature for 5 seconds, 72°C for 15 seconds, and 72°C for 1 minute (ABI Veriti 96 well thermal cycler).

Agarose gel electrophoresis was performed to visualise the size of DNA fragments. Samples were separated on a 1.5% (w/v) agarose gel in 1x TBE buffer. Ethidium Bromide was added in molten gel at a concentration of 0.5 μ g/ml for visualising DNA bands under UV lights.

5 μ l of DNA obtained from PCR reaction were loaded on the gel, and 5 μ l of HyperLadder 100bp DNA ladder was used to quantify the size of DNA products. Samples were electrophoresed at 100 volts for ~1 hour before imaging.

2. 2. 6. Morphometric analysis of the mice

2. 2. 6. 1. Whole body weights

Method:

The measurement of whole-body weight was performed to monitor and compare the growth rate of animals of different genotypes, and mice were weighed at postnatal days 7, 14, 22 days. The measurement of whole-body weight was performed to monitor and compare the growth rate of animals of different genotypes. For analysis, the average weight of each genotype at different time point and standard error of the mean (SEM) were used to generate growth curves for each genotype. ANOVA was adopted to confirm any significant differences between each genotype at different time points.

2. 2. 6. 2. X-ray measurements

Method:

Mice at 7 and 22 days were X-rayed using the Faxitron X-ray radiography system at 23 kV for 5 seconds. 7-day-old mice were subsequently used for RNA-seq analysis and skeletal preparations, 22-day-old mice were used for BrdU labelling and TUNEL assays. To accurately reflect actual bone length of mice, a vertical neutral position was required for imaging. Raw X-ray data were all stored for further bone measurements.

2. 2. 6. 3. X-ray micro-computed tomography (μ CT) quantitative analysis of mice skulls

Reagents:

Dulbecco's Phosphate Buffered Saline (DPBS) (Gibco).

10% formalin solution (Sigma-Aldrich).

Method:

Seven-day-old wild-type (WT) and miR-140^{-/-} (KO) mice were sacrificed by dislocation of neck, subsequently the skin and soft tissue were removed carefully from skull. Skulls were then preserved in DPBS for μ CT scanning following fixation in 10% (v/v) neutral buffered

formalin solution (containing 4% (w/v) formaldehyde) for 48 hours at 4°C. The skull was placed in a µCT X-ray tube appropriate for the particular µCT scanner. All µCT scans were performed using SkyScan 1272v2 µCT analysis instrument in the laboratory of Professor Rob Van't Hof at the institute of Ageing and Chronic Disease, University of Liverpool (UK). Spatial resolution of 9µm was applied to obtain multiple 2D image projections of skulls. The scanning protocol was set for each sample stage on the machine. To generate 3D skull images, 2D images for each skull were stacked and reconstructed using the NRecon (v1.6.4.1, Bucker) programme selecting the region of interest to be constructed. Reconstruction was performed with the smoothing function on, selecting a ring artefact of 5 and beam hardening of 38% and with a Gaussian smoothing kernel in the advanced points. A dynamic range between 0 and 0.11 was then set before starting the process. Reconstructed 3D skull images were used to measure ICD/Skull ratio (skull vertical length/inner canthal distance ratio, was used for analysis of skull shape) by the using CTAn (v1.16) programme. The volume of interest (VOI) to be analysed was set using the Dataviewer programme. Reconstruction parameters and the selected VOI were kept consistent between all samples. Statistical analysis was performed using two-tailed unpaired t-test, 7 wild-type mice and 5 miR-140^{-/-} mice of mixed gender were used for statistical analysis.

2. 2. 6. 4. Bone measurements

Method:

Endochondral ossification of limbs was analysed by quantifying the length of the femur, tibia, and pelvis bones (X-ray analysis). Raw data images were opened in ImageJ software and bone length was measured according to the method showed in Figure 2.1, average measurements of both side of body were calculated per mouse.

Endochondral ossification and intramembranous ossification of skull were analysed by the ICD/skull ration using X-ray and µCT. Raw data was opened in Image J software and dataviewer software, and analysed as shown in Figure 2.1. All skulls for measurements were from 7-day-old mice. In order to visualise skull using µCT, the skulls were isolated from mice

and cleaned free from soft tissue. Skulls were fixed at 10% formalin for 24 hours at 4°C, and then transferred to containers containing DPBS for µCT scanning.

In order to compare the differences between miR-140^{-/-} and WT mice in the cranial base (skull growth plate), mice at 7-days were harvested, and skulls were fixed in 10% formalin solution for 48 hours at 4°C, skulls were then split into two from middle vertical cross-section and processed through the H&E staining process (dissection and staining were performed by Dr Ralf Kist). Skulls were then imaged using a LEICA DM4000 B microscope. Images were opened in Image J software and measurements of the growth plate between BasiOccipital (BasO) and Sphenoid Body (SphB) were calculated. These bones are partially responsible for mouse jaw development.

A student's unpaired t-test was used and the subsequent mean and standard deviation (SD) was carried out to statistically analyse the data obtained from bone measurements.

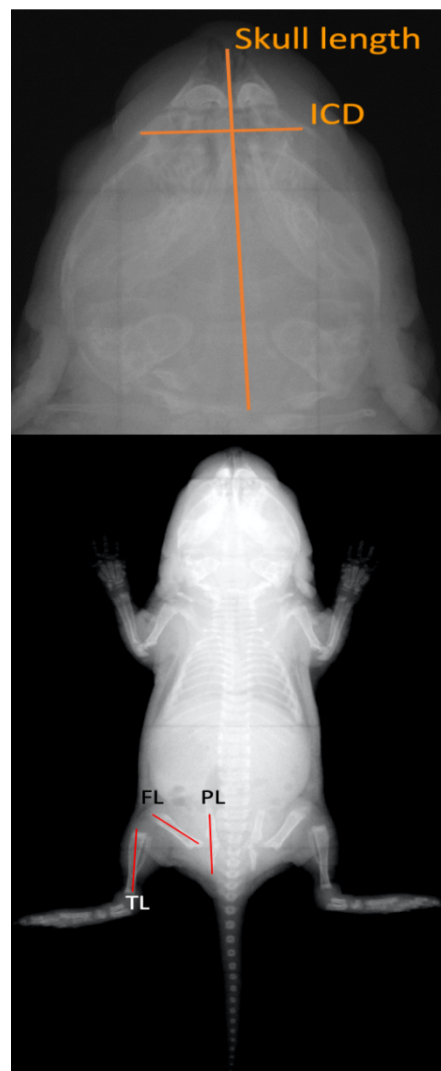


Figure 2.1 Conventional scheme of mouse bone measurement used for X-ray analysis of ICD, femur length (FL), tibia length (TL), and pelvis length (PL).

2. 2. 7. Luciferase assay analysis

2. 2. 7. 1. Generation of 3'UTR constructs and mutant 3'UTR constructs

Ten of the top upregulated miR-140 target genes based on RNA-seq analysis that were also predicted to contain miR-140 binding sites within their 3'UTR (using the TargetScan prediction algorithm; <http://targetscan.org>) were functionally validated with luciferase 3'UTR reporter assays. Luciferase studies were also performed for three putative miR-455 target genes.

Reagents:

In-Fusion HD cloning kit (Clontech/TAKARA).

QuikChange lightning site-directed mutagenesis kit (Agilent Technologies).

PureYield Plasmid miniprep system (Promega).

pmiRGLO Dual-Luciferase miRNA Target Expression Vector (Promega).

NucleoSpin Gel and PCR Clean-Up kit (MACHEREY-NAGEL).

Stellar competent cells (Clontech).

XL10-Gold Ultracompetent cells (Agilent).

Dpn I, *Nhe I*, and *Xba I* restriction endonucleases enzyme (New England Biolabs).

Miniprep kit (QIAGEN).

Method:

To create pmiRGLO-miR-140/miR-455-target 3'UTR vectors, Primer3 software was used to design primers to amplify the 3'UTR of both 10 putative miR-140 (*Abca1*, *Creb3l1*, *Fbn1*, *Med13*, *Ncstn*, *Npr3*, *Tmem123*, *Zeb1*, *Golt1b* and *Nrf2*) and 3 putative miR-455 (*Acan*, *Chst11* and *Ppp1r10*) target genes from mouse genomic DNA. All the primers were chemically synthesised by IDT DNA (Table 2.2). After PCR amplification, DNA was loaded onto 1.5% agarose gel, followed by DNA extraction from the gel using NucleoSpin Gel and PCR

Clean-Up kit. pmiRGLO plasmid vector (Promega) was restriction enzyme digested (*Nhe* I and *Xba* I) and purified after agarose gel electrophoresis, again using the NucleoSpin Gel and PCR Clean-Up kit. The extracted DNA containing designed 3'UTR PCR products were cloned by In-Fusion cloning (Clontech/Takara) between *Nhe* I and *Xba* I sites in the pre-digested pmiRGLO plasmid (Promega). This places the genes 3'UTR sequences downstream of firefly luciferase gene (*luc2*). For the negative control, there is no additional insert within the pmiRGLO plasmid. Bacterial cell transformation was achieved using a mixture of Stellar competent cells and the In-Fusion reaction mix. 100 μ l of transformation mixture were spread on to ampicillin (0.1mg/ml) selective LB-agar plates and incubate overnight at 37°C. Colonies were picked and then incubated with LB solution (with ampicillin) at 37°C overnight. Plasmid DNA were extracted from LB media and Quick miniprep was performed to elute plasmid DNA, *Nhe* I/*Xba* I restriction enzyme digestions were then carried out to determine if the plasmid contained the 3'UTR sequence of interest. Cultures positive for the insert were expanded and DNA purified using PureYield Plasmid miniprep system (Promega) following manufacturer's instructions. The sequence of the 3'UTR report constructs were confirmed using Sanger sequencing.

Table 2.2 Primers designed to create miR-140 target gene's 3'UTR constructs.

Genes	Forward primer (5'-3')	Reverse primer (5'-3')
<i>Abca1</i>	GCTCGCTAGCCTCGACCAGTGCTCAATGTCATCCG	CGACTCTAGACTCGAGGCAGTTACACTATTACAGCA
<i>Creb3l1</i>	GCTCGCTAGCCTCGATCCCTCCTACCACTATCCGT	CGACTCTAGACTCGATGGTGGAGGAGCAGTTGG
<i>Fbn1</i>	GCTCGCTAGCCTCGATTCAACCATTCCAGAGACCAAATAA	CGACTCTAGACTCGACCCTCCAGCCTTAATCCACA
<i>Med13</i>	GCTCGCTAGCCTCGATGCTAACACACCACAGATT	CGACTCTAGACTCGATGAAGACGAATAACAGCTGAGGA
<i>Ncstn</i>	GCTCGCTAGCCTCGAGCATTATGACACGGCTGAGA	CGACTCTAGACTCGAGGAGCAGCAAGTCTACCA
<i>Npr3</i>	GCTCGCTAGCCTCGATAAGACATGCACTGGGACGT	CGACTCTAGACTCGAGCTCCACTGAAATCCTTGA
<i>Tmem123</i>	GCTCGCTAGCCTCGATTCACGGTCACTTGTCACT	CGACTCTAGACTCGACAGTGGAAATGTAAGAGGCAAAT
<i>Zeb1</i>	GCTCGCTAGCCTCGACCCGCAGTGTGGCTATATT	CGACTCTAGACTCGATGCGTTATTGTGAGCTGGG
<i>Golt1b</i>	GCTCGCTAGCCTCGATGTATCGACCCAAGGAAGCC	CGACTCTAGACTCGACCATCCACTACGAACCAAGT
<i>Nrf2</i>	GCTCGCTAGCCTCGAGGATGGAGCCTTTCTGAGC	CGACTCTAGACTCGATAGTTAAGTCATGATATTG

In order to create pmiRGLO-miR-140-5p mutant 3'UTR primers, 3 nucleotide bases in the miR-140-5p binding site (AACCCT) within the 3'UTR of interest were mutated from CAC

into GCG (eg. mutated sequence AACGCGT). All the primers were synthesised by IDT DNA (Table 2.3). Mutant 3'UTR primers were added in a PCR extension reaction with the 'wild-type' 3'UTR plasmid DNA to generate mutant double strand 3'UTR DNA complex, reaction was then treated with restriction enzyme (*Dpn* I) digestion to remove the 'wild-type' construct. The extracted DNA containing designed mutant 3'UTR PCR products were cloned in XL10-Gold Ultracompetent cells and incubated on ampicillin (0.1mg/ml) selective LB-agar plates at 37°C overnight. Colonies were picked and the plasmid DNA were eluted from colonies using PureYield Plasmid miniprep system (Promega) following manufacturer's instructions. The sequence of the 3'UTR report constructs were confirmed using Sanger sequencing.

Table 2.3 Primers designed to create mutant miR-140-5p target gene's 3'UTR constructs.

Mutant binding site	Forward primer (5'-3')	Reverse primer (5'-3')
<i>Creb3l1</i> mutant binding site 1	CCTCCTCCGATAAACGCGTCACTGGCTACCG G	CGGGTAGCCAGTGACGCGTTATCGGAGGA GG
<i>Creb3l1</i> mutant binding site 2	AGTGACCAACGCAACGCGTGTTCCTGGCCCC T	GAGGGGGCCAGGAACACGCGTTGCGTTGGT CACT
<i>Zeb1</i> mutant binding site	AACAAAACCTAAAACGCGTGACTGTGAGAGA AG	CTTCTCTCACAGTCACGCGTTTGAGTTTGTT
<i>Nrf2</i> mutant binding site	GAAAACTAACCAGACGCGTATACTTTTATAT ACTG	CAGTATATAAAAAAGTATACGCGTCTGGTTA GTTTC

2. 2. 7. 2. Luciferase assay

Reagents:

Dual-Luciferase reporter assay system (Promega).

Dharmafect 1 transfection reagent (Horizon/Dharmacon).

FuGENE HD transfection reagent (Promega).

miCon2 control miRNA mimic (Dharmacon).

Method:

For 3'UTR luciferase assays, SW1353 cells (5,000 cells per well) or HEK 293T cells (20,000 cells per well) were plated in each well of a 96-well plate overnight to reach 50% confluence for transfection with 25ng of the 3'UTR constructs using FuGENE HD. 6 wells were transfected per 3'UTR construct. After 4 hours, the cells were transfected with 20µM of miR-140-5p mimic or miRNA mimic nontargeting control #2 using Dharmafect 1. After 24 hours of transfection, cells were washed once in PBS and the lysate harvested with the passive lysis buffer (Promega). Firefly and Renilla luciferase levels were determined using the dual-luciferase assay system (GloMax, Promega). Experiments with each construct were repeated at least twice for each cell line.

2. 2. 8. Destabilisation of the medial meniscus (DMM) surgery model

Reagents:

Isoflurane liquid for inhalation (Forane).

Chlorohexidine (ECOLAB, MN, USA).

Buprenorphine (Vetgesic® Multidose).

Reflex 7mm wound clips (AgnTho's, Reflex Skin Closure System).

Method:

2. 2. 8. 1. DMM surgery

DMM surgery (project licence No. P8A8B649A-1) was approved by the Home Office. DMM surgery and post-surgery mice checks were performed by Hua Lin in the FGU at the Institute of Genetic Medicine of Newcastle University.

Prior to surgery, male mice at 11-weeks of age were anaesthetised separately using 2.5-3.5% of isoflurane in 1-1.5L/min oxygen, and the placed in a recumbent position providing a mask to their head. The left knee was shaved of fur and the area disinfected with chlorohexidine solution (ECOLAB, MN, USA). The animal was weighed and given 0.15ml of 3µg/ml buprenorphine subcutaneously as pre-operation analgesia. In this study, DMM surgery was performed in the left knee joint of 11-week-old C57BL/6 adult male wildtype (weight 25-30g) or transgenic (weight 18-25g) mice.

Anesthetised animals were transferred to the surgery table under a dissecting microscope. A small longitudinal skin incision was made by scissors around the knee joint in order to expose the patellar ligament and the medial side of the main joint capsule. Large blood vessels surrounding the surgical area were cauterised with a tissue cauteriser (Harvard Apparatus UK) before a full-length mediolateral incision from the distal patella to the proximal tibia plateau was made with a scalpel blade (Swann-Moston blade, #11P). The intra-articular fat pad was then moved by a curved forceps (#7) to expose the medial meniscus (MM) and the medial meniscotibial ligament (MMTL). The medial meniscus was destabilized by transecting the MMTL with a needle blade (Medical Sterile Products, Needle 5.0MM Blade), and then pushed to the lateral side. For sham controls, MM and MMTL was exposed but without further dissections. The wound was closed with 2-3 Reflex 7mm wound clips (AgnTho's, Reflex Skin Closure System). The clips were checked later that day and every day post-surgery up to removal of the clips seven days post-surgery.

Post-operation: The animals were located in clean cages and the cages placed at 27°C until the animals regained consciousness. The animals were given two doses of 0.1ml buprenorphine subcutaneously (3µg/ml) as post-operation analgesia the next day (with a 6-8 hours gap between the two doses). Wound clips were removed after 7 days post-surgery under isoflurane.

2. 2. 8. 2. Histological analysis of DMM mice at 8 weeks post-surgery

For histologic examination of osteoarthritis, animals were maintained for 8 weeks post-surgery, then euthanised using CO₂ or by cervical dislocation, both knee joints were harvested and fixed in 10% formalin solution at room temperature overnight (with rotation), before decalcification in pH7.4 20% (w/v) EDTA solution at room temperature for 3 weeks. After decalcification, legs were processed, paraffin-embedded in a patella down orientation, and sectioned as described in section 2.2.4.1.

For each DMM knee joint, 100 serial 5µm-sections were collected on 25 slides, each slide with 4 'sister sections' in order to cover the whole interesting region of interest. Slides #1, #5, #10, #15, #20, and #25 were selected from each joint and subjected to Safranin-O and fast green staining as described in section 2.2.4.2. DMM damage scoring (Table 2.4) was

performed by two different blinded individuals. The OARSI Osteoarthritis Cartilage Histopathology Assessment System (OOCHAS) (Pritzker, Gay et al. 2006) provides clinical and experiment OA assessments for both the depth of cartilage lesion (grade range 0-6) and the horizontal extent of cartilage lesion (stage range 0-4), and 2 independent grades obtained from each section are combined together (score=grade x stage) to generate a grade to reflect OA severity. Both MFC and MTP were scored for each DMM joint. The five worst scores/joint surface for each scorer were averaged. The two individual joint scores were combined together to generate a final summed DMM score. In addition, another widely used scoring system, OARSI scoring system (Table 2.5) (Glasson, Chambers et al. 2010), was applied in our research. This assessment is a semi-quantitative scoring system that provides a simple and rapid method to identify the site of cartilage lesion (with scores from 0 to 6) within the joint that includes medial femoral condyles and tibial plateaus. Similar to the above, two blinded scorers were performed scoring for the same slides used for OOCHAS, Scoring the MFC and MTP for each slide. Again, the worst 5 sections for the MFC and MTP of each animal were averaged for each scorer to a get a mean for each parameter (MFC, MTP and summed score MFC+MTP).

Table 2.4 The recommended semi-quantitative scoring system for assessing cartilage damage on DMM mouse joints. Adapted from (Pritzker et al., 2006).

OA cartilage histopathology grade assessment	
Grade 0	Surface intact, cartilage intact
Grade 1.0	Surface intact, cells intact
Grade 1.5	Surface intact, cell death
Grade 2	Fibrillation through superficial zone
Grade 2.5	Superficial abrasion with matrix loss within superficial
Grade 3.0	Simple fissures
Grade 3.5	Branched/complex fissures
Grade 4.0	Superficial zone delamination
Grade 4.5	Mid zone excavation
Grade 5.0	Bone surface intact
Grade 5.5	Reparative tissue surface present
Grade 6.0	Joint margin osteophytes
Grade 6.5	Joint margin and central osteophytes
OA cartilage histopathology stage assessment	
Stage 0	No OA activity seen
Stage 1	< 10% involvement (surface area)
Stage 2	10% - 25% involvement (surface area)
Stage 3	25% - 50% involvement (surface area)
Stage 4	> 50% involvement (surface area)

Table 2.5 The recommended semi-quantitative scoring system for assessing cartilage damage on DMM mouse joints. Adapted from (Glasson et al., 2010).

Grade	Osteoarthritic damage
0	Normal
0.5	Loss of Safranin-O without structural damage
1	Small fibrillations without loss of cartilage
2	Vertical clefts down to the layer immediately below the superficial layer and some loss of surface lamina
3	Vertical clefts/erosion to the calcified cartilage extending to < 25% of the articular surface
4	Vertical clefts/erosion to the calcified cartilage extending to 25% - 50% of the articular surface
5	Vertical clefts/erosion to the calcified cartilage extending to 50% - 75% of the articular surface
6	Vertical clefts/erosion to the calcified cartilage extending to > 75% of the articular surface

2. 2. 8. 3. Murine medial knee cartilage RNA sequencing

Method:

RNA was extracted from medial knee cartilage isolated from mice pre- or post-DMM surgery at 11-week-old as described in sections 2.2.3.3. The RNA was DNase treated and libraries prepared following Takara SMART-Seq v4 Ultra Low Input RNA kit (which incorporates rRNA depletion as part of the preparation). These were sequenced on an Illumina NovaSeq to identify potential miRNA's target genes in the knee cartilage. RNA from the knee cartilage of 4 mice per genotype was sequenced and all samples passed quality control (QC). QC of the fastq files was performed with FastQC (v0.11.9) and reads were quality trimmed with Trimmomatic (0.39). After sequencing, the bioinformatic analysis of the data was performed with help from Jamie Soul (Newcastle University, Skeletal research group). Kallisto (v0.46.1) was used for pseudo-alignment against the mouse GRCm38 (release 94) transcriptome resulting in quantification with 12.5 to 25 million mapped reads/sample. Mapped transcript expression estimates were summarised to the gene level using Tximport (v1.14.0) and DESeq2 (v1.26.0) was used to calculate log2 fold-change (logFC) and *p*-values, attained by the Wald test corrected for multiple testing using the Benjamini and Hochberg method to provide the false discovery rate (FDR). The volcano plots were generated, and pathway

enrichment determined using R. Data were filtered using an FDR threshold of 0.05 and fold-change threshold ≥ 4 (log2).

2. 2. 9. Laser microdissection (LMD)

Reagents:

Zymo Direct-zol RNA microPrep Kit (Zymo research)

Method:

Frozen longitudinal cryosections (thickness 13 mm) were obtained from 7-day-old proximal tibia of a C57BL6 mouse (stored in OCT embedding compound at -80 °C) using a cryostat (Leica cryostat microtome, Germany), the cryosections were then collected on membrane slides (Leica, Germany), and stored at -20 °C for short-term storage. Slides were thawed and stained with the following modification: air dry sections for 5 min to remove moisture; stained with filtered Mayers Hematoxylin for 5 min; rinse in ddH₂O for 5 min; dip in Eosin for 1 min; dip in distilled H₂O for 1-2 min until the eosin stops streaking; dip in 50% EtOH for 1 min; dip in 75% EtOH for 1 min; equilibrate in 90% EtOH for 30 sec; equilibrate in 100% EtOH for 1 min; air dry slides for 10-15 min and ready for laser microdissection. 2 different size of tibial growth plate proliferative zones were microdissected using the Leica laser microdissection system and collected as four groups (small proliferative section, three small proliferative sections, big proliferative section and three big proliferative sections), all of these groups went straight into the Smart-seq2 lysis buffer (provided by Dr Jonathan Coxhead, Newcastle University, Genomic core facility) and stored at -80 °C prior to library preparation, or were subjected to RNA isolation directly using Zymo Direct-zol RNA microPrep Kit. All of the purified RNAs were DNase treated and passed QC, and were subsequently subjected to low-input RNA-seq (NEB UK).

2. 2. 10. Data/statistical analysis

Method:

Relative genes expression was calculated using the equation $2^{-D} (Ct \text{ gene of interest} - Ct \text{ housekeeping gene})$. For luciferase assay analysis, data of each construct (containing 3'UTR or mutant 3'UTR

sequences of interest) was firstly generated through dividing Firefly by *Renilla* luciferase value and then normalised against the basal level of the control construct, then plotted as fold changes of relative luciferase activity of 3'UTR constructs over control construct levels. Values were given as mean and standard deviation (mean \pm SD) or standard error of the mean (mean \pm SEM). Two-tailed unpaired student's t-test (independent sample groups), one-way analysis of variance (ANOVA) (sample groups across independent experiments), and nonparametric Mann-Whitney test (differences of randomly selected values between sample groups) were used for statistical analysis. Asterisks represent differences with statistical significant at $P<0.05$ (*), $P<0.01$ (**), and $P<0.001$ (***)�.

Chapter 3. Skeletal development of miR-140-/- mice, miR-455-/- mice, and miR-140: miR-455-/- (Double Knock Out, DKO) mice

3. 1. Introduction

Chondrocytes in the growth plate of longitudinal bones drive growth according to a precise balance of cellular proliferation and differentiation. In the developing bone, chondrocytes are divided into three zones in a vertical alignment. During chondrogenesis, flat resting zone chondrocytes are generated, and they subsequently proliferate to form well-organised columnar chondrocytes within the proliferative zone, which further stop proliferating and become 'mature' to form pre-hypertrophic chondrocytes and eventually hypertrophic chondrocytes in the hypertrophic zone. All these processes are precisely regulated by multiple regulatory mechanisms, many discussed in Chapter 1, to allow bone growth through the modulation of gene expression programmes (Kobayashi, Lu et al. 2008).

MicroRNAs are a class of small non-coding RNAs (~22-23 nucleotides in length) that mainly play a negative role at the posttranscriptional level to regulate gene expression through mainly binding to the 3'UTR of their target genes. The RNase III enzymes Drosha and Dicer are essential for generation of mature miRNAs. Kobayashi *et al.* (Kobayashi, Lu et al. 2008) showed that a global reduction of miRNAs in mouse cartilage by deleting *Dicer* in the growth plate, reduced cellular proliferation and accelerated chondrocyte differentiation. The mice exhibited a severe skeletal development defect and premature death probably due to accelerated rib chondrocytes death that affected respiratory function. Kobayashi *et al.* (Kobayashi, Papaioannou et al. 2015) also illustrated that conditional deletion of *Drosha* in the growth plate of mice results in severe skeletal growth defects and early postnatal lethality, phenotypically similar to that of *Dicer* deletion mice. Deletion of *Drosha* in murine articular chondrocytes caused mild osteoarthritis (OA)-like changes in male mice at 6 months of age. Overall, microRNAs play indispensable roles in mice skeletal development and by inhibiting OA progression.

Previously our group have shown *MIR140* and *MIR455* expression are significantly increased in human OA femoral head hip cartilage obtained from joint replacement surgery as compared to normal hip cartilage from patients who have suffered a fracture of neck of

femur (Swingler, Wheeler et al. 2012). Nevertheless, others have shown that the expression of *MIR140* and *MIR455* are decreased in OA cartilage (Iliopoulos, Malizos et al. 2008, Miyaki, Nakasa et al. 2009, Tardif, Hum et al. 2009, Ito, Matsuzaki et al. 2021). Taken together these studies all confirmed that miR-140 expression is dysregulated in OA tissue. We have also observed that expression of *MIR140* and *MIR455* is significantly increased during human BMSCs *in vitro* chondrogenesis (Barter, Tselepi et al. 2015). Thus, in order to illustrate the role of miR-140 and miR-455 in skeletal development and OA pathogenesis *in vivo*, we generated miR-140^{-/-} mice and miR-455^{-/-} mice using CRISPR/Cas9 and crossed these two mouse lines to generate DKO mice – mice lacking both miR-140 and miR-455.

Chapter aims:

- Generation of miR-140^{-/-} mice and DKO mice.
- Confirm the role of miR-140, and investigate the role of miR-455, in murine skeletal growth.
- Confirm the role of miR-140, and investigate the role of miR-455, in murine tibial growth plate development.
- Examine the potential role of miR-140 and miR-455 in chondrocyte proliferation and apoptosis in the tibial growth plate.

3. 2. Results

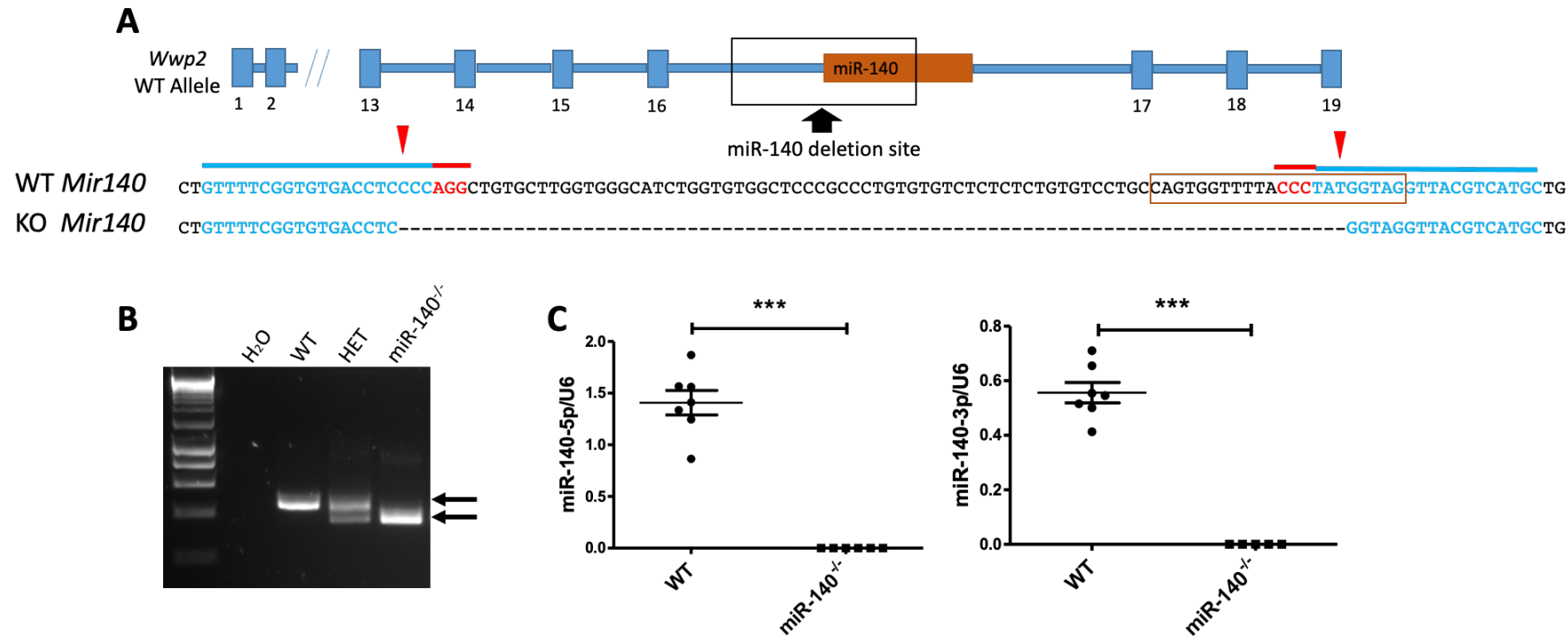
3. 2. 1. Generation and genotyping of miR-140^{-/-} mice, miR-455^{-/-} mice, and DKO mice

3. 2. 1. 1. Generation of miR-140^{-/-} mice

To create targeted deletion of *Mir140* in mice, we used the CRISPR-Cas9 system and designed two gRNAs that targeted *MiR-140* locus for deletion. The region targeted was between exons 16 and 17 of the full-length WW domain-containing E3 ubiquitin protein ligase 2 (*Wwp2*) gene, which contains the *Mir140* gene (Fig. 3.1A). Mir140-null mice were generated as described in material and methods, section 2.2.5.1. From the fifteen F₀ pups of the first litters, DNA was extracted from ear notches of mice to determine the genotype. Of these mice two #13 and #14 contained deletions of approximately the anticipated size. A third line from the mouse #1, was also established since PCR genotyping from this mouse suggested only a very small deletion (later confirmed by Sanger sequencing to be 5bp) of the -5p arm of miR-140 had occurred. We initially hypothesised that this may result in a lack of miR-140-5p but remaining expression of miR-140-3p, however qRT-PCR eventually verified the expression of both -5p and -3p were absent. All three mice were subsequently bred with WT C57BL/6 to ensure the deleted allele was present in the germline and transmitted to offspring. Preliminary analysis of homozygous mice of all three lines indicated an identical phenotype (data not shown). From these mice line #13 was continued hereafter. The size of deletion in line #13 is 82bp as confirmed by Sanger sequencing (Fig. 3.1A & B). Heterozygous line #13 mice (hereafter termed miR-140^{+/−}) were back-crossed five times with WT C57BL/6 to dilute the CBA/ca strain background, after which miR-140^{+/−} mice were interbred to create homozygous wild-type (WT) and miR-140^{-/-} lines.

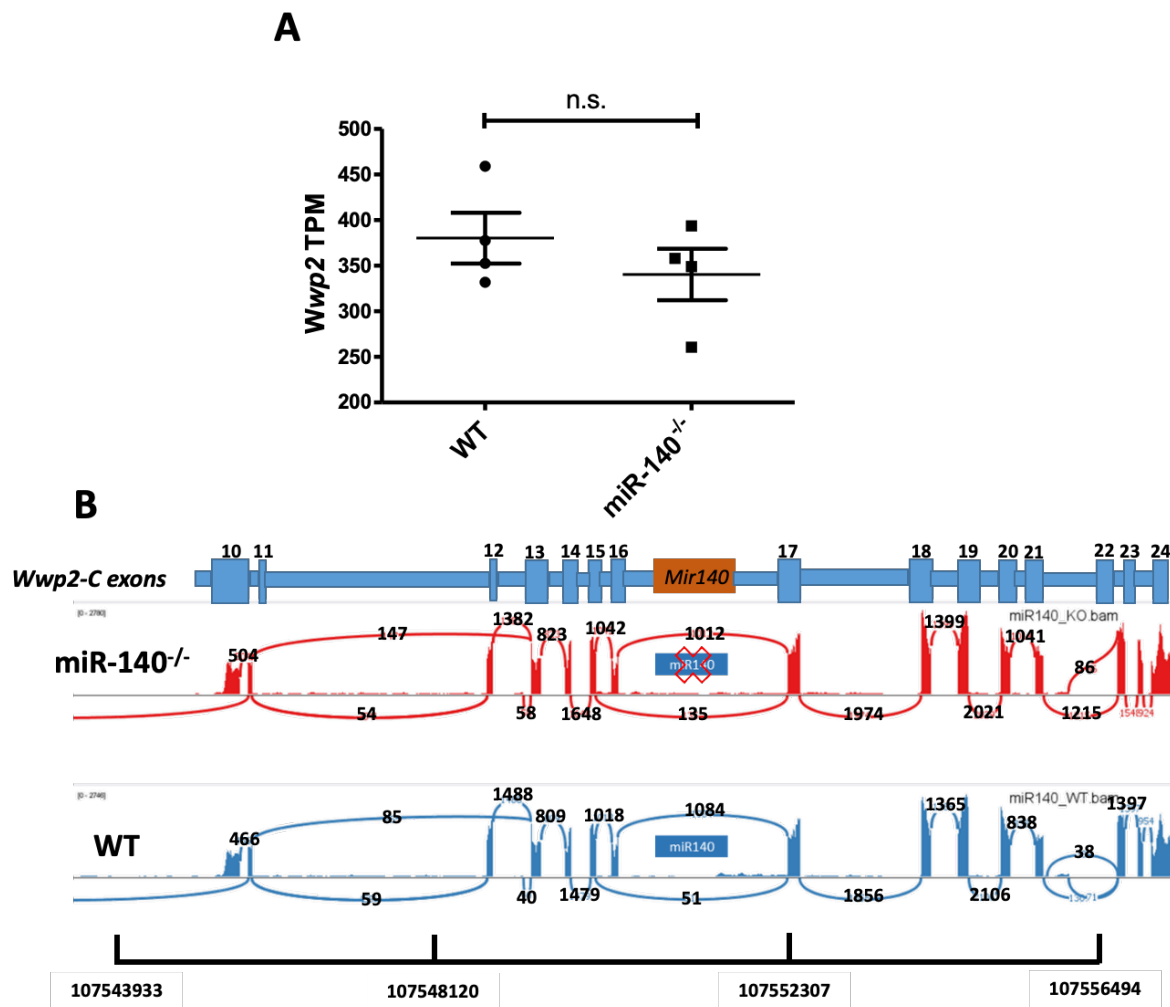
Quantitative real-time PCR analysis was performed to assess the gene expression of miR-140-5p and miR-140-3p in WT and miR-140^{-/-} mice using RNA obtained from rib chondrocytes at 7 days of age. These data confirmed complete absence of both miR-140-5p and miR-140-3p expression in miR-140^{-/-} mice (Fig. 3.1C), as anticipated. RNA-seq analysis of the same RNA (see Chapter 4) confirmed the expression of the miR-140 host gene, *Wwp2*, was not altered in miR-140^{-/-} mice (Fig. 3.2A). A Sashimi plot confirmed that *Wwp2* splicing was not affected by the deletion of *Mir140* locus (Fig. 3.2B).

Figure 3.1 Generation and genotyping of miR-140^{-/-} mice.



(A) Deletion of *Mir140* was attained using the CRISPR/Cas9 system, the black rectangular box indicates the site where deletion occurred, which was also verified by Sanger sequencing (data not shown). The sequences in light blue indicate gRNAs with red bases being the PAM sequence (NGG – note the downstream gRNA is the reverse complement), the brown rectangular box indicates the location of miR-140-5p. (B) DNA was extracted from an ear notch of mice using Phire tissue direct PCR matrix mix kit and subjected to PCR. The 82bp deletion of *Mir140* was confirmed using agarose gel electrophoresis and Sanger sequencing. The arrow above indicates full size of *Mir140*, and the arrow below indicates deletion size. (C) Total RNA was extracted from rib chondrocytes of postnatal day 7 (P7) mice, reverse transcribed to cDNA and subjected to real time qRT-PCR analysis for gene expression of miR-140-5p and miR-140-3p. Values were normalised to *U6*. An unpaired t-test was used for analysis and plotted as mean ± SEM (standard error of the mean) number of samples, WT=7, miR-140^{-/-}=6. *** $p \leq 0.001$.

Figure 3.2 *Wwp2*, the *Mir140* host gene, expression and splicing was unaffected by deletion of *Mir140*.



(A) RNA-seq data analysis of *Wwp2* expression in WT and miR-140^{-/-} mice. RNA was obtained from postnatal day 7 (P7) costal chondrocytes. Data are expressed as TPM, an unpaired t-test was used for analysis and plotted as mean \pm SEM. n=4 animals per group; n.s. not significant. (B) Sashimi plot (derived from RNA-seq BAM files using IGV) showed *Wwp2* splicing junctions were generally unchanged after deleting *Mir140*. The numbers highlighted in black colour are reads which span each exon-exon junction. The data are from merged BAM files of 4 *Mir140*-null and 4 WT mice that were used for RNA-seq. Above is a schematic view of the *Wwp2-C* contains exons (the upstream exons/introns of *Wwp2* gene are not shown) that are correspond to the Sashimi plot.

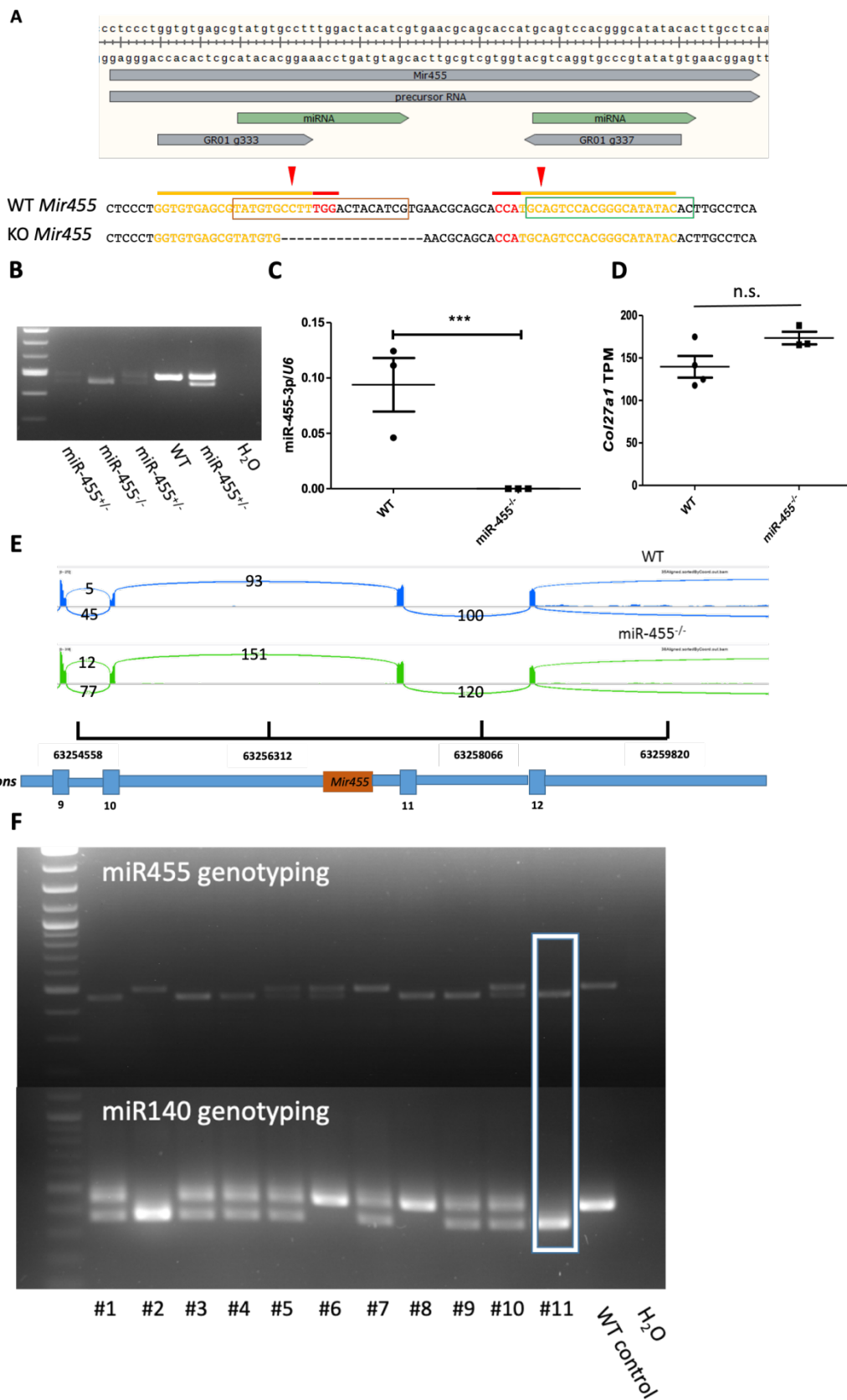
3.2.1.2. Generation of miR-455^{-/-} mice and DKO mice

The generation of C57BL/6 genetic background *Mir455*-null mice was conducted at the University of Manchester using two gRNAs that were designed to target the region between exons of 10 and 11 of the *Col27a1* gene, the host gene of *Mir455* gene. *Mir455*-null mice (two males and two females) were provided by Prof Ian Clark (University of East Anglia, UEA). We confirmed that these mice contained an 18bp deletion of miR-455-3p by genotyping and Sanger sequencing of ear notch genomic DNA (Fig. 3.3A and 3.3B).

Quantitative real-time RT-PCR analysis from RNA isolated from 7-day-old costal chondrocytes of WT and miR-455^{-/-} mice confirmed the absolute absence of miR-455-3p expression in the null animals (Fig. 3.3C). Splicing and expression (measured in TPM) of the *Mir455* host gene, *Col27a1*, was unaffected after deletion of *Mir-455* in mice, as confirmed from RNA-seq analysis of the same costal chondrocyte RNA (Fig. 3.3D & E).

Two other groups have previously generated *Mir140* deletion mice and showed deletion of *Mir140* resulted in a mild skeletal phenotype, including short stature, short tail, and domed skull (Miyaki, Sato et al. 2010, Nakamura, Inloes et al. 2011). Very recently, Ito *et al.* showed no significant differences in skeletal development of mice lacking *Mir455* when compared to age-matched control mice (Ito, Matsuzaki et al. 2021). Although *MIR140* and *MIR455* were confirmed to be highly expressed during human *in vivo* chondrogenesis and in human OA hip chondrocytes, the role of miR-455 in skeletal development and OA pathogenesis is still to be elucidated. To study if *Mir140* and *Mir455* have synergistic or antagonistic effects or antagonism effects in skeletal development and OA pathogenesis, we generated miR-140: miR-455^{-/-} mice (DKO mice), and quantitative real-time RT-PCR and PCR genotyping confirmed the genotype of DKO mice (Fig. 3.3F).

Figure 3.3 Generation and genotyping of miR-455^{-/-} and DKO mice



(A) Deletion of *Mir455* was achieved using CRISPR/Cas9 system, the gap in the sequence (KO allele) indicates the location of the 18bp deleted sequence – determined using Sanger sequencing (data not shown). The sequences in orange indicate gRNAs and in red represent PAM sequence. The rectangle in brown indicates the location of miR-455-5p, and the rectangle in green indicates the location of miR-455-3p. (B) Genotyping of miR-455^{+/−} mice. DNA was extracted from ear notch of mice using Phire tissue direct PCR matrix mix kit and subjected to PCR, 18bp deletion of *Mir455* was then confirmed using agarose gel electrophoresis/Sanger sequencing. The upper product indicates full size of *Mir455*, and the lower product indicates the deleted PCR amplicon. (C) Total RNA, extracted from rib chondrocytes of postnatal day 7 (P7) mice, was subjected to real time qRT-PCR analysis for gene expression of miR-455-3p. Values were normalised to 18S. an unpaired t-test was used for analysis and plotted as mean ± SEM (number of samples, WT=4, miR-455^{+/−} =3, miR-455^{+/−} =3). *** $p \leq 0.001$. (D) RNA-seq data analysis of *Col27a1* expression in WT and miR-455^{+/−} mice. RNA was obtained from postnatal day 7 (P7) costal chondrocytes. Data are expressed as TPM, unpaired t-test was used for analysis and plotted as mean ± SEM, number of animals, WT=4, miR-455^{+/−}=3; n.s. not significant. (E) Sashimi plot (derived from RNA-seq BAM files using IGV) showed *Col27a1* splicing was not significantly changed after deleting *Mir455*. The numbers highlighted in black are reads which span each exon-exon junction. The data are from merged BAM files of 4 *Mir455*-null and 4 WT mice that were used for RNA-seq. The below is a schematic view of the *Col27a1* gene contains exons (the upstream and downstream exons/introns of *Col27a1* gene are not shown) that corresponding to the Sashimi plot. (F) Genotyping of DKO mice. To create DKO mice, we crossed miR-140^{+/−} and miR-455^{+/−} mice to get miR140^{+/−}/455^{+/−} mice, with the offspring subjected to genotyping. Double heterozygous mice were then crossed to generate DKO animals. DNA extraction and PCR amplified were as described. For the miR-140 and miR-455 PCR genotyping assays products 82bp and 18bp shorter, respectively, indicated a deleted allele by agarose gel electrophoresis. In the above representative agarose gel, mouse #11 showed PCR products corresponding to both *Mir455* and *Mir140* deletions, and thus represents a DKO mouse.

3.2.1.3. miR-140^{-/-} mice, miR-455^{-/-} mice, and DKO mice showed defects in endochondral bone growth

miR-140^{-/-} mice, miR-455^{-/-} mice, and DKO were born at a normal Mendelian frequency and survived to reach adulthood. However, all genotypes appeared to have impaired skeletal development compared to their age-matched WT controls. MiR-140^{-/-} mice manifested a mild skeletal short stature phenotype, and miR-455^{-/-} mice were smaller than WT mice, thus DKO mice had a synergistic effect where the growth phenotype is more severe than miR-140^{-/-} mice (Fig 3.7A). *Mir140*-null mice had a domed skull and shorter snout when compared to WT mice and/or miR-455^{-/-} mice, based on measurement of inner canthal distance and skull length (see Chapter 2, section 2.2.6.4). These mild skeletal phenotypes were observed from radiographs of mice (mixed gender) at postnatal day 7 (P7) (Fig. 3.4A).

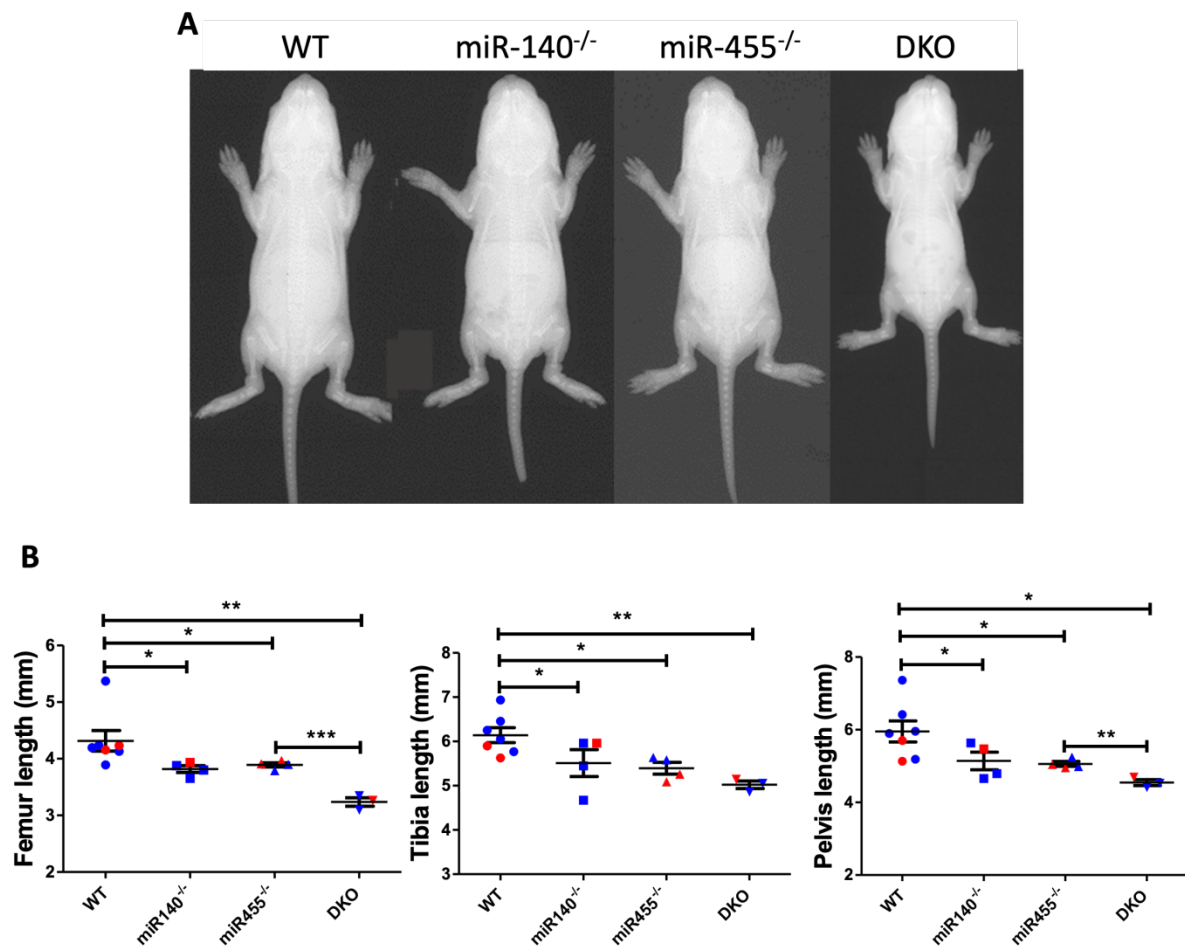
In order to study the role of *Mir140* and *Mir455* in endochondral bone growth, the length of the femur, tibia, and pelvis were measured (Fig. 3.4B). Long bone development was significantly disrupted in miR-140^{-/-} mice and miR-455^{-/-} mice, with the average length of femur (15.3% shorter for *Mir140*-null mice and 9.8% for *Mir455*-null mice), tibia (14% shorter for *Mir140*-null mice and 12.2% for *Mir455*-null mice), and pelvis (16.5% shorter for *Mir140*-null mice and 15% for *Mir455*-null mice) all significantly shorter when compared to the age-matched control mice. DKO mice also showed significant smaller bone length of the femur (25%), tibia (18.2%), and pelvis (23.6%) than WT mice, and with these bones also shorter than single miRNA knock out mice. A hypothesis for the more severe phenotype of the DKO mice is that *Mir140* and *Mir455* act somewhat independently during endochondral ossification.

Visual observation and skeletal preparations indicated that the *Mir140*-null mice and DKO mice had a domed skull and shorter snout when compared to WT mice and/or *Mir455*-null mice (Fig. 3.7B). Microcomputer tomography (μ CT) scanning (section 2.2.6.3) was performed on WT and miR-140^{-/-} P7 skulls to examine the role of *Mir140* in intramembranous and endochondral ossification during craniofacial development. The craniofacial deformities in miR-140^{-/-} mice were characterised by a shorter nasal bone, domed skull, and shorter upper jaw bone; a similar craniofacial phenotype to that observed in cartilage specific-Dicer and Drosha deficient mice as well as previously generated miR-

$140^{-/-}$ mice (Kobayashi, Lu et al. 2008, Miyaki, Sato et al. 2010, Nakamura, Inloes et al. 2011, Kobayashi, Papaioannou et al. 2015) (Fig. 3.5A). To obtain quantitative differences for the domed skull between WT mice and miR- $140^{-/-}$ mice, the ICD/skull ratio (skull vertical length/inner canthal distance ratio) was measured from μ CT images. Compared to WT mice, miR- $140^{-/-}$ mice have a shorter skull length, but larger inner canthal distance (ICD), thus the ICD/skull ratio was significantly (12%) bigger than for WT mice (Fig. 3.5B). We also performed haematoxylin & eosin (H&E) histology staining on skulls of WT and miR- $140^{-/-}$ mice at P7, and measured the length of skull basal growth plate. This showed that the skull basal growth plate of WT mice are bigger than that of miR- $140^{-/-}$ animals (Fig. 3.5C). Although μ CT was not performed for miR- $455^{-/-}$ or DKO mice, based on the radiographs, mice lacking *Mir455* had a similar ICD/Skull ratio as the control mice. Conversely, miR- $140^{-/-}$ mice, as expected based on μ CT analysis, showed a significantly larger ICD/Skull ratio than miR- $455^{-/-}$ or control mice, consistent with μ CT analysis, and DKO mice are intermediate (Fig. 3.5D). In appearance DKO mice showed the domed skull phenotype similar to miR- $140^{-/-}$ mice, but ICD/skull ratios were not statistically significant when compared to that of WT mice (Fig. 3.5D). Furthermore, we observed that DKO and miR- $140^{-/-}$ mice have overgrown mandibular incisors, a phenotype previously observed in *Wwp2*-null mice but possibly a consequence of dysregulated miR-140 expression in these animals (Zou, Chen et al. 2011).

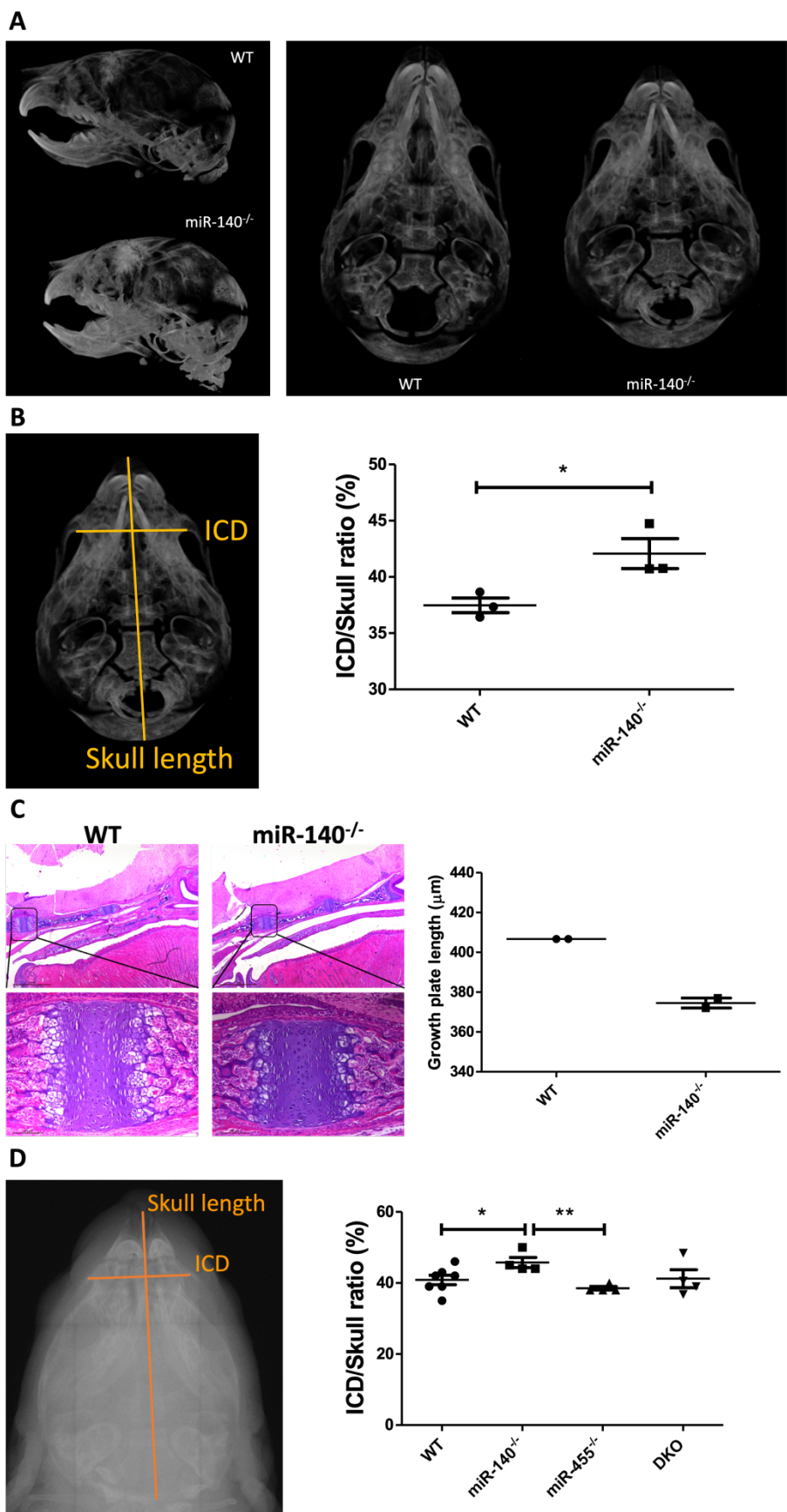
To investigate if the mild short stature skeletal phenotype observed among microRNA deletion mice was associated with reduced body weight and delayed growth, miR- $140^{-/-}$, miR- $455^{-/-}$, DKO, and WT mice were weighed at 7, 14, 22, 28 days of age and weight curves were generated (Fig. 3.6). Genetically modified mice had a significantly lower body weight than control mice at all time points in both sexes ($p<0.05$, ANOVA test), with DKO mice weighing less than other genetic modified mice at all of four time points. MiR- $455^{-/-}$ mice weighed less than miR- $140^{-/-}$ mice at 14 and 22 days, whereas their body weight overtook the miR- $140^{-/-}$ mice at 28 days of age (Fig. 3.6A). Male mice showed the same body weight pattern as sex mixed mice (Fig. 3.6B). In contrast, for female mice, the differences of in body weight between miRNA deficient mice and control mice was much smaller than male mice, but with an overall similar pattern (Fig. 3.6C).

Figure 3.4 Radiographs of mice at 7 days of age.



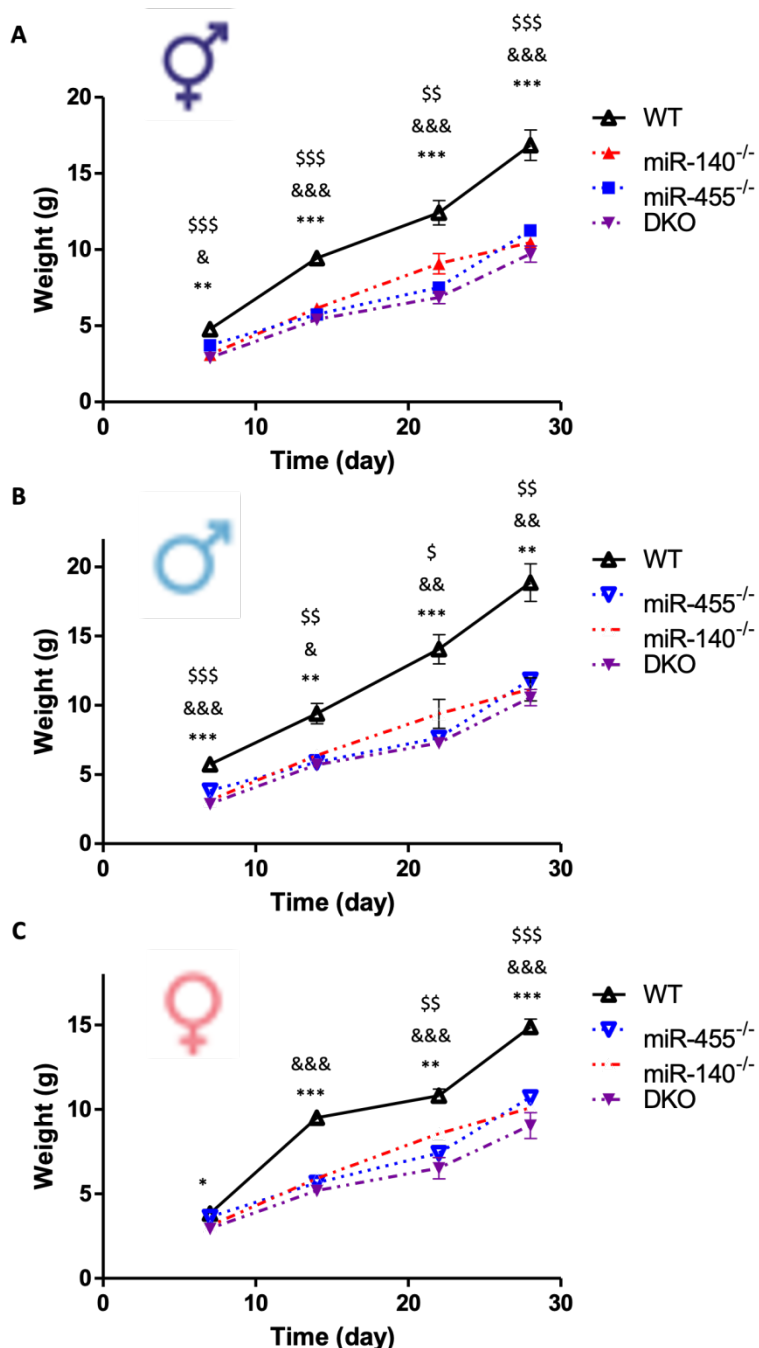
(A) To study the skeletal phenotype following the deletion of *Mir140* and *Mir455*, mice were X-rayed at P7, and compared to WT mice. Images are representative of $n \geq 3$ per genotype. (B) The length of femur, tibia and pelvis were measured at 7 days of age that based on X-ray images. Ablation of miR-140 and miR-455 microRNAs in mice was associated with significantly shorter bone length when compared to WT controls, with miR-140^{-/-} mice and miR-455^{-/-} mice showed similar length of femur, tibia, and pelvis length. DKO mice had a more severe short bone phenotype than other genotypes ($n=3-7$). The blue colours indicate males, and the red colours indicate females. An unpaired t-test was used for analysis and plotted as mean \pm SEM, * $p \leq 0.05$, ** $p \leq 0.01$.

Figure 3.5 Reconstructed μ CT images and radiographs of 7-days skull.



(A) μ CT of miR-140^{-/-} mice skulls (9 μ m of resolution) at 7 days of age showed significant domed shape as compared to wild type mice, n=3 per genotype. (B) Abnormal ICD/skull ratio was observed in μ CT images of miR-140^{-/-} mice, which reflects the domed skull shape. Measurements were performed with ImageJ software, the measurement are outlined in yellow, n=3. An unpaired t-test was used for analysis and plotted as mean \pm SEM, * $p\leq 0.05$. (C) H&E staining was performed on skulls of WT and miR-140^{-/-} mice at P7. Measurement of basal growth plate was performed with ImageJ software, n=2 per genotype, with four matched sections from five locations per mouse were counted, data presented are the mean of the four sections per mouse. (D) Measurement of ICD/Skull ratio was performed based on radiography images, (animal numbers: WT=7, miR-140^{-/-}=4, miR-455^{-/-}=4). An unpaired t-test was used for analysis and plotted as mean \pm SEM, * $p\leq 0.05$, ** $p\leq 0.01$.

Figure 3.6 Weight analysis of mice at 7, 14, 22, and 28 days of age.



Mice were weighed at 7, 14, 22, and 28 days of age to generate weight curves of (A) mixed sex, (B) males only, and (C) females only. The one-way analysis of variance (ANOVA) was used to determine whether there were any statistically significant differences between different genotypes and weight curves were plotted as mean \pm SEM, n=3-11 at all ages and all sexes. Comparisons between WT and miR-140^{-/-} is represented as \$, WT and miR-455^{-/-} is as &, and * stands for the comparison between WT and DKO. P values are reported as: \$/&/* p≤0.05, \$\$&/&/** p≤0.01, \$\$\$&/&&/*** p≤0.001.

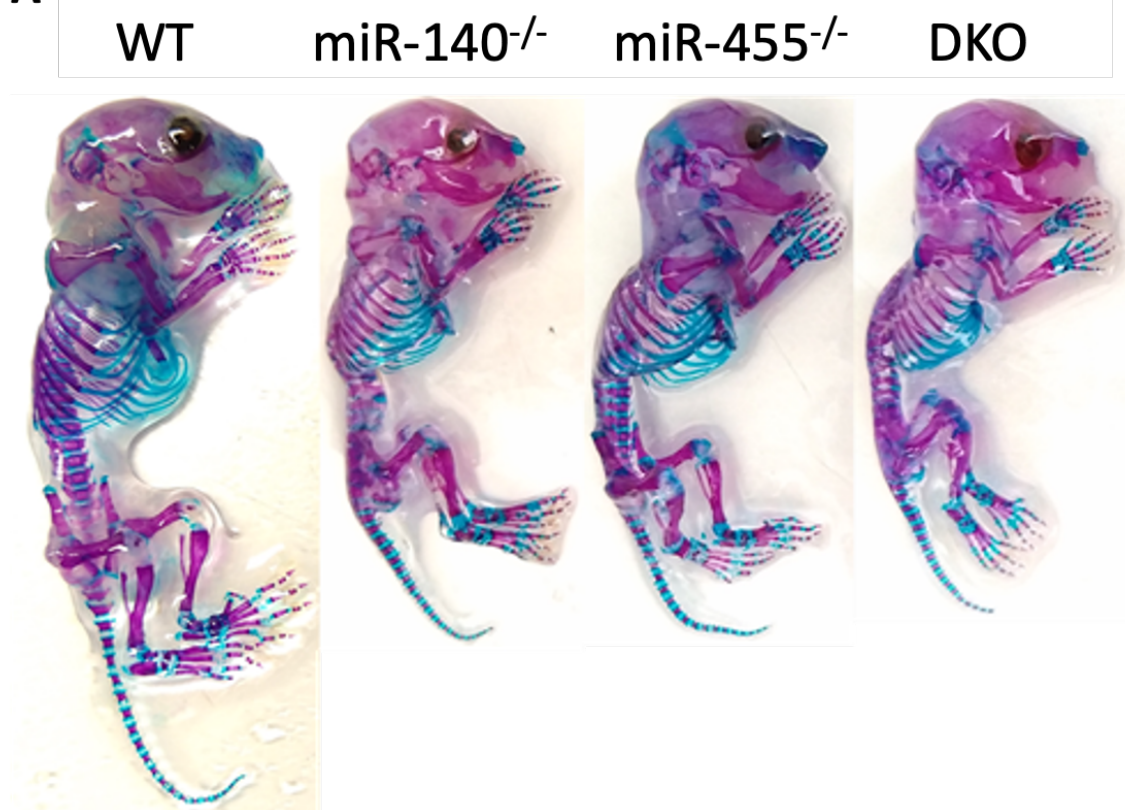
3.2.1.4. miR-140^{-/-} mice, miR-455^{-/-} mice, and DKO mice showed altered skeletal growth

To further analyse the effect of the deletion of *Mir140* and *Mir455* on skeletal development, including endochondral ossification and intramembranous ossification, skeletal preparations were performed at age P7. These were co-staining with Alcian blue (to stain glycosaminoglycans) and Alizarin Red (to stain calcium deposits in bone) (Fig. 3.7 & 3.8). Confirming the radiography, deletion of *Mir140* and *Mir455* either singly or together affected skeletal development of the mice, which manifested as short stature. This was accompanied by larger regions of Alcian blue staining at the wrist joints, metacarpophalangeal joints, interphalangeal joints, and ankle joints in miRNA deficient mice all indicative of delayed endochondral ossification of cartilage. Despite both individual miRNA deletion mice showing a skeletal phenotype, the deletion of both *Mir-140* and *Mir-455* did not severely affect endochondral ossification more than deletion of either microRNA alone. In addition, intramembranous ossification (rudimentary formation of flat bones of the skull) of DKO mice appeared less affected than the severe domed skull of the miR-140^{-/-} mice (Fig. 3.7B). The size of the rib cage in miRNA deletion mice are reduced when compared to WT mice (Fig. 3.8A). The DKO mice showed a slightly shorter spine length and scapula size even when compared to the miR-140^{-/-} mice (Fig. 3.8B and 3.8C). Quantification of body size and tail length revealed that all three miRNA deficient models had significantly shorter body size than WT mice ($p<0.05$, ANOVA), with miR-140^{-/-} and DKO mice also having a significantly shorter tail length (Fig. 3.9). The body size of miR-140^{-/-} mice was intermediate between that of miR-455^{-/-} and DKO mice (Fig. 3.9). The DKO mice had the shortest body size amongst the different genotypes (Fig. 3.9A). WT mice and miR-455^{-/-} mice had very similar tail lengths. However, miR-140^{-/-} mice and DKO mice had significantly shorter tail lengths compared to both WT mice or miR-455^{-/-} mice, although there were no differences in tail length between miR-140^{-/-} and DKO mice.

Interestingly, skeletal development of DKO mice among the genetically modified mice was not always the most severe (shortest or delayed) for all the bones analysed, which again suggests that miR-140 and miR-455 may have some antagonistic roles on skeletal development.

Figure 3.7 Skeletal preparation of mice at 7 days of age.

A

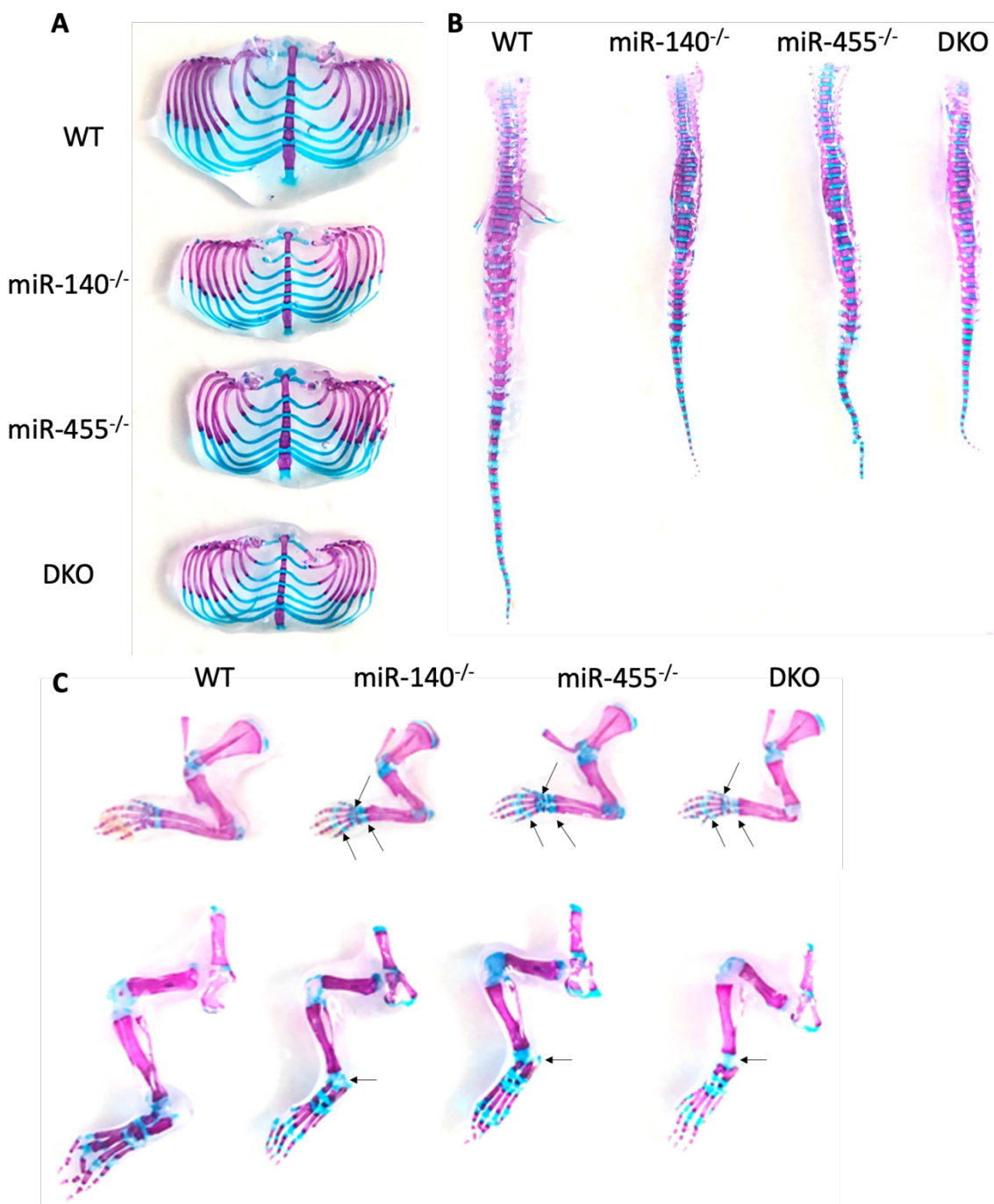


B



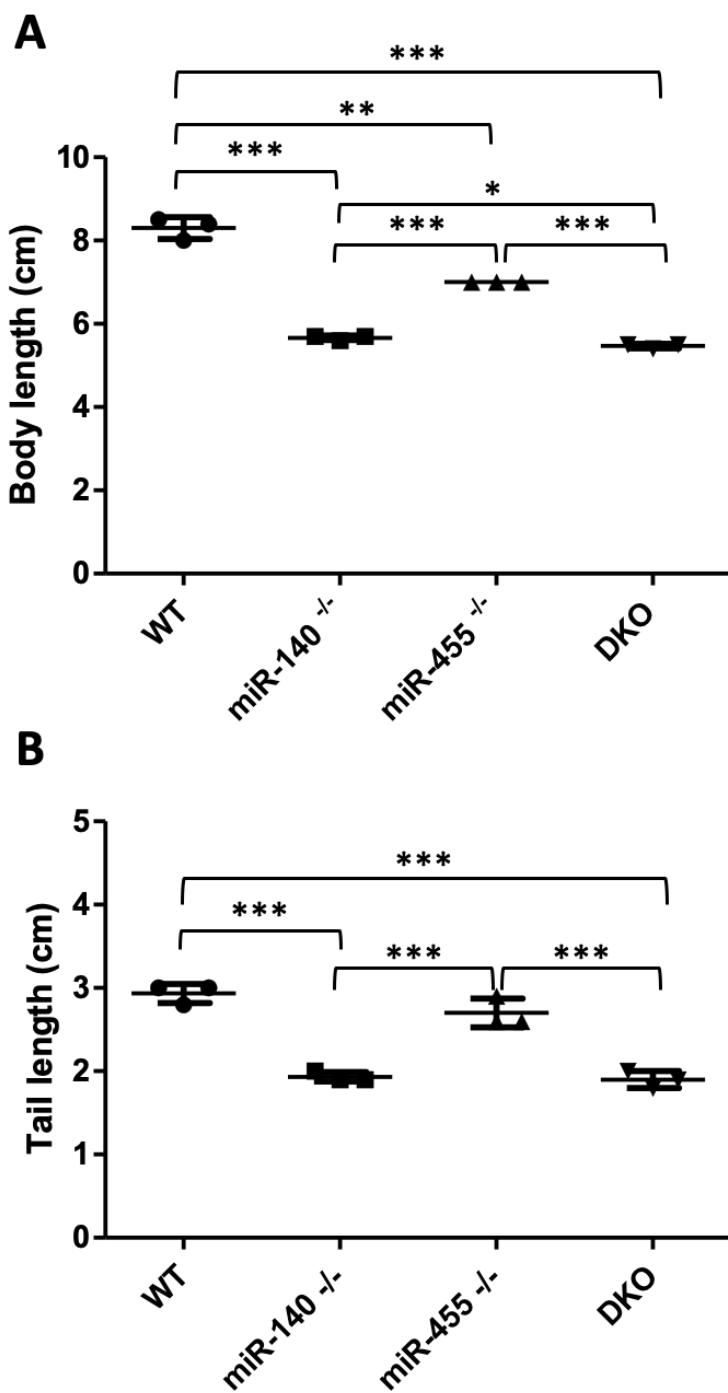
(A) Skeletal preparation with Alcian Blue and Alizarin Red staining on mice at 7 days of age, the whole-mount skeletal staining showed abnormal skeletal development among miRNA deletion mice when compared to WT mice. (B) As had been observed via visual observation and X-ray, miR-140^{-/-} mice and DKO mice have domed skull shape, but with miR-140^{-/-} mice more severe than DKO mice. n=3 per genotype.

Figure 3.8 Endochondral ossification was affected by deleting *Mir140* and *Mir455*.



(A-C) Endochondral ossification development was delayed in miRNA deficient mice. n=3 per genotype. Skeletal preparation with Alcian Blue and Alizarin Red staining on mice at 7 days of age. (A) Rib cage, (B) Spine and (C) fore and hind limbs were dissected for clarity. The arrows point to wrist, metacarpophalangeal, interphalangeal and ankle joints in miRNA deficient mice, indicating where cartilage was still present and replacement with bone tissue had been delayed compared to WT mice.

Figure 3.9 MicroRNA deletion mice showed shorter body and tail length at 7 days of age.



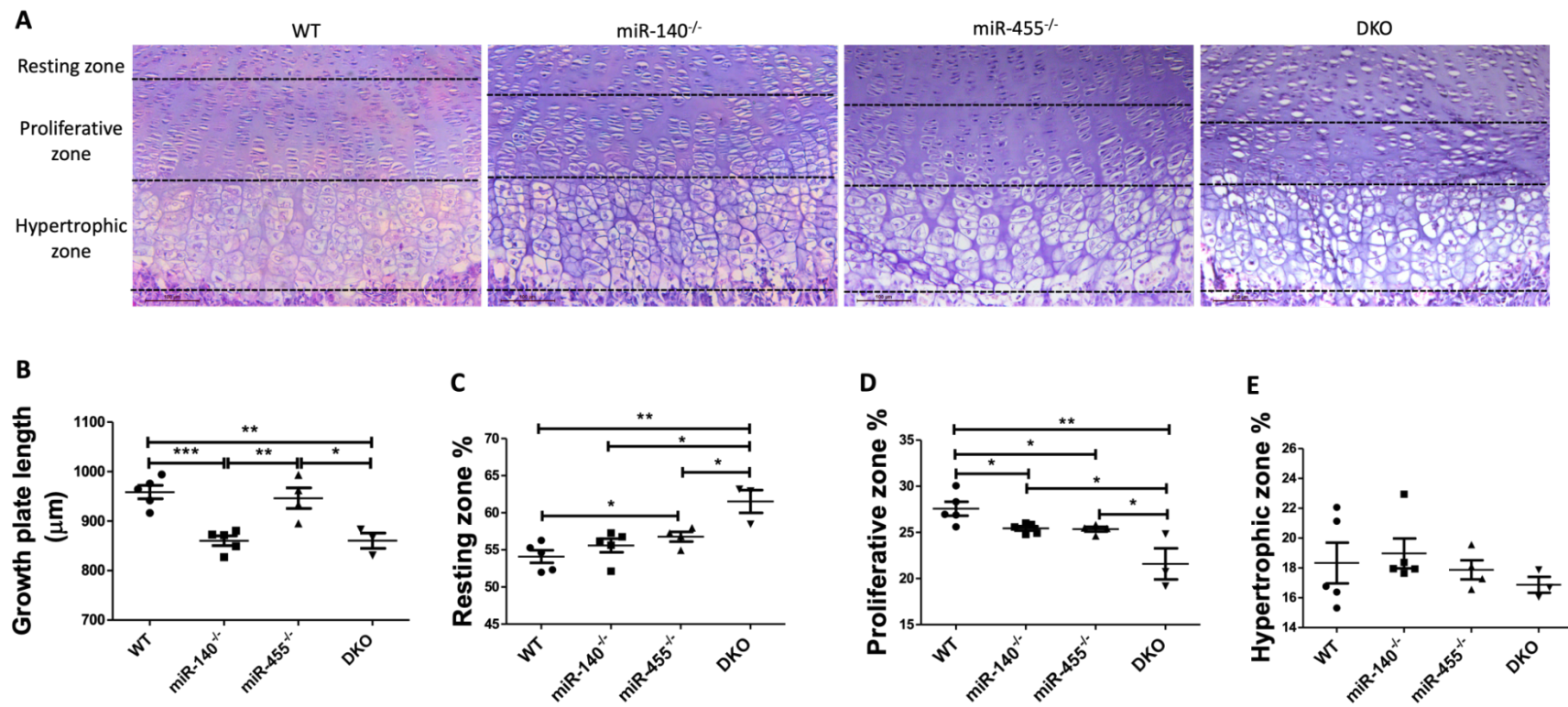
(A) Body length and (B) tail length of the four different genotypes at P7. The value represents as cm. The one-way analysis of variance (ANOVA) was used to determine statistically significant differences between different genotypes. Differences within each genotype were plotted as mean \pm SEM, (n=3)
 * $p \leq 0.05$, ** $p \leq 0.01$, *** $p \leq 0.001$.

3. 2. 1. 5. Deletion of *Mir140*, *Mir455*, and both of *Mir140* and *Mir455* result in abnormal growth plate organisation and chondrocyte morphology

Chondrocytes in the growth plate are indispensable for skeletal development. MiR-140 was previously found to be expressed in proliferative and pre-hypertrophic chondrocytes of tibia growth plate in mice (Miyaki, Sato et al. 2010). For miR-455 expression, miR-455-3p was detected in the skeleton of the developing limbs of chick embryo on day 6.5 and then restricted in the developing joints on day 7.5-8. Its expression was also detected in the growth plate and perichondrium of E18 mouse embryos; others have showed that miR-455 expression was detected in proliferating and pre-hypertrophic chondrocytes of E16.5 mouse limbs (Swingler, Wheeler et al. 2012, Chen, Chen et al. 2016). Here, Haematoxylin & Eosin (H&E) staining was performed on tibial growth plates in the four mouse genotypes to study the skeletal growth plate of mice in the absence of *Mir140* and/or *Mir455*. This showed that the height of the tibia growth plate in miR-140^{-/-} and DKO mice at P7 were reduced compared to P7 WT and miR-455^{-/-} mice (Fig. 3.10A & B). Within the tibial growth plate, the percentage of the growth plate comprised of proliferative zone was significantly reduced in both the miR-140^{-/-} mice and miR-455^{-/-} mice compared with WT mice (Fig. 3.10A & D). In contrast, the percentage of the growth plate comprised of the hypertrophic zone was slightly increased in miR-140 deletion mice (Fig. 3.10A & E). In miR-455^{-/-} mice the resting zone comprised a significantly larger percentage of the growth plate compared with WT mice and miR-140^{-/-} mice (Fig. 3.10A & 3.10C). These finding are in concordance with previous miR-140^{-/-} murine analysis (Miyaki, Sato et al. 2010). DKO mice showed the smallest percentage of the growth plate comprised of the proliferative and hypertrophic zone among 4 different genotypes, but with the largest percentage of the growth plate comprised of the resting zone (Fig. 3.10A, B & C). In these histological staining images, we observed that miR-140^{-/-} mice showed disordered columnar structure when compared to WT controls. In contrast, miR-455^{-/-} mice somewhat lacked the regular columnar structure but only in the central region of the proliferative zone. The tibial growth plate of DKO mice appeared the most disordered, with a lack of clear columns of proliferative chondrocytes and more hypertrophic-like chondrocytes in the growth plate. These findings indicate that the reduced percentage of the growth plate comprised of the proliferative zones in growth

plate may account for the mild, shorter stature, skeletal phenotype observed in miR-140^{-/-}, miR-455^{-/-}, and DKO mice.

Figure 3.10 MicroRNA knockout mice at P7 showed a disrupted growth plate with abnormal chondrocyte morphology.

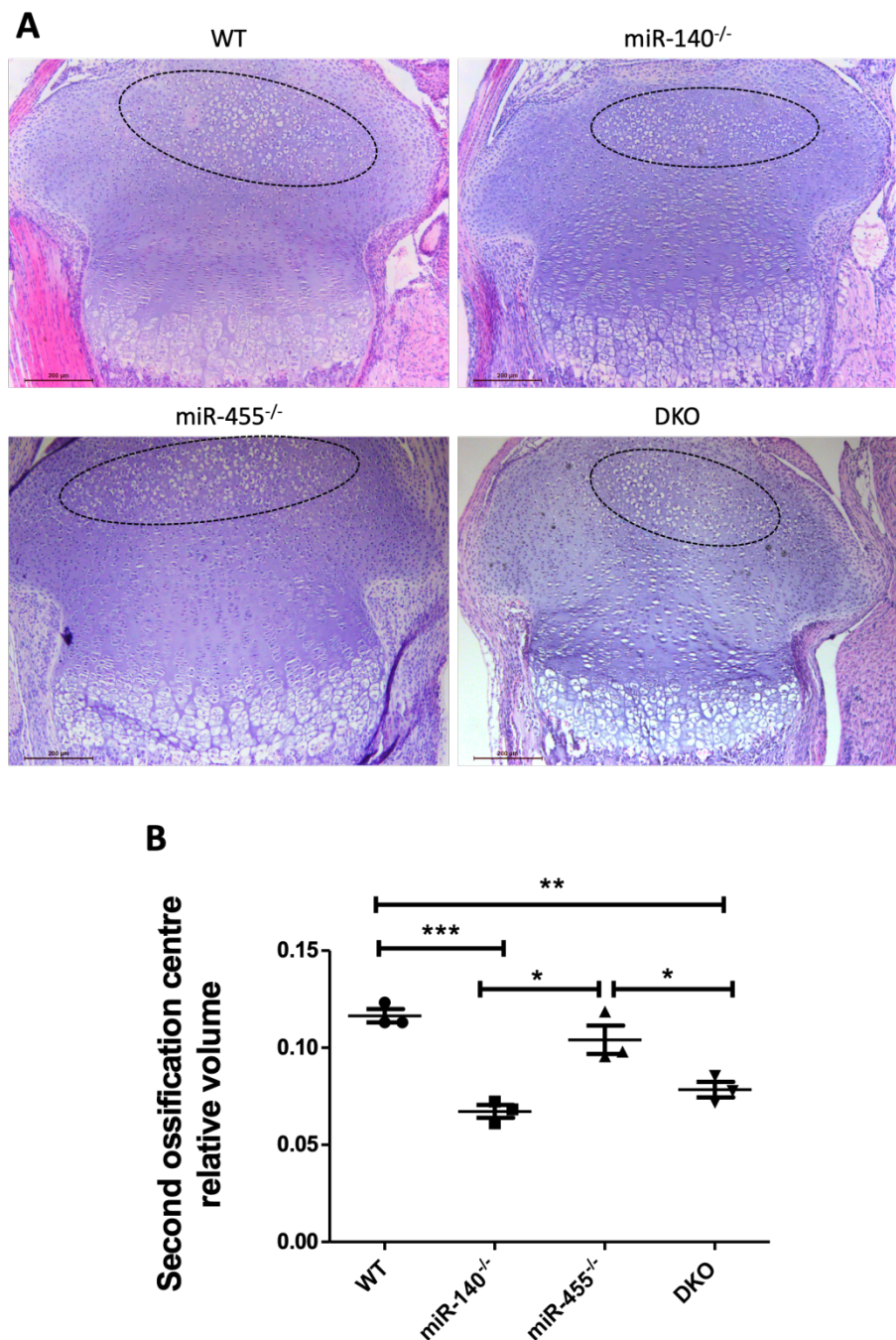


(A) Haematoxylin & Eosin (H&E) staining was performed in WT, miR-140^{-/-}, miR-455^{-/-}, and DKO mice at 7 days of age. Broken lines were used to distinguish different zones in the growth plate, which includes resting, proliferative and hypertrophic zones. n=3, matched sections from 5 locations per genotype were measured (original magnification, x20; scale bar = 100 μ m). (B) The actual growth plate vertical length of four genotypes at P7 were measured using Image J. based on images of H&E staining sections. An unpaired t-test was used for analysis and plotted as mean \pm SEM, (n=3-5). * $p \leq 0.05$, ** $p \leq 0.01$. The percentage size of (C) resting zone, (D) proliferative zone, and (E) hypertrophic zone as a proportion of the whole growth plate were measured using image J, based on images of H&E stained sections. Unpaired t-test was used for analysis and plotted as mean \pm SEM, (n=3-5). * $p \leq 0.05$, ** $p \leq 0.01$.

The secondary ossification centre in the tibia epiphysis appears postnatally and is an important contributor of bone length through regulating hypertrophic chondrocyte apoptosis (Xie, Gol'din et al. 2020) (Fig. 3.11). H&E staining showed that the size of secondary ossification centre in mice at P7 was reduced in miR-140^{-/-} and DKO mice when compared to WT and miR-455^{-/-} mice (Fig. 3.11). Interestingly, DKO mice displayed a slightly larger secondary ossification centre than miR-140^{-/-} mice (Fig. 3.11). However, these mice did have a smaller percentage of the growth plate comprised of the proliferative zone (Fig. 3.10C). These findings may lead to a hypothesis that aspects of the functions of miR-140 and miR-455 may have opposing roles in skeletal growth.

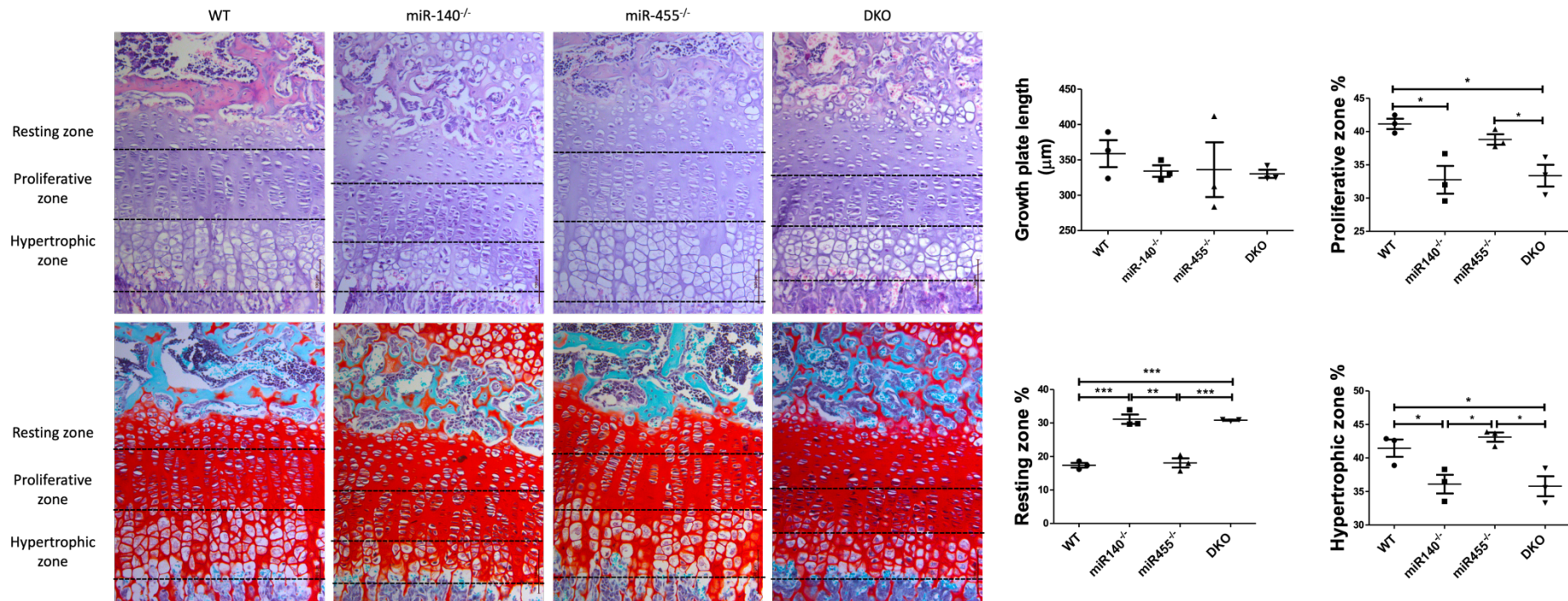
Comparable H&E and Safranin-O staining were performed on 22-day-old mice which showed a similar growth plate organisation as compared to the mice at P7 (Fig. 3.12). We noticed that the relative proportions of the different zones are altered in miR-140^{-/-} and DKO mice (significantly increased percentage of resting zone, decreased percentage of proliferative and hypertrophic zone compared to WT mice). However, there were no significant differences in growth plate composition between WT and miR-455^{-/-} mice. In addition, we noticed that H&E staining showed that nuclei staining in hypertrophic chondrocytes of *Mir140*-null was very dark when compared to other genotypes, possibly indicating increased apoptosis in hypertrophic chondrocytes (Roach and Clarke 2000). Furthermore, the columnar structure defect observed in *Mir455*-null mice at P7 was not that obvious by P22. Safranin-O staining clearly showed that the size of secondary ossification centre in 22-day-old mice was reduced in miR-140^{-/-} and DKO mice compared with WT, which is consistent with the P7 H&E observations (Fig. 3.13). Unlike *Mir455*-null mice at P7, the mice at P22 showed a significantly smaller secondary ossification centre compared to WT mice ($p<0.05$, $n=3$ per genotype), and we noticed that articular cartilage GAG staining was reduced in *Mir455*-null mice compared to other genotypes (Fig. 3.13). Moreover, DKO mice showed the smallest (and thus most delayed) secondary ossification centre development.

Figure 3.11 Secondary ossification is disrupted by depletion of *Mir140* in mice at P7.



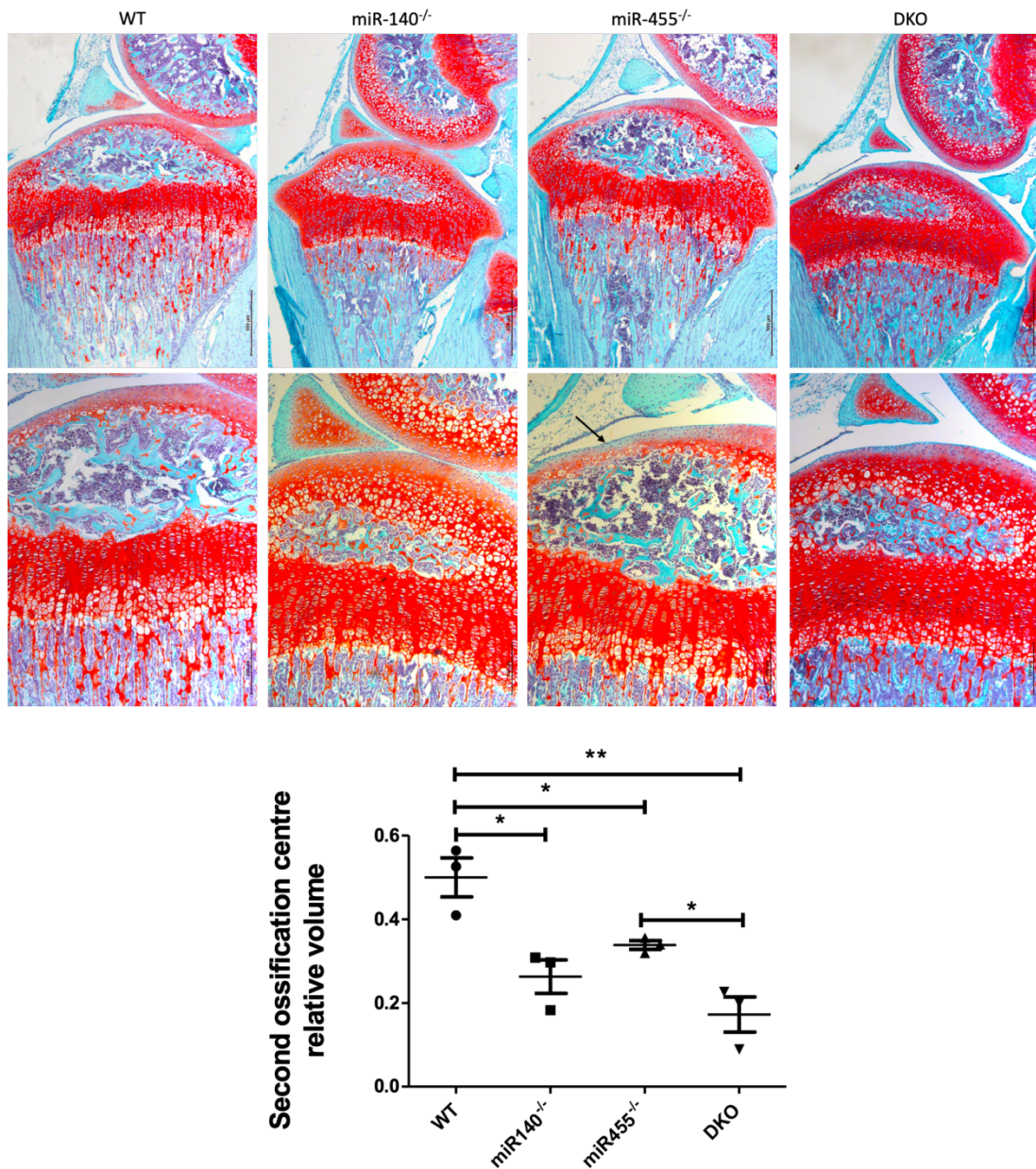
(A) Haematoxylin & Eosin (H&E) staining was performed on the secondary ossification centre and tibial growth plate from WT, miR-140^{-/-}, miR-455^{-/-}, and DKO mice at P7. The black ovals represent the approximate secondary ossification centre in the tibial growth plate (original magnification, X10). (B) Quantitative analysis of second ossification centre of the tibial growth plate were measured using image J software, based on images of H&E stained sections (original magnification, X5). An unpaired t-test was used for analysis and plotted as mean \pm SEM, (n=3). * $p \leq 0.05$, ** $p \leq 0.01$, *** $p \leq 0.001$.

Figure 3.12 MicroRNA knockout mice at P22 showed a disrupted growth plate with abnormal chondrocyte morphology.



Histology staining was performed on the tibial growth plate from WT, miR-140^{-/-}, miR-455^{-/-}, and DKO mice at P22 with H&E (upper images) and Safranin O (bottom images), respectively. The broken lines were used to distinguish different zones in the growth plate, which includes the resting, proliferative, and hypertrophic zones. n=3 (original magnification, x20; scale bar = 100 μm). The percentage size of resting zone, proliferative zone, and hypertrophic zone as a proportion of the whole growth plate were measured using image J. An unpaired t-test was used for analysis and plotted as mean ± SEM, (n=3). * p≤0.05, ** p≤0.01, *** p≤0.001.

Figure 3.13 Secondary ossification is disrupted by depletion of *Mir140* in mice at P22



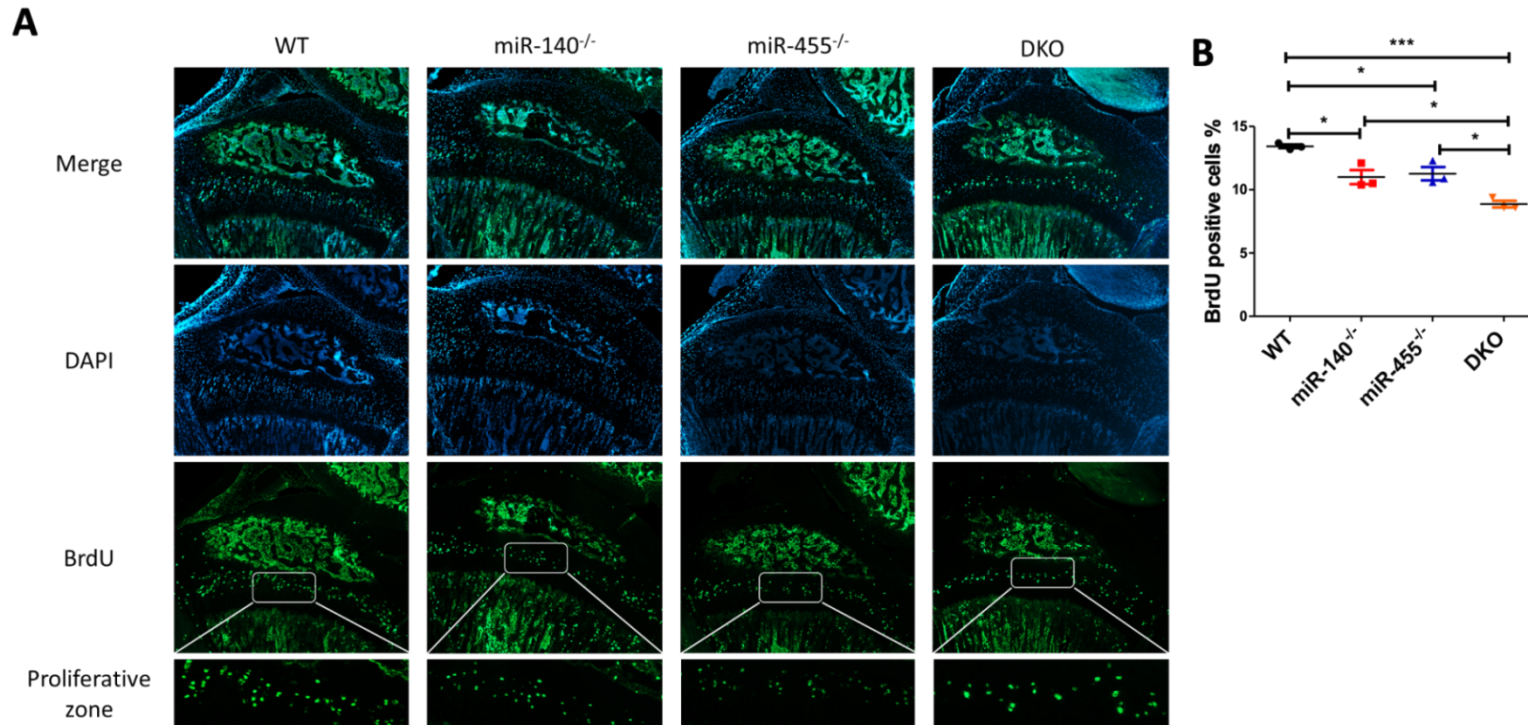
Safranin-O staining was performed on the secondary ossification centre and the tibial growth plate from four genotypes at P22. GAG staining was reduced in the articular cartilage of *Mir455*-null mice (see arrow). Original magnification, x5 (upper line), x10 (bottom line); scale bar = 500 μ m (up); scale bar = 200 μ m (bottom); n=3 per genotype. Quantitative analysis of second ossification centre of the tibial growth plate were measured using image J software, based on images of Safranin-O stained sections (original magnification, X20). An unpaired t-test was used for analysis and plotted as mean \pm SEM, (n=3). * $p \leq 0.05$, ** $p \leq 0.01$, *** $p \leq 0.001$.

3.2.1.6. Deletion of *Mir140*, *Mir455*, and both of *Mir140* and *Mir455*, affects chondrocyte proliferation in the growth plate

To compare the differences in the number of proliferating growth plate chondrocytes amongst the different genotypes, 5-bromo-2'-deoxyuridine (BrdU) was subperitoneal injected into P22 mice two hours before euthanisation and the harvesting of the knee joints. BrdU is a synthetic thymidine analogue that is incorporated into replicating DNA during S phase of the cell cycle, thus proliferating cells can be detected using a specific anti-BrdU antibody.

The size of proliferative zone in miR-140^{-/-} and DKO mice was smaller than in WT mice at P22 and the number of BrdU labelled chondrocytes was also reduced in these mice compared with WT mice (Fig. 3.15A). There were fewer proliferative zone BrdU labelled cells observed in miR-455^{-/-} mice, although there was a slightly larger proliferative zone in these mice when compared to the equivalent WT mice (Fig. 3.14). We thus analysed the number of BrdU-positive chondrocytes as a percentage of the total number of cells in the proliferative zone, per genotype. This was significantly reduced in microRNA-null mice compared with age matched controls, with the DKO mice also having significantly fewer proliferating chondrocytes than the individual microRNA-null animals (Fig. 3.15B), indicating that miR-140 and miR-455 may play a synergistic role in regulating proliferation of chondrocytes in the growth plate.

Figure 3.14 Proliferative chondrocytes in growth plate are disrupted by depletion of *Mir140* and *Mir455*.



(A) Immunocytochemistry using anti-BrdU antibody was performed to detect proliferative chondrocytes in tibia growth plate of mice at 22 days of age which 2 hr before sacrifice had been injected with BrdU. BrdU positive chondrocytes were detected using an AlexaFluro™ 488 secondary antibody (green) and nuclei of chondrocytes were counterstained with DAPI (blue), magnification, x10. A total of nine sections per mouse and three mice per genotype, were imaged by confocal microscopy and the analysed using Image J software. (B) BrdU-positive chondrocytes in the proliferative zone were calculated manually using Image J software and presented as a percentage against the total number of chondrocytes in the proliferative zone. An unpaired t-test was used for analysis and plotted as mean ± SEM, * $p \leq 0.05$, ** $p \leq 0.01$, *** $p \leq 0.001$, n=3 per genotype, with matched sections from nine locations per mouse were counted. Data presented is the mean of the nine sections per mouse.

3.2.1.7. Deletion of *Mir140* and *Mir455* alone or in combination affects chondrocyte apoptosis in the growth plate

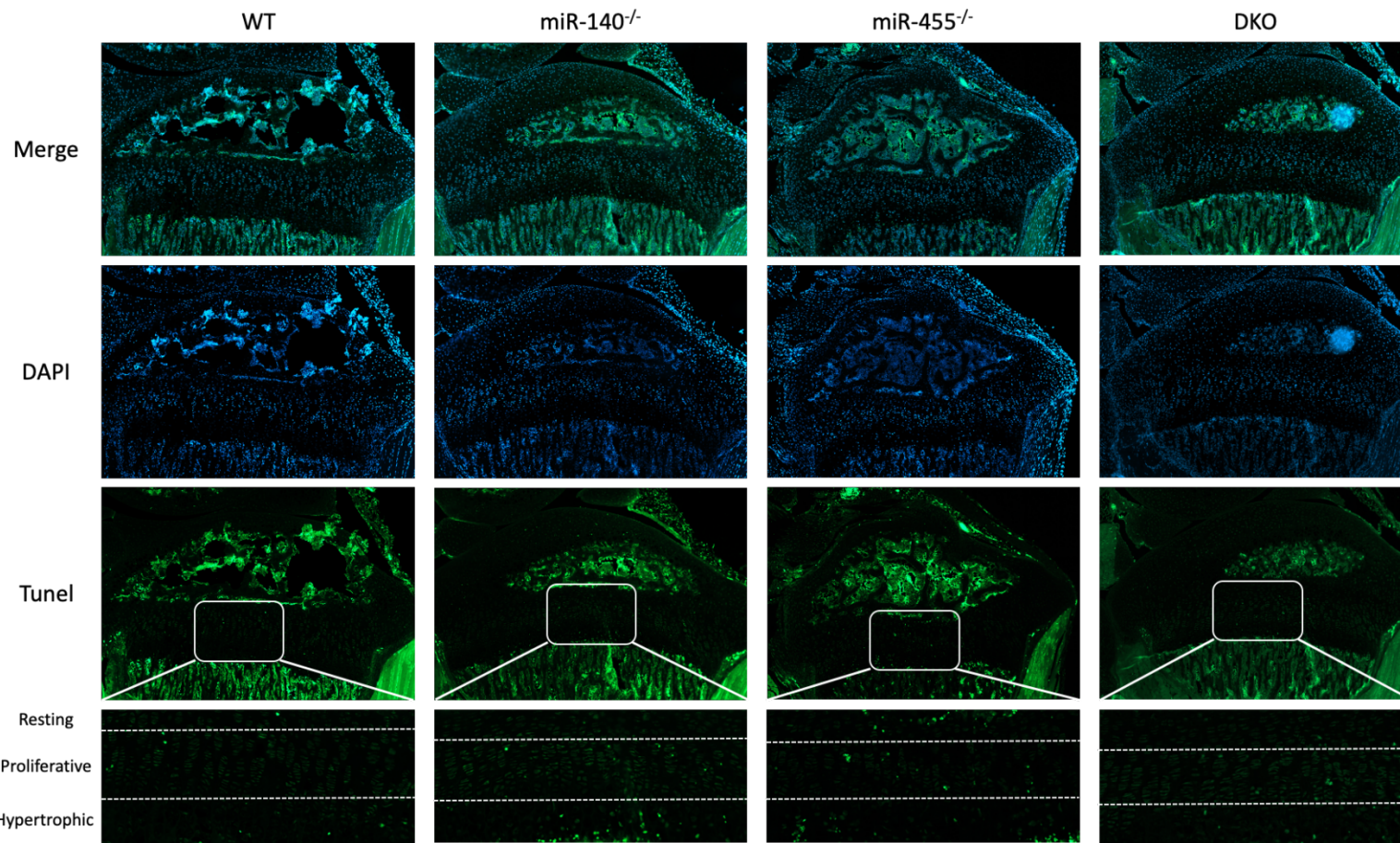
H&E and Safranin-O staining for both P7 and P22 revealed altered percentages of growth plate resting, proliferative and hypertrophic zones in miRNA deficient mice, which could indicate apoptosis of growth plate chondrocytes being affected. To compare the differences in the number of apoptotic chondrocytes in the growth plate amongst the four different genotypes at P22 we used a terminal deoxynucleotidyl transferase dUTP nick end labelling (TUNEL) assay. This assay detects excessive DNA breakage in cells via the enzyme terminal deoxynucleotide transferase (TdT) that attaches deoxynucleotides to the 3'-hydroxyl terminus of DNA double-strand breaks which occur during apoptosis.

The number of apoptotic chondrocytes in the resting, proliferative, and hypertrophic zones in mice were counted. When examining all zones combined, more TUNEL-positive chondrocytes were observed in miR-140^{-/-}, miR-455^{-/-}, and DKO mice (Fig. 3.15) compared to WT mice. As for the BrdU analysis, the proportion of TUNEL-positive chondrocytes in different zones of growth plate against the total number of chondrocytes within that zone was used to compare the level of apoptosis between the different genotypes.

In WT mice, TUNEL positive apoptotic cells were almost exclusively presented in hypertrophic zone, whereas TUNEL-positive chondrocytes could be detected from all three zones of growth plate in miR-140^{-/-} mice, miR-455^{-/-} mice, and DKO mice (Fig. 3.15). Based on DAPI staining and clear distinguishable growth plate structures in these staining images, we manually divided the tibial growth plate into resting, proliferative and hypertrophic zones. We observed that more apoptotic chondrocytes in the resting zone were detected in miR-455^{-/-} mice compared to WT mice (0.83% and 0.35% respectively, $p= 0.023$, Fig. 3.16A), while miR-140^{-/-} mice showed significantly more TUNEL-positive chondrocytes in the hypertrophic zone compared to age-matched WT controls (2.43% and 1.62% respectively, $p= 0.025$, Fig. 3.16C). Though the mean percentage of TUNEL-positive chondrocytes in the proliferative zones of the microRNA deletion mice was increased compared to WT, this was not significant (Fig. 3.16B). Overall, miR-140^{-/-} mice, miR-455^{-/-} mice, and DKO mice all showed higher percentage of apoptotic chondrocytes, and a significant increase in apoptosis was observed in absence of *Mir140* compared to age-matched control mice (1.16% and

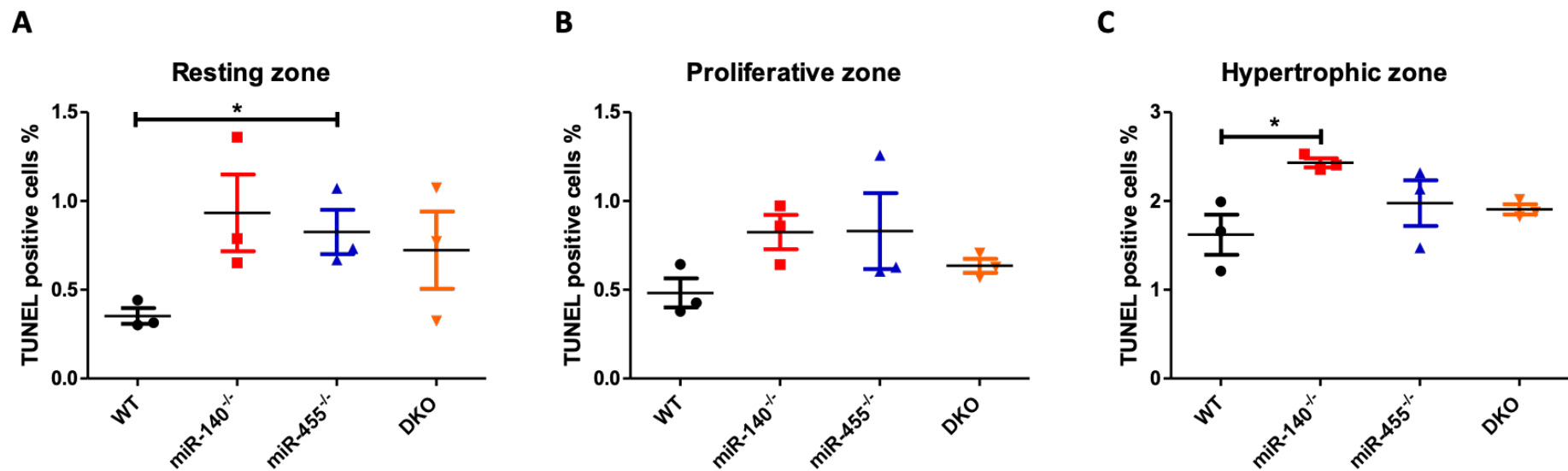
0.9% respectively, $p= 0.01$, Fig. 3.17). However, the DKO mice had less TUNEL-positive chondrocytes than either the miR-140^{-/-} mice or miR-455^{-/-} mice. Again, this could indicate that miR-140 and miR-455 might play an antagonistic role in regulating chondrocyte apoptosis.

Figure 3.15 Apoptosis of chondrocytes in growth plate are affected by depletion of *Mir140* and *Mir455*.



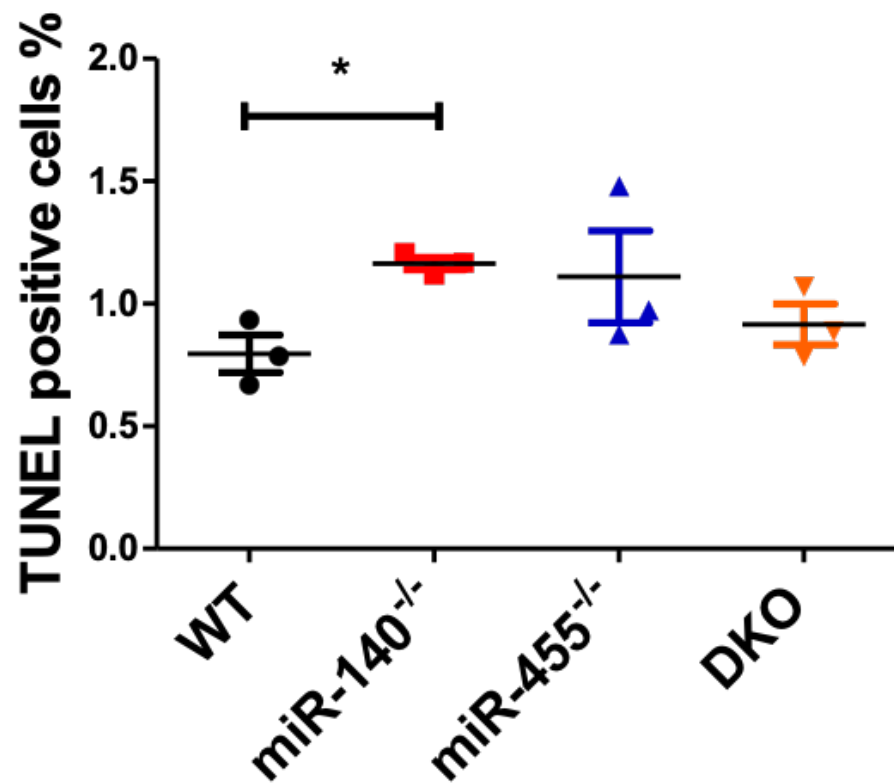
Immunocytochemistry for detecting TUNEL-positive chondrocytes was performed to analyse apoptotic chondrocytes in the tibial growth plate of the four different genotypes at P22. TUNEL positive chondrocytes were detected using an AlexaFluro™ 488 secondary antibody (green) and nuclei of chondrocytes were counterstained with DAPI (blue), magnification, x10.

Figure 3.16 *Mir140* and *Mir455* loss accelerates apoptosis of chondrocytes in tibial hypertrophic and resting growth plate zones, respectively.



TUNEL-positive chondrocytes in different zones of the tibial growth plate of mice at 22 days of age were calculated using Image J software and plotted as a percentage against the total number of chondrocytes in that zone, n=3 per genotype, with matched sections from three locations per mouse quantified. Each datapoint is the mean percentage of positive cells from the three sections per mouse, an unpaired t-test was used for analysis with the bars showing the mean ± SEM, * p≤0.05.

Figure 3.17 Lack of *Mir140* increases apoptosis of chondrocytes in the tibial growth plate.



TUNEL-positive chondrocytes in the tibial growth plate of mice at 22 days of age were calculated using Image J software and plotted as a percentage against the total number of chondrocytes in the growth plate, n=3 per genotype, with matched sections from three locations per mouse quantified. Each datapoint is the mean percentage of positive cells from the three sections per mouse, unpaired t-test was used for analysis with the bars showing the mean \pm SEM, * $p\leq 0.05$.

3. 3. Discussion

The aim of this chapter was to characterise and compare the skeletal phenotype of mouse models lacking either *Mir140* or *Mir455*, or both, using various morphometric and histological methods.

3. 3. 1. *Mir140*-null mice show defects in skeletal bone development

Mir140 knockout mice exhibited a mild skeletal phenotype with shorter bone length, shorter tail, and domed skull compared with WT mice. For example, the bone length of the femur, tibia, and pelvis are all significantly shorter in miR-140^{-/-} mice at P7 compared with age-matched controls, and the ICD/skull ratio was significantly bigger, indicative of a rounded skull shape. Similar to the other *Mir140* knockout mice models at P21 (Nakamura, Inloes et al. 2011, Papaioannou, Inloes et al. 2013), histological staining on our *Mir140* knockout mice at P7 and P22 both showed a smaller height of proliferative zone and an expanded resting zone. However, in the original publication describing mice lacking miR-140, Miyaki *et al.* showed that the height of resting zone in 1-month-old mice was reduced compared with WT mice (Miyaki, Sato et al. 2010). Although subtly different, when taken together these studies confirm that miR-140 regulates chondrocytes differentiation in the growth plate.

Our histological staining showed disrupted tibial growth plate structure in *Mir140*-null, *Mir455*-null and DKO mice (Fig. 3.10 and 3.12), indicating that *Mir140* and *Mir455* seem to play a role in multiple phases of growth plate including proliferation and differentiation. The number of BrdU-labelled proliferative chondrocytes were significantly less in the tibia growth plate of our *Mir140*-null mice at P22 compared with wild-type mice. At P22, the secondary ossification centre in miR-140^{-/-} mice was smaller, indicating that the process of endochondral ossification is delayed in mice in the absence of miR-140. Coupled with H&E and Safranin-O staining of the tibial growth plate at P7 and P22, this suggests miR-140 deficiency might slow down the rate of differentiation for proliferative chondrocytes from resting chondrocytes, affecting the columnar structure. Furthermore, miR-140 deficiency appears to regulate proliferative chondrocytes prematurely differentiating into hypertrophic chondrocytes. Thus, we concluded that miR-140 deficiency delays endochondral bone

development in mice partially through reducing the number of proliferative chondrocytes in growth plate. However, only some of the previous studies have shown difference on the number of proliferative chondrocytes in the tibia growth plate with loss of miR-140. For example, Kobayashi *et al.* found no significant change in the number of BrdU-labelled proliferative chondrocytes in the tibial growth plate of *Mir140*-null mice at E17.5, P3.5, P5.5, P14, or P21 (Nakamura, Inloes *et al.* 2011, Papaioannou, Inloes *et al.* 2013). In contrast, Miyaki *et al.* showed that BrdU-positive chondrocytes were significantly reduced in the *Mir140*-null mice at P21 when compared to WT mice (Miyaki, Sato *et al.* 2010), similar to our findings herein. The above two well described *Mir140*-null mice were generated using constructed vectors to replace the endogenous miR-140 locus with either PGK-neo cassette or FRT-neo cassette, and then the mice were crossed with Meox-Cre TG mice or flpe transgenic mice to remove the cassette, respectively (Miyaki, Sato *et al.* 2010, Nakamura, Inloes *et al.* 2011, Papaioannou, Inloes *et al.* 2013). In contrast, we targeting miR-140 locus using CRISPR/Cas9 system, and microinjected Cas9 protein recombinant zygotes into Albino mice, the mice were then crossed with C57BL/6 mice. Thus, these contradictory findings about growth plate proliferating chondrocytes may result from different mice background, and of course might arise from the use of different methodologies, detecting kit, antibodies, and imaging methods. In the next Chapter I will explore the underlaying mechanism that regulates growth plate chondrocyte proliferation.

We observed that columnar structure of proliferating chondrocytes in the tibial growth plate of our *Mir140*-null, *Mir455*-null and DKO mice were poorly organised at P7. Reduced mechanical joint loading is one cause of columnar disorganisation of chondrocyte in the growth plate (Maeda, Nishida *et al.* 2005, Prein, Warmbold *et al.* 2016, Killion, Mitchell *et al.* 2017). Our miR-null mice all weighed less than age-matched WT mice, presumably causing less mechanical loading on the knee and thus potentially changing the intracolumn and intercolumn collagen network and therefore growth plate chondrocytes arrangement. In fact altered knee loading (following induced-knee OA by the destabilisation of the medial meniscus (DMM) surgical model) has been shown to cause growth plate columnar structure and organisational changes in adult mice (Lamuedra, Gratal *et al.* 2020). Of course disorganisation of the columnar structure could also be due to disruption of signalling pathways that are important for chondrocyte proliferation and hypertrophy. For example,

Shp2 deficiency in mice induces disorganised growth plate proliferative chondrocyte columns, due to dysregulation of the transition between chondrocyte differentiation states through inhibition of the extracellular signal-related kinase (ERK)1/2 pathway (Bowen, Ayturk et al. 2014). *Fgfr3* deficient mice also have disorganised growth plate proliferative chondrocytes, with an accompanied decrease in ERK activity but increased Indian hedgehog (IHH) expression (Zhou, Xie et al. 2015). However, postnatal deletion of *Ihh* in mice also results in a disorganised columnar structure and dwarfism (Maeda, Nakamura et al. 2007). Taken together, altered mechanical/loading or signalling in mice due to a lack of miRNAs could play a role in disrupting the growth plate columnar structure.

Furthermore, the PTHrP pathway plays a critical role in the regulation of endochondral bone development through maintaining chondrocytes proliferation and delaying their further differentiation into pre-hypertrophic and hypertrophic chondrocytes. PTHrP regulates the pace of chondrocyte differentiation in balance with the Indian hedgehog (Ihh) pathway (Chapter 1, 1.2.2.3), a major regulator of PTHrP synthesis in the growth plate. Such a PTHrP-Ihh feedback loop might contribute to the uniformity of proliferating chondrocyte morphology across the growth plate (Kronenberg 2006). PTHrP signalling indirectly regulates phosphorylation of the class II histone deacetylase HDAC4, a described miR-140 target, controlling its nuclear localisation and subsequently the function of the transcriptional regulator MEF2C, all of which combine to regulate chondrocyte hypertrophy (Tuddenham, Wheeler et al. 2006, Paroni, Cernotta et al. 2008, Kozhemyakina, Cohen et al. 2009, Sasagawa, Takemori et al. 2012, Nishimori, Lai et al. 2019).

It is reported that PTHrP overexpression partially rescues the skull phenotype of *Mir140*-null mice (Papaioannou, Mirzamohammadi et al. 2015). The study demonstrated that *Mir140*^{-/-} *PThrP*^{+/+} and *Mir140*^{-/-} *Hdac4*^{+/+} compound mutant mice showed a significant growth defect (shortened size of the proliferative zone and disorganised column proliferating structure) when compare to *Mir140*-null mice, indicating miR140-PThrP and miR140-HDAC4 have synergistical effects on the regulation of columnar chondrocyte differentiation (Papaioannou, Mirzamohammadi et al. 2015). Mechanistically, the level of MEF2C and p38 MAPK signalling were upregulated in *Mir140*-null murine rib chondrocytes, and inhibition of p38 MAPK signalling in *Mir140*-null rib chondrocytes decreased the expression level of MEF2C. p38 MAPKs directly phosphorylate MEF2C to stimulate chondrocyte hypertrophic

differentiation (Papaioannou, Mirzamohammadi et al. 2015). However, the underlying mechanism of activation of p38 MAPK in *Mir140*-null chondrocyte remains unclear. CD38 signalling can lead to activation of p38 and CD38 has been identified as a direct target of miR-140-3p (Jude, Dileepan et al. 2012).

Mice lacking either miR-140 or miR-455 manifested a mild skeletal phenotype, but only mice lacking *Mir140* ($\text{miR140}^{-/-}$ and DKO mice) showed craniofacial deformities. Craniofacial anomalies (CFAs) are typically congenital disorders with either genetic factors and/or environmental causes. An understanding of these causes and mechanisms is therefore useful to understand CFA and skull development *per se*. Two previous *Mir140*-null mice publications have described the craniofacial truncation phenotype in mice in the absence of miR-140 and no change in the transcriptional or protein expression level of the *Mir140* host gene, *Wwp2* (Miyaki, Sato et al. 2010, Nakamura, Inloes et al. 2011). However, Zou *et al.* proposed that this craniofacial phenotype resulted from the loss of *Wwp2* expression in mice (Zou, Chen et al. 2011). The authors propose that *Wwp2* is normally involved in the mono-ubiquitylation of the transcription factor Goosecoid, which in turn regulates *Sox6*, a key transcriptional factor for chondrocyte differentiation. However, in the Zou *et al.* publication the *Wwp2*-null mice ($Wwp2^{\text{GT/GT}}$) were generated by the insertion of a gene-trap cassette between exon 3-4 of the *Wwp2* locus which potentially prevents expression of the downstream exons and introns, including miR-140 (Zou, Chen et al. 2011). The functional relationship between microRNAs and their host gene remains a controversial topic. Our *Mir140*-null mice showed the similar craniofacial phenotype with no overt disruption of *Wwp2* expression, though we were unable to confirm whether *Wwp2* protein level was affected even though we tried several commercial antibodies (data not shown). Inui *et al.* recently generated KO mice of different combinations of *Mir140* and *Wwp2* and examined the craniofacial phenotype using mCT analysis, finding that only the *Mir140*-null mice showed a truncated skull phenotype. Mice with a deletion of just *Wwp2* had no apparent skull defects, and the deletion of both *Wwp2* and *Mir140* did not show a synergistic effect on the *Mir140*-null craniofacial phenotype (Inui, Mokuda et al. 2018, Mokuda, Nakamichi et al. 2019). Our group recently generated a KO mouse lacking the 5'UTR exon of the C-terminal *Wwp2* (*Wwp2-C*) isoform using CRISPR/Cas9. These *Wwp2-C^{-/-}* mice expressed the downstream exons shared with the full length *Wwp2* isoform, which includes the *Mir140*

locus, and miR-140 at approximately 50% of the WT level, equivalent to that expressed by miR140^{+/−} mice (data not shown). Mice lacking Wwp2-C had a very much milder skull shape phenotype compared to the miR-140^{−/−} mice and identical to that of miR^{+/−} mice. Again, this adds weight to the notion that the CFA is caused by a lack of miR-140. With the assistance of Dr Ralf Kist (Newcastle University), we dissected and fixed skulls of *Mir140*-null and WT mice at P7 and performed H&E staining to observe the skull basal cartilaginous regions that locate between BasiOccipital (BasO) and Sphenoid Body (SphB). The structure of this cartilaginous region is similar to that of the tibial growth plate and the regions similarly showed a reduced size of the growth plate in our *Mir140*-null mice compared with the WT mice, indicating miR-140 is also involved in endochondral bone development of the skull. Furthermore, Grigelioniene *et al.* (Grigelioniene, Suzuki *et al.* 2019) identified two independent patients with similar phenotypes (including short stature, short limbs, small hands and feet, small nose, delayed epiphyseal ossification of hip and knee, mild spondylar dysplasia *etc*) who both contained a single base substitution (A→G) within miR-140. These individuals display many phenotypic overlapping features with those seen in the various *Mir140*-null mice, including CFA. However, the specific mutation affects the miR-140-5p seed sequence (A > G), thus the phenotypic consequences could be due to both loss- and gain-of-function (i.e. a new miR-140-5p target repertoire) target effects. In an attempt to resolve this the authors generated a novel mouse with the corresponding single nucleotide substitution (miR-140^{G/G}) and compared these to *Mir140*-null mice, with the conclusion that although both mice have skeletal abnormalities the phenotype of the miR-140^{G/G} mice is more severe (see below). Regardless, together these data lead to the conclusion that the loss of miR-140 causes the craniofacial truncation phenotype.

The secondary ossification centre in tibia of miR-140^{−/−} mice at P7 and P22 are smaller than that of the WT or miR-455^{−/−} mice, especially for P7. Although the tibial secondary ossification centre of miR-455^{−/−} mice was similar to that of WT mice at P7, this was significantly delayed by P22. As described, Grigelioniene *et al.* generated mice (miR-140^{G/G} mice) that genetically copied the mutation identified two skeletal dysplasia patients (Grigelioniene, Suzuki *et al.* 2019). Although both miR-140^{G/G} mice and miR-140^{−/−} mice have shorter stature, truncated nose and delayed secondary ossification development, miR-140^{G/G} mice showed a more severe phenotype of delayed secondary ossification of tubular

and carpal bones than that of miR-140^{-/-} mice, indicating that repressing certain genes delays secondary ossification development. Thus, these data collectively indicate that miR-140, rather than miR-455, significantly delays tibial secondary ossification development in mice, presumably due to de-repression of selective miR-140 target genes that inhibit secondary ossification development.

3. 3. 2. *Mir455*-null mice show defects in endochondral bone growth

MiR-455^{-/-} mice had less severe skeletal phenotype than miR-140^{-/-} mice, with shorter stature but no domed skull compared to WT mice. The difference in long bones between miR-455^{-/-} mice and WT mice at 7 days of age was similar to that of miR-140^{-/-} versus WT controls. These data would suggest that miR-455 functions as an activator of early chondrogenic differentiation. It has been suggested this could partially be by miR-455-3p inhibiting osteogenesis through directly targeting of *Runx2* (Zhang, Hou et al. 2015). Our group previously profiled miRNA expression during chondrogenic differentiation of human bone marrow MSCs by microarray with or without critical factors of chondrogenesis (SOX9, TGF-beta, and high cell density) and highlighted that the expression of miR-140-5p and miR-455-3p changed significantly (Barter, Tselepi et al. 2015); we and others also showed that miR-140-5p and/or miR-455-3p expression strikingly increased during chondrogenic differentiation of mouse ATDC5 cells, human adipose-derived stem cells (hADSCs), and human bone mesenchymal stem cells (hBMSCs) (Swingler, Wheeler et al. 2012, Zhang, Kang et al. 2012, Zhang, Hou et al. 2015, Sun, Zhao et al. 2018, Hu, Zhao et al. 2019, Mao, Kang et al. 2019, Wen, Li et al. 2020, Ito, Matsuzaki et al. 2021). Taken together, coupled with the short stature of mice lacking either miR-140 or miR-455, these data conclude that miR-140 and miR-455 are highly involved in chondrocyte development *in vivo* and *in vitro*, respectively.

The vertical size of the proliferative zone of tibial growth plate in miR-455^{-/-} mice at P7 was smaller, but the height of the resting zone was significantly bigger than WT mice, indicating a retardation of resting chondrocytes differentiating into proliferative chondrocytes, which may account for shorter bone (femur, tibia, and pelvis) length in these animals. The hypertrophic zone was of equal size between WT and miR-455^{-/-} mice at both P7 and P22. This phenotypic observation correlates well with miR-455-3p expression which is limited to

proliferative and pre-hypertrophic chondrocytes of limbs of mouse embryos at E16.5, indicating that miR-455-3p expression pattern in tibia growth plate is like that of miR-140 (Miyaki, Sato et al. 2010, Chen, Chen et al. 2016). In addition, miR-455-3p was observed to regulate early chondrogenic differentiation of ATDC cells, hADSCs and hBMSCs, possibly suggesting that the microRNA plays a negligible role during hypertrophy chondrocytes differentiation (Zhang, Hou et al. 2015, Chen, Chen et al. 2016, Sun, Zhao et al. 2018, Hu, Zhao et al. 2019, Mao, Kang et al. 2019, Wen, Li et al. 2020). There were no publications describing a tibial growth plate phenotype of *Mir455*-null mice, although several studies examined the expression of miR-455-3p in *Mir455*-null and/or WT mice in forelimb of mouse embryos at E16.5 to demonstrate the relationship of expression pattern between miR-455-3p and its target genes or chondrogenesis regulatory genes (Chen, Chen et al. 2016, Hu, Zhao et al. 2019, Mao, Kang et al. 2019). There are possible explanations for why the authors of these studies have not reported a skeletal development phenotype amongst *Mir455*-null and WT mice, including that the phenotype is subtle or that the focus of the publications was not on endochondral bone development. Only very recently has endochondral bone development been assessed in *Mir455*-null in the literature, with Ito *et al.* showing these animals had comparable skull length, trabecular bone volume (femur), volumetric BMD of cancellous bone of the femur, and body weight when compared to age-matched control mice (Ito, Matsuzaki et al. 2021). Interestingly, we obtained the *Mir455*-null line from Prof Ian Clark's laboratory (UEA, UK) and established the line at Newcastle University. Although we observed that our *Mir455*-null mice are smaller than age-matched WT mice in appearance and X-ray analysis, our collaborator cannot detect similar differences, in agreement with Ito *et al.* (Ito, Matsuzaki et al. 2021). This could suggest a genetic-drift such that our line is smaller. Alternatively, the difference could be a consequence of environmental, metabolic (different food source) or microbiome differences. The gut microbiota has been shown to influence skeletal muscle mass and function in mice (Lahiri, Kim et al. 2019) and although data is currently limited the microbiome may also regulate bone metabolism (Charles, Ermann et al. 2015). Although no studies have examined the microbiome and skeletal development, several reports have shown a role for gut flora in OA progression in mice (Favazzo, Hendesi et al. 2020) and joint pain and inflammation in humans (Boer, Radjabzadeh et al. 2019). Of course, our two laboratories used different WT mice for the weight comparisons with the *Mir455*-null mice,

however, the weight of both UEA C57BL/6 and our WT mice were in the well-recognised weight range of C57BL/6 mice (body weight information for C57BL/6J (000664), the Jackson laboratory). In preliminary data, we and our collaborator also observe reduced Safranin-O staining for *Mir455*-null mice knee cartilage (see Chapter 5) when compared with the age-matched WT mice, consistent with the finding of others (Hu, Zhao et al. 2019, Mao, Kang et al. 2019, Wen, Li et al. 2020, Ito, Matsuzaki et al. 2021). Thus, other than the size of the mice our data and that of UEA are comparable, again adding weight to the notion that our skeletal phenotype might arise from environmental influences.

3. 3. 3. DKO mice show defects in skeletal bone growth

DKO mice have a domed skull similar to that of miR-140^{-/-} mice and more severe skeletal phenotype. Histological staining (H&E and Safranin-O) for tibia of DKO mice at P7 showed the vertical size of the hypertrophic zone is similar as in WT mice, however, the height of the proliferative zone is much smaller than miR-140^{-/-} mice and miR-455^{-/-} mice, indicating that miR-140 and miR-455 play a synergistic role in proliferative chondrocyte differentiation. However, DKO mice at P22 had a larger vertical size of the proliferative zone and a smaller height of the hypertrophic zone, a developmental pattern similar to that of miR-140^{-/-} mice, suggesting that miR-455 plays a minor role for hypertrophic chondrocyte differentiation at least at this developmental age, which is consistent with analysis of *Mir455*-null mice alone. The size of secondary ossification centre in DKO mice at 7 days of age was larger than that of miR-140^{-/-} mice but smaller than that of miR-455^{-/-} mice, however, DKO mice at P22 showed the most delayed secondary ossification development of the tibia compared to other genotypes, which is presumably due to the contribution miR-455 loss plays in delaying secondary ossification development at this age, indicating miR-140 and miR-455 function through differing mechanisms to regulate secondary ossification development in the tibial growth plate.

3. 3. 4. Knockout of miR-140 and/or miR-455 in chondrocytes reduces proliferation and increases cell death

Since all our genetically modified mice showed an altered size of the tibial growth plate structure and delayed endochondral bone development (the shorter bone length of femur,

tibia, and pelvis), coupled with histological staining of tibia of mice, this suggests that miR-140 and miR-455 could affect proliferative chondrocyte differentiation. The severe growth plate development defects observed in chondrocytes of mice in the absence of *Dicer* is also reportedly due to a defect in chondrocyte proliferation, suggesting the dominant function of microRNAs in the growth plate is to regulate the proliferation of chondrocytes (Kobayashi, Lu et al. 2008). Miyaki *et al.* observed less proliferating chondrocytes in mice at P10 in the absence of miR-140, which in part results in the short stature of miR-140^{-/-} mice (Miyaki, Sato et al. 2010). Here we performed BrdU labelling analysis and TUNEL assays to determine the role of miR-140 and miR-455 in proliferation and apoptosis of chondrocytes, respectively. The percentage of proliferating chondrocytes (BrdU-positive chondrocytes against DAPI-positive chondrocytes in the proliferative zone) in the proliferative zone was lower in miR-140^{-/-} and miR-455^{-/-} mice at P22 than age-matched WT mice, but even lower in the DKO mice. One of the potential mechanisms by which miR-140 regulates chondrocyte proliferation is proposed to be via direct targeting of the transcription factor Sp1, which can inhibit the cell cycle via the activation of inhibitors p15^{INK4b} (*CDKN2B*) and p21^{Waf1/Clip} (*CDKN1A*) (Yang, Qin et al. 2011). As previously mentioned, HDAC4 is a direct target of miR-140, which acts as a repressor of Runx2 and MEF2C, factors essential for chondrocyte hypertrophy and bone development (Vega, Matsuda et al. 2004, Tuddenham, Wheeler et al. 2006). Runx2 is a potent inducer of *Ihh* expression (Yoshida, Yamamoto et al. 2004), in part via with HDAC4 and R-Smads. The R-Smad, *Smad3* (also a direct target of miR-140), is a well described regulator of chondrocyte proliferation, in part through this regulation of *Ihh* expression (Pais, Nicolas et al. 2010, Wang, Song et al. 2016). Thus, taken together, miR-140 plays a critical role in regulation of chondrocyte proliferation potentially through deregulation of target genes such as *Sp1*, *Hdac4*, and *Smad3*, although as discussed in Chapter 4 other many targets involved remain to be identified and validated.

The reduction in the number of BrdU-labelled chondrocytes in the tibial growth plate of miR-455^{-/-} mice at P22 could similarly involve Runx2 and HDACs, since *Runx2* and *Hdac2/8* have been identified as miR-455-3p direct targets (Zhang, Hou et al. 2015, Chen, Chen et al. 2016). Runx2^{-/-} mice are dwarf due to lack of hypertrophic chondrocytes, Runx2^{-/-} mice but with *Runx2* expression maintained in non-hypertrophic chondrocytes, partially rescued the dwarf phenotype with the ability to induce chondrocyte hypertrophy and subsequently to

express *Ihh*, however, *Runx2* overexpressing mice are also short in stature, but due to precocious chondrocyte maturation due to accelerated hypertrophic chondrocyte differentiation (Takeda, Bonnamy et al. 2001, Ueta, Iwamoto et al. 2001, Chen, Ghori-Javed et al. 2014). Therefore, a plausible explanation for the reduced number of proliferating chondrocytes in tibia growth plate of miR-455^{-/-} mice is that this increases *Runx2* expression which in turn accelerates the differentiation of proliferating chondrocytes into hypertrophic chondrocytes, this could explain why the height of hypertrophic zone of *Mir455*-null mice is larger than other genotypes at P22 (Fig. 3.12). Recently, Ito *et al.* verified *Hif2α* (encoded by *Epas1*) as a target gene of miR-455 (Ito, Matsuzaki et al. 2021). Deletion of *Hif2α* in mouse limb bud mesenchyme causes a modest delay in endochondral bone development, so it is possible that accumulated *Hif2α* in growth plate accelerates endochondral bone development (Araldi, Khatri et al. 2011, Ito, Matsuzaki et al. 2021). However, in our RNA-seq datasets (Chapter4 & 5) we never observed regulation of *Epas1* in the *Mir455*-null chondrocytes. One possible reason should be that Ito *et al.* used a cell-based (HEK293T cell) reporter system to screen the potential miR-455 target genes and then to verify mRNA expression of these targets in mouse primary chondrocyte with transfection of a miR-455 mimic (Ito, Matsuzaki et al. 2021). In contrast, we used murine costal chondrocyte and murine knee cartilage chondrocyte RNA-seq to screen all genes, including miR-455 target genes. Further, Woods *et al.* work showed that miRNA target genes vary between species (Woods, Barter et al. 2019), thus we suggest that *Epas1* is probably not a mouse miR-455 direct target gene (Ito, Matsuzaki et al. 2021). We saw significantly fewer proliferating chondrocytes in DKO mice than others, indicating a synergistic effect of miR-140 and miR-455 on regulation of proliferating chondrocytes.

The mechanisms of chondrocyte death in the growth plate of miR-140^{-/-} mice remains poorly understood. However, it is reported that miR-140-5p inhibits apoptosis of IL-1-induced human chondrocytes through regulating its direct target *HMGB1* (Wang, Shen et al. 2020). In addition, overexpression of miR-140-3p attenuated proliferation and induces apoptosis in colorectal cancer (CRC) cells via direct targeting of *PD-L1* (Jiang, Li et al. 2019). Moreover, overexpression of miR-140-5p in chronic myeloid leukemia (CML) significantly inhibited cell proliferation and promoted cell apoptosis by targeting *SIX1* (Nie, Liu et al. 2019). Altogether these data indicate altered expression level of miR-140 is involved in the

regulation of cell apoptosis. Recent work showed that miR-455-3p could directly target PTEN and reduce apoptosis of chondrocyte through regulating the PI3K/AKT pathway, which has multiple regulation roles in cellular proliferation, apoptosis, and other physiological processes (Janku, Yap et al. 2018, Lee, Chen et al. 2019, Tian, Tang et al. 2019, Xiong, Cao et al. 2019, Yan, Jiang et al. 2019, Yin, Jiang et al. 2019). Interestingly, the number of TUNEL positive cells in the DKO mice was less than in either miR-140^{-/-} and miR-455^{-/-} mice, indicating that miR-140 and miR-455 play an antagonistic effect on the regulation of chondrocyte death in the growth plate.

3. 3. 5. Summary

Previous studies already revealed that miR-140 plays a critical role in skeletal development (Miyaki, Sato et al. 2010, Nakamura, Inloes et al. 2011, Papaioannou, Inloes et al. 2013), however, the role of miR-455 in biological development remains elusive. Here, we have demonstrated that miR-455 is also involved in murine skeletal development, with a similar skeletal growth pattern as that of *Mir140*-null mice (except in skull development). However, there is still very limited information about the molecular mechanisms regulated by miR-140 and miR-455 during endochondral ossification. Even though a significant amount of research has identified developmentally relevant targets of miR-140 in skeletal development, the promiscuous nature of microRNA targetting leads us to the hypothesis that further potentially relevant targets remain to be identified. During this work there were no validated targets of miR-455 in growth plate chondrocytes. Together, the identification of further miR-140 and miR-455 targets will improve our understanding of chondrocyte development.

Chapter 4. *Identification of the growth plate target genes of Mir140 and Mir455*

4. 1. Introduction

Via sequence complementarity microRNAs (miRNAs) bind to the 3' untranslated region (3'UTR) of target messenger RNAs (mRNAs) to repress gene expression (Bartel 2004, Kobayashi, Lu et al. 2008). MiRNAs have been verified to play important roles in various tissues, and many of these miRNAs are evolutionarily conserved. It is reported that mammalian miRNAs could regulate more than one third of all mRNAs, controlling and fine regulating biological homeostasis (Lewis, Burge et al. 2005, Miyaki, Sato et al. 2010). miR-140 is highly conserved among vertebrates, and is highly expressed in the chondrocytes of zebrafish and mice during embryonic development and in human chondrocytes (Nakamura, He et al. 2008, Miyaki, Nakasa et al. 2009, Zhang, Ma et al. 2013). In addition, miR-455-3p is also highly conserved and its expression was observed in the developing limbs of mice and chicks and in human OA cartilage (Swingler, Wheeler et al. 2012, Zhang, Hou et al. 2015, Chen, Chen et al. 2016, Sun, Zhao et al. 2018, Hu, Zhao et al. 2019, Mao, Kang et al. 2019).

As described in Chapter 3, miR-140^{-/-} mice are short in stature and have a domed skull, suggesting that miR-140 is essential for endochondral bone development. To date, although several miR-140 targets have been identified in human OA cartilage and mouse cells *in vitro* (Tuddenham, Wheeler et al. 2006, Miyaki, Sato et al. 2010, Pais, Nicolas et al. 2010, Nakamura, Inloes et al. 2011, Yang, Qin et al. 2011), the functions of this miRNA in skeletal development and OA pathogenesis is still largely obscure. The role of miR-455 in skeletal development remains elusive and convincing mRNA targets of miR-455 await discovery. Thus, identifying the target genes of miR-140 and miR-455 in the mouse growth plate will aid in understanding the role of *Mir140* and *Mir455* during skeletal growth.

Conventional global gene expression assays such as microarray have several technical disadvantages such as high background levels resulting from probe cross-hybridisation and limited dynamic range of detection owing to background and saturation signals (Zhao, Fung-Leung et al. 2014). RNA-sequencing (RNA-seq) is a high throughput sequencing method (also known as next-generation sequencing) to profile transcripts in a population of cells, which

has rapidly developed in recent years. Compared to hybridisation-based approaches, RNA-seq provides several advantages including greater dynamic range of detection, higher sensitivity for gene expression either at low or very high levels and is less biased, since the technique does not rely on transcript-specific probes (Zhao, Fung-Leung et al. 2014). Thus, in this Chapter we performed RNA-seq to compare and define differences in gene expression during chondrogenesis between WT mice, miR-140^{-/-} mice, and miR-455^{-/-} mice with the aim of identifying novel potential targets of these miRNAs. Costal chondrocytes were isolated from mice at 7 days of age, to represent a model of growth plate chondrogenesis. RNA-seq were performed at n=4 for WT mice and miR-140^{-/-} mice and n=3 for miR-455^{-/-} mice. DKO mice were not sequenced to avoid difficulties in dissecting apart *Mir140* and *Mir455* downstream affects and targets.

We also developed methodology to assess the impact of miR-140 loss in the growth plate cartilage and articular cartilage using laser-microdissection of growth plate zones coupled with RNA-seq. However, due to the Covid-19 pandemic we were unable to complete the comparison of wild-type vs. *Mir140*-null mice.

Chapter Aims:

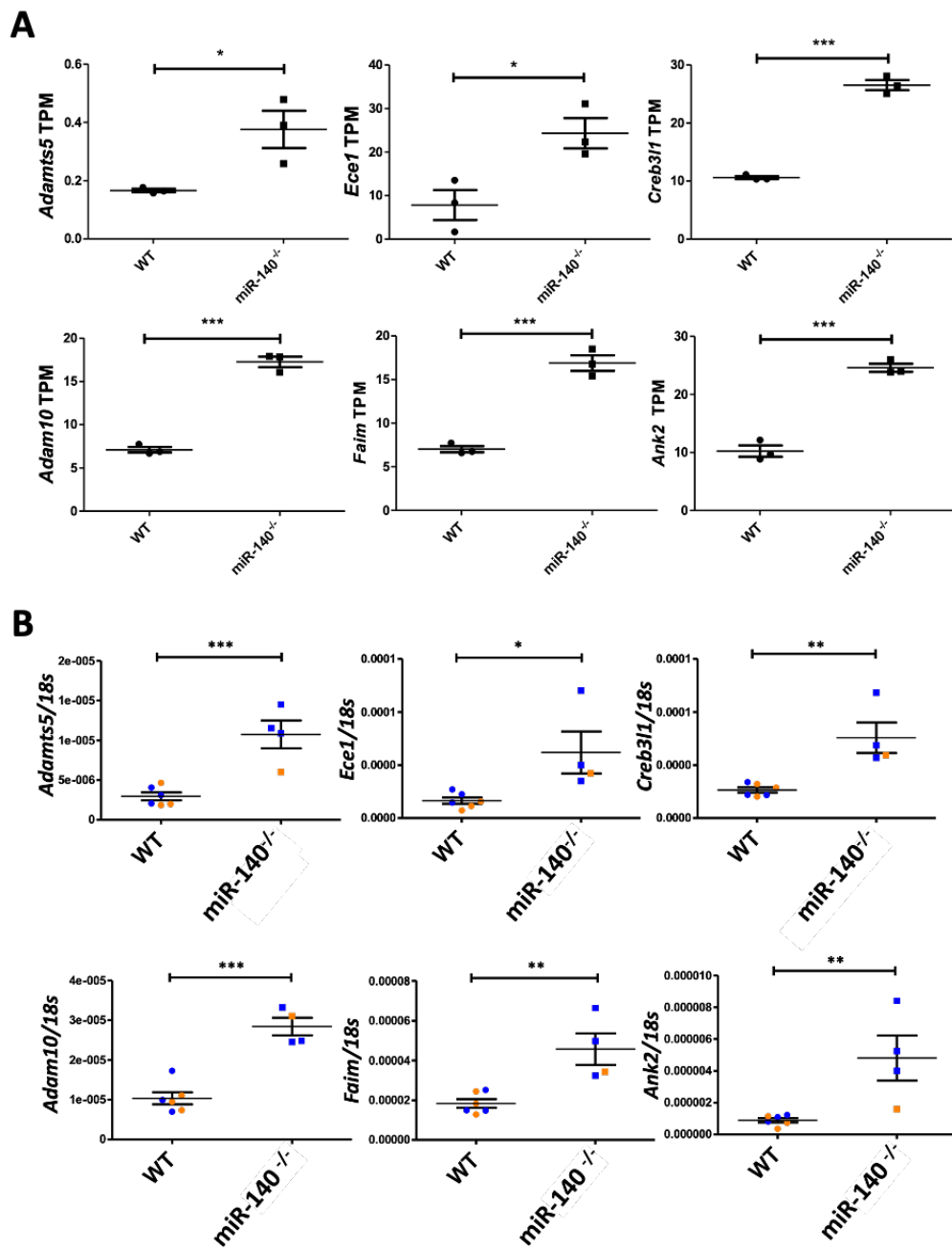
- Isolate RNA from mice costal chondrocytes at 7 days of age and performed RNA-seq analysis.
- Identify potential miR-target mRNAs from the differentially expressed genes in WT vs. miR-140^{-/-} or miR-455^{-/-} mice RNA-seq data.
- Confirm selected novel growth plate target genes of miR-140 and miR-455 via using luciferase reporter assay.
- Elucidate the role of specific target genes of miR-140 in growth plate chondrocytes.
- Profile gene expression in growth plate chondrocytes following laser-microdissection.

4. 2. Results

4. 2. 1. Validation of genes that highly upregulated in published *Mir140*-null dataset

Initially, in part to check the quality of our RNA isolated from costal chondrocyte, real-time qRT-PCR analysis was performed to validate the mRNA expression of five genes significantly upregulated in *Mir140*-null costal chondrocytes (screened from RNA-seq data (GSE98036) and chosen because of high TPM expression values (fig 4.1 A)). In addition, we also examined the expression of the published growth plate miR-140 target, *Adamts5*, which was increased in the GSE98036 dataset. Together, the six genes were all significantly upregulated as determined by qRT-PCR in our murine P7 costal chondrocytes in the absence of *Mir140* (Fig. 4.1B). Taken together, the RT-PCR results revealed that RNA isolated from costal chondrocyte of our *Mir140*-null and WT mice were comparable with published data and adequate for further research, such as RNA-seq.

Figure 4.1 Validation of the mRNA expression of genes filtered from GSE98306



Analysis of RNA-seq data (GSE98036) identified a subset of genes with robust TPM expression and showing differential expression in miR-140^{-/-} mice at 7 days of age compared to the age-matched control mice. Besides high TPM expression (A) this subset includes a previously validated growth plate miR-140 target gene, *Adamts5*. These genes were analysed for differential expression in RNA from our equivalent mice (and control) to validate our RNA prior to RNA-seq analysis (B). Different colours (blue and orange) represent mice from separate litters of animals, with one data point per mouse. Real-time qRT-PCR gene expression was normalised to 18s. Data was plotted as mean \pm standard deviation (SD). (WT mice=6, miR-140^{-/-} mice=4) * $P \leq 0.05$, ** $P \leq 0.01$, *** $P \leq 0.001$.

4.2.2. Quality control (QC) check for RNA isolated from primary costal chondrocytes and RNA-seq analysis

RNA-seq was performed to obtain a quantitative and unbiased identification of differentially expressed genes (DEGs) in primary costal chondrocytes resulting from the ablation of *Mir140* or *Mir455*. Costal chondrocytes from 7-day-old mice were used as an *ex vivo* cell model of chondrogenesis to identify miRNA target genes within the developing growth plate (Peltomaki and Hakkinen 1992, Gebhard, Hattori et al. 2008, Tryfonidou, Hazewinkel et al. 2010, Kim, Feng et al. 2014). RNA was isolated from primary costal chondrocytes at P7 using the mirVana microRNA isolation kit (described in Chapter 2, section 2.2.3.2). All RNA was DNase treated and passed QC. Sequencing was performed by the Genomic Core Facility (Newcastle University) and analysis by Dr Kathleen Cheung (Bioinformatics Support Unit, Newcastle University). All sequencing was single-read 75bp mRNA-seq and all samples generated >16 million reads with >1% of read overrepresented and the expected level of duplication.

4.2.3. RNA-seq data analysis of miR-140^{-/-} mice P7 costal chondrocytes

Principal component analysis (PCA) is a widely used method to extract important information from a multivariate data. In terms of gene expression data, samples with similar expression profiles cluster together. From a PCA plot (Fig. 4.2A), the WT (orange) and *Mir140*-null (green) samples segregated by principle component one (PC1). The WT samples all clustered closely together, however, one of *Mir140*-null sample (green, bottom) was separated from the cluster of the other three null samples, segregating based on PC2. This separation may possibly be explained by the sex of this mouse, which is female whilst the remaining *Mir140*-null samples are male (Fig. 4.2A).

Gene expression analysis was performed using Salmon and DESeq2 by Kathleen Cheung. Known marker genes of a chondrocyte were appropriately expressed including *Col2a1*, *Col10a1* and *Acan*. DEG analysis identified 1894 up- and 1179 down-regulated genes with a fold change > 1.5 and FDR threshold ≤ 0.05 in the comparison of *Mir140*-null mice vs. WT mice (red dots in the volcano plot in Fig. 4.2B). Theoretically, as miRNAs generally suppress

their target genes, *Mir140* targets should be enriched within significantly upregulated genes.

As mentioned in Chapter 1, the pre-miRNA hairpin is cleaved by Dicer enzyme to generate pri-miRNA-5p and pri-miRNA-3p (the 5p is in the first (5') position, the 3p strand in the second of the stem loop). The selection of mature miRNA formation is believed to be influenced by hydrogen-bonding selection, which means that one arm produces abundant miRNA, whilst the other arm produces an inactive miRNA (Griffiths-Jones, Grocock et al. 2006). However, accumulating evidence suggests that either the miRNA-5p or miRNA-3p strand could be functional at specific development stages (Griffiths-Jones, Grocock et al. 2006, Marco, Hui et al. 2010, Cloonan, Wani et al. 2011, Wen, Li et al. 2020, Woods, Charlton et al. 2020, Ito, Matsuzaki et al. 2021). Evolutionary analysis also indicates that both miRNA-5p and miRNA-3p are conserved, although the two strands are not always equally well conserved (Guo and Lu 2010). The best way to determine which strand is ‘functional’ is to use global expression data following miRNA knock-out or overexpression and examine predicted target expression for both microRNA arms.

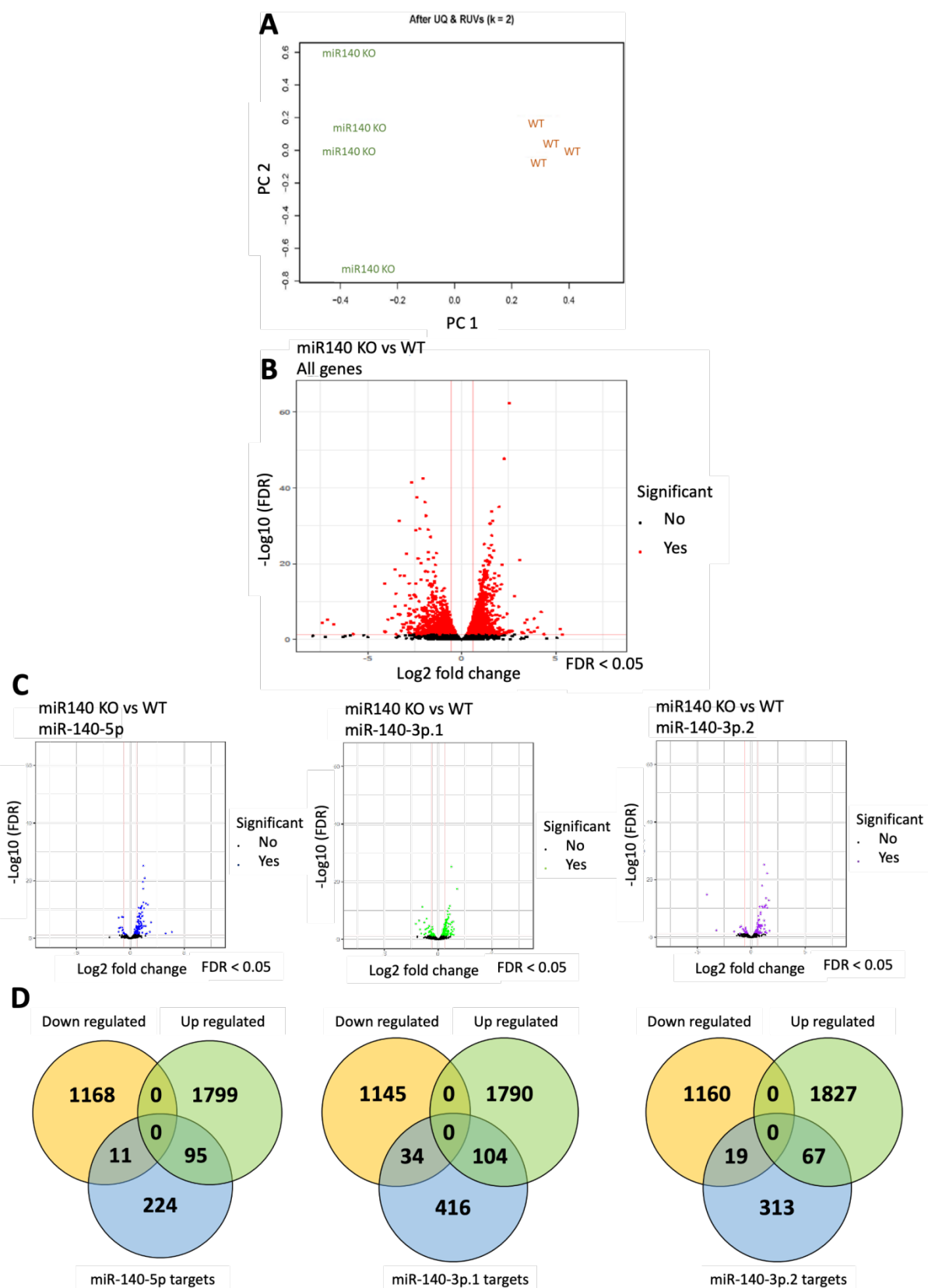
Previous experimental evidence indicated that miR-140-5p (CAGTGGTTTACCTATGGTAG, seed: AGTGGTT) is the dominant strand of miR-140, although data also shows that miR-140-3p is more abundant in cartilage (Crowe, Swingler et al. 2016). miRbase (<http://www.mirbase.org/>; Kozomara et al., Nucliec Acids Res, 2019) analysis of 107 datasets (from various tissues) also concludes that miR-140-3p is the significantly more abundant arm of miR-140. When comparing target prediction data (TargetScan 7.2; conserved) to the P7 costal chondrocytes RNA-seq results, 106 predicated miR-140-5p target genes (of 330) are significantly DEGs, with the vast majority (95/106, 89.6%) upregulated (Fig. 4.2C-left; 4.2D-left Venn diagram). This represents a highly significant (Fisher’s exact test, $p < 1 \times 10^{-5}$) enrichment of predicted target genes in the upregulated gene list.

In terms of the miR-140-3p, this arm is reported to be processed to two main isoforms, termed isomiRs, which possess differing seed sequences and therefore predicted target repertoires. These are miR-140-3p.1 (ACCACAGGGTAGAACCAACGGAC, seed: CCACAGG) and miR-140-3p.2 (TACCACAGGGTAGAACCAACGGA, seed: ACCACAG), respectively (Woods, Charlton et al. 2020). From our data, of the 554 miR-140-3p.1 predicted target genes

(TargetScan 7.2), 138 were differentially expressed in the miR-140^{-/-} mice (Fig. 4.2C-middle), with 104 (75.4%) significantly upregulated (Fig. 4.2D- Central Venn diagram). For the 399 miR-140-3p.2 predicted target genes analysis, 86 were significantly differentially expressed (Fig. 4.2C-right) and of these, 67 (77.9%) were upregulated in the P7 costal chondrocytes RNA-seq data (Fig. 4.2D-right Venn diagram). For both miR-140-3p.1 and miR-140-3p.2 isomiRs, predicted targets were significantly enriched in the upregulated gene list, $p < 0.0006$ and $p < 0.0015$, respectively (Fisher's exact test).

Together, the aims of this section are to identify additional *Mir140* growth plate target genes and to explore their potential function. Based on RNA-seq data, the percentage of predicted targets (by TargetScan) for either miR-140-5p, miR-140-3p.1 or miR-140-3p.2 over all genes with the same trend from our RNA-seq were calculated (Fig. 4.3A), which showed that predicted miR-140-5p targets account for the largest proportion in all upregulated genes compared to either miR-140-3p.1 or miR-140-3p.2, indeed indicating miR-140-5p as the dominant strand of miR-140 in growth plate chondrocytes, but that the miR-140-3p isomiRs are also functional (Woods, Charlton et al. 2020). Furthermore, the mean log2 fold-change of predicted targets of miR-140 compared to all genes consistently showed that the miR-140-5p predict targets are more highly upregulated compared to miR-140-3p.1 and miR-140-3p.2 predict targets (Fig. 4.3B).

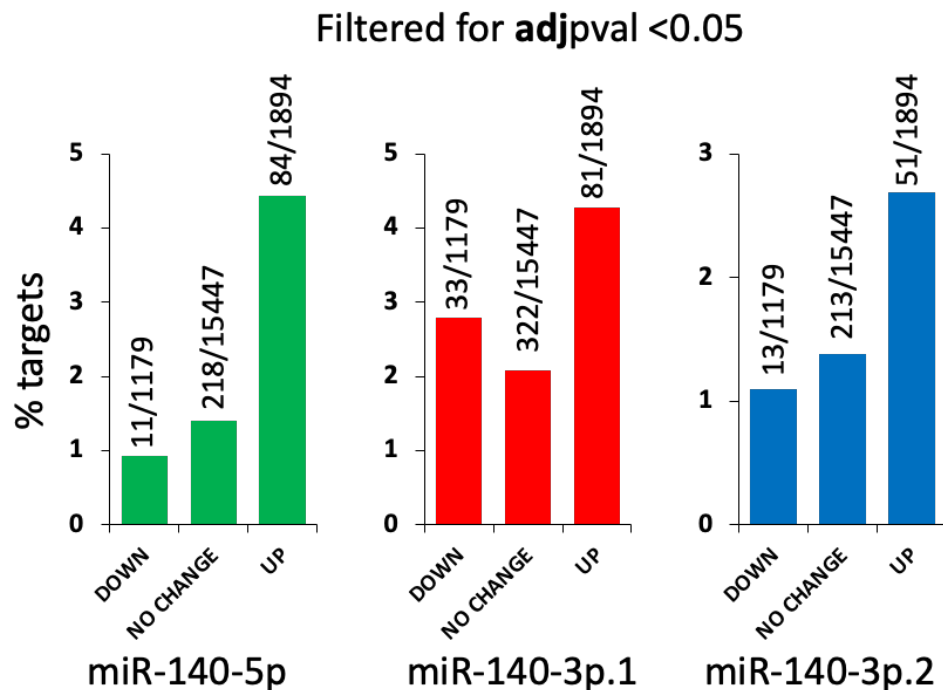
Figure 4.2 An abundance of genes is differentially expressed in *Mir140*-null mice relative to control mice



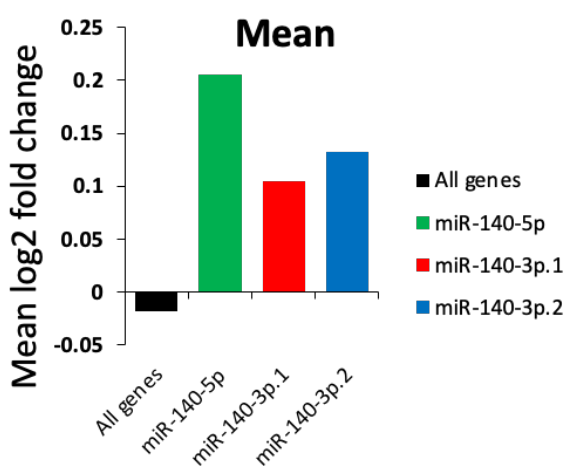
(A) PCA demonstrates that samples cluster by genotype. A PCA plot was generated from normalised RNA-seq data of the wild-type (WT, orange) and miR-140^{-/-} (miR140 KO, green) samples. (B) A Volcano plot of gene fold-change (Log_2 , X axis) against $-\text{Log}_{10}$ FDR (false discovery rate, Y axis) between miR-140^{-/-} and WT mice showed the distribution of the detected genes, demonstrating the distribution of upregulated genes and downregulated genes. The vertical red lines correspond to 0.585 log_2 fold up and down (equivalent to 1.5-fold change), respectively. The red horizontal line denotes an FDR 0.05. Red points represent all significantly differentially expressed genes with an FDR p value ≤ 0.05 and fold change ≥ 1.5 . In total, 1179 genes were found to be significantly downregulated and 1894 genes to be significantly upregulated in miR-140^{-/-} mice. (C) Volcano plots demonstrating the significantly up-regulated and down-regulated genes of miR-140 in miR-140^{-/-} P7 costal chondrocytes that are overlap with predicted miR-140-5p (blue dots, left), miR-140-3p.1 (green dots, centre), and miR-140-3p.2 (purple dots, right) target genes, respectively. The PCA and volcano plots in A-C were generated by Dr Kathleen Cheung in R studio. (D) Venn plot demonstrating the overlap of TargetScan 7.2 conserved predicted targets of miR-140-5p (left), miR-140-3p.1 (centre), and miR-140-3p.2 (right) with the differentially expressed genes in the RNA-seq analysis.

Figure 4.3 MiR-140 targets analysis

A



B

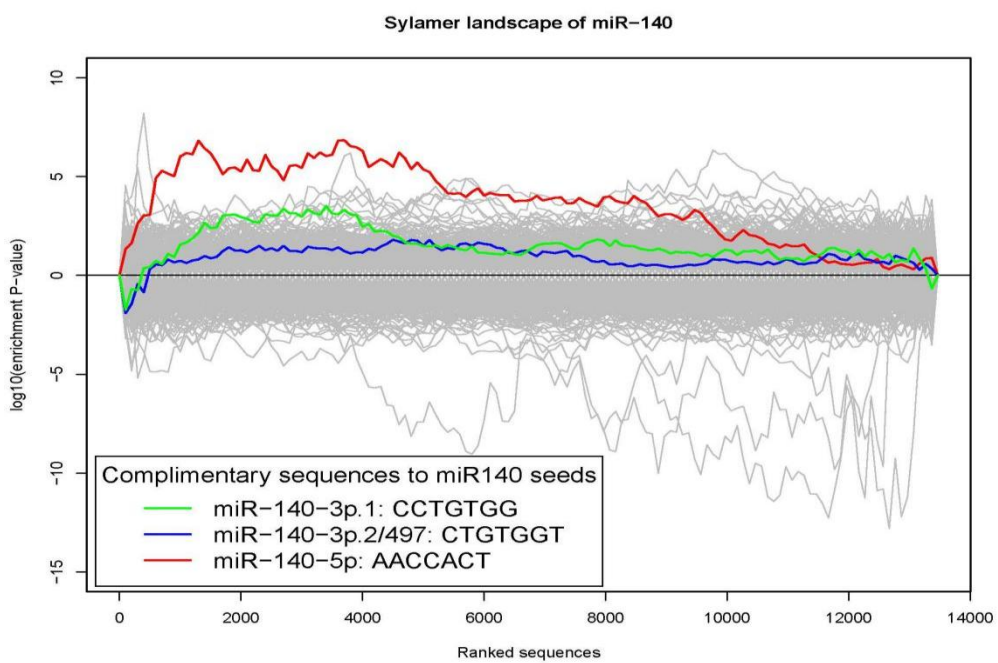


(A) Percentage of the number of TargetScan (v7.2) predicted miR-140-5p (green), -3p.1 (red) and -3p.2 (blue) unique targets from all the genes that were either significantly increased or decreased (fold change > 1.5 and FDR threshold ≤ 0.05) or remained unchanged (no change) in the *Mir140*-null mice compared to age-matched control animals. (B) Mean log2 fold changes of all genes that are predicted targets of only either miR-140-5p (green), -3p.1 (red) or -3p.2 (blue) in the absence of miR-140 in mice.

4.2.4. Confirmation of loss of miR-140-5p effect on genes expression in costal chondrocyte

Next, we used Sylamer (van Dongen, Abreu-Goodger et al. 2008) to determine if our ranked DEG list could identify an enrichment of miR-140 seed sequences in the upregulated genes from our RNA-seq data. Sylamer analysis is an unbiased method that rapidly assesses overrepresentation of nucleotide sequences (words) of a specific length (e.g., 7 for miR seed sequences) in 3'UTRs ranked gene expression lists (van Dongen, Abreu-Goodger et al. 2008). Our Sylamer analysis of RNA-seq data confirmed a significant enrichment in the 3'UTRs of upregulated genes of sequences complementary to the miR-140-5p seed sequences (AACCCT). This was followed by miR-140-3p.1 and then miR-140-3p.2 (Fig. 4.4), again suggesting that loss of miR-140-5p has the most effect on gene expression in the *Mir140*-null rib chondrocyte compared to control chondrocytes, followed by miR-140-3p.1 and then miR-140-3p.2 (Fig. 4.4).

Figure 4.4 Sylamer analysis on miR-140 seed sequence



Sylamer analysis of ranked (fold-change) RNA-seq data revealed the most significant enrichment of miR-140-5p seed sequence (AACCCT - red) among the upregulated genes, followed by miR-140-3p.1 (CCTGTGG – green) and then miR-140-3p.2 seed sequence (CTGTGGT – blue), suggesting that miR-140-5p has the most impact on gene expression. Note: seed sequences given are the reverse complement.

4.2.5. Identification and validation of *Mir140* in the growth plate

4.2.5.1. Identification of *Mir140* growth plate target genes

Previous publications have identified several miR-140 direct target genes in different species (Table 4.1), although relatively few have been validated in growth plate development including *Adamts5* and *Dnpep* (Miyaki, Sato et al. 2010, Nakamura, Inloes et al. 2011). Thus, the identification of additional *Mir140* target genes is required to further understand the role of *Mir140* in skeletal development and potentially osteoarthritis pathogenesis.

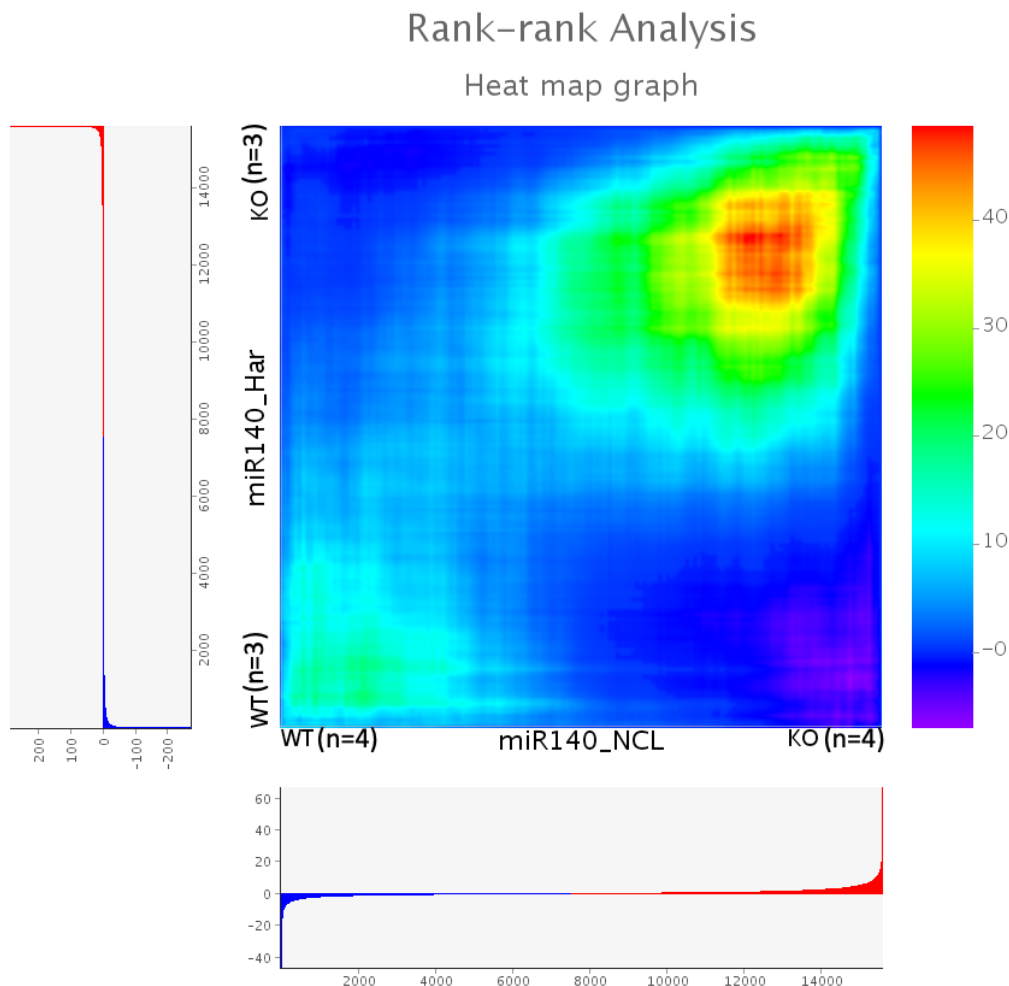
Identifying miRNA targets from RNA-seq data is not straightforward and is confounded by many false-positive genes, including those upregulated because of secondary events. In an attempt to more robustly identify miR-140 targets we were able to obtain early access to a highly comparable RNA-seq dataset from a different miR-140^{-/-} and WT mouse comparison courtesy of Prof T. Kobayashi (Harvard University). As described above, this dataset is now publicly available (NCBI GEO – GSE98036; (Grigelioniene, Suzuki et al. 2019)). As with our data, the RNA was isolated from costal chondrocytes of 7-day old WT and miR-140^{-/-} mice. We predicted that genes upregulated in both datasets would be likely less prone to sampling and experimental error and thus were more likely to be true miR-140 target genes. To directly compare the datasets, we generated ranked DEG lists based on our differential expression *p* value ranking taking into consideration whether the gene was up- or down-regulated. The resulting datasets of ranked lists were thus compared using the Rank-rank Hypergeometric overlap (RRHO) threshold-free algorithm (Plaisier, Taschereau et al. 2010), which reassuringly gave a highly correlative score in the genes upregulated in both miR-140^{-/-} mice (Fig. 4.5).

Table 4.1 Previously validated miR-140 direct targets

Target gene(s)	Species	Reference(s)
<i>Adamts5</i>	Mouse	Miyaki et al., 2010
<i>Dnpep</i>	Mouse	Nakamura et al., 2011
<i>Hdac4</i>	Mouse	Tuddenham et al., 2006
<i>BMP2</i>	Human/Chicken	Nicolas et al., 2011; Hwang et al., 2014
<i>IGFBP-5</i>	Human	Tardif et al., 2008
<i>Sp1</i>	Mouse	Yang et al., 2011
<i>Smad3</i>	Mouse	Pais et al., 2010
<i>Cxcl12</i>	Mouse	Nicolas et al., 2008
<i>Pdgfra</i>	Zebrafish	Eberhart et al., 2008

Genes listed were validated as miR-140 direct targets in different species.

Figure 4.5 Screening *Mir140* target genes

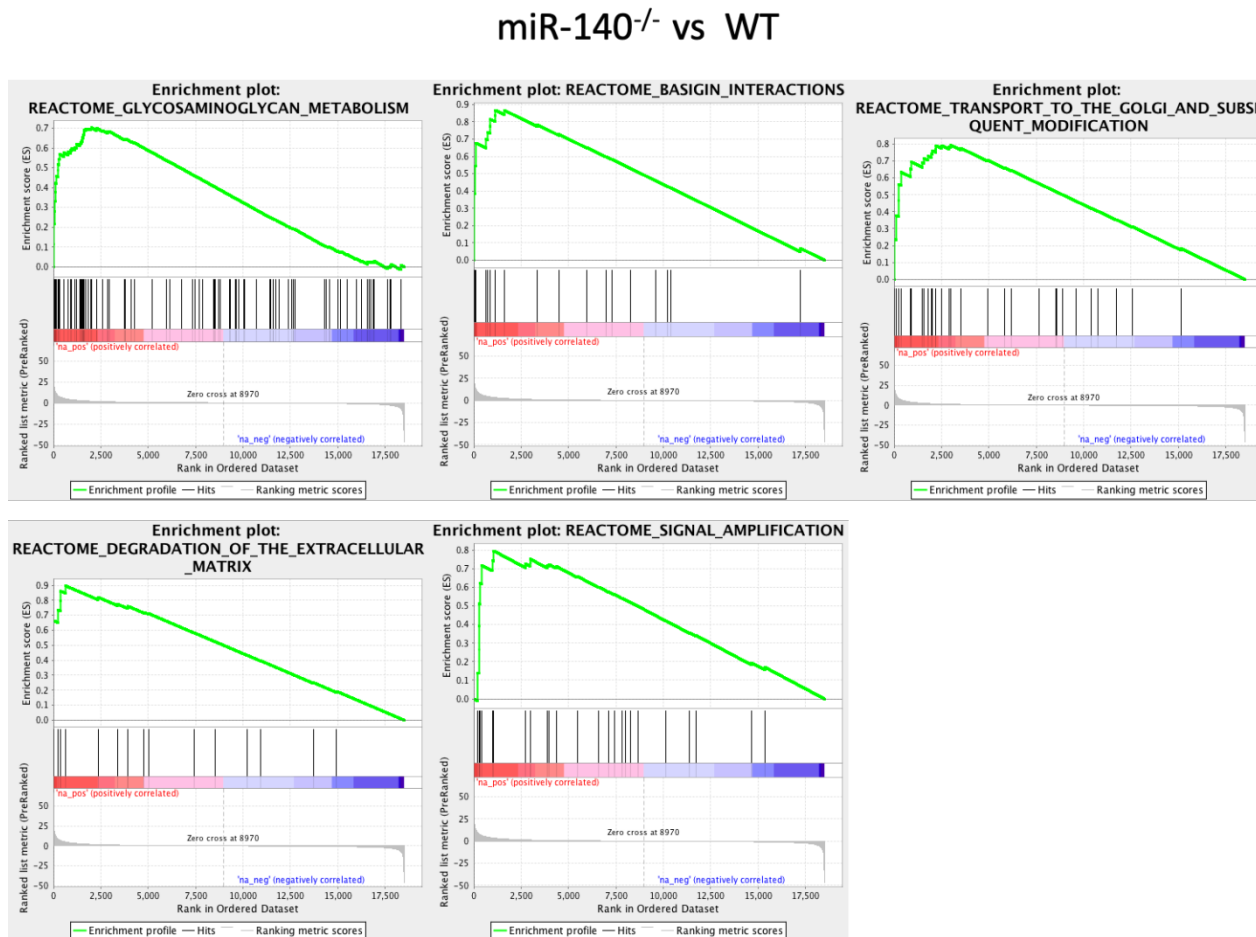


Gene expression profiles from costal chondrocytes of two genetically different miR-140^{-/-} mice lines (Har and NCL: from downregulated genes (blue) to upregulated genes(red)) at 7 days of age and compared to their respective age-matched control mice were used to generate a ranked list (based on *p* value) of genes that are differentially expressed in the absence of *Mir140*. The resulting overlap from the ranked lists, represented as a hypergeometric heat map, identifies an enrichment for upregulated genes in the Newcastle miR-140^{-/-} mice overlap with the Harvard miR-140^{-/-} mice (Harvard n=3/genotype; Newcastle n=4/genotype). Har represents data from Harvard University, NCL is RNA-seq data from the miR-140^{-/-} mouse model generated in Newcastle.

4.2.5.2. Pathway analysis using GSEA

In addition to RRHO analysis, Gene Set Enrichment Analysis (GSEA) (Mootha, Lepage et al. 2003, Subramanian, Tamayo et al. 2005) was used as pathway analysis to compare gene sets between WT and *Mir140*-null mice that are statistically involved in either enriched or depleted functional pathways. False discovery rate values (FDR) below 0.05 were classified as GSEA significant. In total 431 gene pathways were enriched for up-regulated genes in our *Mir140*-null mice when compared to WT mice. Five pathways were significant and are, 'glycosaminoglycan (GAG) metabolism' (due to the presence of genes: *Has2*, *St3gal1*, *Cd44*, *Cspg4*, *Ndst1*, *Hs2st1*, *Chst11*, *Ogn*, *Gpc3*, *Gxylt2*, *Acan* etc); 'basigin interactions' (*Cav1*, *Atp1b1*, *Slc7a11*, *Itga3*, *Atp1b2*, *Slc7a8*, *Itgb1*, *Slc6a1*, *Slc7a6*, *Slc7a7*); 'transport to the Golgi and subsequent modification'; 'degradation of the extracellular matrix' (*Mmp3*, *Timp1*, *Mmp10*, *Mmp13*, *Mmp2*); and 'signal amplification' (*Gna13*, *Gna14*, *Gnb4*, *Pla2g4a*, *Src*, *Gng2*, *Gng5*, *Gnai3*) (Fig. 4.6). The significantly enriched gene pathways are closely correlated with metabolism of extracellular matrix (ECM) proteins. Miyaki *et al.* showed that miR-140^{-/-} mice displayed age-related and accelerated post-traumatic knee OA-like changes characterised as proteoglycan loss of articular cartilage (Miyaki, Sato et al. 2010)). Collectively, these data indicate the miR-140 can function to balance the homeostasis of ECM proteins.

Figure 4.6 GSEA enrichment of miR-140^{-/-} gene sets in mouse costal chondrocytes RNA-seq data



Enrichment analysis on GSEA results (FDR q-value < 0.05) showing affected cellular programs in *Mir140*-null costal chondrocytes. Some of the gene pathways are significantly enriched in the up-regulated genes in miR-140^{-/-} mice when compared to WT mice.

4.2.5.3. Identification and validation of potential novel growth plate targets of miR-140

To prioritise potential novel miR-140 target genes for *in vitro* analysis, thirty significant differentially expressed genes (filtered by an FDR threshold of 0.05, Table 4.2) were identified from the overlapped ranked list of the two RNA-seq datasets. These were then filtered down to ten potential *Mir140* target genes by 1) confirming that their 3'UTR contained predicted miR-140 target sites (Fig. 4.7A, based on TargetScan 7.2) by assessing the role of genes in bone development and osteoarthritis pathogenesis based on publications and online data (Table 4.3). One putative miR-140 target gene is cyclic adenosine monophosphate responsive element binding protein 3-like 1 (*Creb3l1*) which is considered to play a role as a cellular transcription factor to regulate cell proliferation in virus infected cells (Denard, Seemann et al. 2011). This gene is also known as old astrocyte specifically induced substance (OASIS), and acts as an endoplasmic reticulum stress transducer (Guillemyn, Kayserili et al. 2019). In addition, OASIS^{-/-} mice exhibit severe osteopenia including decreased osteoblasts activity and type I collagen expression in the bone matrix (Murakami, Hino et al. 2011). Erythroid-derived 2 p45 related factor 2 (*Nrf2*) is a nuclear factor involved in antioxidant defence regulation. NFR2 regulates chondrocytes hypertrophy differentiation in the growth plate (Chen and Maltagliati 2018), and also negatively regulates chondrogenesis in the ATDC5 murine chondrocyte cell model (Hinoi, Takarada et al. 2007). Rossignol et al., found that Nrf2 act as a protector against rheumatoid arthritis (RA) pathogenesis through decreasing NF- κ B mediated cytokines and chemokines (Le Rossignol, Ketheesan et al. 2018). Zinc finger E-box binding homeobox 1 (*Zeb1*) is a well-known transcription factor involved in the regulation of cell homeostasis through the TGF- β signalling pathway. It is also considered as a negative regulator of *Col2a1* expression in chondrocytes (Murray, Precht et al. 2000). Natriuretic peptide receptor 3 (*Npr3*)^{-/-} mice exhibit elongated bones, increased body length, and decreased weight, the skeletal phenotype somewhat opposing that observed in miR-140^{-/-} mice (Matsukawa, Grzesik et al. 1999). Fibrillin-1, encoded by *FBN1* gene, is a well-known ECM protein, mutations in which are a cause of Marfan syndrome (MFS). Following TGF- β signalling activation, mutation in *FBN1* blocks osteogenesis of embryonic stem cells (Matsukawa, Grzesik et al. 1999). Data shows that Transmembrane Protein 123 (*Tmem123*) could regulate the process of cell death

and cell swelling (Ma, Zhang et al. 2001). Nicastin (*Ncstn*) may regulate cell proliferation and differentiation through Notch and PI3K/AKT signalling pathways and also may be related to craniofacial development (Xiao, He et al. 2016, Wang, Wang et al. 2020). ATP binding cassette subfamily A member 1 (*Abca1*) is involved in cholesterol homeostasis that is important for chondrocyte differentiation and bone formation (Gentili, Tutolo et al. 2005). Mediator Complex Subunit 13 (*Med13*) encodes a component of the Mediator transcriptional coactivator complex. Depletion of *Med13* causes a reduction in the expression cancer acquired superenhancer genes (such as *MYC*), which leads to a decrease in cell proliferation (Kuuluvainen, Domenech-Moreno et al. 2018). Although there is limited information about the function of the *Golt1b* gene, the TPM of *Golt1b* in *Mir140*-null mice (average TPM is 101.50) was very high (> 1.8-fold) compared to control mice (average TPM: 55.01).

Table 4.2 Screening results of predict *Mir140* target genes

Genes	NCL RNA-seq (mean log2 fold change)	Har RNA-seq (mean log2 fold change)	NCL RNA-seq WT (mean TPM)	NCL RNA-seq KO (mean TPM)	Har RNA-seq WT (mean TPM)	Har RNA-seq KO (mean TPM)
<i>Abca1</i>	-0.67481	-1.56102	1.40	2.00	0.97	3.33
<i>Adam10</i>	-0.882	-1.05368	3.91	6.81	7.11	17.27
<i>Aggf1</i>	-0.84651	-0.89364	3.96	6.94	2.70	5.88
<i>Ankib1</i>	-0.79546	-0.54134	3.67	7.66	6.07	10.37
<i>Capn1</i>	-1.02645	-0.82943	1.55	2.65	1.60	3.29
<i>Creb3l1</i>	-1.216	-1.09228	10.41	25.66	10.60	26.53
<i>Eif4g2</i>	-0.41157	-0.16765	565.52	827.28	621.48	815.63
<i>Fbn1</i>	-0.41914	-0.78047	27.60	33.23	17.19	34.64
<i>Fras1</i>	-3.27968	-1.75071	0.13	0.72	0.04	0.40
<i>Golt1b</i>	-0.81274	-0.5955	55.01	101.50	46.85	82.96
<i>Gucd1</i>	-0.65918	-0.52617	8.50	13.43	4.00	7.02
<i>Hspa13</i>	-0.83334	-0.95134	6.47	12.86	10.55	23.88
<i>Ipo7</i>	-0.55081	-0.54881	56.55	97.87	30.76	52.59
<i>Lonrf1</i>	-0.77163	-0.54166	4.45	9.00	4.23	7.28
<i>Mecom</i>	-1.43047	-0.74563	2.93	7.14	4.94	9.79
<i>Med13</i>	-0.77586	-0.34706	24.69	48.86	6.25	9.32
<i>Ncstn</i>	-1.14047	-0.39711	12.79	29.07	17.50	27.01
<i>Ndst1</i>	-0.99971	-0.60172	4.66	9.50	4.19	7.47
<i>Nrf2</i>	-0.61288	-0.44533	32.84	52.62	31.71	50.44
<i>Npr3</i>	-1.11626	-1.28706	0.68	1.28	1.18	3.41
<i>Numbl</i>	-0.63833	-0.49712	15.02	26.31	7.07	11.69
<i>Pdgfra</i>	-0.93569	-0.70245	16.48	34.22	5.11	9.90
<i>Rad21</i>	-0.34481	-0.51035	14.91	19.24	30.14	50.28
<i>Rap1b</i>	-1.20626	-0.43818	99.95	261.51	33.50	56.22
<i>Rhou</i>	-0.62894	-1.50557	4.70	7.42	0.55	1.83
<i>Tjp1</i>	-0.75977	-0.53143	10.86	19.08	12.20	20.78
<i>Tmem123</i>	-0.97248	-0.7051	6.07	11.55	10.51	20.07
<i>Yes1</i>	-0.9272	-0.61638	7.47	16.98	4.89	8.76
<i>Zeb1</i>	-0.67522	-1.40964	152.10	226.30	4.09	6.63
<i>Zim1</i>	0.649967	-0.63313	46.16	26.93	9.88	17.64

Based on our comparison of the two datasets, 30 of predicted *Mir140* growth plate target genes are listed. Finally, we filtered this to 10 potential *Mir140* target genes (red) by assessing if the gene play published roles in bone development or in arthritis (Har represents data from Harvard University, NCL is RNA-seq data from the miR-140^{-/-} mouse model generated in Newcastle). The log2 fold change column is derived from WT/KO.

Table 4.3 Functions of potential miR-140 target genes in cell

Gene	Cellular function(s)
<i>Creb3l1</i>	Transducer in cells. Effects osteoblast activity and type I collagen expression.
<i>Nrf2</i>	Chondrocytes hypertrophy differentiation in the growth plate. Chondrogenesis in an ATDC5 cell model.
<i>Zeb1</i>	Effects Col2a1 expression in chondrocytes Cell homeostasis through the TGF-β signalling pathway.
<i>Npr3</i>	Bone development.
<i>Fbn1</i>	Marfan syndrome. Osteogenesis of embryonic stem cells through TGF-β signalling pathway.
<i>Tmem123</i>	Cell death.
<i>Ncstn</i>	Cell proliferation and differentiation through Notch and PI3K/AKT signalling pathways.
<i>Abca1</i>	Chondrocyte differentiation.
<i>Med13</i>	Cell proliferation.

Cellular function(s) of potential miR-140 target genes described from scientific publications.

Having selected ten genes for further study, we performed qRT-PCR on RNA isolated from new litters of mice to validate that these genes are significantly increased in *Mir140*-null costal chondrocytes (Fig. 4.7B). This confirmed that all ten genes were significantly upregulated in miR-140^{-/-} mice. To determine if ten genes are miR-140-5p direct target genes, we cloned their 3'UTRs into the luciferase reporter vector pmiRGLO. These vectors were transfected in human SW1353 chondrosarcoma cells, in combination with a control (non-targetting miR) or miR-140-5p mimic and relative luciferase activity measured. As hypothesised, all of the 3'UTRs sequences, with the exception of the *Golt1b* 3'UTR sequence (Sanger sequencing verified the wrong *Golt1b* 3'UTR sequence in the construct), had a

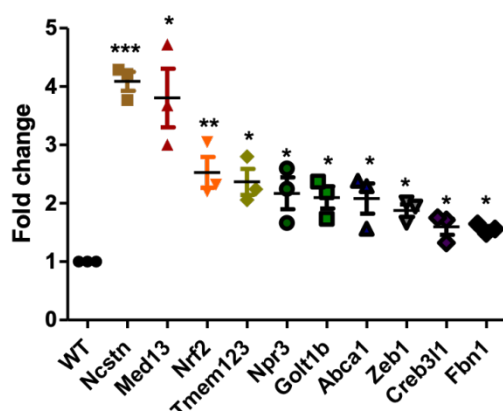
significant reduction in luciferase activity in the presence of miR-140-5p mimic (Fig. 4.7C). This indicates that miR-140-5p directly regulates the expression of the candidate genes via their 3'UTR sequences. To further confirm that these candidate genes are direct miR-140-5p targets, we selected the *Creb3l1*, *Nrf2*, and *Zeb1* luciferase constructs and performed mutagenesis to ablate the seed sequence for miR-140-5p. *Nrf2* and *Zeb1* each possess one putative miR-140-5p binding site within their 3'UTR, while *Cre3bl1* has two miR-140-5p binding sites, both of which were mutated separately and in combination (Fig. 4.7D). None of the *Creb3l1*, *Nrf2* and *Zeb1* 3'UTR target constructs with mutant seed sequences were subsequently significantly repressed by the miR-140-5p mimic, and mutation of both binding sites within *Ceb3l1* 3'UTR reduced the repressive effect of miR-140-5p mimic more than mutation of either site alone. Together these data illustrate that these genes are likely to be direct targets of the microRNA as mutation of the recognition sequence inhibits the miR-140-5p-mediated repression (Fig. 4.7E). *Npr3* and *Med13* are predicted to be miR-140-3p.1 and miR-140-3p.2 target genes respectively (Fig. 4.8A), thus we similarly assessed their 3'UTRs using the pmirGLO reporter vector but transfection of neither miR-140-3p.1 nor miR-140-3p.2 mimic significantly altered luciferase activity (Fig. 4.8B), suggesting these genes may not be direct targets of either miR-140-3p.1 or miR-140-3p.2 as initially predicted.

Figure 4.7 Confirmation of *Mir140* target genes filtered from RNA-seq analysis

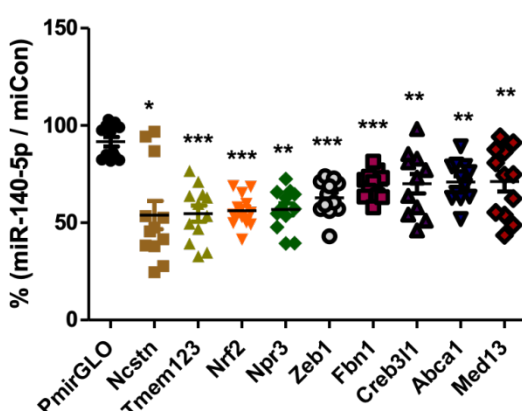
A

mmu-miR-140-5p	CAGUGGUUUUACCUAUGGUAG	CAGUGGUUUUACCUAUGGUAG
<i>Creb3l1</i> 3'UTR	CTCACCAAAATAGCCTCCCTG.....	GT TCACCA CCGAACCAAGTGATA...
<i>Nrf2</i> 3'UTR	AT TCACCA GACCAATCAAAGTTA...	
<i>Zeb1</i> 3'UTR	GT TCACCA AAAAACTCAAACAAAC...	
<i>Abca1</i> 3'UTR	TT TCACCA AGGGTAATGTATTGT...	
<i>Fbn1</i> 3'UTR	TT TCACCA ACCAACTTGATCCTAG...	
<i>Med13</i> 3'UTR	AT TCACCA AAATTCTTTCAAATC...	
<i>Tmem123</i> 3'UTR	TT TCACCA AAATATAGAGGTTTCAC...	
<i>Ncstn</i> 3'UTR	AT TCACCA AAACAAGGGTCGGCCTG...	
<i>Npr3</i> 3'UTR	AT TCACCA ATTACGCTATAAACTT...	
<i>Golt1b</i> 3'UTR	AT TCACCA TTCTATTTATCACGA...	

B



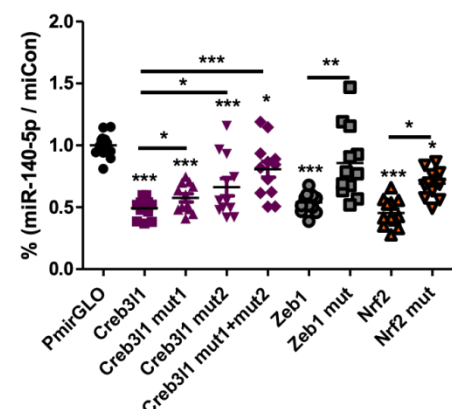
C



D

mmu-miR-140-5p	CAGUGGUUUUACCUAUGGUAG	CAGUGGUUUUACCUAUGGUAG
<i>Creb3l1</i> 3'UTR mutant	GT TCACCA AAATAGCCTCCCTG.....	GT TCACCA CCGAACCAAGTGATA...
<i>Nrf2</i> 3'UTR mutant	AT TCACCA GACCAATCAAAGTTA...	
<i>Zeb1</i> 3'UTR mutant	GT TCACCA AAACTCAAACAAAC...	

E



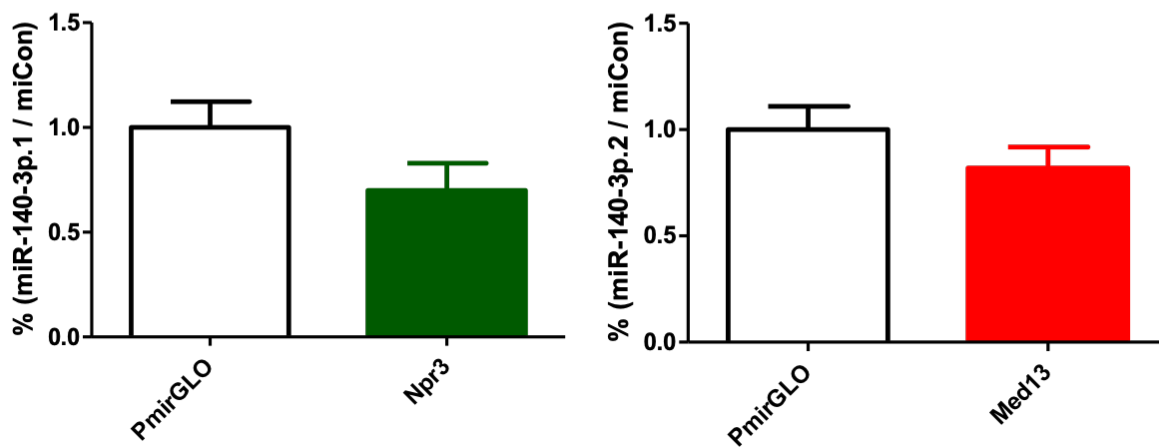
(A) Schematic illustrating the sequences of miR-140-5p and their potential binding sites (8mer, 7mer-8m binding sites and 7mer-A1 binding sites) within targets predicted by TargetScan. The seed sequence of miR-140-5p is shown in red. (B) Real time qRT-PCR validation of predicted *Mir140* target genes identified by RNA-seq analysis. All genes selected were significantly upregulated in our miR-140^{-/-} mice. Differences within each genotype were normalised to 18s and plotted as mean ± SEM, an unpaired Student's t-test was used for analysis, (n=3) * $p\leq 0.05$, ** $p\leq 0.01$, *** $p\leq 0.001$. (C) The relative luciferase to *renilla* activity was determined in SW1353 chondrosarcoma cells following co-transfection of miR-140-5p target genes' 3'UTR constructs with either control mimic or miR-140-5p mimic for 24 hours. Data is the percentage luciferase activity when co-transfected with miR-140-5p mimic relative to the control non-targeting mimic. Data is the mean ± SEM of two experiments, with six wells transfected per construct. An unpaired Student's t-test was used for analysis, * $p\leq 0.05$, ** $p\leq 0.01$, *** $p\leq 0.001$. (D) Schematic illustrating the sequences of miR-140-5p and their potential binding sites (8mer, 7mer-8m binding sites and 7mer-A1 binding sites) within targets predicted by TargetScan. The seed sequence of miR-140-5p is shown in red. Mutant miR-140-5p binding sites within target genes for luciferase assay are shown in blue. (E) Relative luciferase activity was determined in SW1353 cells following co-transfection of miR-140-5p target genes' 3'UTR constructs, containing non-mutant or mutant miR-140-5p binding sites, with either non-targeting mimic or miR-140-5p mimic for 24 hours.

Figure 4.8 Validation of miR-140-3p growth plate target genes

A

mmu-miR-140-3p.1	A CCACAGG GUAGAACCA CGGAC
<i>Npr3</i> 3'UTR	T AGGTGTC AGTACTCAGGAGTG...
mmu-miR-140-3p.2	U ACCA CAG GGUAGAACCA CGG
<i>Med13</i> 3'UTR	G TGGTGTC AAACTAACGTGTGT...

B



(A) Schematic illustrating the sequences of both miR-140-3p.1 and miR-140-3p.2 and their potential binding sites (7mer-A1 binding sites and 7mer-8m binding sites respectively) within their targets predicted by TargetScan. The seed sequence of either miR-140-3p.1 or miR-140-3p.2 is shown in red. (B) Relative luciferase activity was determined in SW1353 cells following co-transfection of miR-140-3p target genes' 3'UTR constructs with either non-targeting mimic or miR-140-3p isomiR mimics for 24 hours. For both A and B, data was plotted as mean \pm SEM luciferase assay of mimic co-transfection relative to co-transfection with the control non-targeting mimic, each construct was repeat twice (n=6/repeat experiment), * $p \leq 0.05$, ** $p \leq 0.01$, *** $p \leq 0.001$.

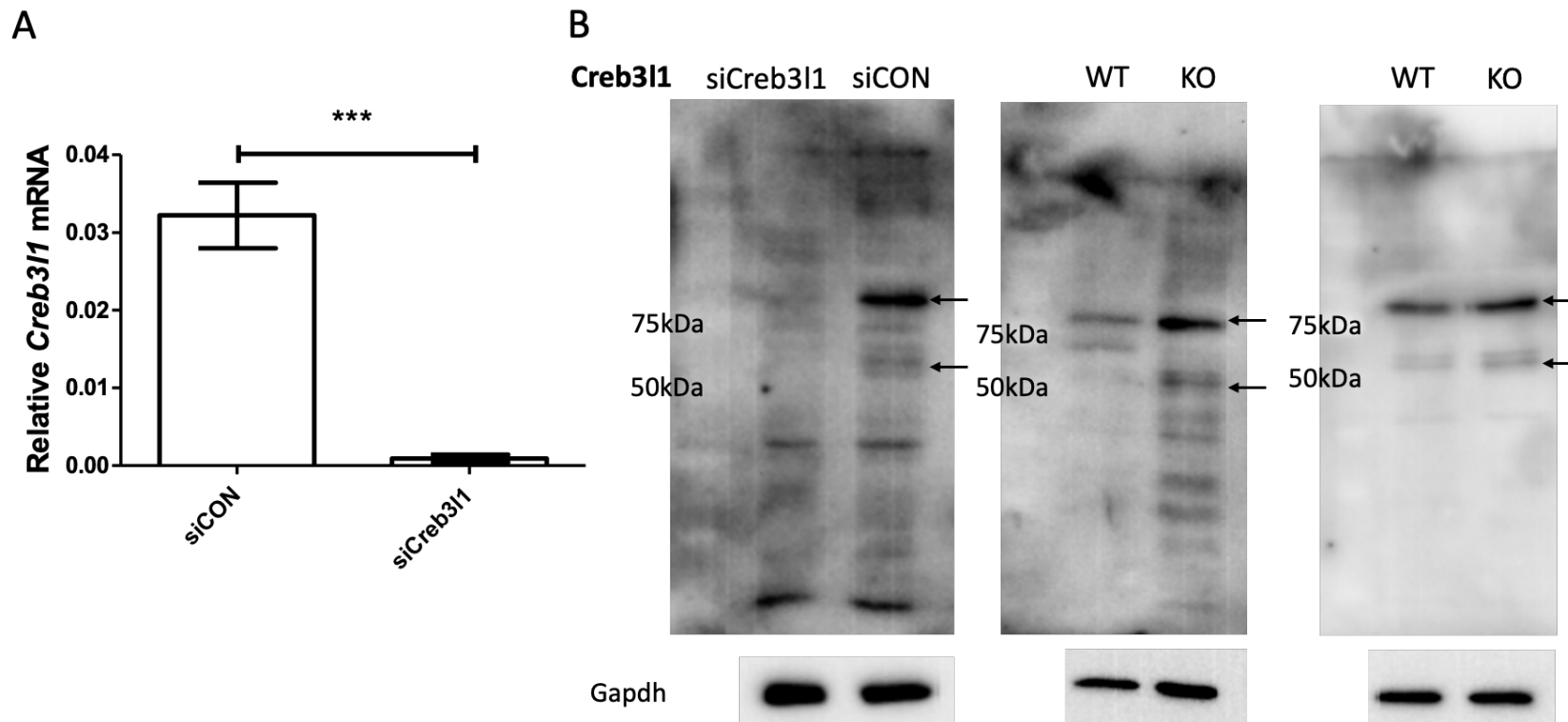
4.2.5.4. Are CREB3L1, NRF2 and ZEB1 increased at protein level in *Mir140*-null chondrocytes?

Having identified several targets of miR-140-5p differentially expressed in the growth plate of costal chondrocytes, we sought to investigate if the expression of those targets increased at the protein level. We focussed on Creb3l1/OASIS, Nrf2 and Zeb1. To initially validate the antibodies against these target proteins in immunoblotting analysis, we performed siRNA mediated knock-down of target genes by transfection of 7-day-old WT mice costal chondrocytes. Real time RT-PCR was used to first confirm mRNA depletion by the siRNA (Fig. 4.9A, 4.10A and 4.12A), with all three siRNAs shown to be highly effective.

For *Creb3l1* mRNA expression was significantly decreased by more than 90% (*p* value < 0.0001) following the transfection of siCrb3l1 (Fig. 4.9A). Immunoblot analysis detected the presence of two bands at the predicted molecular weight of Creb3l1, a 70 kDa (full length protein) and 50 kDa and 55kDa polypeptides corresponding to the size of a known cleaved form of the protein (Murakami, Kondo et al. 2006) (Fig. 4.9B). Both bands were reduced in cells transfected with the siCrb3l1 compared to those transfected with control siRNA (siCON). Furthermore, when comparing Creb3l1 expression in wild-type and *Mir140*-null costal chondrocytes both forms of the protein were increased in the cells lacking miR-140. This was clearer and more reproducible for the full-length form because of low levels of the processed protein, and together this confirms that the antibody detects Creb3l1 (Fig. 4.9B). Similar siRNA knockdown experiments were performed for Nrf2, which decreased *Nrf2* mRNA levels by ~90% (*p* value < 0.0001) (Fig. 4.10A). Immunoblotting confirmed that a protein of the predicted 110 kDa size was reduced upon siRNA treatment, and this protein has increased expression in *Mir140*-null costal chondrocytes (Fig. 4.10B). *Zeb1* siRNA knockdown experiments showed that *Zeb1* mRNA expression level was decreased by ~64% (*p* value < 0.001) in WT costal chondrocytes upon *Zeb1* siRNA treatment (Fig. 4.12A). However, due to an unsatisfactory *Zeb1* antibody we are unable to confirm the actual molecular weight of *Zeb1* protein (predicted molecular weight is ~124kDa) from siRNA knockdown experiment and therefore unable to compare expression differences between WT and *Mir140*-null costal chondrocytes (Fig. 4.12B-D).

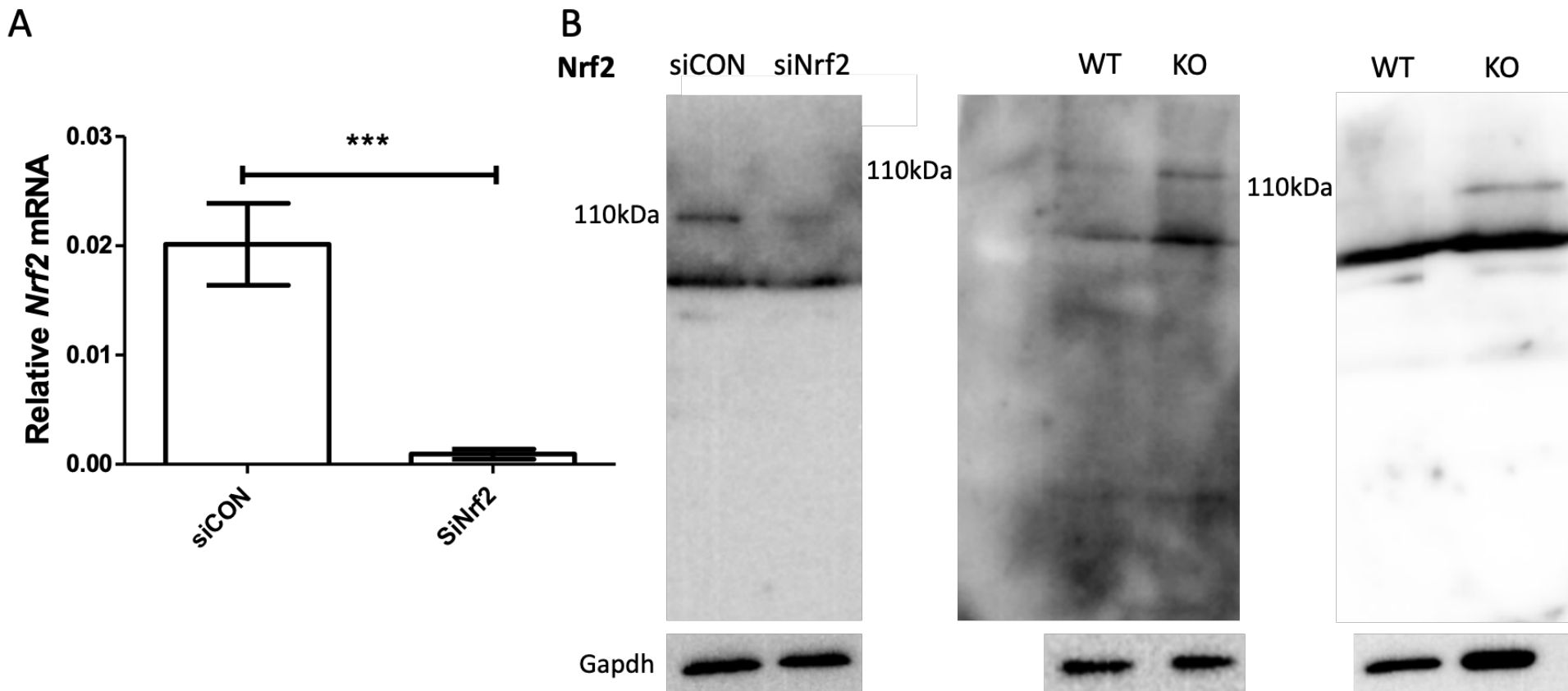
To summarise, qRT-PCR and luciferase reporter assays confirmed that nine putative candidate genes analysed were upregulated in miR-140^{-/-} mice, and that overexpression of a miR-140-5p mimic reduced luciferase expression when regulated by the 3'UTR of these genes. Mutation of miR-140-5p seed sequence(s) within the 3'UTRs of *Creb3l1*, *Nrf2*, and *Zeb1* confirmed these genes are directly regulated miR-140-5p. Furthermore, the protein expression of the *Creb3l1* encoding OASIS and Nrf2 are increased in miR-140^{-/-} costal chondrocytes.

Figure 4.9 Protein encoded by *Creb3l1* is differentially expressed in miR-140^{-/-} chondrocytes



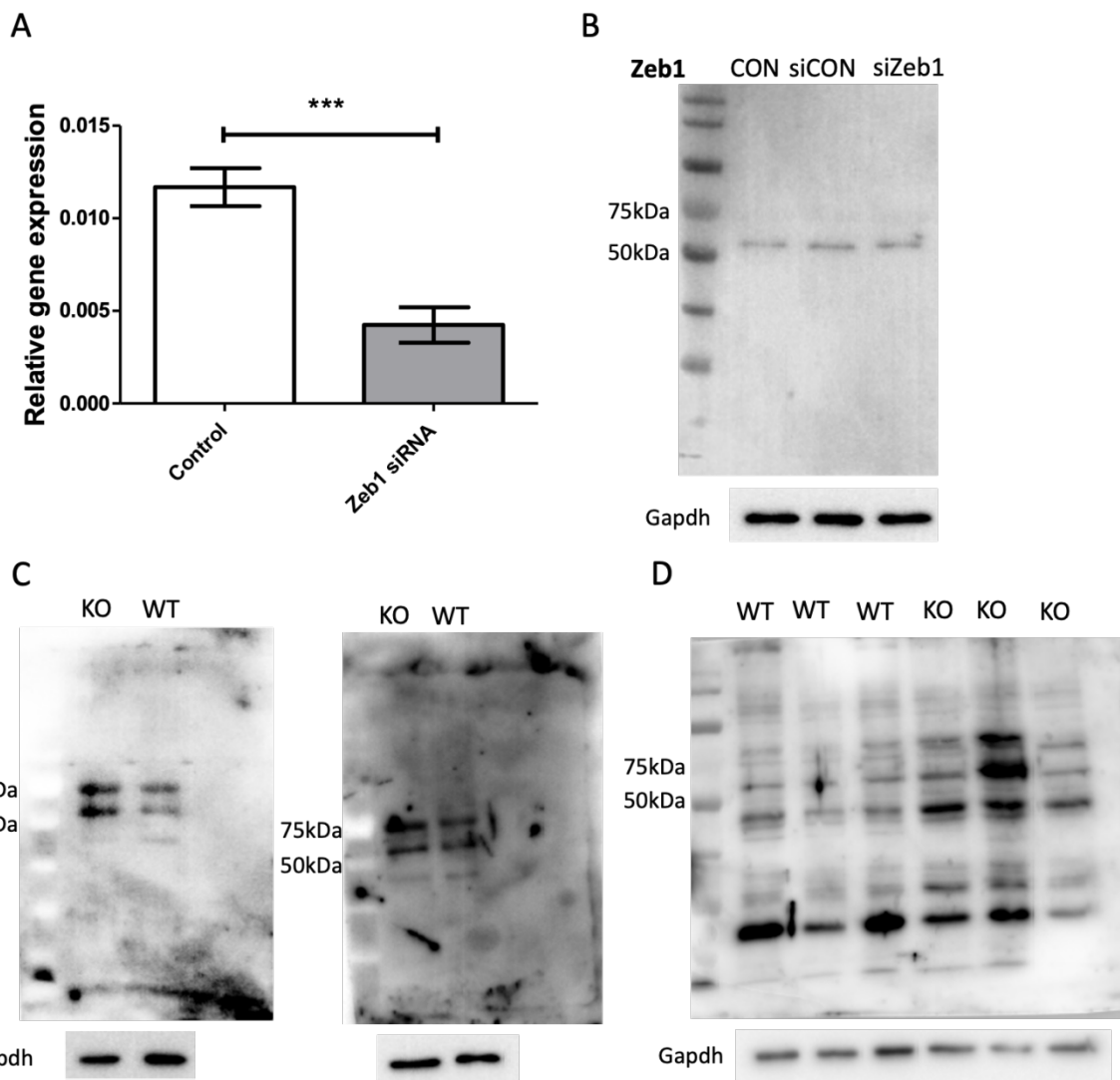
(A) Real time qRT-PCR analysis of *Creb3l1* mRNA in 7-day-old WT mice costal chondrocytes following transfection of either control siRNA (siCON) or *Creb3l1* siRNA (siCreb3l1). Values were normalised to *Gapdh* and represented as mean \pm SEM with one experiment performed in sextuplet. An unpaired Student's t-test was used for analysis, *** $P \leq 0.001$. (B) Western blot analysis (left) of *Creb3l1* protein in 7-day-old WT mice costal chondrocytes following either control siRNA or *Creb3l1* siRNA transfection for 24 hr. Western blot analysis (centre and right) of *Creb3l1*/Oasis protein in 7-day-old miR-140^{-/-} mice (KO, n=2) costal chondrocytes and age matched WT mice (WT n=2) costal chondrocytes. The arrow above indicates the full-size isoform of *Creb3l1*, and the arrow below cleaved isoform of *Creb3l1*. The bands between two arrows are either cleaved isoform of *Creb3l1* or background bands. *Gapdh* immunoblot was used as a loading control. Migration of the 50 and 75 kDa marker ladder on each blot are indicated.

Figure 4.10 Protein encoded by *Nrf2* increased in expression in miR-140^{-/-} chondrocytes



(A) Real time qRT-PCR analysis of *Nrf2* mRNA in 7-day-old WT mice costal chondrocytes following transfection of either control siRNA (siCON) or *Nrf2* siRNA (siNrf2). Values were normalised to *Gapdh* and represented as mean \pm SEM with one experiment performed in sextuplet. An unpaired Student's t-test was used for analysis, *** $P \leq 0.001$. (B) Western blot analysis (left) of Nrf2 protein in 7-day-old WT mice costal chondrocytes following either control siRNA or *Nrf2* siRNA transfection for 24 hr. Western blot analysis (centre and right) of Nrf2 protein in 7-day-old miR-140^{-/-} mice (KO, n=2) costal chondrocytes and age matched WT mice (WT, n=2) costal chondrocytes. *Gapdh* immunoblot was used as a loading control.

Figure 4.11 Immunoblot analysis of protein encoded by *Zeb1*



(A) Real time qRT-PCR analysis of *Zeb1* mRNA in 7-day-old WT mice costal chondrocytes following transfection of either control siRNA (siCON) or *Zeb1* siRNA (si*Zeb1*). Values were normalised to *Gapdh* and represented as mean \pm SEM with one experiment performed in sextuplet. An unpaired Student's t-test was used for analysis, *** $P \leq 0.001$. (B) Western blot analysis (left) of *Zeb1* protein in 7-day-old WT mice costal chondrocytes following either no treatment (CON), control siRNA (siCON) or *Zeb1* siRNA (si*Zeb1*) transfection for 24 hr. (C) Western blot analysis of *Zeb1* protein in 7-day-old miR-140^{-/-} mice (KO, n=2) costal chondrocytes and age-matched WT mice (WT, n=2) costal chondrocytes. (D) Western blot analysis of *Zeb1* protein in 7-day-old miR-140^{-/-} mice (KO, n=3) femoral head chondrocytes and age-matched WT mice (WT, n=3) femoral head chondrocytes. *Gapdh* immunoblot was used as a loading control. Predicted molecular weight of *Zeb1* is 124kDa.

4.2.5.5. Exploration of the role of *Mir-140* target genes

From the previous *in vivo* proliferation assay results (section 3.2.1.4), we identified that the replication rate of proliferative chondrocytes is impaired in miR-140^{-/-} mice compared to control animals. Based on the published literature, upon activation CREB3L1 can act as an inhibitor of cell proliferation (Sherr and Roberts 1999, Bailey and O'Hare 2007, Denard, Seemann et al. 2011, Kondo, Hino et al. 2012). Furthermore, stable overexpression of Nrf2 in ATDC5 cells significantly inhibited mRNA expression of chondrocyte markers such as type II collagen (Hinoi, Takarada et al. 2007), thus the expression of Nrf2 in chondrocyte and chondrogenesis is negatively correlated while Zeb1 is involved in TGF-β signalling (Murray, Precht et al. 2000, Hinoi, Takarada et al. 2007). The WST-1 cell proliferation assay was therefore performed on P7 costal chondrocytes to further explore the role of *Mir140* target genes in chondrocyte proliferation.

In order to understand the role of target genes in chondrocytes proliferation, we carried out two separate experiments using 7-day-old *Mir140*-null costal chondrocytes and age-matched control costal primary chondrocytes, either directly following isolation (P0) or after one passage (P1). Initially, we examined whether the reconstitution of miR-140 could (restore) increase the proliferative activity of *Mir140*-null chondrocytes. Indeed, the proliferation activity significantly increased (15.8%, *p* value < 0.05) in P1 cultured *Mir140*-null costal chondrocytes treated with the miR-140-5p mimic (Fig. 4.12A-4.12B). However, in P0 chondrocytes a similar treatment did not improve their proliferation rate. Real-time qRT-PCR analysis was used to confirm that transfection of microRNA mimic increased miR-140 mRNA levels in P1 chondrocytes (Fig. 4.12C). Furthermore, following miR-140-5p mimic transfection in the null cells (P1) immunoblot analysis resulted in decreased expression of Creb3l1 and Nrf2 (Fig. 4.12D).

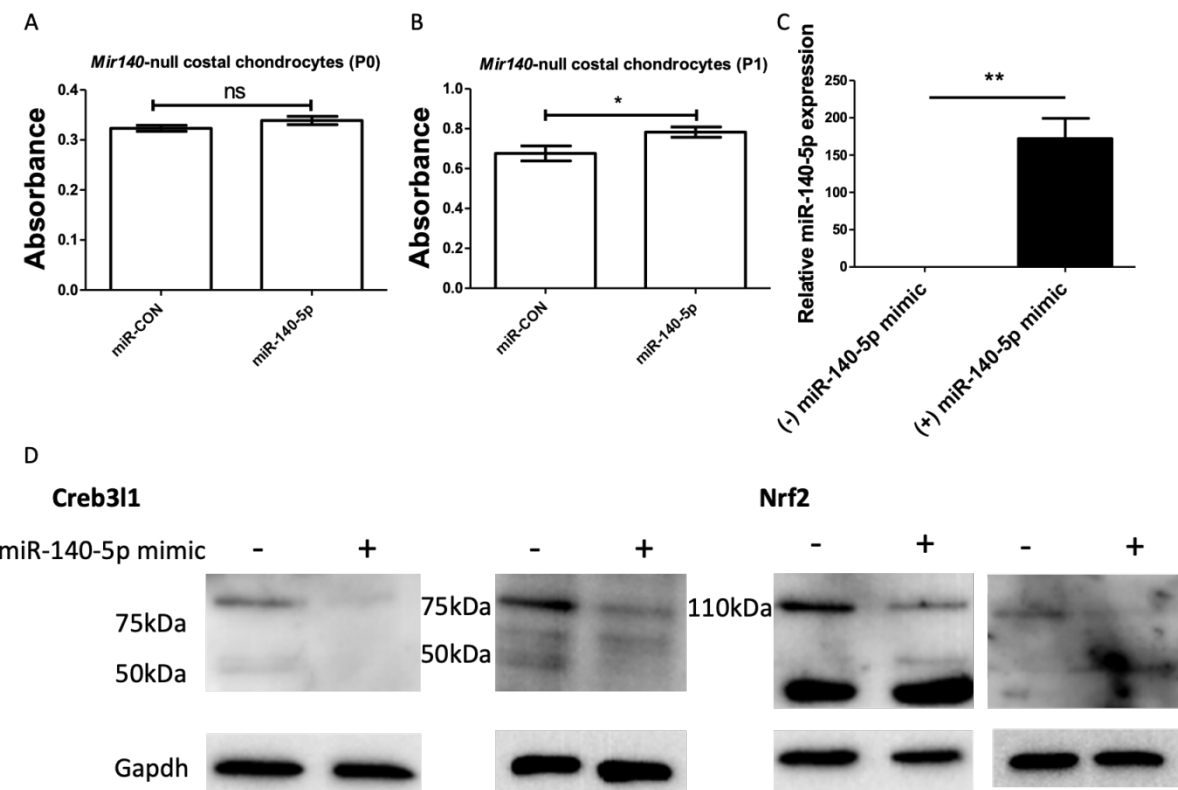
Next, the effect of *Creb3l1*, *Nrf2*, and *Zeb1* on P7 costal chondrocyte proliferation was examined using siRNA mediated knock-down – decreased expression of *Creb3l1* and *Nrf2* was confirmed at the protein level by immunoblotting and *Zeb1* mRNA knockdown was confirmed by qRT-PCR (Fig. 4.11A) due to the lack of a suitable antibody. For *Mir140*-null costal chondrocytes, although proliferation activity of P0 chondrocytes increased upon treating with the *Zeb1* siRNA (31%, *p* value < 0.01) (Fig. 4.13A), no significant difference was

observed with cultured P1 cells (Fig. 4.13B). In contrast, increased proliferation activity of *Mir140*-null costal chondrocytes was only observed in cultured P1 cells treated with *Nrf2* siRNA relative to P0 chondrocytes (Fig. 4.13B). What is noteworthy is that *Mir140*-null costal chondrocytes treated with *Creb3l1* siRNA both at P0 or P1 consistently had increased cell proliferative activity (Fig. 4.13A-B). Furthermore, the biggest effect on proliferation of *Mir140*-null costal chondrocytes at P0 was observed when treating with *Zeb1* siRNA, but *Creb3l1* siRNA had the largest effect on P1 *Mir140*-null costal chondrocytes (Fig. 4.13).

The same siRNA experiments were repeated in WT costal chondrocytes (Fig. 4.14). No differences were observed in the proliferation of WT chondrocytes transfected with miR-140-5p mimic (Fig. 4.14A), presumably because of the already high expression level of this microRNA in chondrocytes. siRNA knockdown of *Creb3l1*, *Nrf2* and *Zeb1* did not affect proliferation of P0 primary WT costal chondrocyte, but significantly increased proliferative activity was observed in P1 cultured WT chondrocytes following *Creb3l1* and *Nrf2* siRNA treatment (Fig. 4.14B). Intriguingly, a significant increased proliferative activity was observed in cultured P2 WT costal chondrocytes after *Zeb1* siRNA treatment (Fig. 4.14B), although no effect of *Zeb1* siRNA was observed at either P0 or P1. The overall effect of miR-140-5p target genes on cell proliferative activity of chondrocytes at different cell culture passage is listed in Table 4.4.

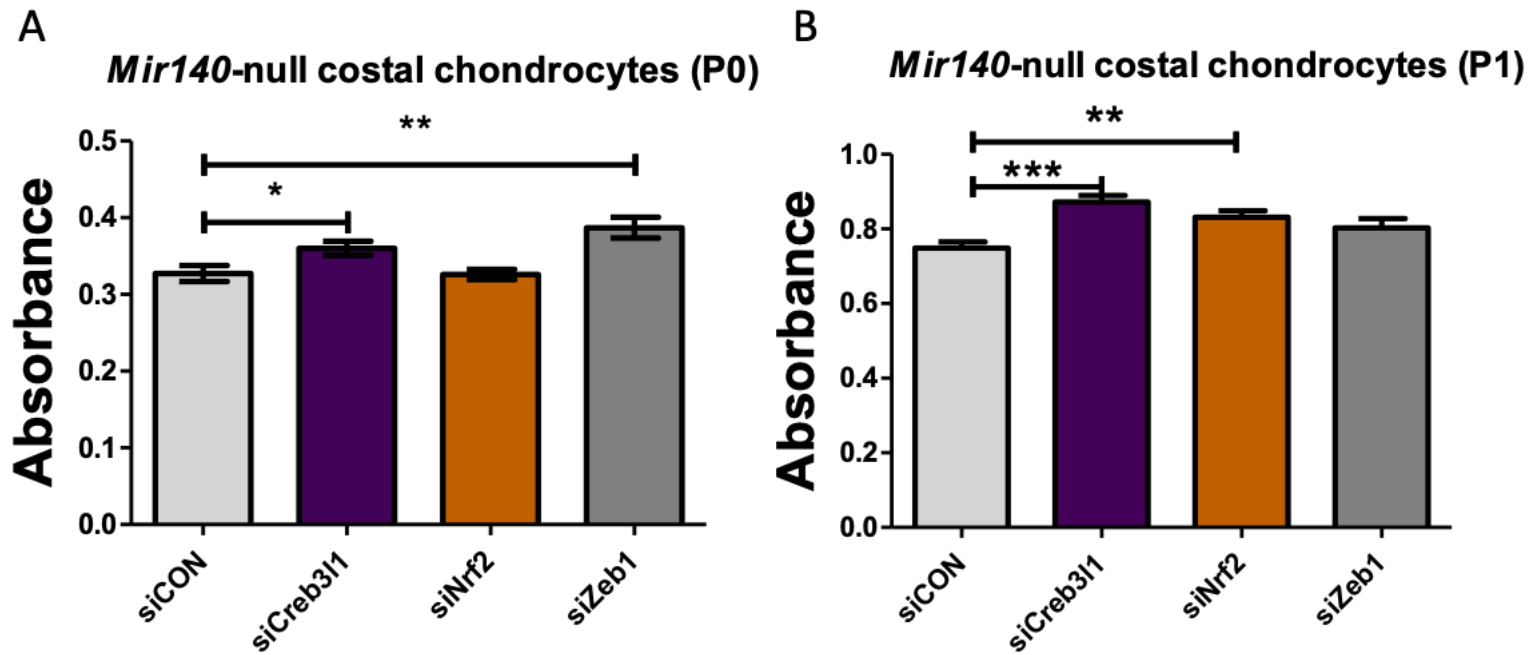
To summarise, we have confirmed that reducing *Creb3l1* and *Nrf2* expression levels, or reintroducing miR-140-5p, in *Mir140*-null costal chondrocytes resulted in increased chondrocytes proliferative activity. When coupled with the significant increased proliferation activity in either WT costal chondrocytes or *Mir140*-null costal chondrocytes with *Creb3l1* and *Nrf2* siRNA treatment, these data suggest that *Creb3l1* or *Nrf2* are potential regulators of chondrocyte proliferation in the murine growth plate.

Figure 4.12 *Mir140* regulates chondrocyte proliferation through decreasing the expression of *Creb3l1* and *Nrf2*



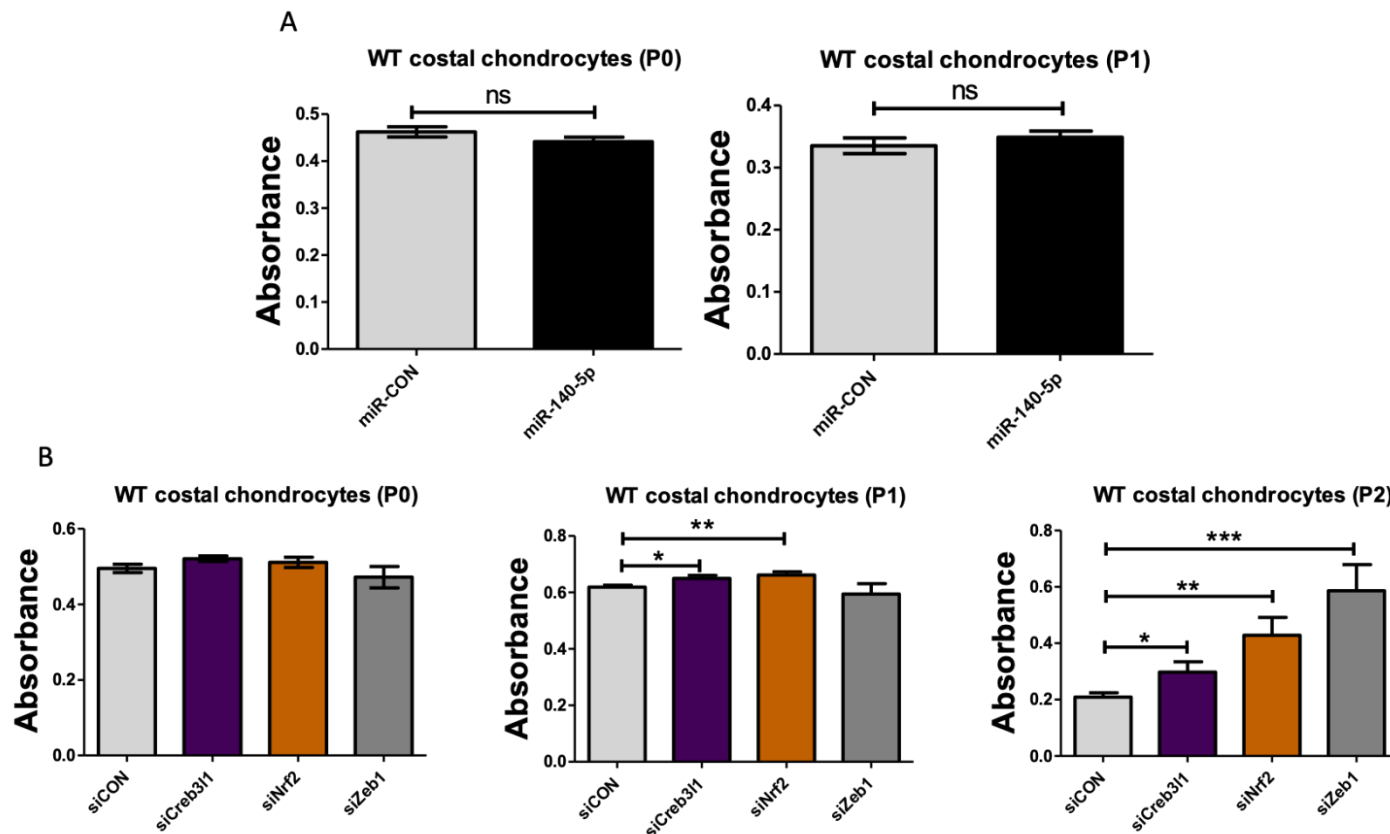
(A-B) WST-1 proliferation assay with costal chondrocytes isolated from 7-day-old WT mice with either control mimic or miR-140-5p mimic. P0 refers to primary costal chondrocyte and P1 stand for cultured primary costal chondrocytes. Data are represented as mean \pm SEM, and the experiment was performed twice (n=6/experiment), ns represents not significant, * $P\leq 0.05$. (C) 7-day-old *Mir140*-null costal chondrocytes were cultured for one passage then treated with either miR-140-5p mimic or control non-targeting mimic (miR-CON). RNA and protein were extracted from cells followed either control mimic or miR-140-5p mimic treatment. For the RNA qRT-PCR analysis of miR-140-5p was performed and expressed relative to *U6*. Data are represented as mean \pm SEM (n=6/experiment). ** $P\leq 0.01$. (D) Western blot analysis for *Creb3l1* (left) and *Nrf2* (right) after overexpression miR-140-5p in *Mir140*-null costal chondrocytes (n=2) with *Gapdh* used to monitor protein loading.

Figure 4.13 *Creb3l1* and *Nrf2* play role in regulating proliferation of chondrocytes without *Mir140*



(A) WST-1 proliferation assay was performed on costal chondrocytes isolated from 7-day-old *Mir140*-null mice with either control siRNA or *Mir140* target genes' siRNA. P0 refers to primary costal chondrocyte. Data are represented as mean \pm SEM, and the experiment was performed twice (n=6/experiment). * $P \leq 0.05$, ** $P \leq 0.01$. (B) The costal chondrocytes were isolated from 7-day-old *Mir140*-null mice and cultured with DMEM medium at 37°C until 90% confluent, cells were then passaged (thus P1) and prepared for WST-1 proliferation assay with either control siRNA or *Mir140* target genes' siRNA. Data are represented as mean \pm SEM, and the experiment was performed twice (n=6/experiment). * $P \leq 0.05$, ** $P \leq 0.01$, *** $P \leq 0.001$.

Figure 4.14 *Creb3l1* and *Nrf2* affect proliferation of WT rib chondrocyte



(A) WST-1 proliferation assay with costal chondrocytes isolated from 7-day-old WT mice with either control mimic (miR-CON) or miR-140-5p mimic P0 refers to primary costal chondrocytes and P1 stand for cultured primary costal chondrocytes. Data are represented as mean \pm SEM, and the experiment was performed twice (n=6/experiment). (B) WST-1 proliferation assay with costal chondrocytes isolated from 7-day-old WT mice with either control siRNA (siCON) or *Mir140* target genes' siRNA. P0 refers to primary costal chondrocytes, P1 stand for cultured primary costal chondrocytes and P2 for when these cells were passaged again. Data are represented as mean \pm SEM, and the experiment was performed twice (n=6/experiment). ns represents not significant, *** $p\leq 0.001$.

Table 4.4 The effect of miR-140 target genes on chondrocyte proliferative activity

<i>Mir140</i>-null P7 costal chondrocytes proliferation activity			
Cell culture passage	P0	P1	P2
miR-140-5p mimic	No effect	Increase	NA
siCreb3l1	No effect	No effect	NA
siNrf2	No effect	No effect	NA
siZeb1	Increase	No effect	NA
WT P7 costal chondrocytes proliferative activity			
Cell culture passage	P0	P1	P2
miR-140-5p mimic	No effect	No effect	NA
siCreb3l1	No effect	Increase	Increase
siNrf2	No effect	Increase	Increase
siZeb1	No effect	No effect	Increase

List of the effect of siCreb3l1, siNrf2, siZeb1, and miR-140-5p mimic on cell proliferative activity of WT and *Mir140*-null costal chondrocytes at different passage. NA = not applicable/tested.

4.2.6. RNA-seq data analysis on miR-455^{-/-} mice

MicroRNA-455 (miR-455) was implied from our previous study to be involved in human OA pathogenesis (Swingler, Wheeler et al. 2012), and a recently published study confirmed that loss of miR-455 accelerate development of OA-related phenotypes in the mouse (Mao, Kang et al. 2019, Wen, Li et al. 2020, Ito, Matsuzaki et al. 2021). To reveal the role of miR-455 in endochondral bone development and osteoarthritis development, we generated a *Mir455*-null mouse as described in Chapter 3. Total RNA was isolated from WT (bred from miR-140^{+/+} mice initially) and *Mir455*-null costal chondrocytes of animals at P7, which was then subjected to RNA-seq analysis, with the aim of providing information about the function of miR-455 in the growth plate. Sample and data quality control was as described above in section 4.2.2.

In the PCA plot of miR-455^{-/-} mice P7 costal chondrocytes against control chondrocytes, the two genotypes separate on PC1 (Fig. 4.15A). Two of miR-455^{-/-} samples clustered together (blue, bottom), with the third miR-455^{-/-} sample (blue, top, female) isolated from the other two samples (male), possibly a sex effect. Although the control mice (orange) do not cluster closely together, they are clearly distinguished from miR-455^{-/-} mice.

Compared to the 3073 significant DEG genes identified in the *Mir140*-null mice, there were far fewer significantly up- and down-regulated genes identified by RNA-seq analysis of *Mir455*-null costal chondrocytes versus WT chondrocytes (1527 genes in total, using the same criteria mentioned in section 4.2.2.1, fold change ≥ 1.5 , FDR ≤ 0.05). A total of 530 genes (Fig. 4.15B, red dots, left) were found to be significantly downregulated and 997 genes (red dots, right) to be significantly upregulated in miR-455^{-/-} mice when compared with WT mice. Predicted miR-455-5p (TATGTGCCTTGGACTACATCG, seed: ATGTGCC) target genes (from TargetScan 7.2) were compared to the list of miR-455 DEGs. Thirty predicted target genes were significantly differentially expressed (Fig. 4.15C-left), with 21 out of 30 (70%) being upregulated when *Mir455* was absent (Fig. 4.15D-left), though this enrichment was not significant (Fisher's exact test, $p = 0.7$).

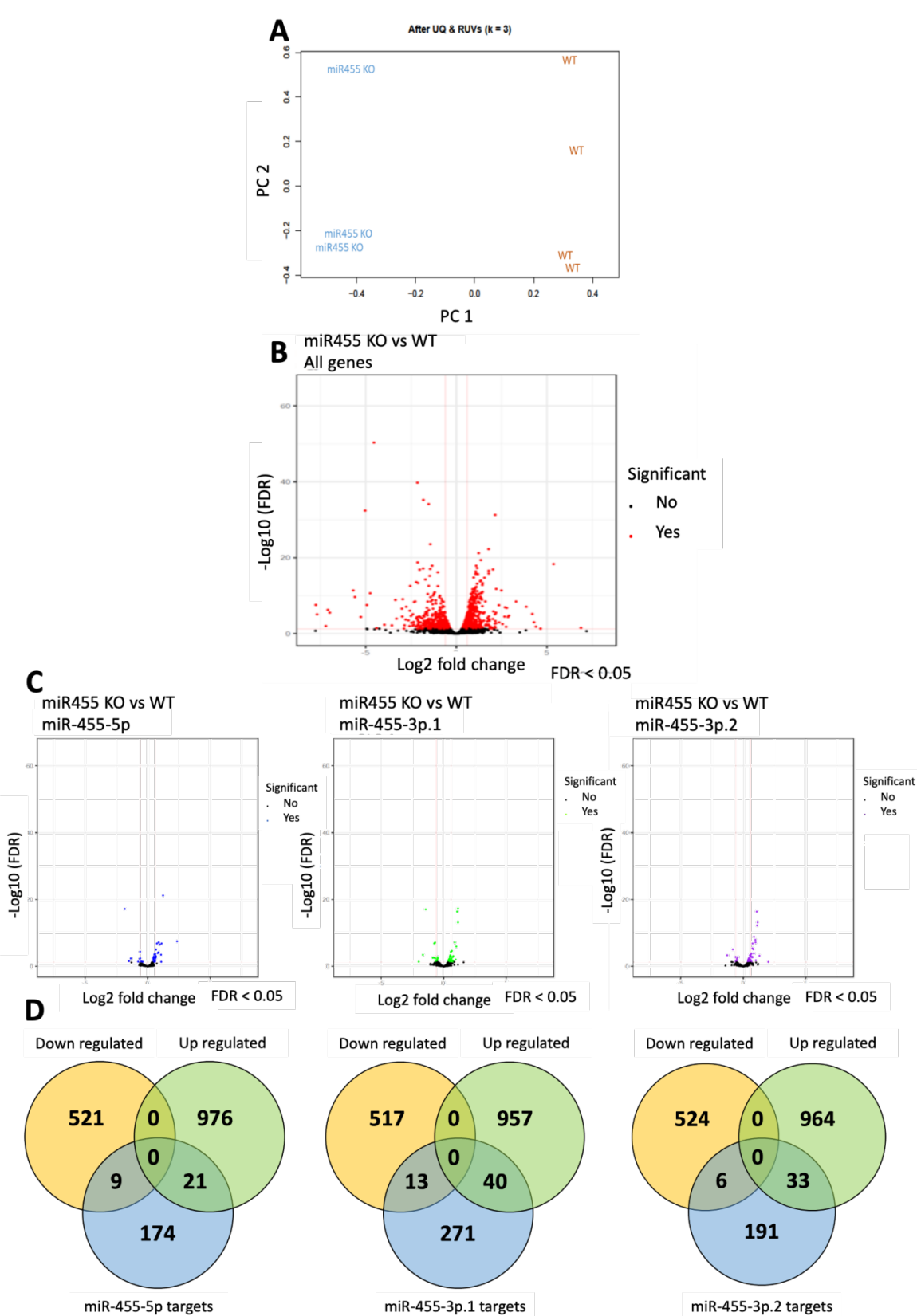
The dominant strand of miR-455 is considered to be miR-455-3p, and recent evaluation also suggest that, like miR-140-3p, this arm is processed to two dominant 5' isomiRs which differ in their seed sequence and therefore predicted targets (Woods, Charlton et al. 2020). For

miR-455-3p.1 (GCAGTCCACGGGCATATACA, seed: CAGTCCA), Fifty-three predicted targets are significantly differential expressed in miR-455^{-/-} costal chondrocytes compared to control costal chondrocytes (Fig. 4.15C-middle), with forty (75.5%) being significantly upregulated (Fig. 15D-middle), though again this did not represent a significant enrichment (Fisher's exact test, $p = 0.1414$). For miR-455-3p.2 (ATGCAGTCCACGGGCATATACAC, seed: TGCAGTC) target gene analysis, thirty-nine overlapping genes are differentially expressed (Fig. 15C-right), with thirty-three (84.6%) are significantly upregulated in the RNA-seq data (Fig. 15D-right). For miR-455-3p.2 isomiRs, predicted targets were significantly enriched in the upregulated gene list ($p < 0.01$, Fisher's exact test).

Based on RNA-seq data, the percentage of predicted targets (by TargetScan 7.2) for either miR-455-5p, miR-455-3p.1 or miR-455-3p.2 relative to all genes, were calculated for the downregulated DEGs, upregulated DEGs and unchanged genes (Fig. 4.16A). This showed that predicted miR-455-3p.1 targets account for the largest proportion in all upregulated genes (4%) compared to either miR-455-5p or miR-455-3p.2 (2.1% and 3.1%, respectively). However, the mean log₂ fold-change of predicted targets of miR-455 compared to all genes consistently showed that the miR-455-3p.2 predict targets are more highly upregulated compared to miR-455-3p.1 and miR-455-5p predict targets, indicating miR-455-3p.2 is potentially the dominant strand of miR-455 in the growth plate chondrocytes (Fig. 4.16B).

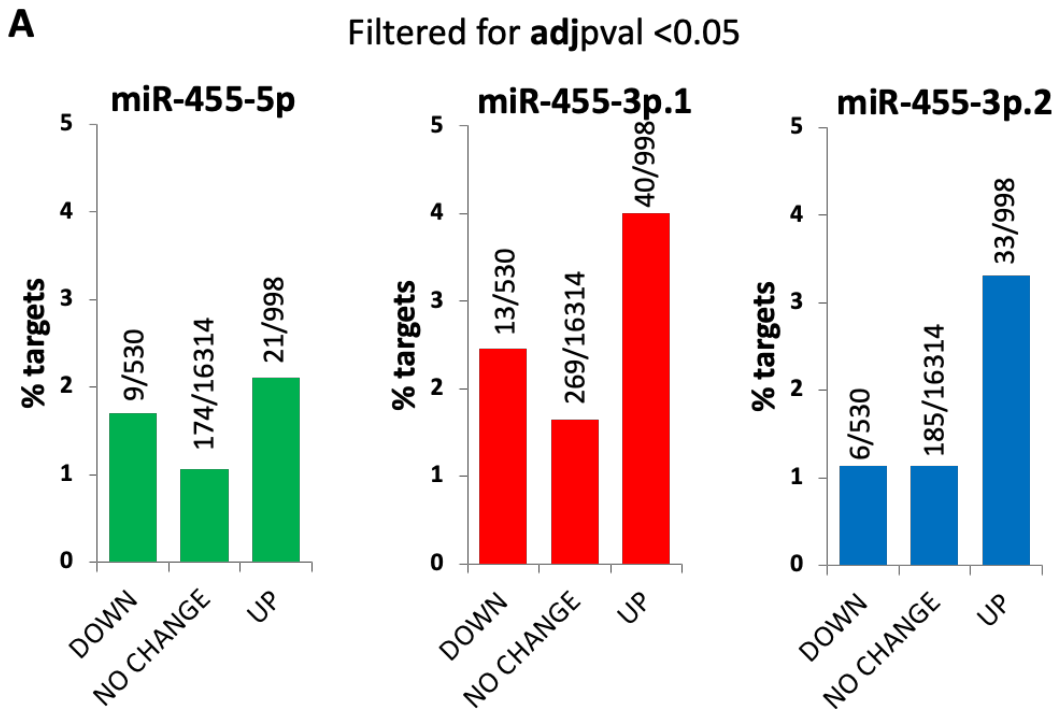
Through our collaboration with Prof Ian Clark and PhD student Paige Paddy (UEA) we were also able to obtain RNA-seq data from 12-week-old mouse knee cartilage chondrocytes of WT and *Mir455*-null mice. Comparing these data with our costal expression dataset, ranked gene lists for costal chondrocytes and knee cartilage chondrocytes) were generated based differential expression p value ranked taking into consideration whether the gene was up- or down-regulated. The resulting datasets of ranked lists were thus compared using the Rank-rank Hypergeometric overlap (RRHO) threshold-free algorithm (Cahill, Huo et al. 2018), which reassuringly gave a highly correlative score in the genes upregulated in the miR-455^{-/-} mice (Fig. 4.17).

Figure 4.15 An abundance of genes are differentially expressed in *Mir455*-null mice relative to control mice

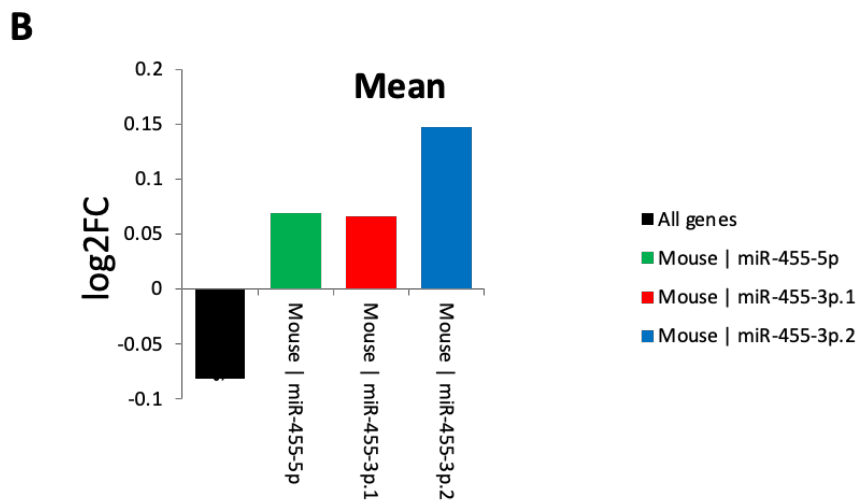


(A) Samples cluster by genotype using PCA. A PCA plot was generated from normalised RNA-seq data of the wild-type (WT, orange) and miR-455^{-/-} (miR455 KO, blue) samples. (B) A volcano plot of gene fold-change (\log_2 , X axis) against $-\log_{10}$ FDR (false discovery rate, Y axis) between miR-455^{-/-} and WT mice showed the distribution of the detected genes, demonstrating the distribution of upregulated genes and downregulated genes. The vertical red lines correspond to 0.585 \log_2 fold up and down (equivalent to 1.5-fold change), respectively. The red horizontal line denotes an FDR 0.05. Red points represent all significantly differentially expressed genes with an FDR P value ≤ 0.05 and fold change ≥ 1.5 . In total, 530 genes were found to be significantly downregulated and 997 genes to be significantly upregulated in miR-455^{-/-} mice. (C) Volcano plots demonstrating the significantly upregulated and downregulated genes in miR-455^{-/-} P7 costal chondrocytes that overlap with predicted miR-455-5p (blue dots, left), miR-455-3p.1 (green dots, middle), and miR-455-3p.2 (purple dots, right) target genes, respectively. The PCA and Volcano plots in A-C were generated by Dr Kathleen Cheung in R studio. (D) Venn diagrams demonstrating the overlap of TargetScan conserved respectively predicted miR-455-5p (left), miR-455-3p.1 (centre), and miR-455-3p.2 (right) target genes and the differentially expressed genes in the RNA-seq analysis.

Figure 4.16 MiR-455 targets analysis

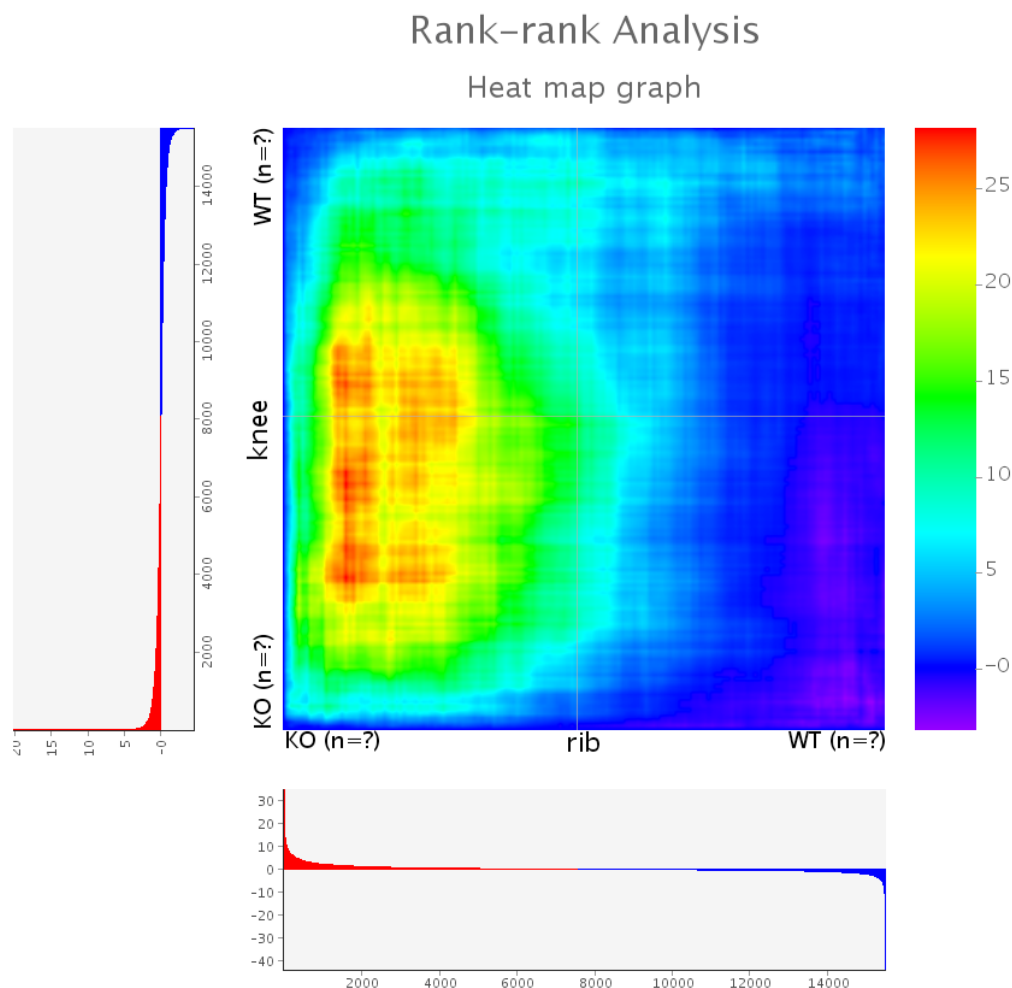


	5p not 3p.1 or 3p.2	3p.1 not 5p or 3p.2	3p.2 not 3p.1 or 5p		total number of genes
DOWN	9	13	4	DOWN	530
NO CHANGE	174	269	185	NO CHANGE	16314
UP	21	40	33	UP	998



(A) Percentage of the number of TargetScan (v7.2) predicted miR-455-5p (green), -3p.1 (red) and -3p.2 (blue) unique targets from all the genes that either increased, decreased (\log_2 fold change > 1.5 and FDR threshold ≤ 0.05) or remained unchanged in our *Mir455*-null mice compared to age-matched control animals. (B) Mean \log_2 fold changes of all genes that are predicted targets of only either miR-455-5p (green), -3p.1 (red) or -3p.2 (blue) in the absence of miR-455 in mice.

Figure 4.17 Screening *Mir455* target genes



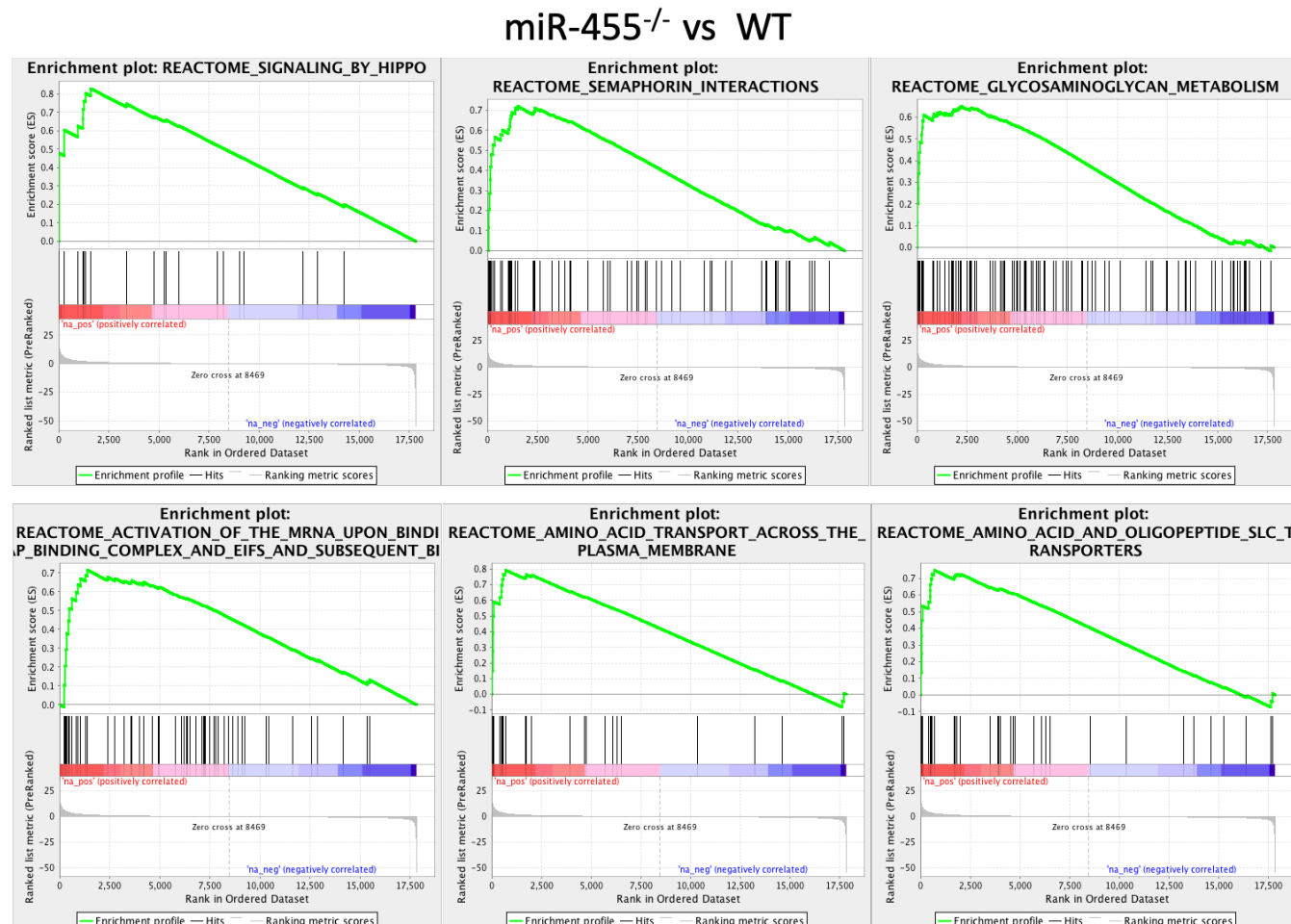
Gene expression profiles from costal and knee chondrocytes of miR-455^{-/-} mice lines at 7-days and 12-weeks old respectively, compared to their respective age-matched control mice, were used to generate a ranked list (based on *p* value) of genes that are differentially expressed in the absence of *Mir455*. The resulting overlap from the ranked lists, represented as a hypergeometric heat map, identifies an enrichment for upregulated genes in our miR-455^{-/-} mice costal chondrocytes overlap with that of knee chondrocytes.

4.2.7. Identification and validation of *Mir455* in the growth plate

4.2.7.1. Pathway analysis using GSEA

In addition to RRHO analysis, GSEA was used as pathway analysis to compare gene sets between WT and *Mir455*-null mice to identify functional pathways that are enriched or depleted for differentially expressed genes. False discovery rate values (FDR) below 0.05 was classified as GSEA significance. There were six pathways enriched for up-regulated genes in *Mir455*-null mice when compared to WT mice, six showed significance and these include, ‘signalling by hippo’ (*Tjp2*, *Last1*, *Ywhab*, *Mob1a*, *Amotl2*, *Wwtr1*, *Tjp1*, *Sav1*); ‘semaphorin interactions’ (due to the presence of genes: *Met*, *Plxna1*, *Hsp90aa1*, *Rock2*, *Sema7a*, *Itgb1*, *Fyn*, *Rhoc*); ‘glycosaminoglycan (GAG) metabolism’ (due to the presence of genes: *Chst11*, *Glace*, *St3gal1*, *Chsy3*, *Has2*, *Slc9a1*, *Gspg4*, *Acan* etc); ‘activation of the mRNA upon binding of the cap binding complex and Eifs and subsequent binding to 43S’ (*Eif2s2*, *Eif4a1*, *Pabpc1*, *Eif4e*, *Eif3a*, *Eif3c*, *Eif4g1*, *Eif4bp1*, *Rps7*, *Rps15a*, *Eif2s1*, *Eif3d*); ‘amino acid transport across the plasma membrane’; and ‘amino acid and oligopeptide Slc transporters’ (Fig. 4.18). The significantly enriched gene pathways are closely correlated with cell proliferation and apoptosis (signalling by hippo), and GAG metabolism (glycosaminoglycan metabolism). Although there is limited information about miR-455 targets, Zhao *et al.* showed that *Eif4e* (significantly up-regulated in our *Mir455*-null costal chondrocytes and involved in enriched pathway ‘activation of the mRNA upon binding of the cap binding complex and Eifs and subsequent binding to 43S’) is a target gene of miR-455-3p in prostate cancer (Zhao, Yan *et al.* 2017). Collectively, these data are reliable and indicate the miR-455 is involved in GAG metabolism.

Figure 4.18 GSEA enrichment of miR-455^{-/-} gene sets in mouse costal chondrocytes RNA-seq data



Enrichment analysis on GSEA results (FDR q-value < 0.05) showing affected cellular programs in *Mir455*-null costal chondrocytes. Some of the gene pathways are significantly enriched in the up-regulated genes in miR-455^{-/-} mice when compared to WT mice.

4.2.7.2. Identification of *Mir-455* growth plate target genes

We filtered our RNA-seq data of WT versus *Mir455*-null murine costal chondrocytes by overlapping the upregulated DEGs with those predicted to have conserved *Mir455* sites within their 3'UTR (TargetScan 7.2, Fig. 4.19A). We concentrated on miR-455-3p.1 as this is predicted and published to be more functional arm and isomiR of miR-455 (Crowe, Swingler et al. 2016), even though our RNA-seq data above indicated that miR-455-3p.2 has the highest percentage of genes that overlapping with predicted miR-455 targets. From this, we selected *Acan*, *Chst11*, and *Ppp1r10* as miR-455-3p.1 candidate target genes. These genes are all highly upregulated in the miR-455^{-/-} mice RNA-seq data and *Acan* and *Chst11* are involved in GAG metabolism, a pathway enriched in the GSEA. Furthermore, Safranin-O histological staining on knee cartilage of *Mir455*-null mice by ourselves and our collaborator Ian Clark in UEA, demonstrated that GAG staining is reduced compared to WT mice, which is consistent with published findings (Mao, Kang et al. 2019). We also observed significantly reduced GAG staining on the lateral side of the knee joint during destabilisation of the medial meniscus (DMM)-mediated OA-induction in *Mir455*-null mice compared to WT control animals (Chapter 5). In general, the lateral side of the joint shows less histological evidence of OA than the medial region. Although counter-intuitive, we hypothesised that an up-regulation of *Acan* (which encodes Aggrecan, the major cartilage proteoglycan core protein whose chondroitin sulphate modifications are stained by Safranin-O) expression might result in an imbalance of chondroitin sulphate per protein molecule and therefore the phenotype. Similarly, *Chst11*, a chondroitin sulphotransferase, is involved in GAG formation. Deletion of the enzyme shifts the balance of chondroitin sulphation which alters growth factor signalling during cartilage morphogenesis leading to severe skeletal abnormalities (Kluppel, Wight et al. 2005). SNPs within intron 2 of the human *CHST11* gene are also associated with hip OA (arc, arc et al. 2012). *Ppp1r10* does not have a described role in GAG formation but has been suggested to be an inflammatory biomarker for OA (Hellvard, Zeitlmann et al. 2016).

To validate that these genes are significantly increased in expression in *Mir455*-null costal chondrocytes compared to age-matched control costal chondrocytes, we performed qRT-PCR on RNA isolated from a new litter of mice (Fig. 4.19B). Only *Ppp1r10* mRNA expression

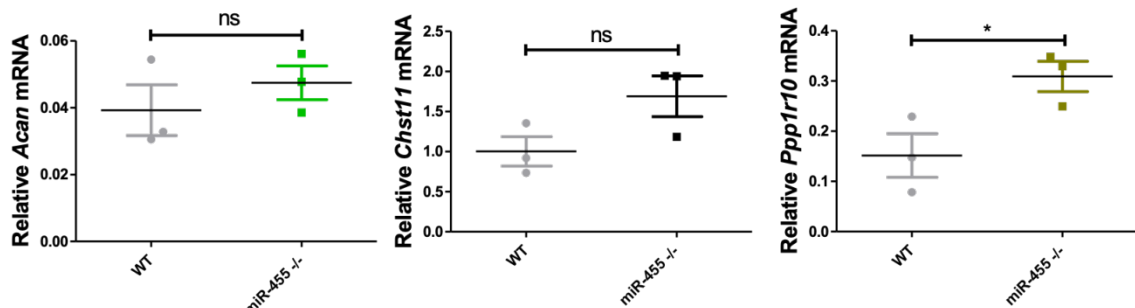
was significantly increased in *Mir455*-null costal chondrocytes. *Acan* and *Chst11* mRNA expression increased but not significantly, potentially due to the small group size analysed. Regardless, *Acan*, *Chst11*, and *Ppp1r10* 3'UTR luciferase reporter constructs were created, and luciferase activity was measured following miR-455-3p.1 mimic treatment. However, none of the 3'UTRs assayed displayed significantly decreased luciferase activity compared to control (fig. 4.19C), indicating the selected genes are not direct targets of miR-455-3p.1. In addition, *Chst11* was also predicted as miR-455-3p.2 target gene (TargetScan 7.2). However, because of time-constraints due to the Covid-19 pandemic we were unable to test if this gene was a potential target of miR-455-3p.2

Figure 4.19 Identification of miR-455 growth plate target genes

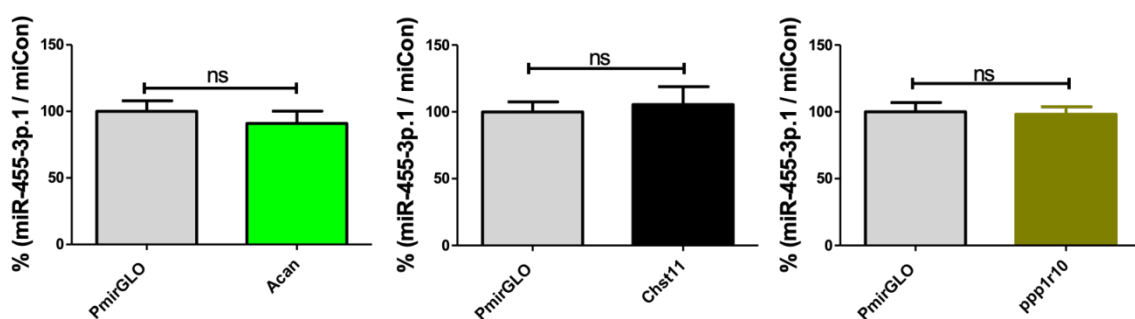
A

mmu-miR-455-3p.1	G CAGUCCA CGGGCAUAUACAC
<i>Acan</i> 3'UTR	G GTCAGGT GCCCAATGTCACT...
<i>Chst11</i> 3'UTR	A GTCAGG ACGACTGTTCTCC...
<i>Ppp1r10</i> 3'UTR	C GTCAGGT GTCCCACGCCCAT...

B



C



(A) Schematic illustrating the sequences of miR-455-3p.1 and its potential binding sites (7mer-A1 binding sites and 7mer-8m binding sites) within their targets predicted by TargetScan. The seed sequence of miR-455-3p.1 is shown in red. (B) Real-time qRT-PCR validation of predicted *Mir455* target genes identified by RNA-seq analysis and published studies. Only *Ppp1r10* expression was significantly upregulated in our miR-455^{-/-} mice. Differences within each genotype were normalised to *Gapdh* and plotted as mean \pm SD, (n=3 mice/ genotype), ns represents not significant, * $p\leq 0.05$. (C) The relative luciferase activity was determined in SW1353 chondrosarcoma cells following co-transfection of miR-455-3p.1 target genes' 3'UTR constructs with either non-targeting mimic (miR-Con) or miR-455-3p.1 mimic for 24 hours. Data was plotted as mean \pm SEM (the experiment for each construct was performed twice), ns represents not significant.

4.2.8. Separation of murine growth plate proliferative zone using laser microdissection (LMD)

Articular and growth plate cartilage both arise from the same origin but subsequently develop important histological and functional differences. Both articular and growth plate cartilage are composed of three distinct zones of chondrocytes: the superficial, mid, and deep zones for articular cartilage and the resting, proliferative and hypertrophic zones for growth plate cartilage. To investigate and directly compare the impact of *Mir140* loss in the articular cartilage and growth plate, we planned to use LMD to separate murine growth plate and articular cartilage from the proximal tibial bone. Before doing this, we developed a methodology for purifying RNA from laser dissected sections of murine growth plate proliferative zones followed by rRNA depletion and RNA sequencing. We initially focused on the proliferative zone of the tibial growth plate since miR-140 is mainly expressed in this zone of P10 mice (Miyaki, Sato et al. 2010) and therefore represents the tissue most likely to have developmentally important miR-140 targets that would be dysregulated in the miRNA-null mice.

Growth plate proliferative zone chondrocytes from the proximal tibias of 7-day-old C57BL6 mice were dissected using LMD (Fig. 4.20). Two different techniques were used to 'extract' RNA from the dissected sections and samples were split into four different groups, for each technique (Table 4.5, the total eight groups are represented from A to H). All the eight groups of chondrocyte RNA were subjected to low-input RNA-sequencing and the profile of gene expression obtained. Bioinformatic analysis performed with the assistance of Dr Jamie Soul (Newcastle University, Skeletal Research Group) showed group G had the largest numbers of total reads (51.4M) and the highest percentage aligning with mouse genes (30.5%), this was followed by group E (26.9%). Lower mapped rate were shown in groups that were prepared with Smart-seq lysis buffer (group C: 7%; group D: 8%). For each group, the percentage of total counts for the top ranked 50 genes were used as input into 'Enrichr', a web based tool for gene set analysis, for analysis (Kuleshov, Jones et al. 2016, Xie, Bailey et al. 2021) (<https://maayanlab.cloud/Enrichr/enrich>), and then to overlapped with the ARCHS4 database of mouse genes, which verified all the samples as 'Chondrocyte' (Torre, Lachmann et al. 2018, Xie, Bailey et al. 2021). Group B (a small proliferative section), D

(three small proliferative sections), and G (three big proliferative sections) all showed the highest overlap rate amongst the eight groups, with 18 out of 50 genes which were classed as mouse ‘Chondrocyte’ genes. Overall, group G showed the lowest adjust *p*-value (Table 4.6).

To test whether our LMD expression data does corresponds to mouse growth plate proliferative zone gene expression, we correlated our data to published, publicly available data. Dataset GSE114919 contains mouse 1-week-old phalanx proliferative zone and 1-week-old mouse tibial proliferative zone samples (Lui, Jee et al. 2018). Dataset GSE158337 consists of RNA-seq of mouse hippocampus and was chosen as a control. This dataset was generated within our laboratory and was therefore derived from mice of a similar genotype and housed in the same facility as our LMD mouse. When comparing our samples (A-H) to the mouse phalanx proliferative zone (Fig. 4.21A), the correlation coefficient is ranged from 0.819 to 0.899. When compared to mouse tibial growth plate proliferative zone, the correlation coefficient range was between 0.83 to 0.896 (Fig. 4.21B). In general, the correlation coefficients between our samples were higher with the data from tibial proliferative zone than that taken from the phalanx proliferative zone. Not surprisingly, the lowest correlation coefficient range (from 0.626 to 0.694) was when our data was compared to the control hippocampal samples (Fig. 4.21C).

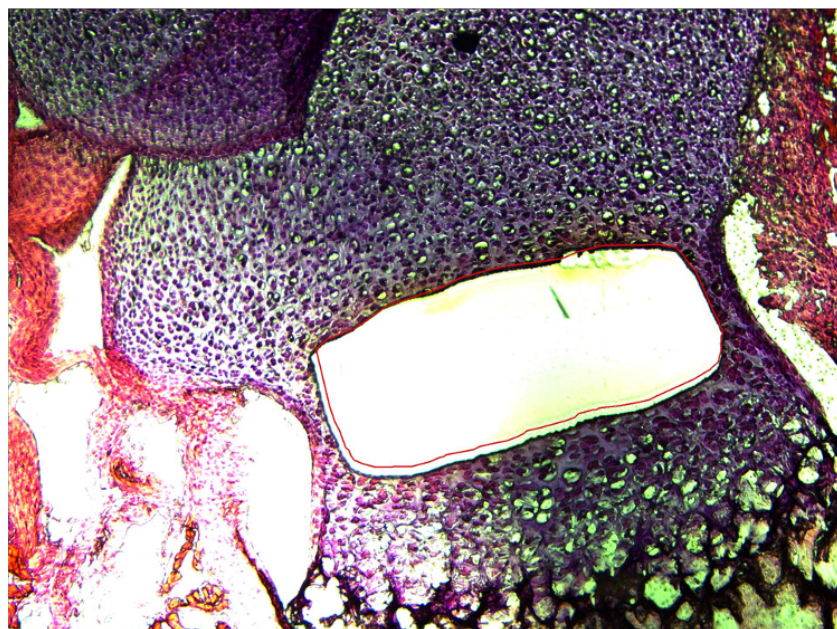
In addition, the top 50 ranked genes obtained from RNA sequencing for each group were plotted in ranked order, with groups B, G, and H displaying the smoothest spread of gene expression. These data indicate that RNA extracted using the column-based method (Zymo) was probably more effective than the Smart-seq lysis buffer method (Fig. 4.22), but that a large section of the proliferative zone is required for this to be most effective. Furthermore, we selected several zonal gene markers, collagens and other chondrocytes selective genes, and plotted these as a heatmap to directly compare the differences in relative gene expression between the groups and treatments (Fig. 4.23). The zone markers selected in this study were *Prg4* for the superficial zone of articular cartilage, *Sfrp5* for the deep zone of articular cartilage and resting zone of growth plate cartilage, *Gdf10* and *Prelp* for the proliferative zone of growth plate cartilage, and *Col10a1* for the hypertrophic zone of growth plate cartilage. Both group B and G showed a higher level of detection/expression of

proliferative zone gene *Prelp*, while Group B showed high detection of *Gdf10*, another marker of proliferative chondrocytes.

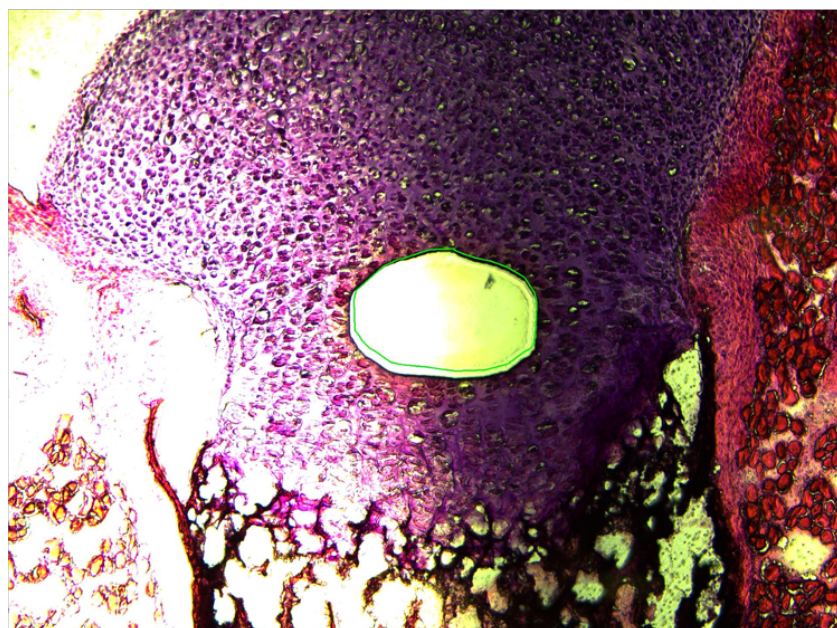
From the heatmap, Sample G displayed an apparent TPM expression distribution that would be predicted, with a high relative expression of matrix genes, especially the selected collagens, except for *Col10a1* whose expression was low, as predicted.

Figure 4.20 Laser dissected growth plate proliferative zone from 7-d-old murine proximal tibias

A big proliferative section



A small proliferative section



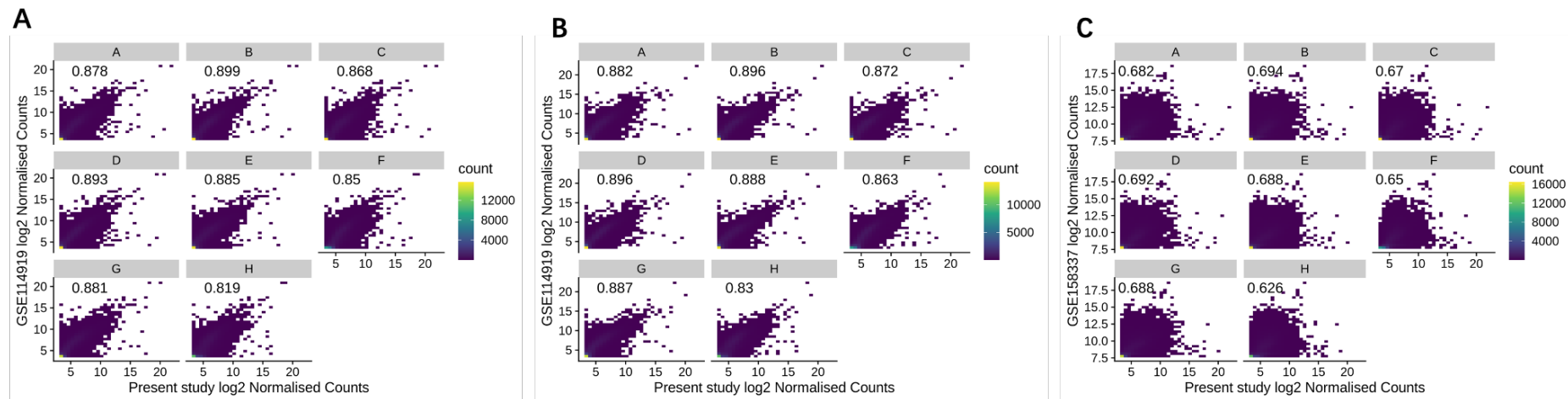
An example image of a haematoxylin & eosin stained (thickness 13 mm) cryosection was obtained from 7-d-old proximal tibia of a C57BL6 mouse (stored in OCT embedding compound at -80 °C). The cryosections were collected on membrane slides and stored at -20 °C. An example of section of the proliferative zone (e.g., a big proliferative section vs. a small proliferative section) was removed by targetted laser microdissection (LMD) and either stored in Smart-seq lysis buffer or directly subjected to RNA isolation using Zymo Direct-zol RNA microPrep Kit. RNA was 'isolated' as described in Table 4.5. Materials and methods section 2.2.9.

Table 4.5 The different sizes of laser dissected sections and treatments used for miRNA sequencing

Shortened form	Samples	Total reads (M)	Mapped	Genes with TPM > 1
A (Lysis buffer)	A big proliferative zone	50.1	19.9%	8628
B (Lysis buffer)	A small proliferative zone	35.6	10.8%	9293
C (Lysis buffer)	Big proliferative zone x 3	35.8	7.0%	6732
D (Lysis buffer)	Small proliferative zone x 3	38.7	8.0%	10209
E (Zymo)	A big proliferative zone	42.8	26.9%	10856
F (Zymo)	A small proliferative zone	44.7	13.8%	18280
G (Zymo)	Big proliferative zone x 3	51.4	30.5%	10846
H (Zymo)	Small proliferative zone x 3	37.2	12.3%	17352

Two different reagents were used to extract RNA for sequencing, they were Smart-seq lysis buffer (highlighted in grey) and Zymo Direct-zol RNA microPrep Kit (highlighted in orange), materials and methods section 2.2.9. For each treatment, four different sizes of sections were isolated sequencing as described. All eight groups were labelled from A to H. Total reads, percentage of mapped reads to mouse genes, and number of genes with a TPM > 1 of each group, are provided.

Figure 4.21 Comparison between our laser captured proliferative samples to published online data



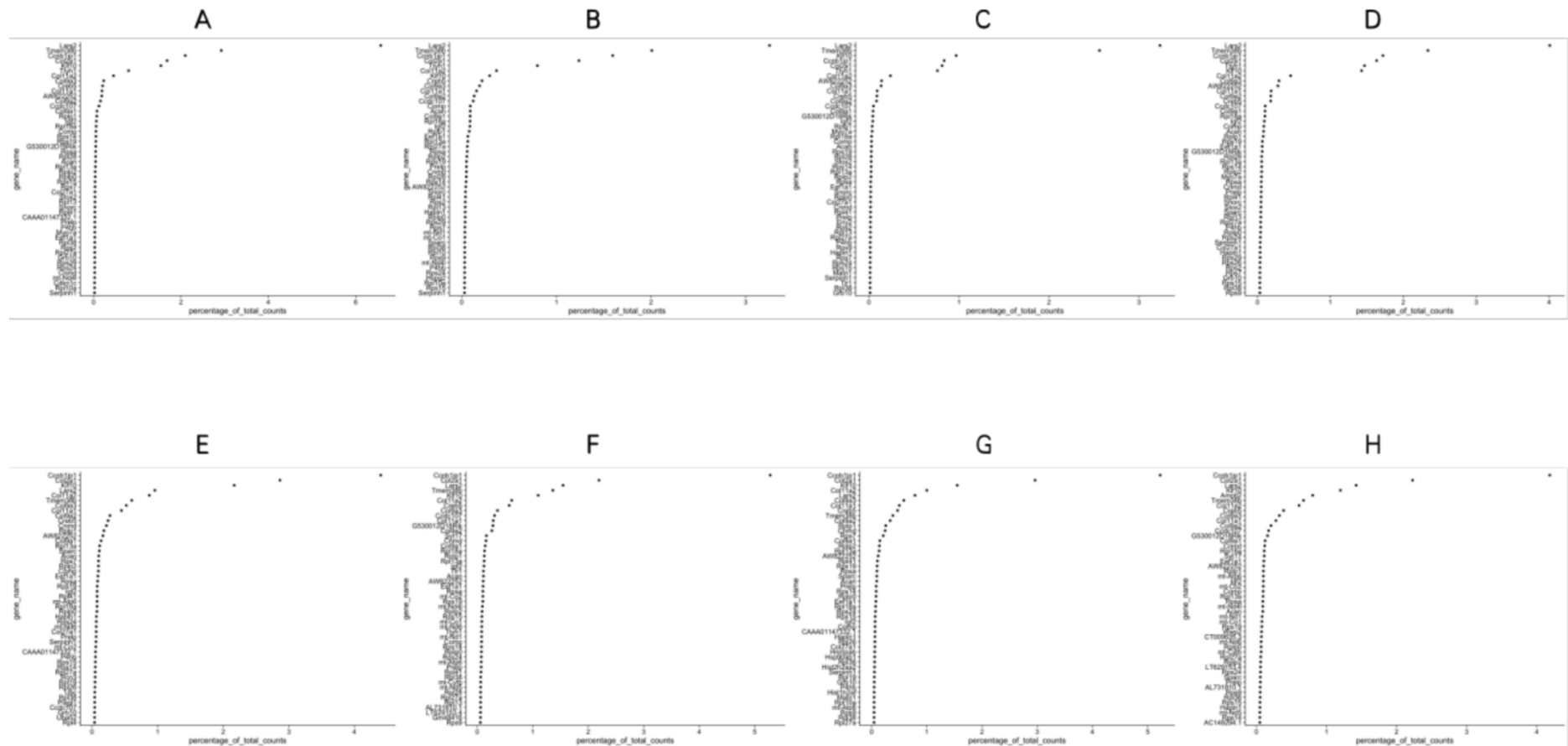
Comparison of our 1-week-old LMD tibial growth plate proliferative zone samples to the mean log2 normalised counts from published online data. The correlation plots were generated by Dr Jamie Soul. GSE114919 contains samples of 1-week-old mouse phalanx proliferative zone (A) and 1-week-old tibial proliferative zone (B). GSE158337 mouse hippocampus RNA-seq was used as an irrelevant tissue control (C). The data we selected were analysed using the same pipeline as our LMD RNA-seq we analysed (QC with fastqc, fastqscreen, trimming with trimmomatic, transcript quantification with kallisto, gene summarisation with tximport and normalisation of counts using DESeq2 with variance stabilising transformation). Scale (count) refers to the number of genes. Plots are colored by density and the text in each plot is the Pearson correlation coefficient.

Table 4.6 The top 50 ranked genes confirmed that dissected sections contain chondrocytes

Sample	Term (1 st ranking)	Overlap	P-value	Adjusted P-value	Genes
A	CHONDROCYTE	17/2316	2.61E-05	0.00278783	SPARC;LRP1;COL11A1;COL11A2;XYLT1;PRELP;HSPG2;THBS1;HAPLN1;COMP;ACAN;COL2A1;COL9A1;COL9A3;COL9A2;MATN3;CREB5
B	CHONDROCYTE	18/2316	6.07E-06	6.50E-04	SPARC;LRP1;COL11A1;COL11A2;PRELP;HSPG2;THBS1;HAPLN1;COMP;ACAN;COL2A1;COL9A1;COL9A3;CSPG4;COL9A2;FMOD;MATN3;CREB5
C	CHONDROCYTE	16/2316	1.03E-04	0.01109395	SPARC;COL11A1;COL11A2;PRELP;HSPG2;THBS1;HAPLN1;COMP;ACAN;COL2A1;COL9A1;COL9A3;COL9A2;FMOD;MATN3;CREB5
D	CHONDROCYTE	18/2316	6.07E-06	6.56E-04	SPARC;LRP1;COL11A1;COL11A2;PRELP;HSPG2;THBS1;HAPLN1;COMP;ACAN;COL2A1;COL9A1;COL9A3;CSPG4;COL9A2;FMOD;MATN3;CREB5
E	CHONDROCYTE	17/2316	2.61E-05	0.00273572	SPARC;LRP1;COL11A1;COL11A2;PRELP;HSPG2;THBS1;HAPLN1;COMP;ACAN;COL2A1;COL9A1;COL6A3;COL9A3;COL9A2;CREB5;PLEC
F	CHONDROCYTE	13/2316	3.72E-03	0.3906602	SPARC;COL11A1;COL11A2;PRELP;HSPG2;THBS1;COMP;ACAN;COL2A1;COL9A1;COL9A3;COL9A2;CREB5
G	CHONDROCYTE	18/2316	6.07E-06	6.32E-04	SPARC;LRP1;COL11A1;COL11A2;PRELP;HSPG2;THBS1;HAPLN1;COMP;C1QTNF3;ACAN;COL2A1;COL9A1;COL6A3;COL9A3;COL9A2;FMOD;CREB5
H	CHONDROCYTE	14/2316	1.23E-03	0.12057743	SPARC;COL11A1;COL11A2;PRELP;HSPG2;THBS1;COMP;ACAN;COL2A1;COL9A1;AMOTL2;COL9A3;COL9A2;CREB5

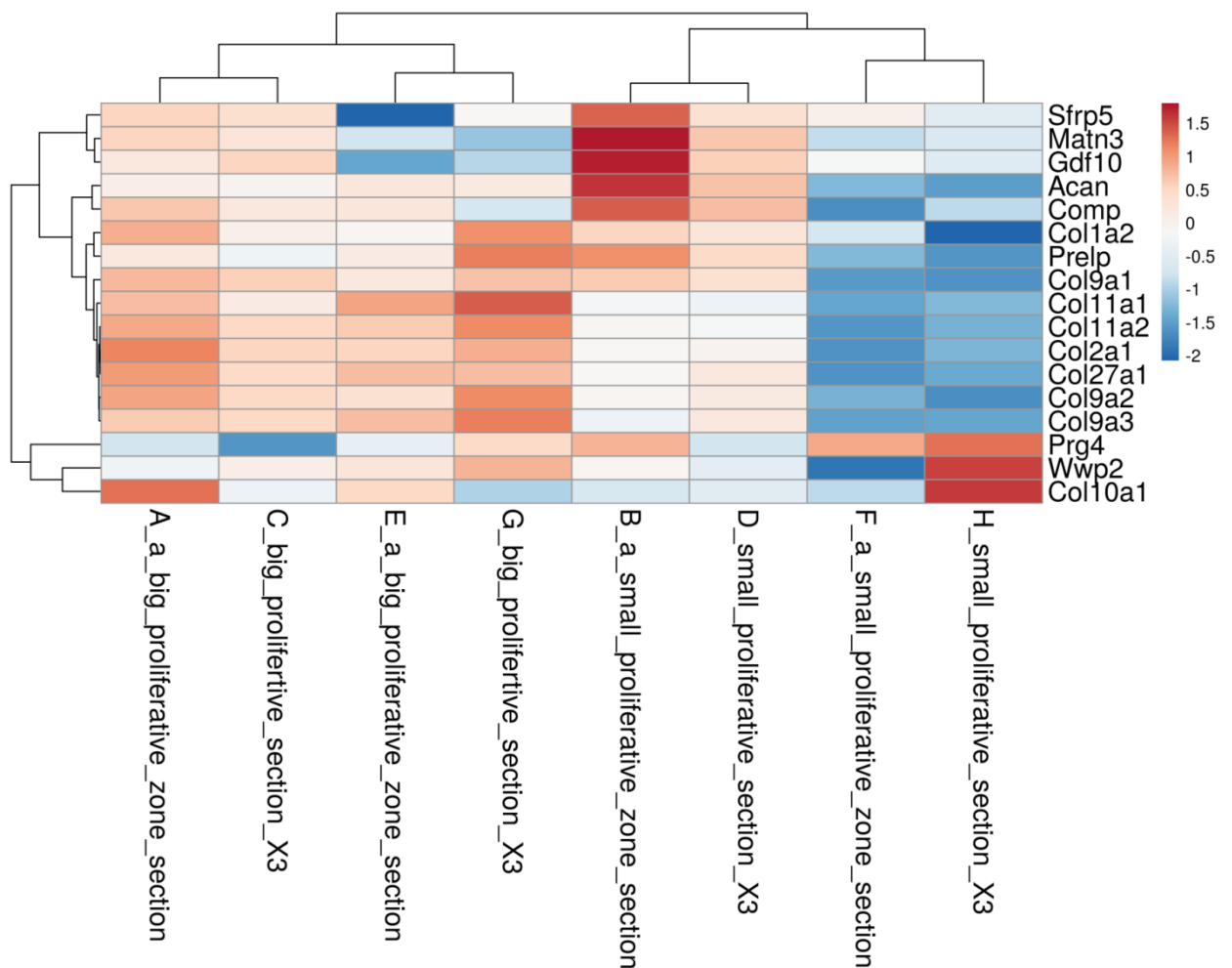
Top 50 ranked genes from each group were used for analysis using an online tool (<https://maayanlab.cloud/Enrichr/enrich>), the results showed that all eight groups are confirmed as chondrocytes. Details include p-value, adjusted p-value, and confirmed genes that overlap with 'mouse chondrocyte genes'.

Figure 4.22 Top 50 gene counts



The percentage of top 50 gene counts against total counts of each group were plotted in ranked order. Group B, G and H showed the smoothest distribution compared to other groups.

Figure 4.23 Expression of zone markers among the LMD groups



Articular cartilage and growth plate cartilage zone marker genes were selected for comparison between the samples. The normalised TPM of selected genes from different groups were used for analysis, using an online tool (<https://biit.cs.ut.ee/clustvis/>).

4. 3. Discussion

4. 3. 1. Screening and validation of miR-140 growth plate target genes

MiRNAs have attracted much attention in recent years. Studies have revealed roles of miRNAs in various biological processes including development, immunity, and diseases related biological process (Stefani and Slack 2008, Xiao and Rajewsky 2009). However, the mechanisms of miRNAs in those biological events remain poorly characterised, partially because of the difficulties in determining the direct targets of miRNAs (Chiba, Kurimoto et al. 2021). MiRNA transgenic mice have been widely used to elucidate the role of specific miRNA in tissue development and in determining target genes, including in cartilage. For example, Papaioannou *et al.* identified that cell cycle regulators cell division cycle 34 (Cdc34) and E2F transcription factor 5 (E2F5) are direct target of the highly conserved miRNA *let-7* in chondrocytes and are responsible for negatively regulating chondrocytes proliferation (Papaioannou, Inloes et al. 2013). Of particular interest here, Miyaki *et al.* validated *Adamts5* as a *Mir140* direct target in *Mir140* transgenic mice, which the authors propose would explain the spontaneous age-related OA phenotype in miR-140^{-/-} mice (Miyaki, Sato et al. 2010). Although many studies have focused on *Mir140* in cartilage, chondrocyte development and related diseases, there is still limited information about *Mir140* target genes.

In term of *Mir455* analysis, the upregulated genes were composed of the highest percentage of miR-455-3p.1 predicted targets relative to either miR-455-5p or miR-455-3p.2 (Fig. 4.16A), however, from the mean log2 fold-change data predicted miR-455-3p.2 targets had the largest increase in expression (Fig. 4.16B). We initially performed RNA-seq comparison between WT and *Mir455*-null costal chondrocytes from animal at P7 to screen miR-455 direct growth plate target genes, but none of candidate targets were validated by luciferase assay analysis. Similar to our combined analysis for miR-140 to better predict targets, additional *Mir455*-null (or overexpression) datasets would aid in the identification of targets. Only at the end of

the work on this thesis did we obtain knee RNA-seq from *Mir455*-null mice. Up-regulated genes in both datasets would be considered as strong potential direct targets. The reasonable proposal would be to focus more on miR-455-3p.1 target genes rather than miR-455-3p.2, since the former isomiR is the predominant strand in sRNA-seq data (miRbase analysis of 104 datasets (from various tissues) shows that miR-455-3p.1 is the significantly more abundant arm of miR-455), including in cartilage (Crowe, Swingler et al. 2016, Woods, Charlton et al. 2020), and is predicted to be the most functional from analysis by others (Zhang, Hou et al. 2015, Chen, Chen et al. 2016, Sun, Zhao et al. 2018, Hu, Zhao et al. 2019, Mao, Kang et al. 2019, Wen, Li et al. 2020) and during some of our target analysis here.

RNA-seq has rapidly developed during last the decade to provide an unbiased data to reveal the presence and quantity of the RNA transcriptome from separate samples at a given time point. Prior to initiating RNA-seq we confirmed that the mRNA expression of previous *Mir140* target genes *Adamts5* and *Dnpep* (data not shown, $p = 0.025$) were both significantly increased in RNA of our miR-140^{-/-} mice. We were also able get early access to an, at the time, unpublished RNA-seq dataset of WT and *Mir140*-null mice from Prof Kobayashi et al. (this data is now publicly available) (Grigelioniene, Suzuki et al. 2019). Their *Mir140*-null mice were generated by a standard gene targeting vector approach (Nakamura et al. 2011), and the phenotypic appearance of the mice is similar to our *Mir140*-null mice. However, subtle differences are possible between the two mouse lines. For example, RNA-seq data revealed that the mean TPM of *Zeb1* of our mice as much higher than in the mice Harvard University generated (Table 4.2). In addition, compared to our finding that BrdU labelled proliferative chondrocytes significantly decreased in the tibia of *Mir140*-null mice at P22, no significant proliferation defects were detected in their chondrocytes of their mice at P5.5. This could reflect a difference due to the day sampled, however, using RNA from P7 costal chondrocytes, mRNA expression level of *Pdgfra* (which has been validated as miR-140 target in zebrafish) (Eberhart, He et al. 2008) was not significantly changed in their *Mir140*-null mice, but is significantly

increased ($p < 0.0001$) in our animals. Our analysis of this data also provides us with several other potential miR-140 target genes to test in our RNA, all of which were confirmed upregulated in our null mouse samples. Once our RNA-seq was complete we initially compared the significance ranked data with that from Prof Kobayashi, which was highly correlative, especially in terms of genes upregulated following deletion of the miRNA. The overlapped portion of differentially expressed genes from 2 separate RNA-seq datasets provided stronger evidence for further identification of target genes.

Various computational prediction approaches mimic and weight different aspects of the interaction between miRNA and its targets, such as seed match, conservation, free energy, and site accessibility (Peterson, Thompson et al. 2014). The seed match is a Watson-Crick (WC) match between the first 2-8 nucleotides starting at the 5' end of miRNA and its target. The commonly used seed match types include: 1. 6mer: A perfect WC match between miRNA seed (6 nucleotides) and mRNA; 2. 7mer-m8: A perfect WC match between miRNA seed (from nucleotides 2-8) and mRNA; 3. 7mer-A1: A perfect WC match from nucleotides 2-7 of miRNA seed in addition to an adenine across from the miRNA nucleotide 1; 4. 8mer: A perfect WC match of the miRNA seed (from nucleotides 2-8) in addition to an adenine binding to the miRNA nucleotide 1. Conservation refers to miRNA seed region across the species while free energy means the stability between interaction between miRNA and mRNA. Site accessibility describes the ease of miRNA:mRNA hybridisation (Peterson, Thompson et al. 2014). Among the many prediction tools, both TargetScan and miRDB provide access to 3' complementary pairing (suitable for the method we used to identify miR-140/miR-455 targets in this project) in addition to the four commonly used features described above. Compared to miRDB, TargetScan provides users the ability to search 8mer, 7mer, and 6mer sites in the seed sequence of miRNA and to obtain predicted target efficacy in addition to allowing guanine (G): uracil (U) pairing in the seed (Agarwal, Bell et al. 2015, Wong and Wang 2015). Thus, we used TargetScan (v7.2) as the miRNA target prediction tool of choice. From this we initially obtained

30 miR-140 predicted significant differentially expressed target genes when applied with the rank-rank analysis. Based on cellular function(s) of these predicted miR-140 targets, we then selected 10 genes for further validation, *Creb3l1*, *Nrf2*, *Zeb1*, *Npr3*, *Fbn1*, *Med13*, *Tmem123*, *Ncstn*, *Abca1*, and *Golt1b*. Furthermore, we applied the significantly up-regulated genes in our mouse RNA-seq data to compare with miR-140 predicted targets from miRDB and TargetScan (v7.2), and we obtained 51 overlapped genes (data not shown). Importantly, of the 51 overlapped genes, 8 are confirmed as miR-140 target genes in our research include *Creb3l1*, *Med13*, *Npr3*, *Ncstn*, *Fbn1*, *Zeb1*, *Abca1*, *Nrf2*.

Many studies are limited by effective methods to precisely identify gene regulatory networks by altered miRNAs expression. MiRNA act as a specific guide for RNA-induced silence complex (RISC) factor Argonaute (AGO) to mRNA via sequence-specificity to mediate its posttranscriptional silencing and as such immunoprecipitation of miRNA-mRNA-AGO complexes can be used to identify direct targets. When applied with HITS-CLIP (high-throughput sequencing of RNAs isolated from crosslinking immunoprecipitation) or a modified CLIP technique termed CLEAR (covalent ligation of endogenous Argonaute-bound RNAs)-CLIP, mapping comparisons can be made between, for example, endogenous miRNA-mRNA-AGO complexes from WT and transgenic mice or overexpressed/inhibited miRNA in cells (Chi, Zang et al. 2009, Moore, Zhang et al. 2014, Moore, Scheel et al. 2015). Since endogenous RNAs could be regulated by multiple miRNAs, some of these methods fail to provide information about which miRNA led the incorporation of the mRNA within RISC. In addition, the precipitation of AGO from cell lysates, particularly primary cells, is challenging and may increase experimental noise, which subsequently affect downstream analysis (Majoros, Lekprasert et al. 2013, Wolter, Kotagama et al. 2014). In contrast, the dual luciferase reporter system is sensitive and calculable for measuring direct interactions between miRNA and 3'UTR of target mRNA containing either miRNA binding sites or mutant binding sites. Furthermore, since the 3'UTR construct is co-transfected with miRNA mimic in cells in culture, this

method also provides an opportunity to ‘simultaneously’ measure the expression of the target gene protein in extracts (Wolter, Kotagama et al. 2014). Thus because of its simplicity we chose to validate miR-140 additional growth plate direct targets using a luciferase reporter system.

We failed to validate target genes of miR-140-3p isomiRs (miR-140-3p.1 and miR-140-3p.2). In human cartilage miR-140-3p is more than 10-fold higher in abundance than miR-140-5p (Crowe, Swingler et al. 2016). However, mouse sRNA-seq data suggests that the read count of both miR-140-3p.1 and miR-140-3p.2 are lower than miR-140-5p (Chiang, Schoenfeld et al. 2010, Woods, Charlton et al. 2020). Our mouse RNA-seq data showed that the most enrichment for miR-140-5p 7m8 binding sites within up-regulated genes, over miR-140-3p.1 and miR-140-3p.2. MiR-140-3p.2 does not possess a U at position 2 of 5' isomiR, when compared to miR-140-3p.1, resulting in both a differing repertoire of targets for the isomiRs and a potential decrease in the miRNAs effectiveness on a single target (Manzano, Forte et al. 2015). In addition, miR-140-3p.1 and miR-140-3p.2 have 3' Adenine (A) additions, which are described to decrease targeting ability (Burroughs, Ando et al. 2010). Together, divergent 5' isomiRs and 3' A addition of miR-140-3p isomiRs probably contribute to a poor target repression of miR-140-3p when compared to miR-140-5p.

4. 3. 2. Exploring the role of selected miR-140 growth plate target genes

Predicted miR-140-5p target genes for further validation included *Creb3l1*, *Nrf2*, and *Zeb1*. The upregulation of these genes following miR-140 loss were validated in RNA from new litters of mice by real time qRT-PCR analysis. To confirm these genes to be direct targets of *Mir140* we used the classical 3'UTR luciferase assay, including the use of 3'UTR luciferase reporters where the miR-140-5p seed binding sequences were mutated. Finally, for these three targets we used immunoblot analysis, which (except for *Zeb1*) was able to confirm their regulation by miR-140. Having identified and validated in the abundance of these proteins could be in part responsible for the phenotype of the mice. One of the phenotypic consequences of loss of miR-140 was

a reduction in chondrocyte proliferation in the growth plate. *Creb3l1* has been proposed to be proteolytically cleaved in response to cellular stimuli, which allows its cleaved N-terminus to translocated into nucleus to induce multiple genes encoding cell cycle inhibitors thus blocking cell proliferation (Denard, Seemann et al. 2011). Therefore, we employed the WST-1 proliferation assay to elucidate the role of all three validated target genes in chondrocyte proliferation. Primary mouse chondrocytes isolated from the frontal part of rib cages of new-born mice express a fully differentiated phenotype in monolayer culture, containing high amounts of mRNA of cartilage-specific collagen II, IX, and X. Accordingly, the monolayer culture of mouse costal chondrocytes had been recommended to characterise the phenotypes of transgenic mice in studies of cartilage diseases where the mechanism involves chondrogenesis (Lefebvre, Garofalo et al. 1994). Thus, a large number of studies focused on the function of miRNAs in OA or in endochondral bone development adapted this primary cell culture system (Miyaki, Sato et al. 2010, Nakamura, Inloes et al. 2011, Papaioannou, Inloes et al. 2013, Grigelioniene, Suzuki et al. 2019). Therefore similarly, we utilised primary mouse costal chondrocytes to explore the function of miR-140-5p growth plate targets in cell proliferation. However, after 1 or 2 weeks in culture (or after 3 passages) the levels of cartilage-specific mRNA in these cells decreases progressively, accompanied with an increase in the amount of collagen I mRNA, indicating differentiation with the chondrocytes finally becoming fibroblast-like cells (Lefebvre, Garofalo et al. 1994). Therefore, we only passaged the costal cells at most twice (P2) to go through the WST-1 cell proliferation assay experiments. The mechanism of using WST-1 cell proliferation assay for spectrophotometric quantification is described in Chapter 2, section 2.2.3.12. in principle, the greater the number of viable cells (metabolically active cells), the greater the absorbance obtained. In the *Mir140*-null chondrocytes, downregulation of *Creb3l1* or *Nrf2* resulted in a significantly higher proliferation activity (higher values of absorbance) in mouse costal chondrocytes, suggesting *Creb3l1* or *Nrf2*, as a direct target of *Mir-140*, negatively control the proliferation activity of chondrocytes, but the mechanism that *Creb3l1* and *Nrf2* regulate

proliferation is still not clear. Although the WST-1 assay is highly sensitive and simple to perform for detection of cell proliferative activity *in vitro*, it is actually monitoring mitochondrial activity instead of cell proliferation. Furthermore, inaccurate results might be obtained due to its overestimation of cell viability. Since our BrdU assay showed very comparable differences of growth plate proliferative chondrocytes between genotypes, also performing a BrdU assay, as an additional method, to assess cell proliferation *in vitro*. Other methods, including flow cytometric methods could also be used.

4. 3. 3. Screening and validation of miR-455 growth plate target genes

Similar to the miR-140 RNA-seq, we obtained our miR-455 RNA-seq data from RNA of costal chondrocytes of WT and *Mir455*-null mice. However, there were less significantly differentially expressed genes when comparably filtered to our miR-140 RNA-seq analysis. This would be expected since the skeletal phenotype of our *Mir455*-null mice is milder than *Mir140*-null mice and because fewer samples were sequenced. Since we and others found that the Safranin-O staining on *Mir455*-null mouse knee cartilage is less than that of WT mice, we then selected *Acan* as a miR-455 potential target, even though it is not predicted as a miR-455 target from TargetScan (v7.2) (Mao, Kang et al. 2019, Wen, Li et al. 2020). Both *ppp1r10* and *Chst11* were highly expressed in our miR-455 RNA-seq data and are predicted as both miR-455-3p.1 and miR-455-3p.2 targets from TargetScan (v7.2). However, we were unable to validate these genes as miR-455-3p.1 direct target from dual luciferase reporter analysis. Furthermore, we obtained an RNA-seq data from 12-week-old knee cartilage chondrocytes of WT and *Mir455*-null mice. We then compared this with our miR-455 rib RNA-seq data via the Rank-rank analysis (Fig. 4.17), which gave overlapping genes that were differently upregulated in both knee and costal chondrocytes, including *Chst11* and *Ppp1r10*. Again, further techniques such as AGO-HITS-CLIP or CLEAR-CLIP could be better at identifying miR-455 targets. Additionally, recently a luciferase reporter library system has been successfully

applied to screen target genes of specific miRNAs including miR-455, identifying *EPAS1* as a target gene of miR-455 (Ito, Matsuzaki et al. 2021). However, since the COVID-19 pandemic shut-down our laboratory we were unable to proceed to further identify and validate potential miR-455 targets.

4. 3. 4. An optimised methodology developed to assess the impact of *Mir140* loss

in proliferative zone cartilage using LMD

Previously published work has confirmed that microdissection methods allow us to better understand gene expression patterns and cartilage development in the growth plate through isolation of zonal tissue (Belluoccio, Bernardo et al. 2008, Belluoccio, Etich et al. 2010, James, Stanton et al. 2010). We used LMD followed by RNA-seq to profile expression patterns of genes in the growth plate proliferative chondrocytes using different numbers of captured cells and two different purification techniques. When comparing our results to online published data, we found that our data better correlated with data from 1-week-old mouse tibial proliferative zone than to data from 1-week-old mouse phalanx proliferative zone (average correlation coefficients of 0.877 and 0.872 when compared to tibia proliferative zone or phalanx proliferative zones, respectively). Although still relatively well correlated, the values when our data was compared to that of an irrelevant tissue (hippocampus) were much lower (average 0.674), adding confidence that we were reliably detecting growth plate proliferative zone gene expression. Our results confirmed that all the groups contained chondrocytes, but group G (Zymo + three big proliferative sections) overall had several key advantages over the other groups. Group G gave the lowest adjusted *p*-value on verification that the isolated cells were chondrocytes. Additionally, group G gave the highest percentage of mapped reads (group C has the lowest percentage of mapped reads, the average percentage of mapped reads of samples using Direct-zol RNA MicroPrep Kit was 23.4%, however, the average percentage of mapped reads of samples using Smart-seq lysis buffer was 11.4%) and showed robust expression of proliferative

marker genes, *Prelp* and *Gdf10*, as well as high expression of several collagen genes which typify the proliferative growth plate, but with low expression of the hypertrophic zonal specific collagen, *Col10a1*. The precise isolation and enrichment of the proliferative zone would be required to identify differences in gene expression following *Mir140* loss, important since the microRNA is generally considered to be most specifically expressed in this zone in the growth plate. Of course, a major limitation of our study is that each condition was only performed once, due to the cost of optimisation, however, taken together, using the Direct-zol RNA MicroPrep Kit to extract RNA from laser dissected growth plate sections, combined with using three large histological sections would be the most efficient method to profile the expression of growth plate zonal genes for future study.

4.3.5. Summary

To summarise, we have evidence that 9 genes are miR-140-5p direct target genes in growth plate, however, the role of those genes in endochondral bone and cartilage development is still elusive. *Npr3*^{-/-} mice exhibit dome-shaped skulls, elongated femurs, tibias, tails, and body length (Matsukawa, Grzesik et al. 1999), a skeletal phenotype contrary to *Mir140*-null mice. However, *OASIS*^{-/-} mice are short in stature and have a lower bone mineral density (BMD) at the age of 12-week-old than age-matched controls (Murakami, Hino et al. 2011). After validating differential expression of targets by immunocytochemistry, a logical next step to confirm if a predicted target gene is responsible for phenotype of the *Mir140*-null mice would be to genetically delete/repress these targets in the *Mir140*-null background. For example, though *Adamts5* was confirmed as a miR-140 target gene, which could be a part of reason of that *Mir140*-null mice showed age-related OA-like changes in knee cartilage (Miyaki, Sato et al. 2010), *Adamts5*-null mice are phenotypically normal and indistinguishable from their littermate controls and thus may not explain the phenotype of *Mir140*-null mice (Stanton, Rogerson et al. 2005). In zebrafish, *Pdgfra* was validated as a miR-140 target and was identified as directly responsible for the

platatogenesis phenotype of the *Mirn140*-null fish (Eberhart, He et al. 2008). However, chondrocyte-specific depletion of *Pdgfra* in mice causes only a mild shortening in the longitudinal length of skull and this deletion in *Mir140*-null mice was not able to rescue the long bones growth defect of these animals (Nakamura, Inloes et al. 2011). Accordingly, in order to understand mechanisms of miR-140 in endochondral bone development and OA pathogenesis, validation of additional miR-140 target genes is required. To precisely down-size the range of miR-140 or miR-455 potential target genes, combinations of multiple RNA-seq analysis (ie. Rib RNA-seq vs knee RNA-seq or deletion/overexpress of specific microRNA in human/mouse cells + RNA-seq, etc) and target validation techniques are required. Thus, in addition to isolating RNA from knee cartilage of WT and genetically modified mice (*Mir140*-null, *Mir455*-null, and DKO) before and/or post DMM surgery (Chapter 5), our intention was to isolate and sequence RNA from differing zones of the tibial growth plate, but concentrating on the proliferative zone, of WT and *Mir140*-null mice using laser microdissection, with the aim of identifying targets in cells where miR-140 would be predicted to be most functional. However, this experiment was stymied by the global Covid-19 pandemic. Together, we anticipate that combining various methods, cells and development stages, coupled with our mouse costal chondrocyte RNA-seq, could be an effective method to better understand the role of miRNAs in chondrocyte development, cartilage homeostasis and OA pathogenesis.

Chapter 5. *Identification the role of Mir140 and Mir455 in murine knee cartilage*

5. 1. Introduction

Evaluating the progression of knee OA is challenging because many factors (e.g., age, gender, environment factors, diet, activity, and genetic susceptibility) are involved in pathogenesis of the disease and the degree of participation of these factors varies between individuals (McNulty, Loeser et al. 2011). Previous studies have demonstrated that aged C57BL/6 mice spontaneously developed OA (Sokoloff 1956, Silberberg and Silberberg 1962, Kwok, Onuma et al. 2016), and C57BL/6 mice with miR-140 depletion indeed developed more severe OA characteristics (Miyaki, Sato et al. 2010). Accumulating studies revealed that murine OA exhibits the similar histological features as the human OA, which are characterised as loss staining of proteoglycan, fibrillation, vertical clefts, erosion and denudation of cartilage matrix (Glasson, Chambers et al. 2010). This is despite the fact that the human knee joint bears much more weight and different directions of joint forces than the murine knee joint. Thus, a better understanding of mechanisms of murine OA model will impart us an analogous example to study human OA development. In addition, transgenic murine models of OA have been widely adopted in research to replicate the genetic impact on OA development (Vincent 2020). Mice afford a more uniform, and thin knee cartilage for which OA can rapidly progresses OA without the need for disruption of other factors involved during human knee cartilage OA, thus offering a better way to understand the critical role of genetic factor on OA progression.

To date, new advanced techniques were applied to evaluate the severity of knee OA progression, such as radiographic biomarkers (Lim, Wen et al. 2020). Histological assessment, a classic method, is widely used for evaluating murine and human OA severity, though recently a more advanced imaging methodology has been described (Butterfield, Curry et al. 2021). The standard current OA assessment histological

methods have drawbacks in reliability and reproducibility, thus, accurate and consistent OA histological assessments are required in to study the effects of interventions on progression, prevention and treatment of the disease. To date, several histological assessments of knee joint have been used in various human and murine studies, including the Mankin Histological-Histochemical Grading System (HHGS), the Osteoarthritis Research Society International (OARSI) scoring system, the OARSI osteoarthritis cartilage histopathology assessment system (OOCHAS), and a scheme developed by McNulty *et al.* (McNulty, Loeser *et al.* 2011). The Mankin HHGS scheme has been the most extensively used in many animal models for evaluating OA severity (with score ranging from 0 (normal) to 14(severe)), but the scheme has low specificity and is neither reliable nor reproducible identified in human Knee samples (Ostergaard, Andersen *et al.* 1999, Moussavi-Harami, Pedersen *et al.* 2009). The OARSI scoring system (system 1) was subsequently developed to provide a simple and rapid method to identify the site of cartilage lesion within the joint with scores ranging from 0 to 6 for the medial and lateral femoral condyles and tibial plateaus. However, this method is insufficient to provide the information regarding the depth of cartilage damage (Glasson, Chambers *et al.* 2010). In contrast, OOCHAS (system 2) provides clinical and experiment OA assessments for both the depth of cartilage lesion (grade range 0-6) and the horizontal extent of the cartilage lesion (range 0-4). Thus, the 2 independent grades obtained from each section are combined to generate a final score (score = grade x stage) to reflect OA severity (Pritzker, Gay *et al.* 2006). Similarly, McNulty *et al.* established another histological scoring system (system 3) to comprehensively and semi-quantitatively identify the cartilage lesions of mice knee OA that either naturally occurred or surgically induced. For this system, articular cartilage is valued using a combination of abnormality of articular cartilage structure score (ACS, range from 0-12) and Safranin-O staining score (Safranin-O, range from 0-12) (McNulty, Loeser *et al.* 2011).

Growth plate and articular cartilage are relatively independent tissue but arise from a common cartilaginous condensation (described in section 1.2.2), and both tissues

have comparable spatial architectures of chondrocytes arrangements (growth plate cartilage: resting, proliferative and hypertrophic zones; articular cartilage: superficial, middle and deep zones). We have provided a methodology to capture tissue from the growth plate proliferative zone using laser-microdissection and then subjected to RNA-seq (see Chapter 4). Furthermore, to investigate the similarities and differences between growth plate and articular cartilage transcriptional changes in the absence of either *Mir140*, and/or *Mir455* and to validate *Mir140* and *Mir455* articular cartilage target genes, we performed manual dissection of 11-week-old WT and microRNA-null mice knee articular cartilage, RNA-seq analysis and bioinformatics. In addition, we also performed a DMM-time course RNA-seq for *Mir140*-null and age-matched mice, bioinformatic analysis was followed to visualise the role of miR-140 during OA pathology.

Chapter aims:

1. Compare DMM-induced damage amongst four different genotypes (WT, *Mir-140*-null, *Mir-455*-null, and DKO mice).
2. To optimise a DMM-induced damage assessment that fits our demands of a reliable, reproducible and adequate grade range.
3. To generate and analyse a gene expression DMM-timecourse of dissected cartilage in WT and miR-140^{-/-} mice to establish the role of the miRNA in disease progression.
4. To compare the knee cartilage transcriptome of our miR-null mice with either comparable growth plate datasets (Chapter 4).

5. 2. Results

5. 2. 1. RNA-seq data analysis of miR-140^{-/-} mice 11-week-old medial knee articular cartilage

As described in section 2.2.8.1 (Chapter 2) was dissected the MTP articular cartilage away from the underlying bone (Fig. 5.1) and isolated RNA using the miRVana protocol as described. This method does not isolate pure articular cartilage and does contain contamination by bone, which we confirmed histologically. However, overall we felt the results would be less variable than taking the ‘whole joint’ forward for analysis as others have done previously (Burleigh, Chanalaris et al. 2012).

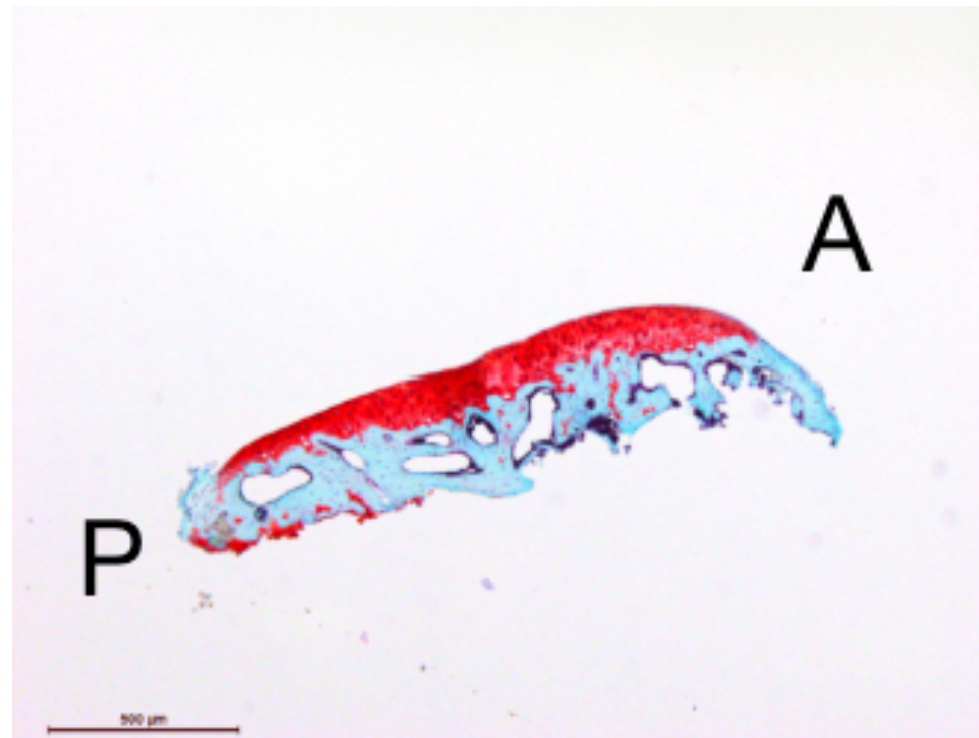
RNA was extracted from 11-week-old murine knee cartilage (Pre-DMM) and went through RNA-seq to obtain a quantitative and unbiased identification of differentially expressed genes (DEGs) in knee cartilage chondrocytes resulting from the ablation of *Mir140*. All RNA was DNase treated and passed QC. Sequencing was performed by the Genomic Core Facility (Newcastle University) and analysis was done with the help of Dr Jamie Soul (Skeletal research group, Newcastle University). DEG analysis identified 51 up- and 46 down-regulated genes with a fold change > 1.5 and FDR threshold ≤ 0.05 in the comparison of *Mir140*-null mice vs. WT mice (blue dots in the volcano plot in Fig. 5.2A).

Theoretically, *Mir140* knee cartilage targets should be enriched within significantly upregulated genes. When comparing target prediction data (TargetScan 7.2; conserved) to the RNA-seq results of knee chondrocytes, only one predicated miR-140-5p target gene (*Cemip*) was significantly differentially expressed, but this was actually downregulated in *Mir140*-null knee cartilage (Fig. 5.2B-left). There are no predicted miR-140-3p.1 or miR-140-3p.2 target genes that passed our significance threshold when comparing the WT versus *Mir140*-null knee cartilage data (Fig.5.2B-middle and right).

Given that only 138 genes were significant differentially expressed genes (FDR threshold ≤ 0.05), a heatmap was generated to visualise the differences of gene expression between WT and *Mir140*-null mice (Fig. 5.3). unsurprisingly, the differentially expressed genes caused clear hierarchical separation of WT and *Mir140*-null samples.

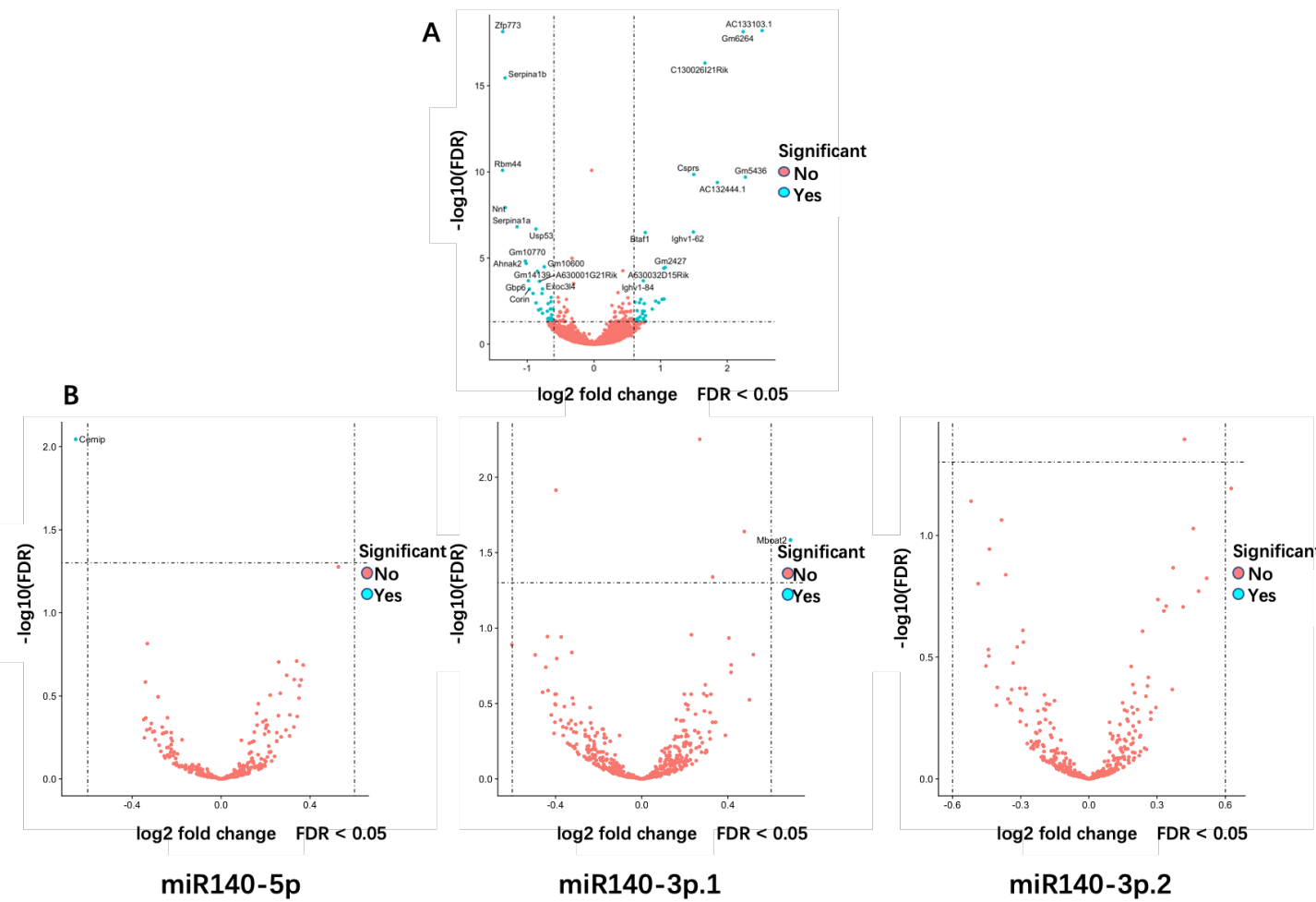
Gene Set Enrichment Analysis (GSEA) was used as pathway analysis to compare between WT and *Mir140*-null mice. Pathways with a False discovery rate values (FDR) below 0.05 were classified as GSEA significant. In total 254 gene pathways were enriched in the up-regulated genes in our *Mir140*-null mice when compared to WT mice, in contrast, 55 gene pathways were enriched for down-regulated genes in *Mir140*-null mice. Only one pathway was significantly enriched in up-regulated genes in *Mir140*-null knee cartilage: 'cellular senescence' (due to the presence of genes: *Rb1*, *Hist1h1a*, *Hist2h2aa1*, *Ccne2*, *Ccne1*). Two pathways were significantly enriched in the down-regulated genes in *Mir140*-null knee cartilage: 'collagen degradation' (*Col10a1*, *Col4a3*, *Col12a1*, *Col8a2*, *Col4a4*, *Mmp2*, *Mmp13*, *Col5a3*, *Col3a1*, *Col13a1*, *Col6a3*, *Col6a1*, *Col5a1*, *Col5a2*, *Furin*, *Col6a2*, *Col4a1*, *Mmp14*, *Col1a2*); and 'degradation of extracellular matrix' (*Col10a1*, *Col4a3*, *Col12a1*, *Col8a2*, *Col4a4*, *Mmp2*, *Capn2*, *Mmp13*, *Col5a3*, *Col3a1*, *Capn3*, *Col13a1*, *Ctss*, *Fbn1*, *Col6a3*, *Timp1*, *Col6a1*, *Lamc2*, *Col5a1*, *Scube1*, *Col5a2*, *Furin*, *Adamts5*, *Timp2*, *Col6a2*, *Col4a1*, *Hspg2*, *Mmp14*, *Fn1*, *Bcan*, *Col1a2*, *Adamts4*, *Lama3*, *Dcn*, *Ctsk*) (Fig. 5.4). The significantly enriched gene pathways are closely correlated with extracellular matrix (ECM) proteins, but the direction was the opposite to our hypothesis. The significant enriched in the up-regulated genes of the cellular senescence pathway, may subsequently affect the synthesis of ECM protein and of itself is well linked to osteoarthritis (Coryell, Diekman et al. 2021). Collectively, these data indicate that miR-140 potentially plays multiple complex roles in murine knee cartilage to balance ECM homeostasis.

Figure 5.1 Histological assessment of articular cartilage isolation for RNA-seq analysis.



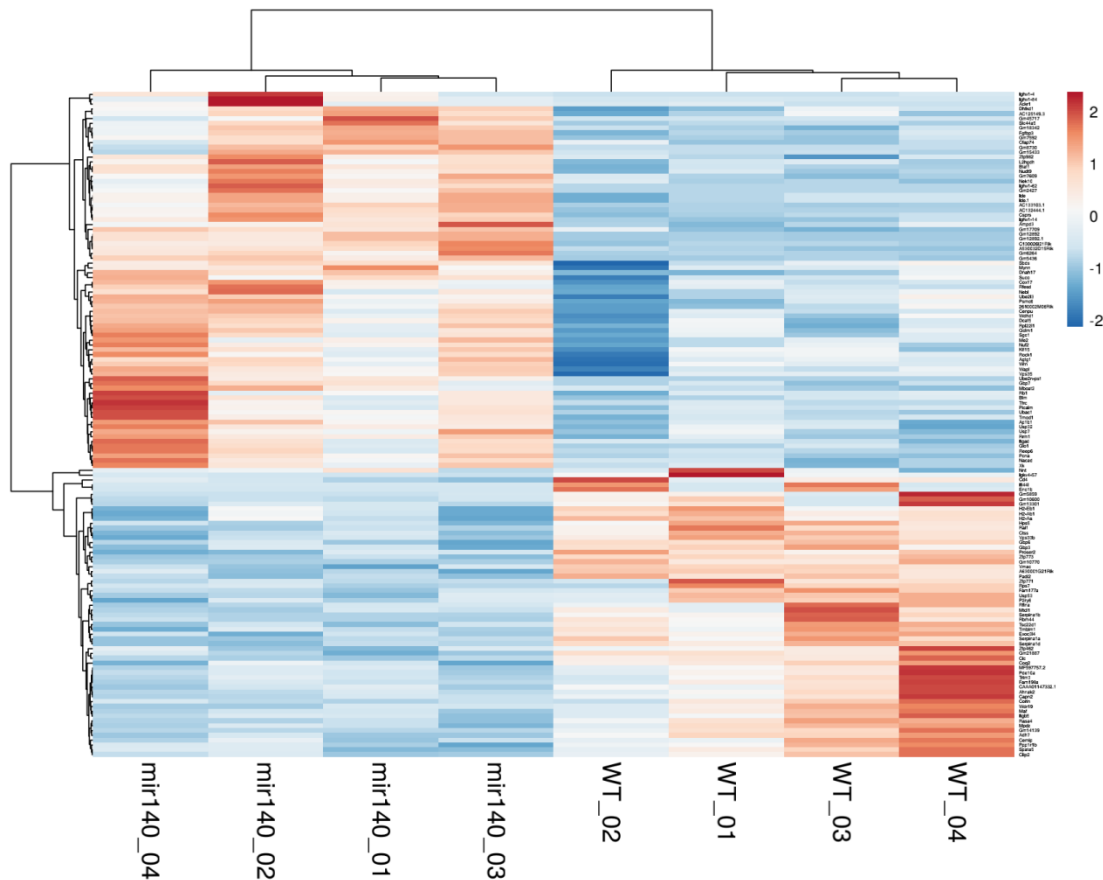
Medial MTP cartilage was isolated from male mouse 1-day pre-DMM, 3-, 7-, and 42-days post-DMM surgery at 11-week-old by Hua Lin (SRG, Newcastle University). We attempted to clean and remove bone marrow and bone tissue as much as possible, and the whole isolation process was completed with 5 min to avoid RNA degradation. A represents anterior of medial tibial knee cartilage, and P and A represent the posterior and anterior respectively of medial tibial knee cartilage, scale bar = 500 μ m.

Figure 5.2 The disruption of differentially expressed genes in *Mir140*-null murine knee cartilage relative to control mice



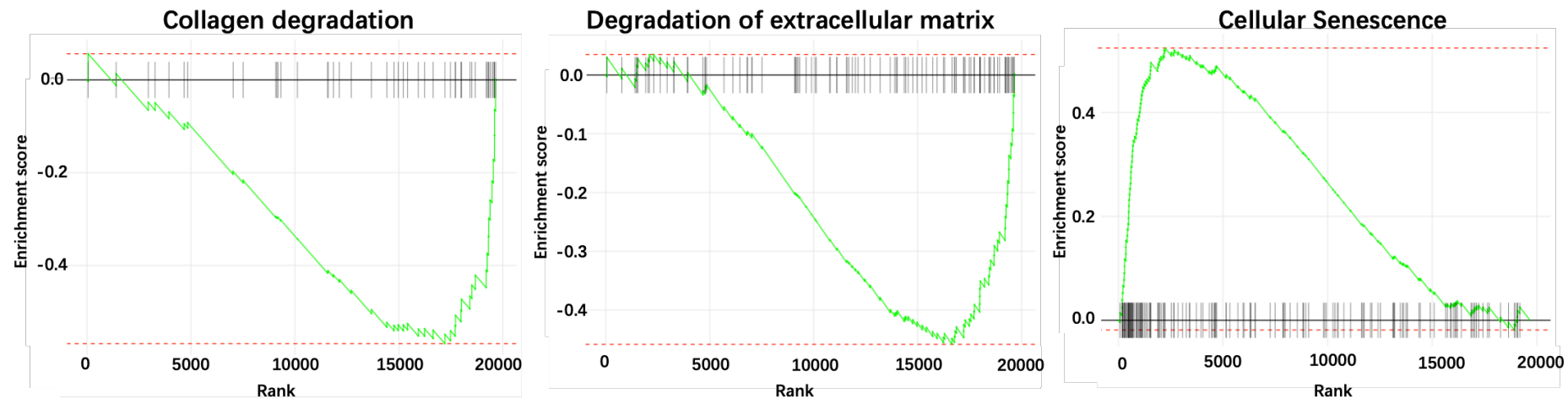
(A) A Volcano plot of gene fold-change (Log_2 , X axis) against $-\text{Log}_{10}$ FDR (false discovery rate, Y axis) between miR-140^{-/-} and WT, demonstrating the distribution of upregulated genes and downregulated genes. The vertical red lines correspond to $\pm 0.6 \text{ log}_2$ foldchange (equivalent to 1.5-fold change). The red horizontal line denotes an FDR of 0.05. Red points represent all significantly differentially expressed genes with an FDR p value ≤ 0.05 and fold change ≥ 1.5 . In total, 97 genes were found to be significantly downregulated and 51 genes to be significantly upregulated in miR-140^{-/-} mice. (B) Volcano plots demonstrating the significantly up-regulated and down-regulated predicted target genes of miR-140 (miR-140-5p (left), miR-140-3p.1 (centre), and miR-140-3p.2 (right)) in miR-140^{-/-} 11-week-old cartilage. The volcano plots were generated in R studio.

Figure 5.3 Profile of significant differentially expressed genes expression in murine knee cartilage between WT and *Mir140*-null mice



Heatmap of the relative expression of the top 138 differentially expressed genes (FDR ≤ 0.05) in WT versus *Mir140*-null knee cartilage (n=4/genotype). Heatmap was generated using an online tool known as ClustVis, which uses internally pheatmap R package (version 0.7.7) for plotting this heatmap. The TPM of each gene per mouse was chosen as the source of data import. Both rows and columns in this plot were clustered using correlation distance and average linkage.

Figure 5.4 GSEA enrichment of miR-140^{-/-} gene sets in mouse knee cartilage RNA-seq data



Enrichment analysis on GSEA results (FDR q-value < 0.05) showing affected cellular programs in *Mir140*-null knee cartilage. ‘Collagen degradation’ and ‘degradation of extracellular matrix’ pathways are significantly enriched in the down-regulated genes in miR-140^{-/-} mice when compared to WT mice. However, the ‘cellular senescence’ pathway is significantly enriched in the up-regulated genes in miR-140^{-/-} mice.

5.2.2. RNA-seq data analysis of miR-455^{-/-} mice 11-week-old medial knee

articular cartilage

Essentially as described in section 5.2.3 cartilage and RNA was extracted from knee cartilage of 11-week-old miR-455^{-/-} mice and underwent RNA-seq. DEG analysis identified 21 up- and 6 down-regulated genes with a fold change > 1.5 and FDR threshold ≤ 0.05 in the comparison of *Mir455*-null mice vs. WT mice (blue dots in the volcano plot in Fig. 5.5A). *Mir455* knee cartilage targets should be enriched within significantly upregulated genes.

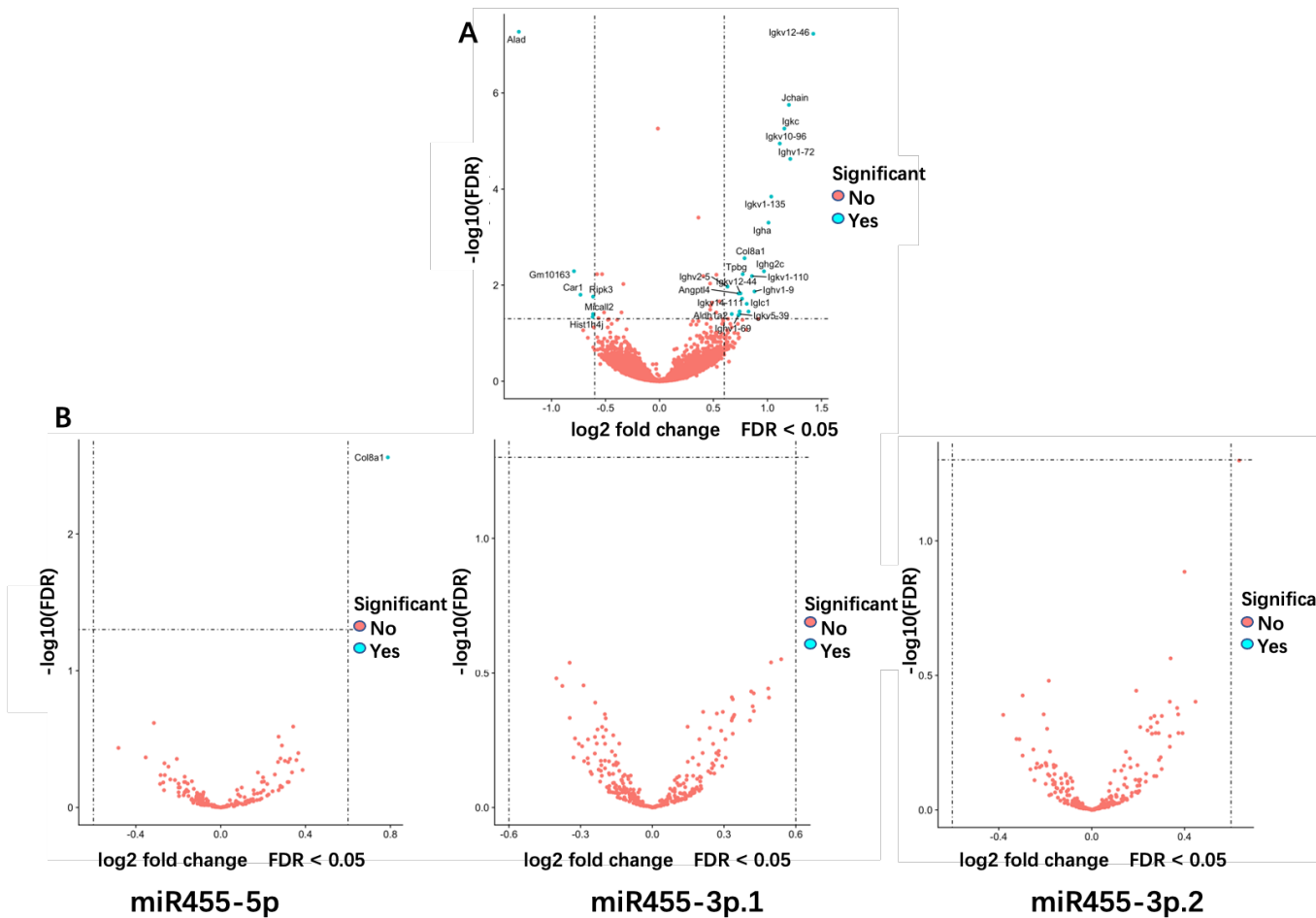
Theoretically, *Mir455* knee cartilage targets should be enriched within significantly upregulated genes. When comparing target prediction data (TargetScan 7.2; conserved) to the RNA-seq results of knee chondrocytes, only one predicated miR-455-5p target gene (*Col8a1*) was significantly differentially expressed, but this was actually downregulated in *Mir455*-null knee cartilage (Fig. 5.5B-left). There are no predicted miR-455-3p.1 or miR-455-3p.2 target genes that passed our significance threshold when comparing the WT versus *Mir455*-null knee cartilage data (Fig. 5.5B-middle and right).

Given that only 45 genes were significant differentially expressed genes (FDR threshold ≤ 0.05), a heatmap was generated to visualise the differences of gene expression between WT and *Mir455*-null mice (Fig. 5.6). unsurprisingly, the differentially expressed genes caused clear hierarchical separation of WT and *Mir455*-null samples.

Gene Set Enrichment Analysis (GSEA) was used as pathway analysis to compare between WT and *Mir455*-null mice. Pathways with a False discovery rate values (FDR) below 0.05 were classified as GSEA significant. In total 47 gene pathways were enriched for up-regulated genes in our *Mir455*-null mice when compared to WT mice. Three pathways were significantly enriched in the down-regulated genes in *Mir455*-null knee cartilage: 'collagen degradation' (*Col8a1*, *Mmp15*, *Col18a1*,

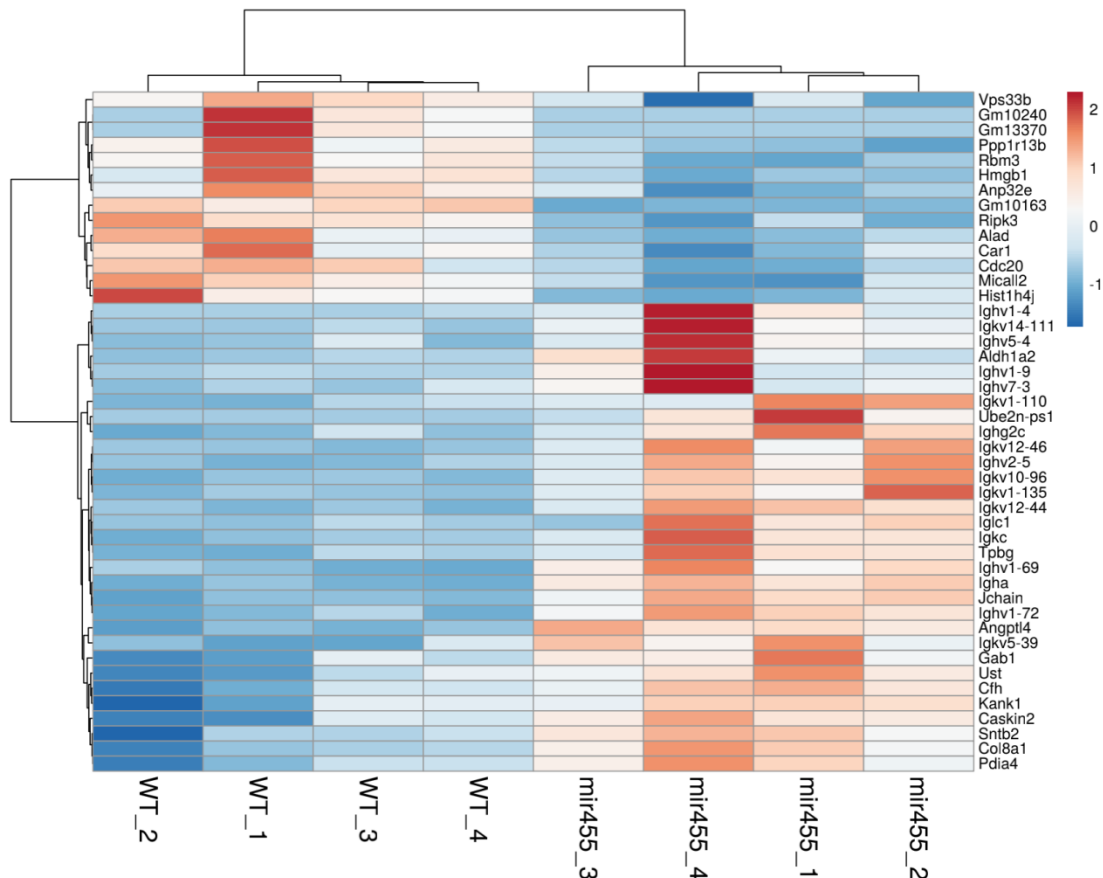
Mmp14, Col15a1, Col6a2, Mmp13, Mmp8, Col4a2, Col10a1, Col6a1, Col6a3, Col5a1, Mmp9, Col4a1, Mmp2, Col5a2, Col1a1); ‘degradation of the extracellular matrix’ (due to the presence of genes: *Col8a1, Mmp15, Scube3, Capn11, Fbn1, Eln, Col18a1, Scube1, Mmp14, Col15a1, Fbn2, Adamts4, Col6a2, Dcn, Mmp13, Adam15, Spp1, Mmp8*); and ‘activation of matrix metalloproteinase’ (*Mmp15, Col18a1, Mmp14, Mmp13, Mmp8, Mmp17, Timp2, Mmp9, Mmp24, Mmp2, Klkb1*) (Fig. 5.7). These significantly enriched gene pathways are closely correlated with degradation of extracellular matrix (ECM) proteins. Our DMM histological staining showed that miR-455^{-/-} mice displayed accelerated post-traumatic knee OA-like changes characterised as proteoglycan loss of articular cartilage (Chapter 5, 2.5.2). Collectively, these data indicate that miR-455 potentially plays multiple complex roles in murine knee cartilage to accelerate degradation of ECM proteins.

Figure 5.5 The disruption of differentially expressed genes in *Mir455*-null murine knee cartilage relative to control mice



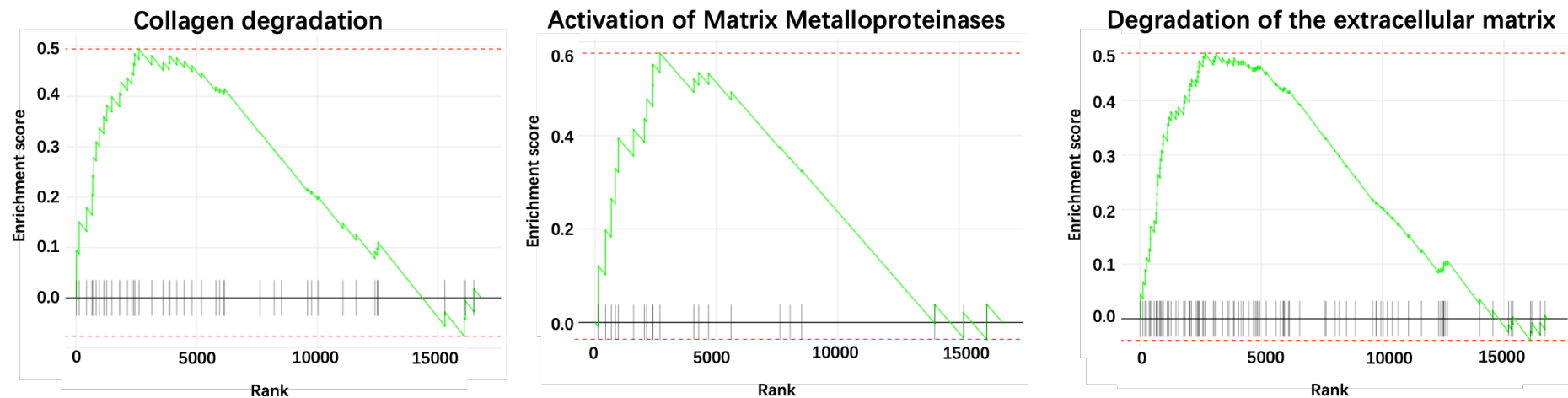
(A) A Volcano plot of gene fold-change (Log_2 , X axis) against $-\text{Log}_{10}$ FDR (false discovery rate, Y axis) between miR-455^{-/-} and WT, demonstrating the distribution of upregulated genes and downregulated genes. The vertical red lines correspond to $\pm 0.6 \text{ log}_2$ foldchange (equivalent to 1.5-fold change). The red horizontal line denotes an FDR of 0.05. Red points represent all significantly differentially expressed genes with an FDR p value ≤ 0.05 and fold change ≥ 1.5 . In total, 27 genes were found to be significantly downregulated and 21 genes to be significantly upregulated in miR-455^{-/-} mice. (B) Volcano plots demonstrating the significantly up-regulated and down-regulated predicted target genes of miR-455 (miR-455-5p (left), miR-455-3p.1 (centre), and miR-455-3p.2 (right)) in miR-455^{-/-} 11-week-old cartilage. The volcano plots were generated in R studio.

Figure 5.6 Profile of significant differentially expressed genes expression in murine knee cartilage between WT and *Mir455*-null mice



Heatmap of the relative expression of the top 45 differentially expressed genes (FDR ≤ 0.05) in WT versus *Mir455*-null knee cartilage (n=4/genotype). Heatmap was generated as previously described.

Figure 5.7 GSEA enrichment of miR-455^{-/-} gene sets in mouse knee cartilage RNA-seq data



Gene Set Enrichment Analysis (FDR q-value < 0.05) showing affected cellular programs in *Mir455*-null knee cartilage. ‘Collagen degradation’, ‘Activation of matrix metalloproteinase’ and ‘Collagen degradation’ pathways are significantly enriched in the up-regulated genes in miR-455^{-/-} mice when compared to WT mice.

5.2.3. RNA-seq data analysis of DKO mice 11-week-old medial knee articular cartilage

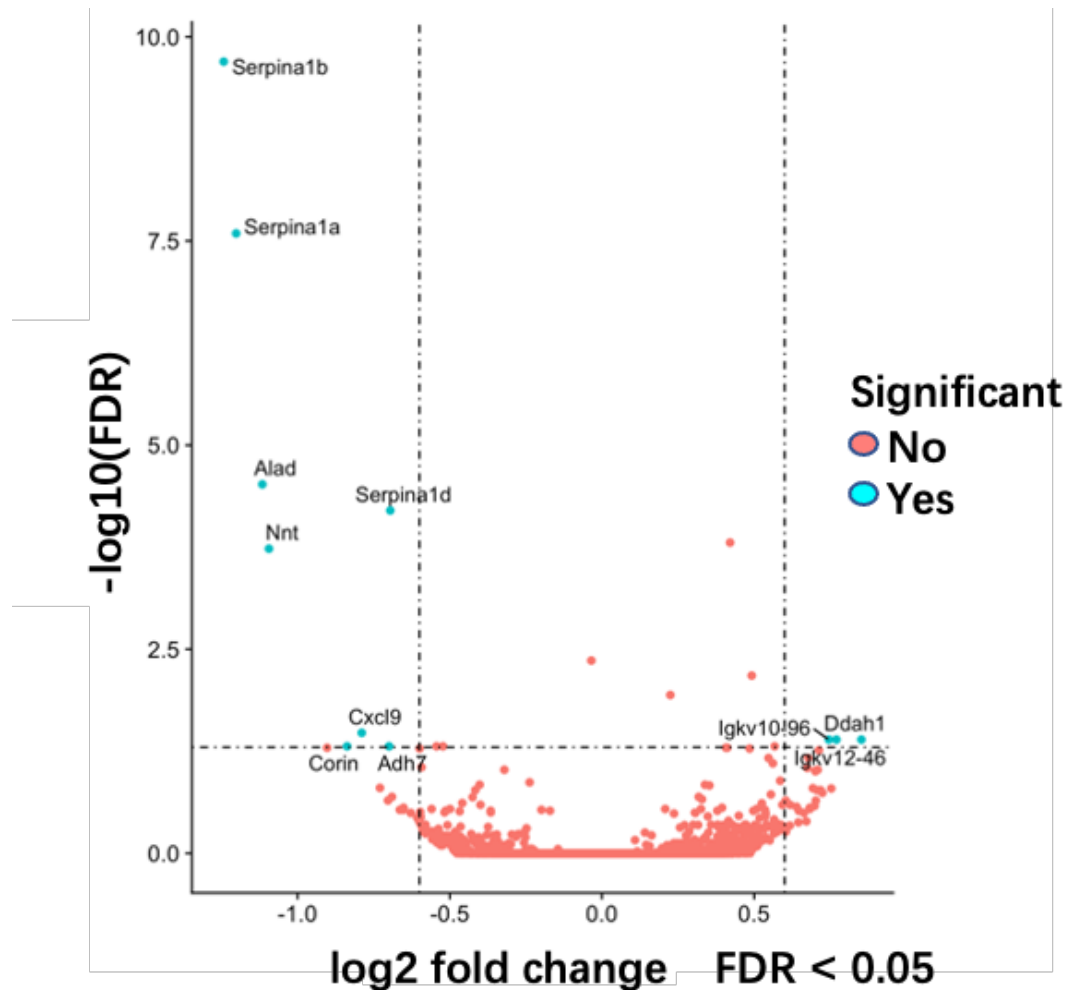
RNA was extracted from knee cartilage of 11-week-old DKO mice and underwent RNA-seq. DEG analysis identified 3 up- and 8 down-regulated genes with a fold change > 1.5 and FDR threshold ≤ 0.05 in the comparison of DKO vs. WT mice (blue dots in the volcano plot in Fig. 5.8).

Given that only 18 genes were significant differentially expressed genes (FDR threshold ≤ 0.05), a heatmap was generated to visualise the differences of gene expression between WT and DKO mice (Fig. 5.9). Unsurprisingly, the differentially expressed genes caused clear hierarchical separation of WT and DKO samples. Given all significant differentially expressed genes (FDR threshold ≤ 0.05) amongst *Mir140*-null, *Mir455*-null and DKO knee cartilage chondrocytes, a Venn plot was generated to visualise the overlapping of genes between *Mir140*-null, *Mir455*-null and DKO mice. There was only one gene (*Ube2n-ps1*) that was significantly differential expressed among in *Mir140*-null, *Mir455*-null and DKO knee cartilage chondrocytes. Seven genes (*Serpina1b*, *Ifi44l*, *Nnt*, *Serpina1a*, *Corin*, *Serpina1d*, *Adh7*) were significantly differential expressed in *Mir140*-null and DKO knee cartilage chondrocytes versus the controls. While three genes (*Alad*, *Igkv12-46*, *Igkv10-96*) were significantly differential expressed in *Mir455*-null and DKO knee cartilage chondrocytes versus the control animals. Two genes (*Ighv1-4*, *Vps33b*) were also significantly differential expressed in both *Mir140*-null and *Mir455*-null knee cartilage chondrocytes versus the controls (Fig. 5.10).

For GSEA analysis, there were no significant pathway identified when comparing the DKO knee cartilage with WT knee cartilage. This could be due to variability in the data but could also indicate an antagonistic effect of miR-140 and miR-455 in knee cartilage, consistent with the results we obtained from rib chondrocytes.

Figure 5.8 The disruption of differentially expressed genes in DKO murine knee

cartilage relative to control mice



A Volcano plot of gene fold-change (\log_2 , X axis) against $-\log_{10}$ FDR (false discovery rate, Y axis) between DKO and WT, demonstrating the distribution of upregulated genes and downregulated genes. The vertical red lines correspond to ± 0.6 \log_2 foldchange (equivalent to 1.5-fold change). The red horizontal line denotes an FDR of 0.05. Red points represent all significantly differentially expressed genes with an FDR p value ≤ 0.05 and fold change ≥ 1.5 . In total, 8 genes were found to be significantly downregulated and 3 genes to be significantly upregulated in DKO mice.

Figure 5.9 Profile of significant differentially expressed genes expression in murine knee cartilage between WT and DKO mice

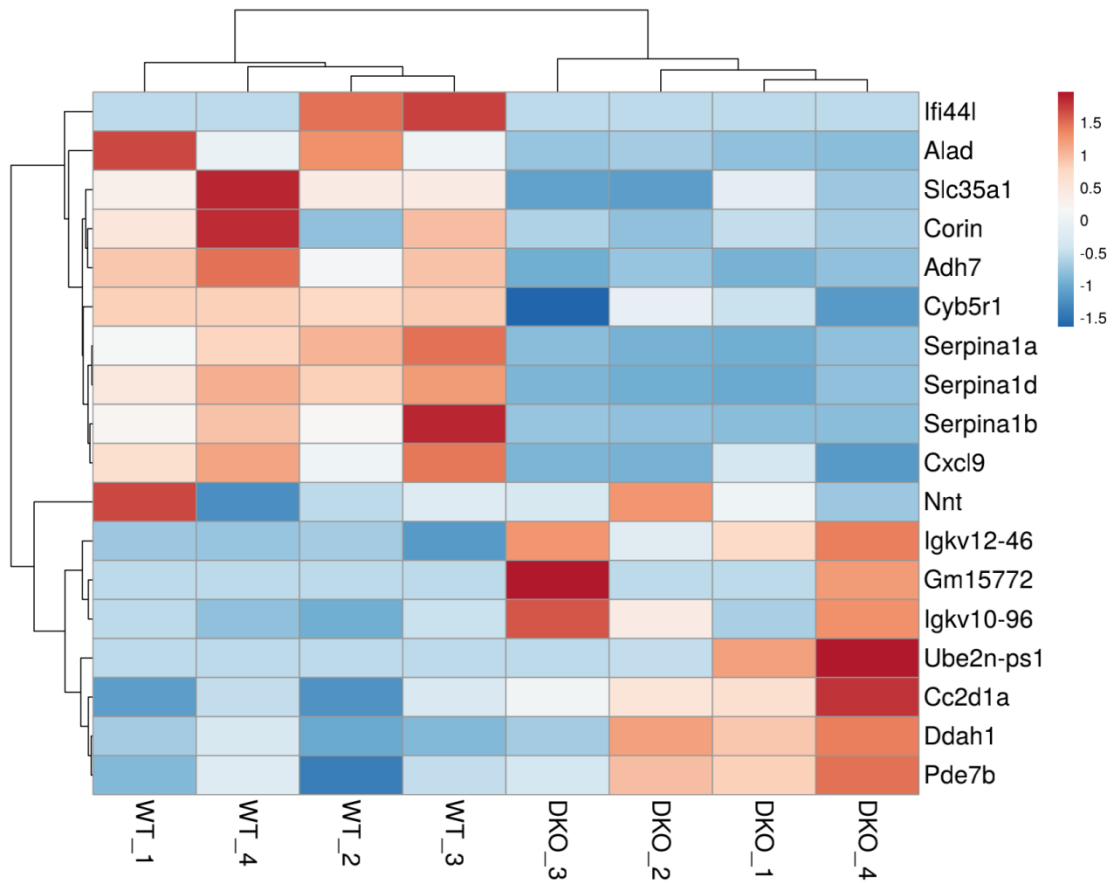
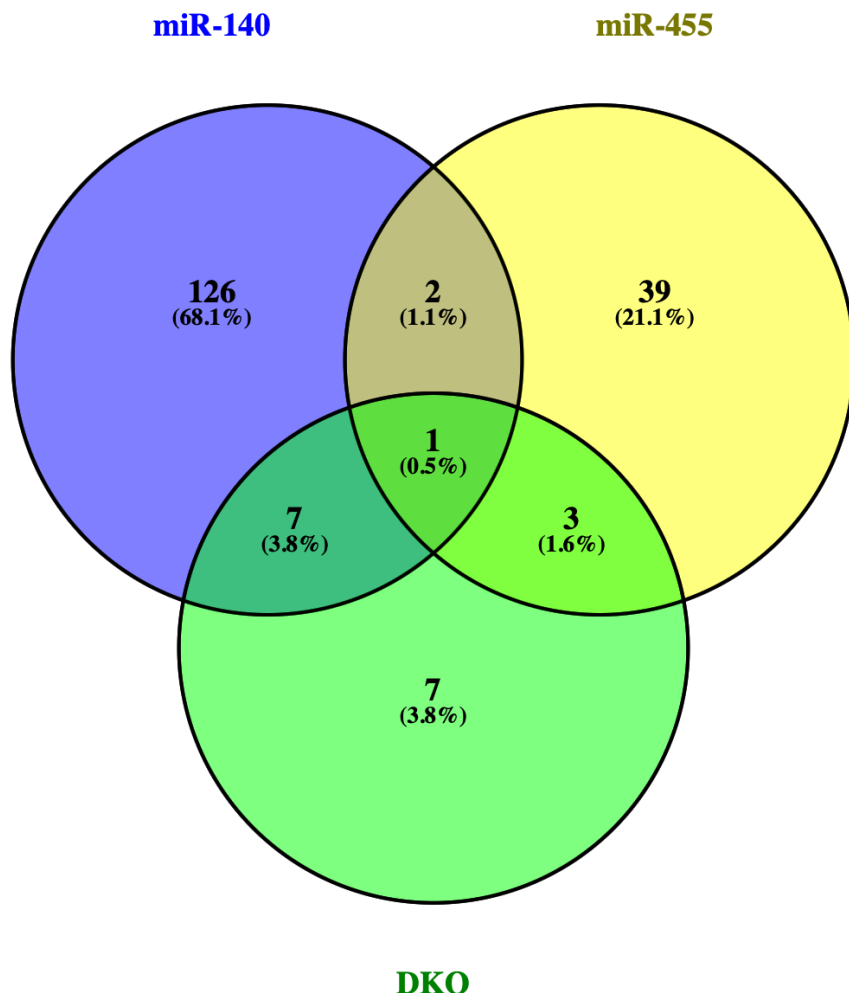


Figure 5.10 Profile of significant differentially expressed genes expression in murine knee cartilage between *Mir140*-null, *Mir455*-null and DKO mice



Venn plot demonstrating the overlap of significant differentially expressed genes in *Mir140*-null, *Mir455*-null, and DKO knee cartilage.

5.2.4. Selection of murine DMM histological assessment

Previous studies have shown that the expression of miR-140 and miR-455-3p were reduced in human OA cartilage (Iliopoulos, Malizos et al. 2008, Miyaki, Nakasa et al. 2009, Mao, Kang et al. 2019), however, our comparison between adult human normal and OA articular hip cartilage revealed that the expression of miR-140-5p and miR-455-3p were significantly increased in OA cartilage (Swingler, Wheeler et al. 2012). Miyaki *et al.* (Miyaki, Sato et al. 2010) showed that an age-related onset of OA changes was observed in miR-140^{-/-} mice at 3-month-old, 8-month-old and 12-month-old, which was significantly more severe than that of matched control WT mice (Miyaki, Sato et al. 2010). In addition, the loss of miR-140 resulted in increased severity of early-onset OA after surgery (resecting MMTL) was performed in mice, and this phenotype was rescued by overexpression of miR-140 in the knee joint (Miyaki, Sato et al. 2010). MiR-455 deletion mice at 12-month-old showed more severe cartilage matrix defects when compared with matched WT animals, and these defects were rescued by treatment with an agomir-455-3p (Mao, Kang et al. 2019). Ito *et al.* showed that their 6-month-old *Mir455*-null mice had significantly more GAG staining loss when compared to control animals, and knockdown the expression of the identified target gene, *Epas1*, rescued abnormally increased expression of cartilage degenerative-related genes like *Mmp3* and *Mmp13* (Ito, Matsuzaki et al. 2021). As gene expression differences were identified between miRNA-null and control knee cartilage, DMM was performed on our mice in order to examine if miRNA deletion impacted on cartilage damage post DMM.

We performed DMM surgery on left leg of wild-type and genetically modified male mice (*Mir140*-null, *Mir455*-null, and DKO) at 11 weeks old, and the joints were harvested 8 weeks post-surgery. Our expectation and experience showed that the effect of miRNA deletion on DMM-histological assessment was minor. Therefore, we wanted to examine different histological scoring systems which could generate a broader range of scores from the generally used Glasson OARSI scoring system.

To do this we selected 20 knee sections/images, stained with Safranin-O and fast green, ranging from normal to severe OA, and scored those images by three experienced scorers (David Young, Matt Barter and Hua Lin) and two novice scorers (Dan Hayman and Yao Hao), all of whom were blinded to the pre-determined (using the Glasson scheme) severity. These sections were assessed using the 3 different assessments listed above, but not the Mankin-HHGS, which is considered too old.

To achieve an impartial optimisation that maximally avoids a single impact factor (i.e., microRNA deletion) on murine knee OA progression induced by surgery (DMM), twenty DMM histological images were selected for assessment. These were from several different genotypes including one miR-324^{+/+} (from miR-324⁺⁻ inter-cross) mouse, two miR-455⁺⁻, five Col9a3^{DELexon3}, two c-Wwp2⁺⁻, two miR-324⁺⁻, two Col9a3^{+/+} (from Col9a3⁺⁻ inter-cross), four Col9a3⁺⁻ mice, and one c-Wwp2^{+/+} (from c-Wwp2⁺⁻ inter-cross) mouse. All these mouse joints were harvested 8 weeks post DMM surgery performed at 10-weeks of age. In addition, one ageing c-Wwp2^{+/+} mouse (one year old) was included in this assessment to balance the surgery-induced OA bias.

All the five scorers gave independent grades (0 to 6) for the medial femur condyle (MFC) and medial tibia plateau (MTP) according to the system 1 scoring criteria (Table 5.1) and the data plotted as linear graph (Fig. 5.11). This showed clear scoring differences for MFC between images 4 to 11, and for MTP from images 3 to 10. Within these images, all three experienced scorers were more consistent with each other (near the mean) relative to two novice scorers.

For system 2 (Table 5.2), the score is in two parts. For the depth of articular cartilage damage (II A, advanced grade range: 0-6.5), the MFC grades showed more variation (again mainly for image 4 to 11) than MTP grades. In contrast, the extent of articular cartilage damage (II B, articular cartilage surface damage area, grade range: 0 to 4) surprisingly varied amongst scorers for both the MFC and MTP images. The overall

score for system 2 (II C) is the product of II A and II B, which offers a range from 0 to 24, and showed less varied scoring results between scorers than II B (Fig. 5.12).

As with system 2, system 3 (Table 5.3) also provides two independent score values for both the MFC and MTP. These are an articular cartilage structure score (ACS) and a Safranin-O staining score (Saf-O), both of which range from 0 to 12. All the five scorers gave similar results for ACS of both the MFC and MTP, but disagreement on Safranin-O staining assessment for both the MFC and MTP (Fig. 5.13).

To test scorer-mean correlation and inter-scorer correlation, Pearson analysis was performed. When comparing either each scorer to the mean score for the three schemes (Table 5.4), each scorer is significantly positively correlated with either the mean score or each other. System 1 results in a Pearson score from 0.8425 to 0.959 for MFC and from 0.8693 to 0.9603 for MTP. System 2 (II C) showed a range from 0.8175 to 0.9582 for MFC, and from 0.9264 to 0.9815 for MTP. For system 3 (III A), the Pearson score was between 0.9492 to 0.9818 for MFC and 0.979 to 0.9885 for MTP; in addition, for the III B, 0.8492 to 0.9418 for MFC and 0.7442 to 0.9656 for MTP. However, when comparing the correlation between each scorer (Table 5.5), we found that the average Pearson correlation score for system 1 was from 0.7441 to 0.8438 for MFC and 0.78 to 0.8816 for MTP; system 3 (III A) gave a range from 0.8913 to 0.9367 for MFC and 0.9545 to 0.9668 for MTP, and a range of MFC (0.7309 to 0.8189) and MTP (0.6051 to 0.7818) for scheme 3 (III B); In contrast, the system 2 (II C) gave a range from 0.6943 to 0.8501 for MFC and 0.8462 to 0.9055 for MTP.

Although in general system 3 gave highly correlate inter-scorer data, part III B actually showed the lowest average Pearson correlation score for MTP, which we deduced to be due to varied scoring of Safranin-O staining loss amongst 5 scorers. Thus, we performed an additional test for system 3 (III B) (using the original scoring system and a simplified version, data not shown) and for system 2, which was the user preferred scoring system. This analysis revealed that the system 3 (III B) gave us

the highest inter-scorer consistency at MFC, however, system 2 overall showed the highest inter-scorer consistency (data not shown).

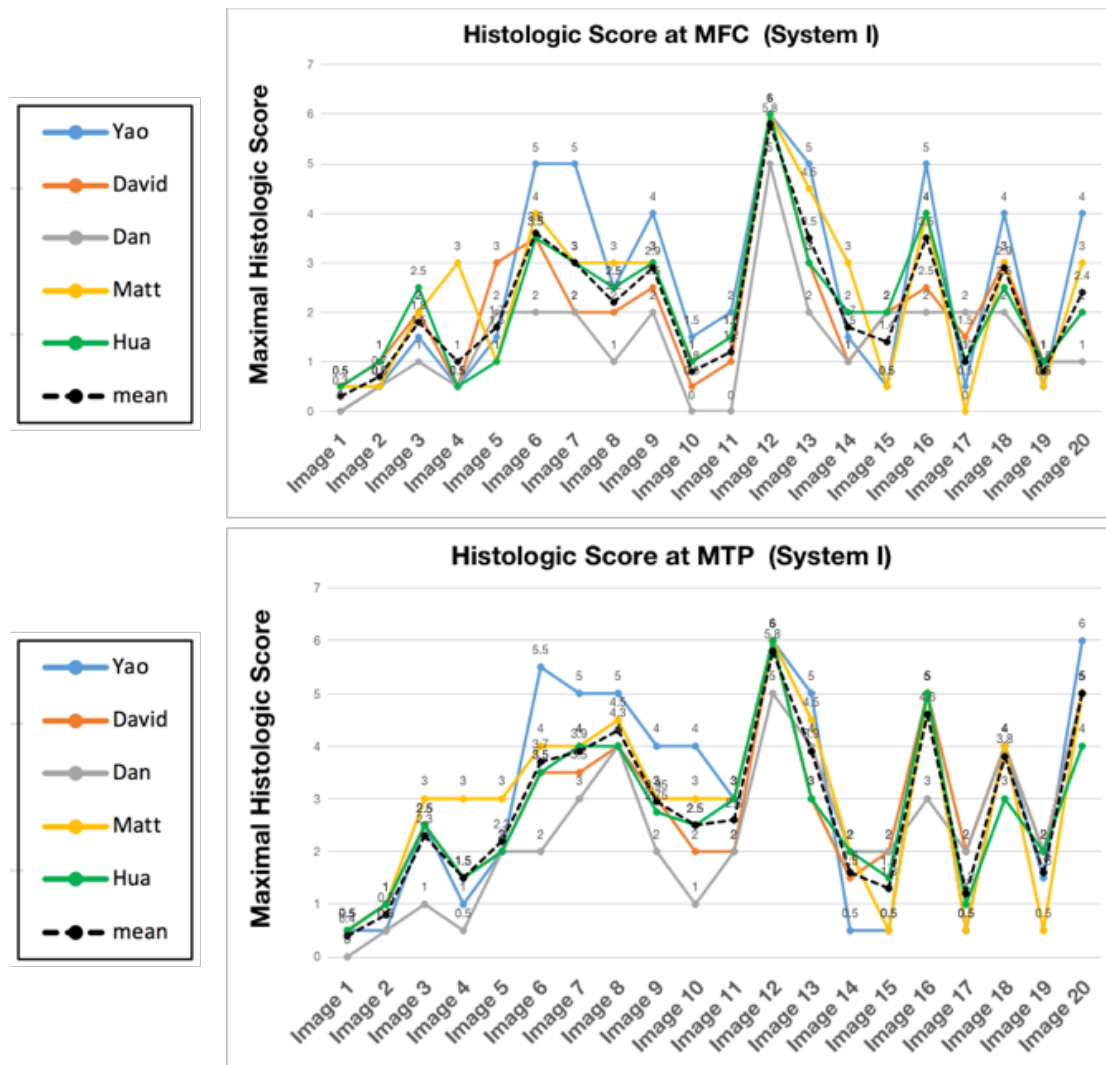
In summary, system 2 gave the highest interscorer consistency and reproducibility for MFC and MTP assessment (especially when combining data together). Although more time consuming than the standard Glasson/OARSI scoring system (system 1), this system provided a broader range of data and was relatively simple to perform. Thus, we applied the OOCHAS (Table 5.2) to evaluate damage of our murine DMM knee joints.

Table 5.1 The semi-quantitative scoring scheme for system 1

Grade	Osteoarthritic damage
0	Normal
0.5	Loss of Safranin-O without structural damage
1	Small fibrillations without loss of cartilage
2	Vertical clefts down to the layer immediately below the superficial layer and some loss of surface lamina
3	Vertical clefts/erosion to the calcified cartilage extending to < 25% of the articular surface
4	Vertical clefts/erosion to the calcified cartilage extending to 25% - 50% of the articular surface
5	Vertical clefts/erosion to the calcified cartilage extending to 50% - 75% of the articular surface
6	Vertical clefts/erosion to the calcified cartilage extending to > 75% of the articular surface

Description of the system 1 scoring system, which is recommended to apply to all four quadrants of the joints: medial femoral condyle (MFC), medial tibia plateau (MTP), lateral femoral condyle (LFC), and lateral tibia plateau (LTP). Specific features within each OA grade are indicated with a detailed explanation on the right column of table (Glasson, Chambers et al. 2010).

Figure 5.11 Scoring trend of selected 20 test DMM images using system 1



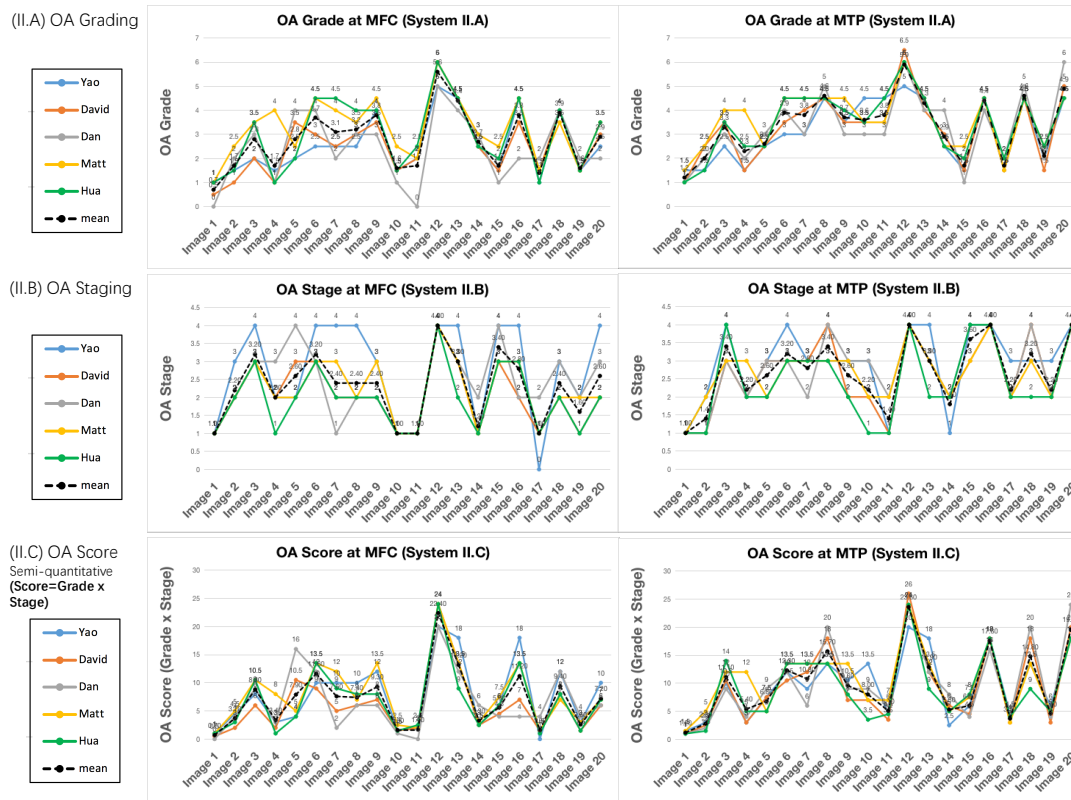
The five scorers scored the selected DMM murine knee joints (MFC and MTP) with severity from normal to severe (double blind, random order) according to the system 1 guidance (Table 5.1).

Table 5.2 The semi-quantitative scoring scheme for system 2

Grade (description)	Associated criteria	Stage	% Involvement (area)
0 (normal)	Intact, uninvolved cartilage	0	No OA activity seen
1 (cells intact)	Matrix: superficial zone intact, edema and/or fibrillation		
1.5 (cells death)	Cells: proliferation (clusters), hypertrophy Reaction must be more than superficial fibrillation only		
2.0 (fibrillation through superficial zone)	As above + Discontinuity at superficial zone	1	< 10%
2.5 (surface abrasion with matrix loss within superficial zone)	± Cationic stain matrix depletion (Safranin-O or Toluidine blue) upper 1/3 of cartilage (mid zone) ± Disorientation of chondron columns		
3.0 (simple fissures)	As above	2	10-25%
3.5 (branched/complex fissures)	± Cationic stain matrix depletion (Safranin-O or Toluidine blue) into lower 2/3 of cartilage (deep zone) ± New collagen formation (polarized light microscopy, Picro Sirius Red Stain)		
4.0 (superficial zone delamination)	Cartilage matrix loss, cyst formation within cartilage matrix	3	25-50%
4.5 (mid zone excavation)			
5.0 (bone surface intact)	Surface is sclerotic bone or reparative tissues including fibrocartilage		
5.5 (reparative tissue present)		4	>50%
6.0 (joint margin osteophytes)	Bone remodeling. Deformation of articular surface contour (more than osteophyte formation only)		
6.5 (joint margin and central osteophytes)	Includes: microfracture and repair		

Advanced grading methodology (0-6.5) was applied in this research to determine the consequences of microRNA loss in the *Mir140*-null, *Mir455*-null and DKO mice during OA pathogenesis. Specific features within each OA grade are indicated with a detailed explanation on the next column of the table. Four OA stages (0-4) are defined to measure the horizontal extent of the involved cartilage area as seen in the microscopic section. This methodology is recommended to reflect early or mild OA severity (Pritzker, Gay et al. 2006).

Figure 5.12 Scoring trend of selected 20 test DMM images using system 2



The five scorers scored the selected DMM murine knee joints (MFC and MTP) with severity from normal to severe (double blind, random order) according to the system 2 guidance (Table 5.2).

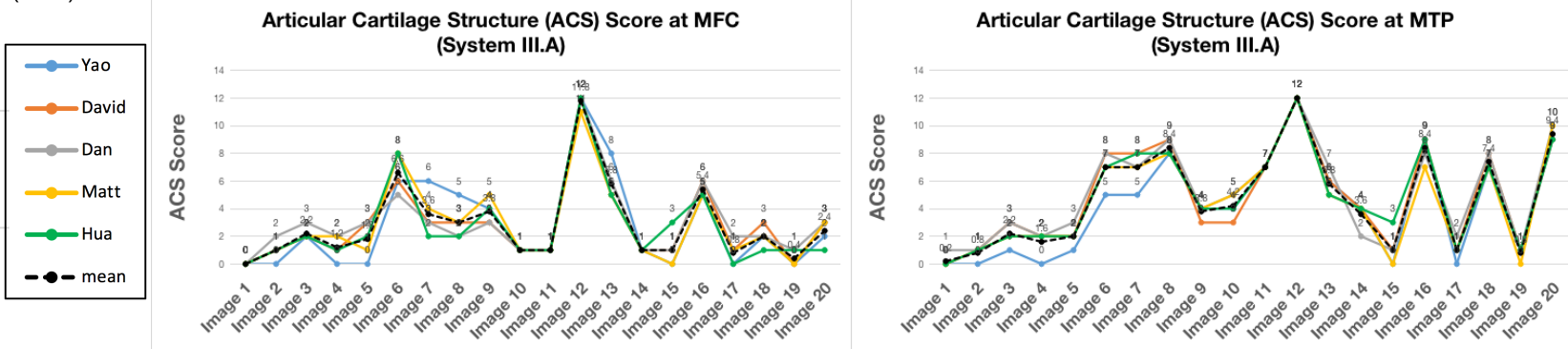
Table 5.3 The semi-quantitative scoring scheme for system 3

Histological parameter	Description
Articular cartilage structure scores (ACS)	
Grade 0	Articular surface smooth and intact
Grade 1-3	Fibrillation and/or clefts and/or loss of cartilage involving 1/4 or less of articular cartilage thickness involving $\leq 1/3$, $>1/3$ and $\leq 2/3$, or $>2/3$ of the plateau or condyle, respectively
Grade 4-6	Fibrillation and/or clefts and/or loss of cartilage involving 1/2 or less of articular cartilage thickness involving $\leq 1/3$, $>1/3$ and $\leq 2/3$, or $>2/3$ of the plateau or condyle, respectively
Grade 7-9	Fibrillation and/or clefts and/or loss of cartilage involving $>1/2$ of articular cartilage but less than full thickness involving $\leq 1/3$, $>1/3$ and $\leq 2/3$, or $>2/3$ of the plateau or condyle, respectively
Grade 10-12	Fibrillation and/or clefts and/or loss of cartilage involving the full thickness of articular cartilage involving $\leq 1/3$, $>1/3$ and $\leq 2/3$, or $>2/3$ of the plateau or condyle, respectively
Safranin-O staining score (Saf-O)	
Grade 0	Uniform staining throughout the articular cartilage
Grade 1-3	Loss of staining in the matrix (but not cells) in $<1/2$ of the articular cartilage and involving $\leq 1/3$, $>1/3$ and $\leq 2/3$, or $>2/3$ of the plateau or condyle, respectively
Grade 4-6	Loss of staining in the matrix (but not cells) in $>1/2$ of the articular cartilage and involving $\leq 1/3$, $>1/3$ and $\leq 2/3$, or $>2/3$ of the plateau or condyle, respectively
Grade 7-9	Complete loss of staining in $<1/2$ of the articular cartilage and involving $\leq 1/3$, $>1/3$ and $\leq 2/3$, or $>2/3$ of the plateau or condyle, respectively
Grade 10-12	Complete loss of staining in $>1/2$ of the articular cartilage and involving $\leq 1/3$, $>1/3$ and $\leq 2/3$, or $>2/3$ of the plateau or condyle, respectively

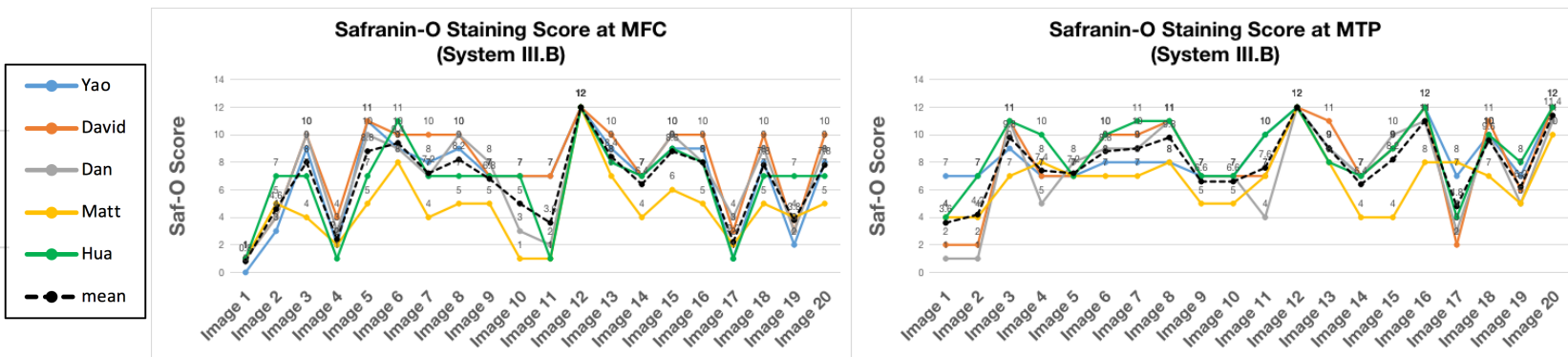
Two semi-quantitative parameters (ACS and Saf-O, 0-12) were used to evaluate articular cartilage damage. Specific features within each OA grade are indicated with a detailed explanation on the right column of the table (McNulty, Loeser et al. 2011).

Figure 5.13 Scoring trend of selected 20 test DMM images using system 3

(III.A) Articular Cartilage Structure Score (ACS)



(III.B) Safranin-O Staining Score (Saf-O)



The five scorers scored the selected DMM murine knee joints (MFC and MTP) with severity from normal to severe (double blind, random order) according to the system 3 guidance (Table 5.3).

Table 5.4 Summary of correlation between scorer and the mean (Pearson)

System	Region	Parameters	Yao vs. mean	David vs. mean	Dan vs. mean	Matt vs. mean	Hua vs. mean
I.	MFC	Pearson r	0.9306	0.9129	0.8425	0.901	0.959
		P-Value	***	***	***	***	***
	MTP	Pearson r	0.951	0.9603	0.8693	0.9421	0.9602
		P-Value	***	***	***	***	***
II.A	MFC	Pearson r	0.9306	0.9568	0.8362	0.8942	0.9356
		P-Value	***	***	***	***	***
	MTP	Pearson r	0.9244	0.976	0.9237	0.9108	0.9646
		P-Value	***	***	***	***	***
II.B	MFC	Pearson r	0.8895	0.9499	0.759	0.9283	0.9327
		P-Value	***	***	***	***	***
	MTP	Pearson r	0.8813	0.9379	0.9049	0.9044	0.9002
		P-Value	***	***	***	***	***
II.C	MFC	Pearson r	0.9104	0.9582	0.8175	0.9399	0.9516
		P-Value	***	***	***	***	***
	MTP	Pearson r	0.9264	0.9815	0.9425	0.9385	0.9329
		P-Value	***	***	***	***	***
III.A	MFC	Pearson r	0.9492	0.9818	0.9653	0.9744	0.9568
		P-Value	***	***	***	***	***
	MTP	Pearson r	0.979	0.9885	0.9832	0.9878	0.9854
		P-Value	***	***	***	***	***
III.C	MFC	Pearson r	0.9329	0.9369	0.9418	0.8492	0.8847
		P-Value	***	***	***	***	***
	MTP	Pearson r	0.8236	0.9656	0.9225	0.7442	0.9059
		P-Value	***	***	***	***	***

Comparison of scorer-mean correlation between the three different scoring systems.

Pearson score for MFC and MTP. *** $P \leq 0.001$.

Table 5.5 Summary of interscorer correlation (Pearson)

Interscorer Pearson Correlation									
Region	System	Scorers					Average		
		Yao	David	Dan	Matt	Hua	By method	By measurement	By system
MFC	I	0.784 5	0.811 2	0.744 1	0.754 2	0.843 8	0.7876	0.7876	0.7876
	II.A	0.812 9	0.839 0	0.698 4	0.771 4	0.812 6	0.7868	0.7666	0.7770
	II.B	0.719 5	0.819 9	0.612 6	0.784 7	0.795 0	0.7463		
	II.C	0.786 2	0.850 1	0.694 3	0.822 4	0.836 7	0.7979	/	
	III.A	0.891 3	0.936 7	0.917 8	0.925 5	0.905 8	0.9154	0.8496	0.8496
	III.B	0.801 0	0.805 6	0.818 9	0.730 9	0.762 8	0.7838		
MTP	I	0.852 5	0.881 6	0.780 0	0.847 0	0.877 1	0.8476	0.8476	0.8476
	II.A	0.835 8	0.895 0	0.829 5	0.826 2	0.886 3	0.8546	0.8152	0.8319
	II.B	0.743 6	0.811 2	0.775 0	0.784 1	0.765 9	0.7759		
	II.C	0.846 2	0.905 5	0.856 3	0.863 2	0.854 5	0.8651	/	
	III.A	0.954 5	0.968 8	0.960 5	0.966 1	0.963 2	0.9622	0.8354	0.8354
	III.B	0.690 0	0.781 8	0.723 4	0.605 1	0.742 8	0.7086		

Comparison of interscorer correlation between the three different scoring systems.

Highlighted in bold and red; the scoring system which gives the highest consistency and reproducibility: highlighted in bold; for each system, the scorer who shares the highest correlation with others.

5.2.5. Effect of miR-140^{-/-} and/or miR-455^{-/-} mutations on murine knee articular cartilage stability

Having selected a scoring system that gave a reliable and detailed histological assessment of our DMM model, we proceeded to assess the role of miR-140 and miR-455 in the development of early-onset OA in mice, by performing DMM surgery on the left knee of male mice at 11-week-old, and harvested the knee joints 8 weeks after surgery. Histological assessment was subsequently performed as discussed (Pritzker, Gay et al. 2006). In total we performed DMM surgery on WT (n=8), *Mir140*-null (n=15), *Mir455*-null (n=10) and DKO (n=12) male mice following the procedure described in section 2. Two experienced, independent and blinded scorers performed the assessment, and the two separated data were then combined to generate average values. In this study, articular cartilage degeneration (Grade and Stage assessment) post-surgery was evaluated on the femoral condyle and tibia plateau of medial side (operated knee) and the severity of OA was indicated by the combination of two parameters. Moreover, we also performed GAG staining loss (Stage assessment) for the lateral side (unoperated knee) to evaluate the impact of loss of miRNA (miR-140 and/or miR-455) on cartilage degeneration.

At 8 weeks post-surgery, scores (Grade assessment, the mean value of the 5 worst sections per mouse were chosen to represent each mouse) of the relative to damage of MFC cartilage showed a similar level of cartilage degeneration between four genotypes (Fig. 5.14A & B). Similar cartilage changes (Grade assessment) were observed in MTP cartilage (Fig. 5.14A & B). In terms of GAG staining (Stage assessment, the mean value of the 5 worst sections per mouse was chosen to represent each mouse) for both MFC and MTP, all miRNA-null mice (except *Mir455*-null mice for MTP) showed significantly less Safranin-O staining (proteoglycan) when compared to the matched WT controls, with the DKO mice displaying the most severe lack of proteoglycan staining in MTP (Fig. 5.14B). We also observed significantly less proteoglycan staining in the MFC of *Mir455*-null mice than for the

Mir140-null mice (Fig. 5.14B). When we combined Grade and Stage assessments together (Grade x Stage), all the mutant mice (except *Mir140*-null mice) showed a significant increase in their OA severity at the MFC compared to WT animals, with *Mir455*-null mice exhibiting the most severe OA changes to their joints (Fig. 5.14C). All the miRNA-null mice had more severe MTP cartilage damage than the WT mice, and *Mir140*-null and DKO mice gave higher scores when combining scores for the MFC and MTP together (Fig. 5.14C).

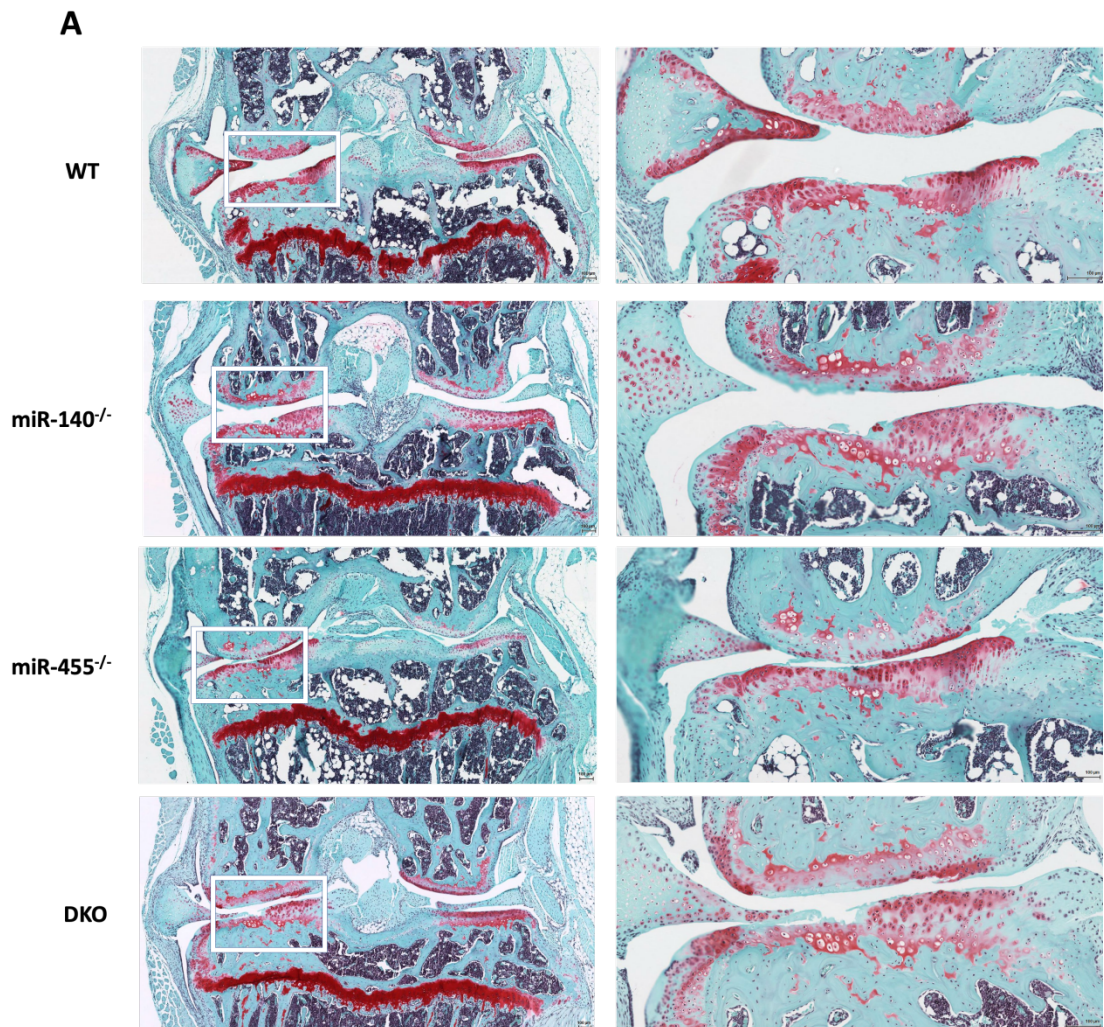
We also examined the mean value of all scored sections for each mouse to represent individuals. In this analysis, all the miRNA-null mice showed no distinguishable histological differences when compared to the WT mice (Fig. 5.14D) but did have more GAG staining loss (Fig. 5.14D), which is similar to as described above. *Mir140*-null mice showed significant differences at MFC (grade x stage) when compared to WT mice, and DKO mice ranked the most severe amongst the four genotypes at either MFC (grade x stage) or MTP (grade x stage), or MFC (grade x stage) + MTP (grade x stage) (Fig. 5.14E).

Subsequently, we assessed the susceptibility to degradation of articular cartilage in the lateral side of knee joints. In mutant mice the MFC and MTP all showed significant proteoglycan loss when compared to WT mice (Fig. 5.15A & B). This indicated miR-140 and miR-455 are both involved in GAG pathways, thus loss of miR-140 and/or miR-455 might cause a lower rate of GAG synthesis or higher turnover. This finding is consistent with our costal chondrocyte RNA-seq data (Chapter 4, section 4.2.5.2 and 4.4.7.1).

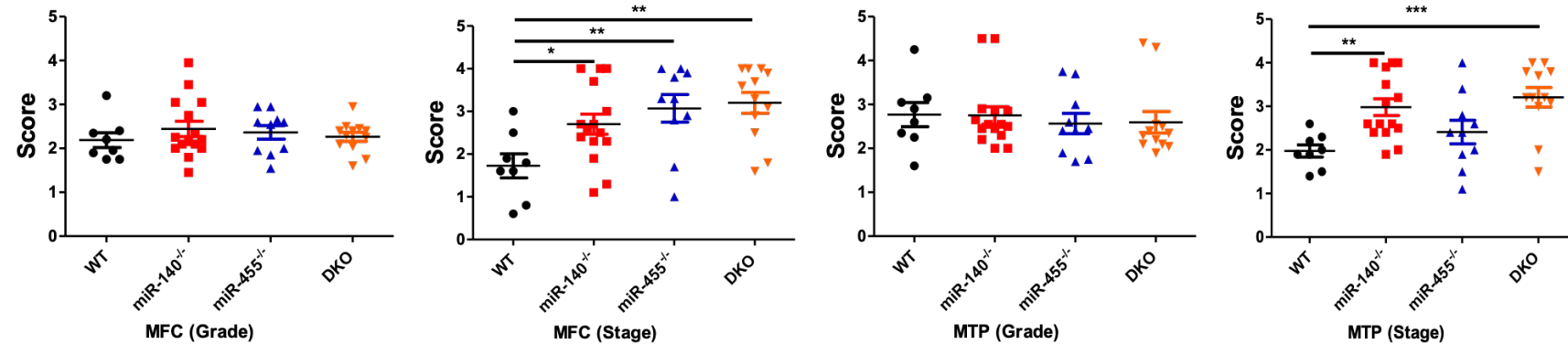
Furthermore, in order to more comprehensively evaluate articular cartilage degeneration post-surgery in the absence of miRNA(s), we performed additional cartilage assessment (Glasson, Chambers et al. 2010) using the same sections used for the scheme 2 assessment. However, similar to the Grade assessment for MFC and MTP (Fig. 5.14A & B), no statistically significant alterations in their OA

phenotype were observed with either the 5 worst section assessment (Fig. 5.16A) or the assessment of mean value of all sections of individuals (Fig. 5.16B).

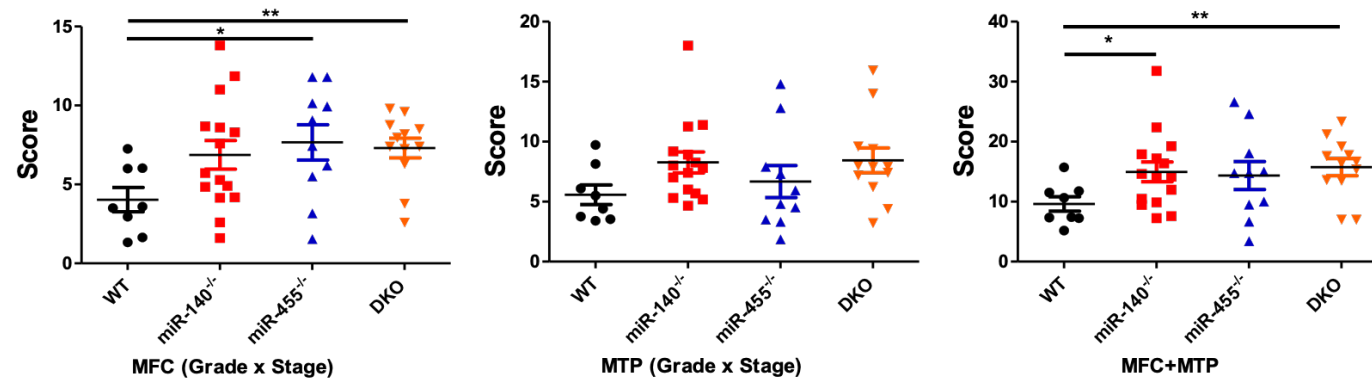
Figure 5.14 DMM-induced OA in mice



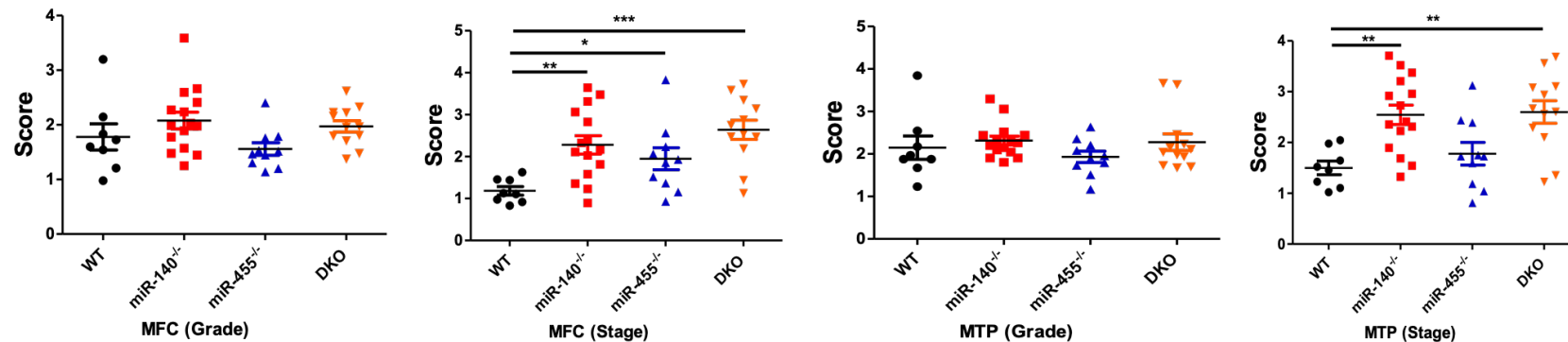
B The system 2 scores of WT, *Mir140*-null, *Mir455*-null and DKO mice 8-weeks post-DMM surgery at 11-week-old (5 worst)



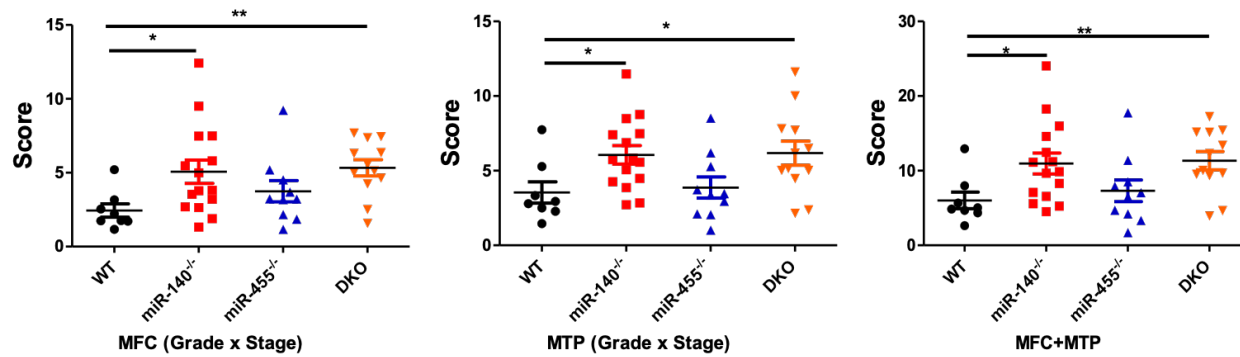
C The combined scores of WT, *Mir140*-null, *Mir455*-null and DKO mice 8-weeks post-DMM surgery at 11-week-old (5 worst)



D The system 2 scores of WT, *Mir140*-null, *Mir455*-null and DKO mice 8-weeks post-DMM surgery at 11-week-old (mean value)

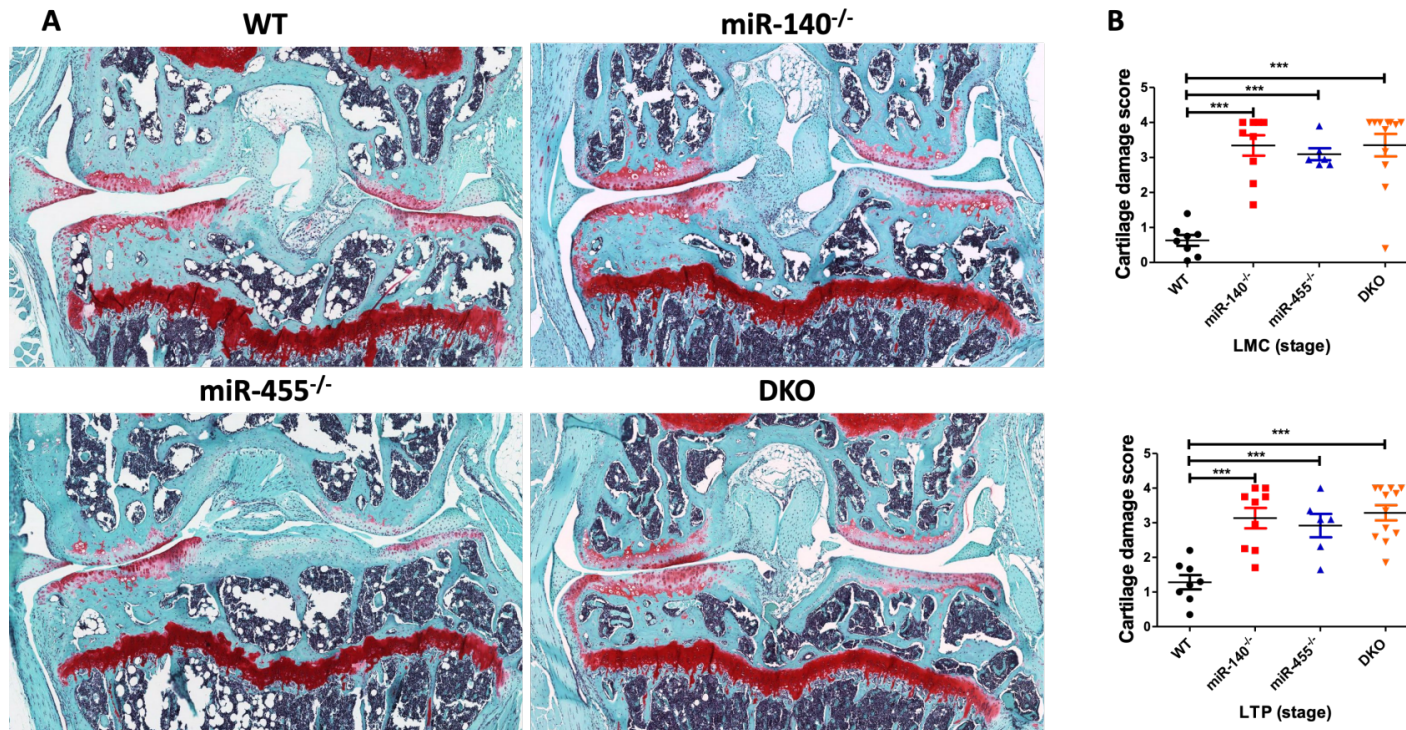


E The combined scores of WT, *Mir140*-null, *Mir455*-null and DKO mice 8-weeks post-DMM surgery at 11-week-old (mean value)



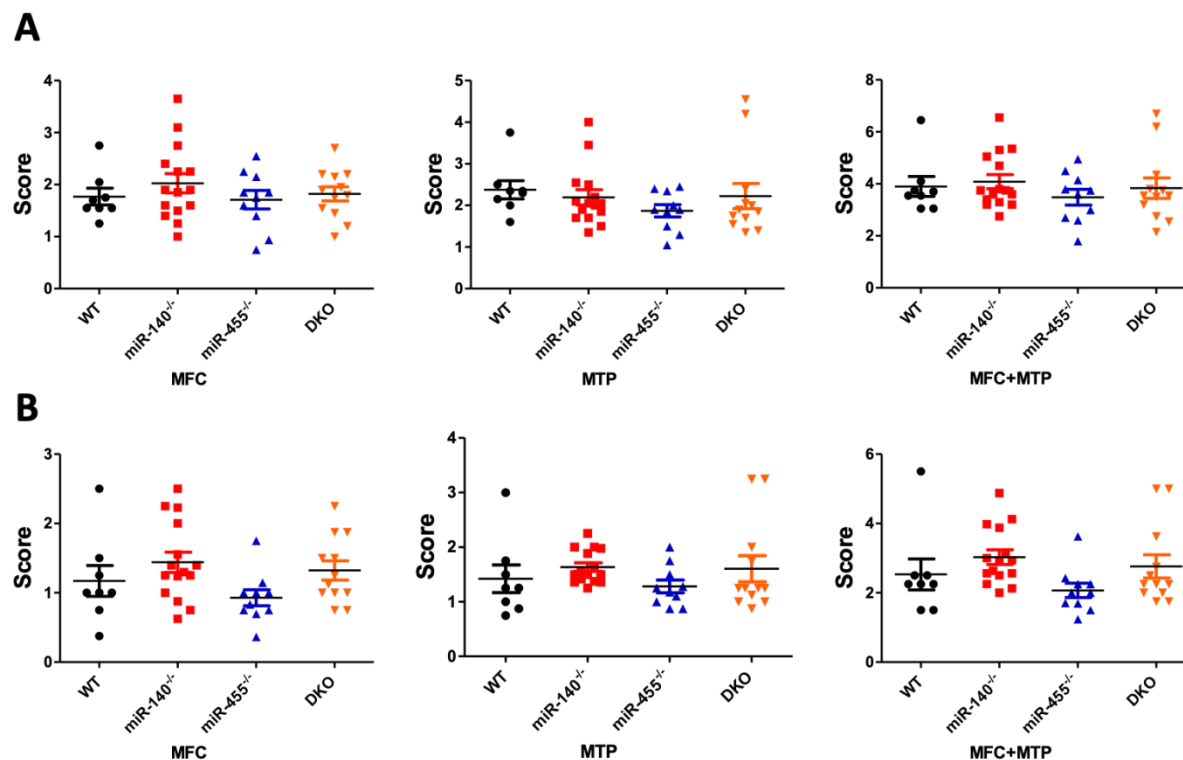
11-week-old WT (n=8), *Mir140*-null (n=15), *Mir455*-null (n=10) and DKO (n=12) male mice were subjected to DMM surgery and the operated legs harvested 8 weeks post-surgery and processed for histological staining. (A) Representative coronal sections of the knee joints from each mouse, analysed by staining with Safranin-O and Fast Green. Scale bars = 100 μ m. (B) Graphs showing the results (5 worst sections represent for each mouse) of histological assessment (grade and stage assessment) of OA (Pritzker et al., 2006) for the operated knee joints (medial side, MFC and MTP) of four DMM operated group. (C) Graphs showing combined data for either MFC or MTP or MFC+MTP of four DMM groups. (D) Graphs showing the results (the mean value of all scored sections per mouse stands for individual mouse) of histological assessment (grade and stage assessment) of OA (Pritzker et al., 2006) for the operated knee joints (medial side, MFC and MTP) of four DMM operated group. (E) Graphs showing combined data for either MFC or MTP or MFC+MTP of four DMM groups. Two blind histological assessment was performed by two scorers on twenty-four sections for each mouse, with the five worst per joint region averaged. Line and error bars are mean \pm SEM. A Mann-Whitney U test was used for analysis. * $p \leq 0.05$, ** $p \leq 0.01$, *** $p \leq 0.001$.

Figure 5.15 MiR-140 and miR-455 are involved in GAG metabolism in articular chondrocytes



(A) Representative coronal sections of the knee joints from each mouse, analysed by staining with Safranin-O and Fast Green. Scale bars = 100 μ m. (B) Graphs showing the results of histological assessment of GAG staining (Pritzker et al., 2006) for the lateral knee joints (lateral side) of four DMM operated group. Two blind histological assessment was performed by two scorers on twenty-four sections for each mouse, with the five worst per joint region averaged. Line and error bars are mean \pm SEM. A Mann-Whitney U test was used for analysis. *** P≤0.001.

Figure 5.16 OA evaluation using the OARSI (Glasson) scoring system



Graph showing the results of histological assessment of OA (Glasson et al., 2010) for the operated knee joints (medial side) of four DMM operated mouse groups. Blinded histological assessment was performed by two scorers on twenty-four sections for each mouse. (A) the 5 worst sections were selected to represent for each mouse; (B) the mean value of all scored sections of each mouse were chose to represent for individual mouse. Line and error bars are mean \pm SEM. A Mann-Whitney U test was used for analysis.

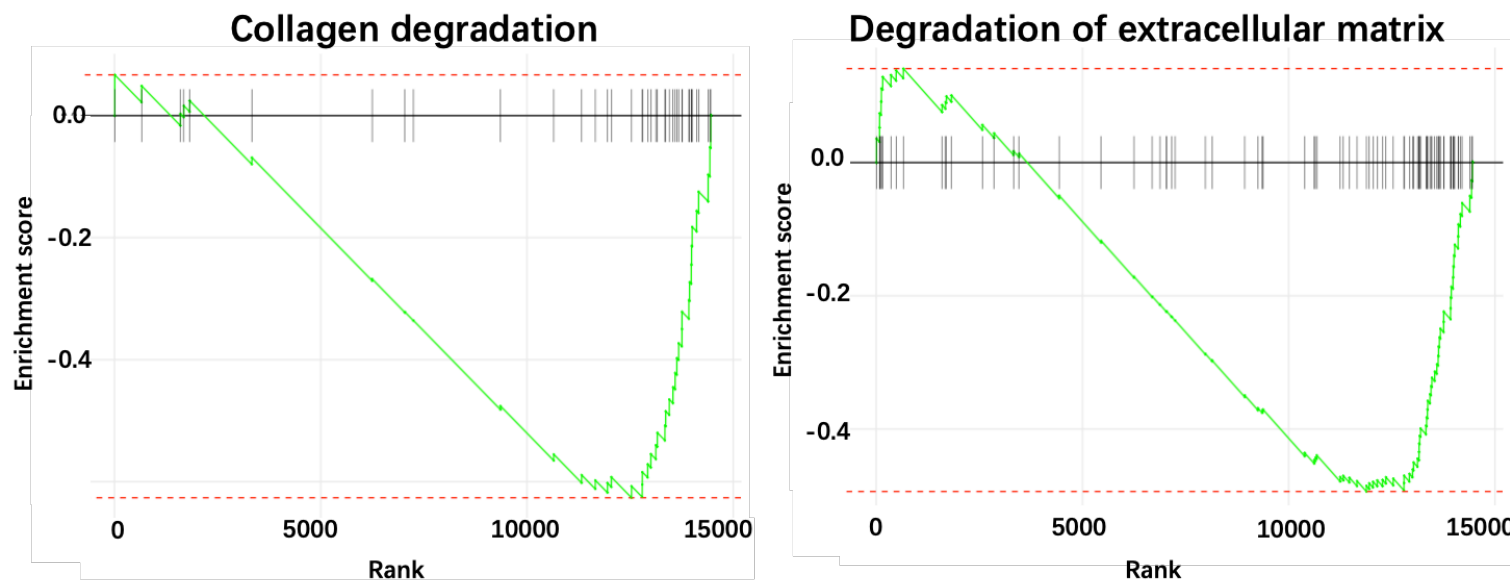
5.2.6. RNA-seq data analysis of WT mice pre- and post-DMM surgery at 11-week-old

Prior to completing our histological analysis of DMM-induced OA in the different miRNA-null mice, and given the previous literature linking miR-140 loss on increased ageing and surgically-induced OA (Miyaki, Sato et al. 2010), we undertook experiments to begin to unravel how miR-140 increased the susceptibility to the disease using an RNA-seq approach of articular cartilage pre- and post-DMM.

When comparing RNA-seq data of WT mice 3-, 7- and 42-days post-DMM surgery at 11-weeks of age to that of WT mice pre-DMM surgery, we identified 3268, 4823 and 1543 genes that were significant differentially expressed (FDR < 0.05), respectively. GSEA analysis revealed that 204 pathways were significantly enriched (adjust *p*-value < 0.05) in WT chondrocytes 3-days post-DMM surgery at 11-weeks old age when compared to WT chondrocytes pre-DMM surgery, of which 'cellular senescence', 'collagen degradation' and 'degradation of the extracellular matrix' pathways were all significantly enriched in the down-regulated genes of WT chondrocytes 3-days post-DMM (Fig. 5.17). However, for WT chondrocytes 7-days post-DMM surgery, when compared to WT chondrocytes pre-DMM surgery, there were 276 pathways that were significantly enriched (adjust *p*-value < 0.05) in the up-regulated genes of WT chondrocytes 7-days post-DMM, including 'collagen degradation', 'degradation of the extracellular matrix' and 'activation of matrix metalloproteinases' pathways (Fig. 5.18). There were 359 pathways significantly enriched (adjust *p*-value < 0.05) in the up-regulated genes of WT chondrocytes 42-days post-DMM surgery when compared to WT chondrocytes pre-DMM, such as 'collagen degradation' and 'degradation of the extracellular matrix' pathways (Fig. 5.19). The explanation could be that at day 3 post-DMM surgery, though surgery has occurred, the mice are given analgesics, which may suppress normal levels of these pathways. The mouse limb is also held stable with staples to help the wound heal. This could prevent the normal loading biomechanics and thus alter the expression of what is a normal cartilage

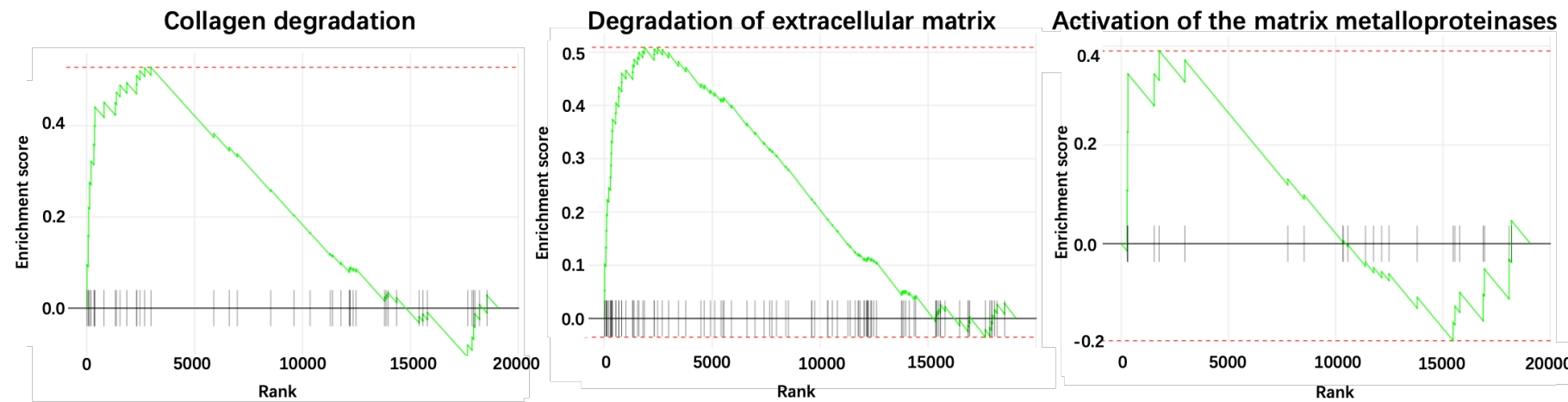
homeostatic mechanism. Published work has demonstrate that joint immobilisation can prevent DMM-induced OA (Burleigh, Chanalaris et al. 2012) and experience in our laboratory has shown that retaining staples for the 8-week post-DMM also diminishes cartilage OA histological scores (unpublished data). Taken together, this confirmed that DMM surgery triggered knee articular cartilage degradation at least later than 3-days post-DMM surgery.

Figure 5.17 GSEA enrichment of pathways in WT mouse knee cartilage RNA-seq data 3 days post-DMM treatment



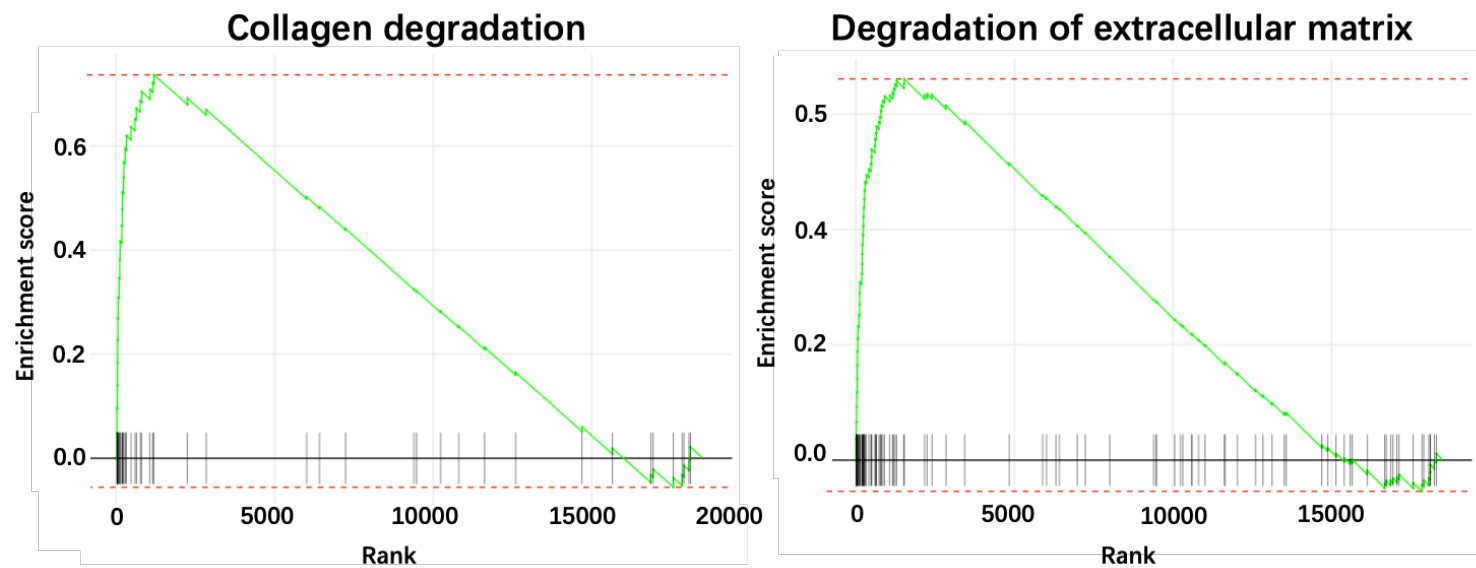
Enrichment analysis on GSEA results (FDR q-value < 0.05) showing affected cellular programs in WT knee cartilage 3 days post-DMM surgery. 'Collagen degradation' and 'degradation of the extracellular matrix' pathways were significantly enriched in the down-regulated genes in WT mice 3-days post-DMM surgery when compared to WT mice pre-DMM surgery.

Figure 5.18 GSEA enrichment of pathways in WT mouse knee cartilage RNA-seq data 7 days post-DMM treatment



Enrichment analysis on GSEA results (FDR q-value < 0.05) showing affected cellular programs in WT knee cartilage 7 days post-DMM surgery. 'Collagen degradation', 'degradation of the extracellular matrix' and 'activation of the matrix metalloproteinases' pathways were significantly enriched in the up-regulated genes in WT mice 7-days post-DMM surgery when compared to WT mice pre-DMM surgery.

Figure 5.19 GSEA enrichment of pathways in WT mouse knee cartilage RNA-seq data 42 days post-DMM treatment



Enrichment analysis on GSEA results (FDR q-value < 0.05) showing affected cellular programs in WT knee cartilage 42 days post-DMM surgery. 'Collagen degradation' and 'degradation of the extracellular matrix' pathways were significantly enriched in the up-regulated genes in WT mice 42-days post-DMM surgery when compared to WT mice pre-DMM surgery.

5.2.7. RNA-seq data analysis of *Mir140*-null medial knee articular cartilage 3-

days post-DMM surgery

DMM surgery was performed on 11-week-old male WT and *Mir140*-null mice and RNA was extracted from murine knee cartilage 3 days post-DMM essentially as described previously. The RNA subsequently sequenced to obtain a quantitative and unbiased identification of differentially expressed genes (DEGs). DEG analysis identified 284 up- and 281 down-regulated genes with a fold change > 1.5 and FDR threshold ≤ 0.05 in the comparison of *Mir140*-null mice vs. WT mice (blue dots in the volcano plot in Fig. 5.20A).

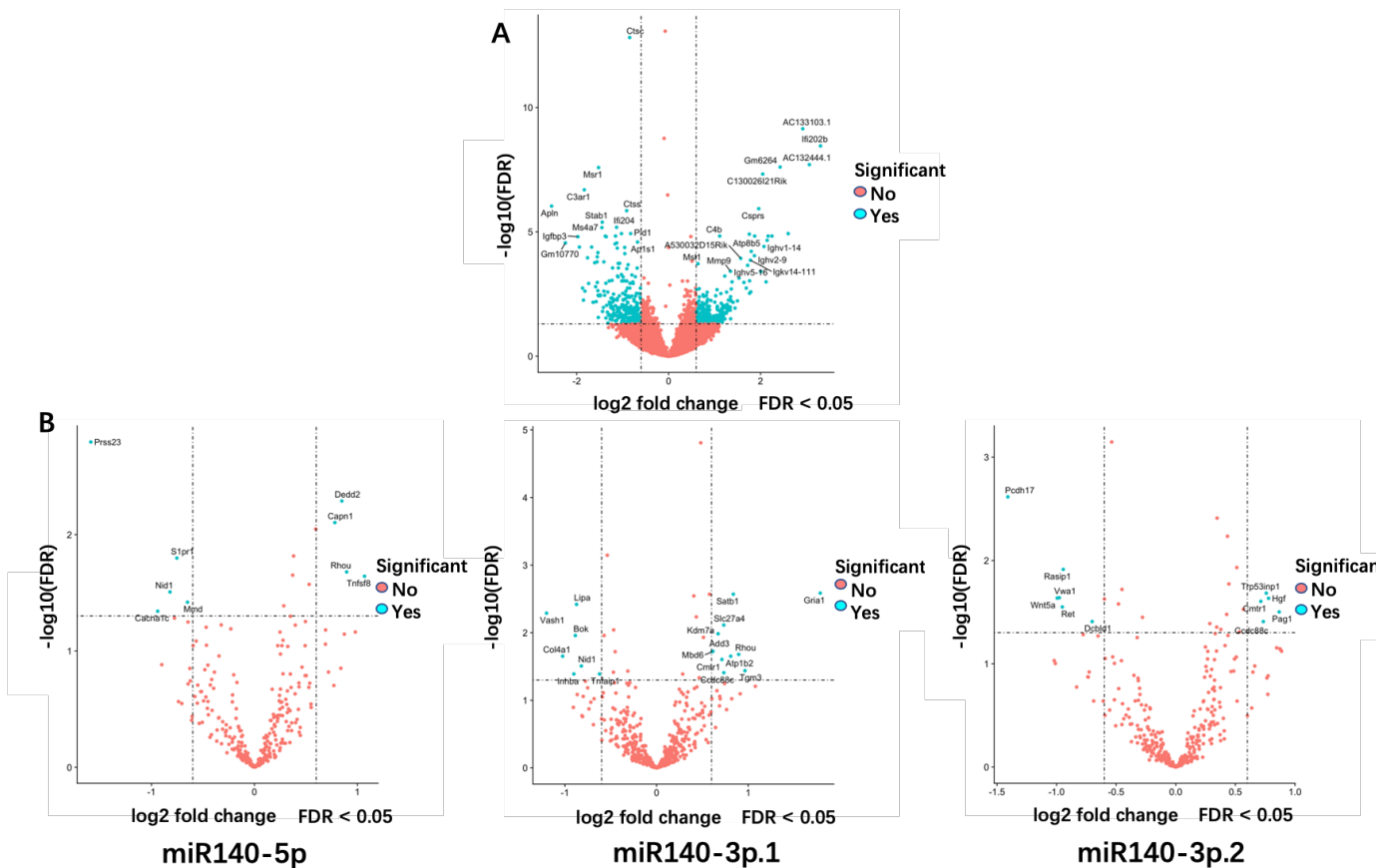
When comparing target prediction data (TargetScan 7.2; conserved) to the RNA-seq results, four predicated miR-140-5p target genes were significantly DEGs (Fig. 5.21B-left). There were ten predicted miR-140-3p.1 target genes and five predicted miR-140-3p.2 target genes that were significantly differentially expressed in *Mir140*-null knee cartilage when compared to WT knee cartilage (Fig. 5.20B-middle and right).

In all there were 781 significant DEGs (FDR threshold ≤ 0.05), a heatmap was generated to visualise the differences of gene expression between WT and *Mir140*-null mice (Fig. 5.21). The differentially expressed genes caused clear hierarchical separation of WT and *Mir140*-null samples.

For GSEA analysis, in total 68 gene pathways were enriched in the up-regulated genes in our *Mir140*-null mice when compared to WT mice, in contrast, 11 gene pathways were enriched for down-regulated genes. There were two pathways that were significantly enriched in up-regulated genes: 'cellular senescence' (due to the presence of genes: *ps6ka1*, *Hist1h3h*, *Rps6ka2*, *Hist1h3c*, *Kdm6b*, *Mapk14*, *Cbx6*, *Hist1h4h*), and 'metalloprotease DUBs' (*Hist3h2a*, *Hist1h2ad*, *Hist1h2ag*, *Nlrp3*, *Hist1h2ai*, *Hist1h2ap*, *Hist1h2ab*, *Hist2h2aa1*, *Hist2h2aa2*, *Hist1h2ae*, *Hist2h2ac*, *Bard1*, *Ep300*, *Stambpl1*, *Hist2h2ab*, *Hist1h2ac*, *Stambp*, *Hist1h2ao*, *Babam2*, *Hist1h2an*, *Kat2b*). There was one pathway that was significantly enriched in the

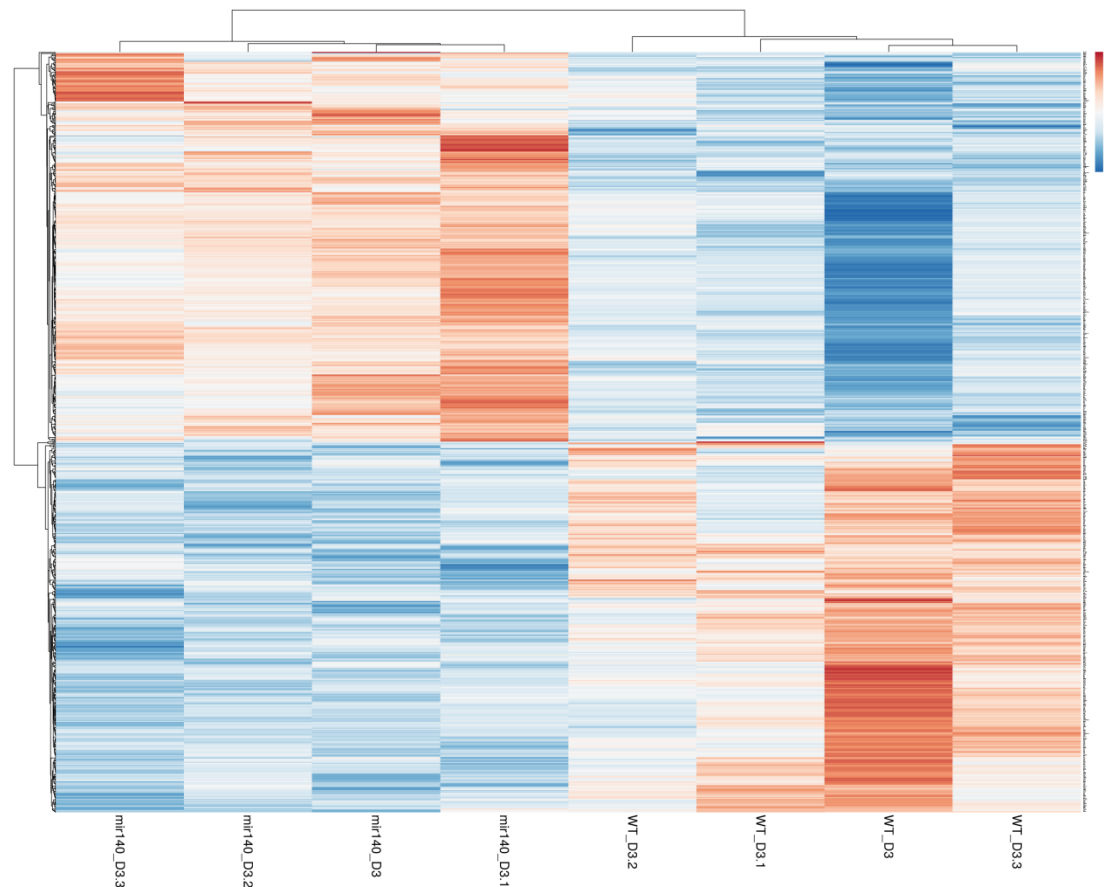
down-regulated genes in *Mir140*-null knee cartilage: 'collagen formation' (due to the presence of genes: *Col4a2*, *Col4a1*, *Pxdn*, *Ctss*, *Loxl3*, *Col8a1*, *Mmp13*, *P4ha1*, *Col20a1*, *Ctsb*, *Col18a1*, *Col5a3*, *Col6a3*, *Col12a1*, *Col10a1*, *Serpinh1*, *Loxl2*, *Dst*) (Fig. 5.22). Compared to the data shown in the Section 5.2.3, fewer significant pathways were identified after DMM surgery, indicating articular cartilage homeostasis had shifted when injury occurred to knee.

Figure 5.20 The disruption of differentially expressed genes in *Mir140*-null murine knee cartilage with 3-days post-DMM treatment relative to control mice



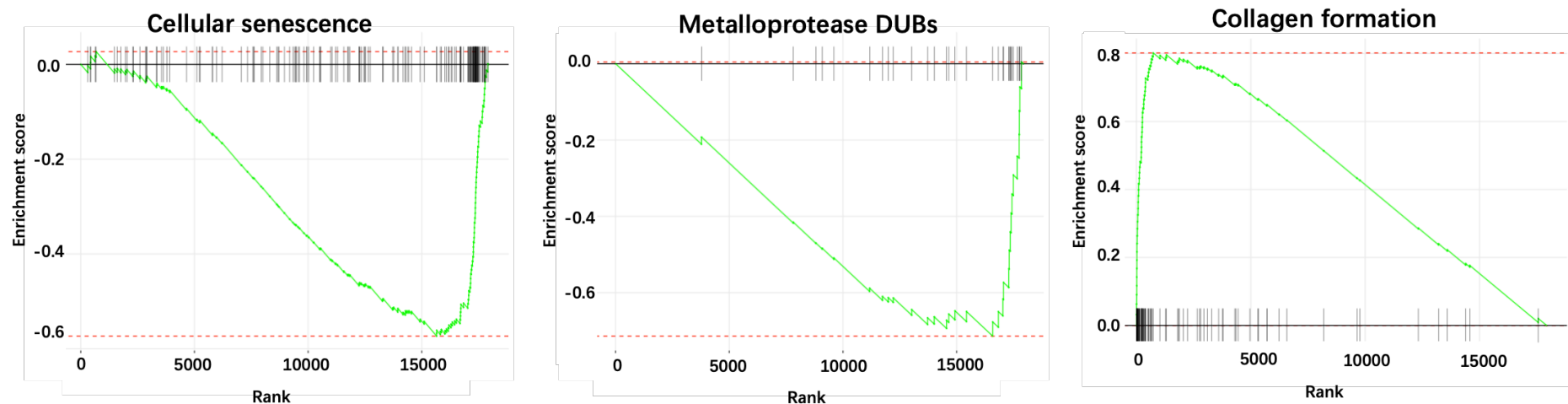
(A) A Volcano plot of gene fold-change (Log_2 , X axis) against $-\text{Log}_{10}$ FDR (false discovery rate, Y axis) between miR-140^{-/-} and WT, demonstrating the distribution of upregulated genes and downregulated genes. The vertical red lines correspond to $\pm 0.6 \text{ log}_2$ foldchange (equivalent to 1.5-fold change). The red horizontal line denotes an FDR of 0.05. Red points represent all significantly differentially expressed genes with an FDR p value ≤ 0.05 and fold change ≥ 1.5 . In total, 284 genes were found to be significantly downregulated and 281 genes to be significantly upregulated in miR-140^{-/-} mice. (B) Volcano plots demonstrating the significantly up-regulated and down-regulated predicted target genes of miR-140 (miR-140-5p (left), miR-140-3p.1 (centre), and miR-140-3p.2 (right)) in miR-140^{-/-} cartilage 3 days post-DMM surgery at 11-week-old. The volcano plots were generated in R studio.

Figure 5.21 Profile of significant differentially expressed genes expression in murine knee cartilage between WT and *Mir140*-null mice that are 3-days post DMM surgery



Heatmap of the relative expression of the top 781 differentially expressed genes (FDR ≤ 0.05) in WT versus *Mir140*-null knee cartilage 3 days post-DMM surgery (n=4/genotype). Heatmap was generated as previously described.

Figure 5.22 GSEA enrichment of miR-140^{-/-} gene sets in mouse knee cartilage RNA-seq data 3 days post-DMM



Enrichment analysis on GSEA results (FDR q-value < 0.05) showing affected cellular programs in *Mir140*-null knee cartilage 3 days post-DMM surgery. 'Collagen formation' pathway was significantly enriched in the down-regulated genes in miR-140^{-/-} mice when compared to WT mice. However, 'Cellular senescence' and 'Metalloprotease DUBs' pathways were significantly enriched in the up-regulated genes in miR-140^{-/-} mice.

5.2.8. RNA-seq data analysis of *Mir140*-null medial knee articular cartilage 7-

days post DMM surgery at 11-week-old

DMM surgery was performed on 11-week-old male WT and *Mir140*-null mice and RNA was extracted from murine knee cartilage 7 days post-DMM essentially as described previously. The RNA subsequently sequenced to obtain a quantitative and unbiased identification of differentially expressed genes (DEGs). DEG analysis identified 75 up- and 87 down-regulated genes with a fold change > 1.5 and FDR threshold ≤ 0.05 in the comparison of *Mir140*-null mice vs. WT mice (blue dots in the volcano plot in Fig. 5.23A).

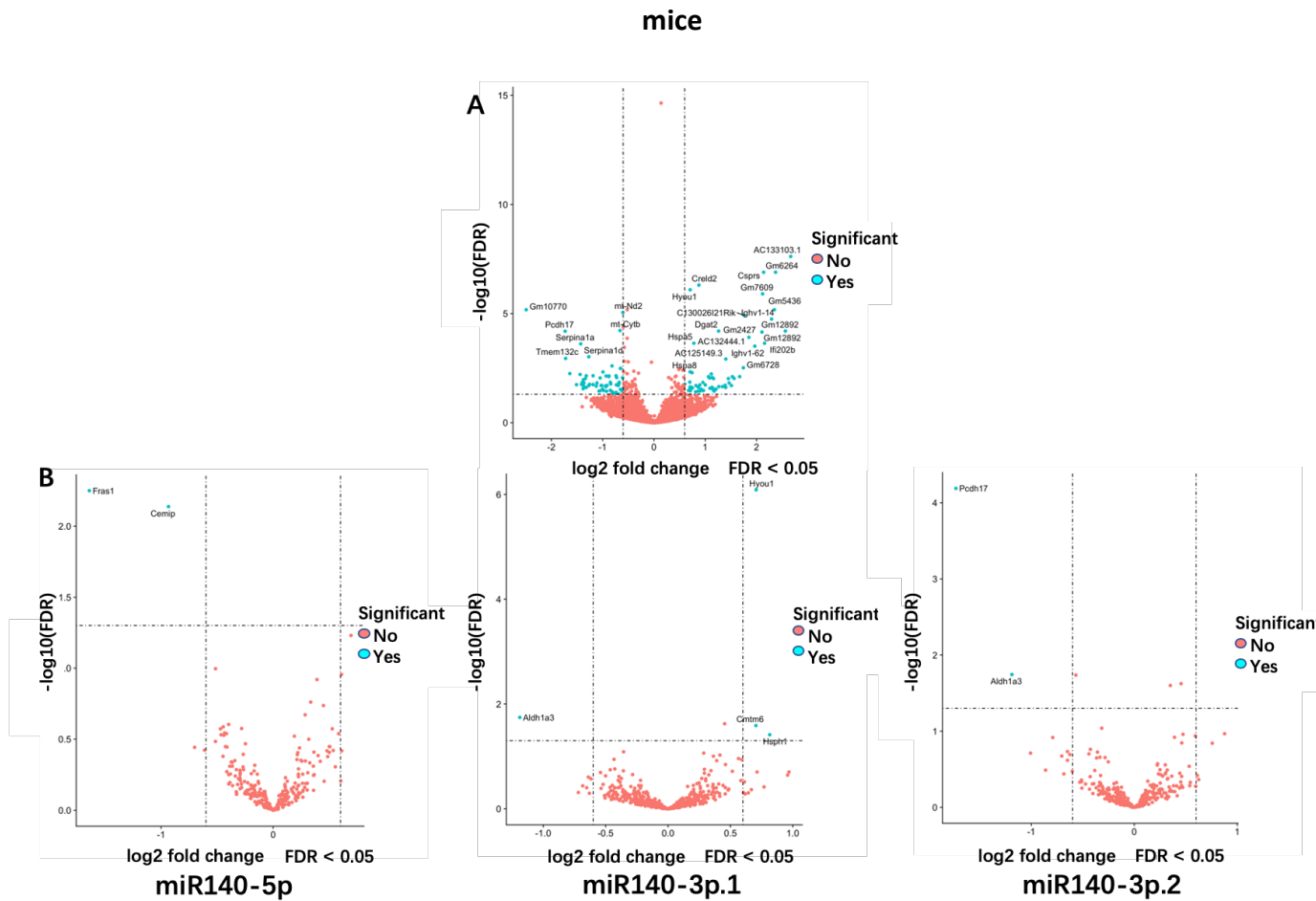
When comparing target prediction data (TargetScan 7.2; conserved) to the RNA-seq results, no predicated miR-140-5p or miR-140-3p.2 target gene was significantly up-regulated in *Mir140*-null knee cartilage chondrocytes (Fig. 5.23B-left and right). There were three predicted miR-140-3p.1 target genes that were significantly differentially expressed in *Mir140*-null knee chondrocytes when compared to WT knee chondrocytes (Fig. 5.23B-middle).

For all 197 significant differentially expressed genes (FDR threshold ≤ 0.05), a heatmap was generated to visualise the differences of gene expression between WT and *Mir140*-null mice (Fig. 5.24). The differentially expressed genes of WT and *Mir140*-null samples were well segregated.

For GSEA analysis, in total 142 gene pathways were enriched in the up-regulated genes in our *Mir140*-null mice when compared to WT mice, in contrast, 45 gene pathways were enriched for down-regulated genes in *Mir140*-null mice. There were two pathways that were significantly enriched in up-regulated genes in *Mir140*-null knee cartilage: 'cellular senescence' (due to the presence of genes: *Rps6ka1*, *Ccne1*, *Cbx8*, *Ccna2*, *Fzr1*, *Hist1h2ao*, *Rb1*, *Hist1h3h*, *Mapk10*, *Hist1h4a*, *Hist1h1d*, *H2afx*, *Rps6ka2*), and 'Metalloprotease DUBs' (*Bard1*, *Hist1h2ao*, *Nlrp3*, *Hist1h2ai*, *Ep300*, *Hist1h2ab*, *Hist1h2ag*, *Hist3h2a*, *Hist2h2ab*, *Hist1h2ae*, *Hist2h2ac*, *Hist2h2aa2*,

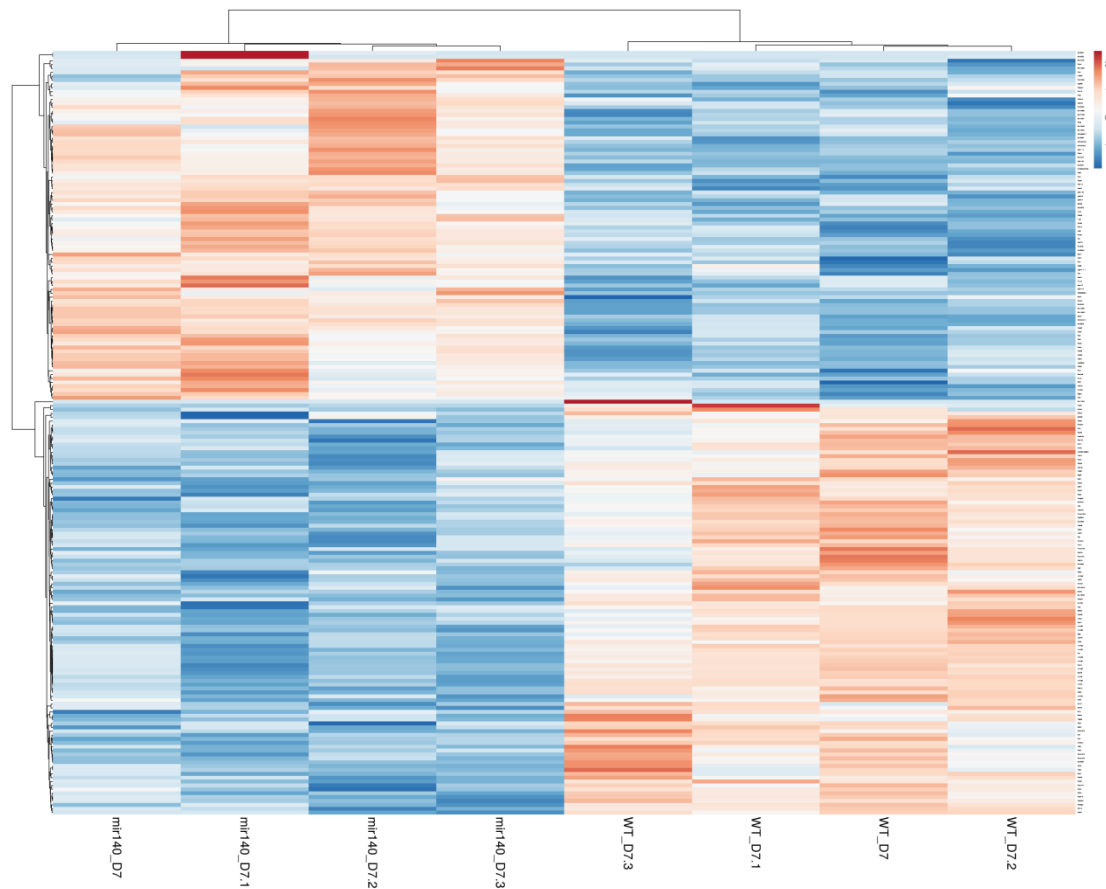
Brca1, Hist1h2ac, Hist2h2aa1, Ubc, Mysm1). There were two pathways that were significantly enriched in the down-regulated genes in *Mir140*-null knee cartilage and are: 'Collagen degradation' (due to the presence of genes: *Col7a1, Ctsk, Col10a1, Col4a3, Col8a1, Mmp14, Mmp13, Col12a1, Col18a1, Col4a4, Mmp9, Col11aM1, Col5a2, Mmp11*); 'Degradation of the extracellular matrix' (due to the presence of genes: *Capn11, Col7a1, Ctsk, Adamts4, Col10a1, Col4a3, Col8a1, Spp1, Dcn, Timp1, Mmp14, Lamc2, Mmp16, Mmp13*) (Fig. 5.25). Compared to the data showed in the Section 5.2.3, collagen degradation, degradation of the extracellular matrix and cellular senescence pathways are regulated in the opposite direction, indicating knee traumatic injury associated with depletion of miR-140 has changed knee cartilage microenvironment.

Figure 5.23 The genes differentially expressed in *Mir140*-null murine knee cartilage with 7-days post-DMM treatment relative to control



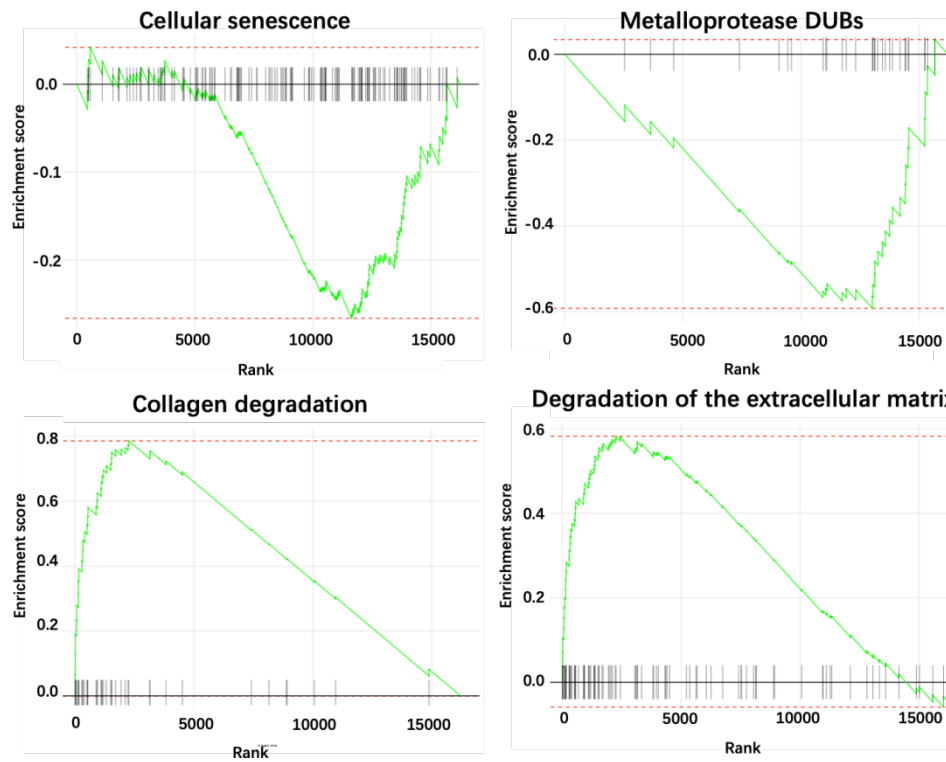
(A) A Volcano plot of gene fold-change (Log_2 , X axis) against $-\text{Log}_{10}$ FDR (false discovery rate, Y axis) between miR-140^{-/-} and WT, demonstrating the distribution of upregulated genes and downregulated genes. The vertical red lines correspond to $\pm 0.6 \text{ log}_2$ foldchange (equivalent to 1.5-fold change). The red horizontal line denotes an FDR of 0.05. Red points represent all significantly differentially expressed genes with an FDR p value ≤ 0.05 and fold change ≥ 1.5 . In total, 75 genes were found to be significantly downregulated and 87 genes to be significantly upregulated in miR-140^{-/-} mice. (B) Volcano plots demonstrating the significantly up-regulated and down-regulated predicted target genes of miR-140 (miR-140-5p (left), miR-140-3p.1 (centre), and miR-140-3p.2 (right)) in miR-140^{-/-} cartilage 7 days post-DMM surgery at 11-week-old. The volcano plots were generated in R studio.

Figure 5.24 Profile of significant differentially expressed genes expression in murine knee cartilage between WT and *Mir140*-null mice 7-days post DMM surgery



Heatmap of the relative expression of the top 197 differentially expressed genes (FDR ≤ 0.05) in WT versus *Mir140*-null knee cartilage 7 days post-DMM surgery (n=4/genotype). Heatmap was generated as previously described.

Figure 5.25 GSEA enrichment of pathways in $\text{miR-140}^{-/-}$ mouse knee cartilage RNA-seq data 7 days post-DMM treatment



Enrichment analysis on GSEA results (FDR q-value < 0.05) showing affected cellular programs in *Mir140*-null knee cartilage 7 days post-DMM surgery. ‘Collagen degradation’ and ‘degradation of the extracellular matrix’ pathways were significantly enriched in the down-regulated genes in $\text{miR-140}^{-/-}$ mice when compared to WT mice. However, ‘cellular senescence’ and ‘metalloprotease DUBs’ pathways are significantly enriched in the up-regulated genes in $\text{miR-140}^{-/-}$ mice.

5.2.9. RNA-seq data analysis of *Mir140*-null medial knee articular cartilage 42-

days post DMM surgery at 11-week-old

DMM surgery was performed on 11-week-old male WT and *Mir140*-null mice and RNA was extracted from murine knee cartilage 42 days post-DMM essentially as described previously. The RNA subsequently sequenced to obtain a quantitative and unbiased identification of differentially expressed genes (DEGs). DEG analysis identified 292 up- and 308 down-regulated genes with a fold change > 1.5 and FDR threshold ≤ 0.05 in the comparison of *Mir140*-null mice vs. WT mice (blue dots in the volcano plot in Fig. 5.26A).

When comparing target prediction data (TargetScan 7.2; conserved) to the RNA-seq results of knee chondrocytes, only seven predicated miR-140-5p target gene was significantly differentially expressed (Fig. 5.26B-left). There were two predicted miR-140-3p.1 and two predicted miR-140-3p.2 target genes that passed our significance threshold when comparing the WT versus *Mir140*-null knee cartilage data (Fig. 5.26B-middle and right).

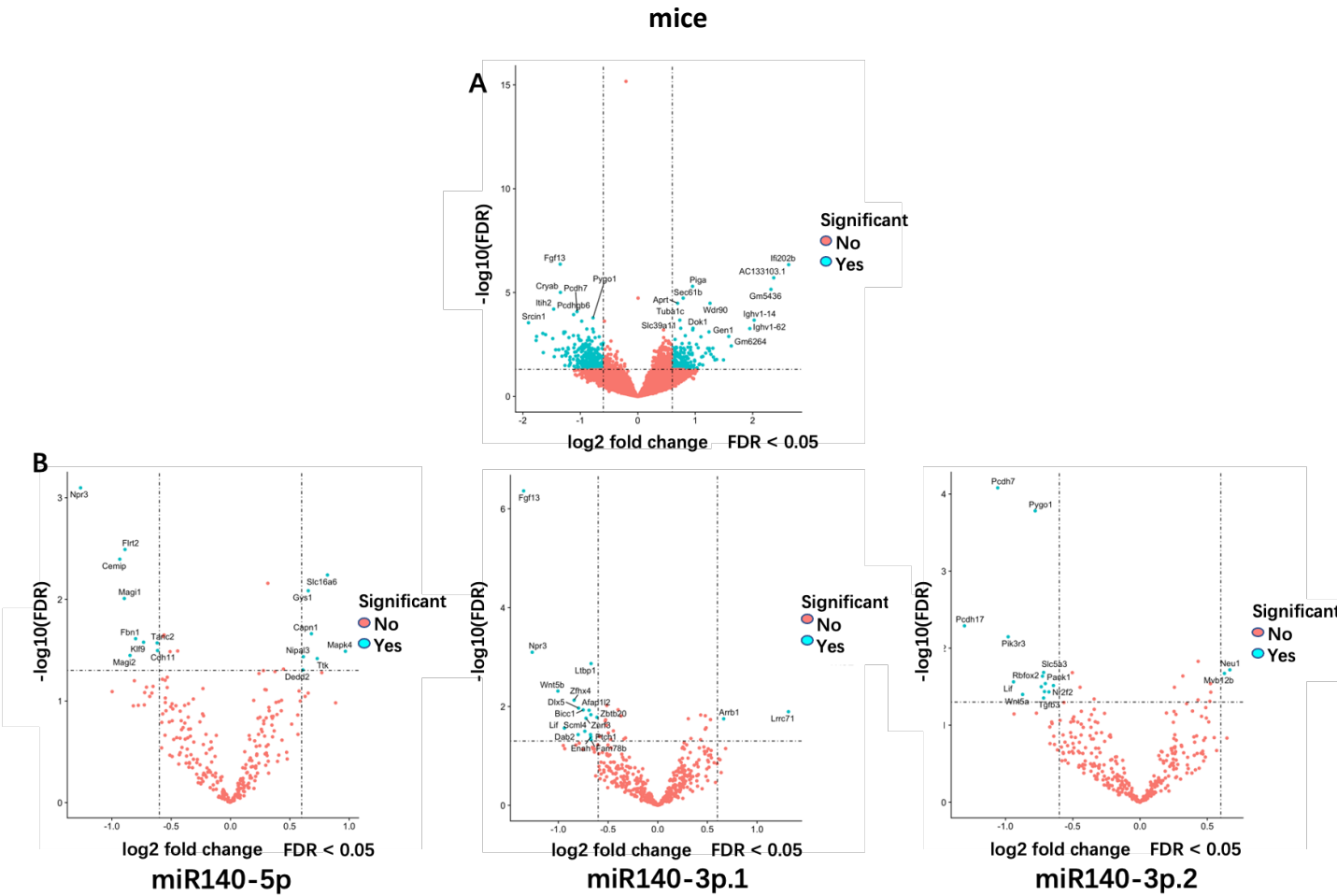
Given that only 946 genes were significant differentially expressed genes (FDR threshold ≤ 0.05), a heatmap was generated to visualise the differences of gene expression between WT and *Mir140*-null mice (Fig. 5.27). The differentially expressed genes caused clear hierarchical separation of WT and *Mir140*-null samples.

Gene Set Enrichment Analysis (GSEA) was used as pathway analysis to compare between WT and *Mir140*-null mice. Pathways with a False discovery rate values (FDR) below 0.05 were classified as GSEA significant. In total 324 gene pathways were enriched for up-regulated genes in our *Mir140*-null mice when compared to WT mice. In contrast, 78 gene pathways were enriched for down-regulated genes in *Mir140*-null mice. There are five pathways that significantly enriched in up-regulated genes in *Mir140*-null knee cartilage chondrocytes: 'apoptosis' (due to the presence

of genes: *Cdh1*, *Bmx*, *Hist1h1d*, *Hmgb2*, *Casp3*, *Casp7*, *Hist1h1c*, *Hist1h1e*, *Hist1h1b*, *Gas2*, *Hist1h1a*, *Tradd*, *Bid*, *Bak1*, *Dsp*, *Lmnb1*); ‘cellular senescence’ (due to the presence of genes: *Uba52*, *Ccne2*, *Hist1h1a*, *Cdk4*, *Ccne1*, *H2afj*, *Rps6ka2*, *Hist1h2ao*, *Cdk6*, *Lmnb1*); ‘HDACs deacetylate histones’ (due to the presence of genes: *Hist1h3h*, *Hist1h4n*, *Hist1h3c*, *Hist1h4h*, *Hist2h4*, *Hist1h3f*, *Hist1h4k2*); ‘metalloprotease DUBs’ (*Hist1h2ad*, *Hist1h2ai*, *Hist3h2a*, *Hist1h2ag*, *Hist1h2ab*, *Hist1h2ac*, *Bard1*, *Hist1h2ap*, *Hist2h2aa1*, *Brca1*, *Hist2h2aa2*, *Hist1h2ae*, *Hist2h2ab*, *Hist2h2ac*, *Uba52*, *Hist1h2ao*); and ‘programmed cell death’ (due to the presence of genes: *Cdh1*, *Bmx*, *Hist1h1d*, *Hmgb2*, *Casp3*, *Casp7*, *Hist1h1c*, *Hist1h1e*, *Hist1h1b*, *Uba52*, *Gas2*, *Hist1h1a*, *Tradd*, *Bid*, *Bak1*, *Dsp*, *Lmnb1*). There is one pathway that significantly enriched in the down-regulated genes in *Mir140*-null knee cartilage chondrocytes: ‘collagen degradation’ (due to the presence of genes: *Col10a1*, *Col6a6*, *Col13a1*, *Col6a3*, *Col3a1*, *Col5a2*, *Col6a1*, *Col15a1*, *Col6a2*, *Mmp2*, *Mmp13*, *Col18a1*, *Col5a1*, *Col5a3*, *Mmp11*) (Fig. 5.28). Compared to the data showed in the Chapter 5.2.3, more pathways like apoptosis, HDACs deacetylate histones and programmed cell death pathways are significantly enriched in up-regulated genes in *Mir140*-null knee cartilage chondrocytes.

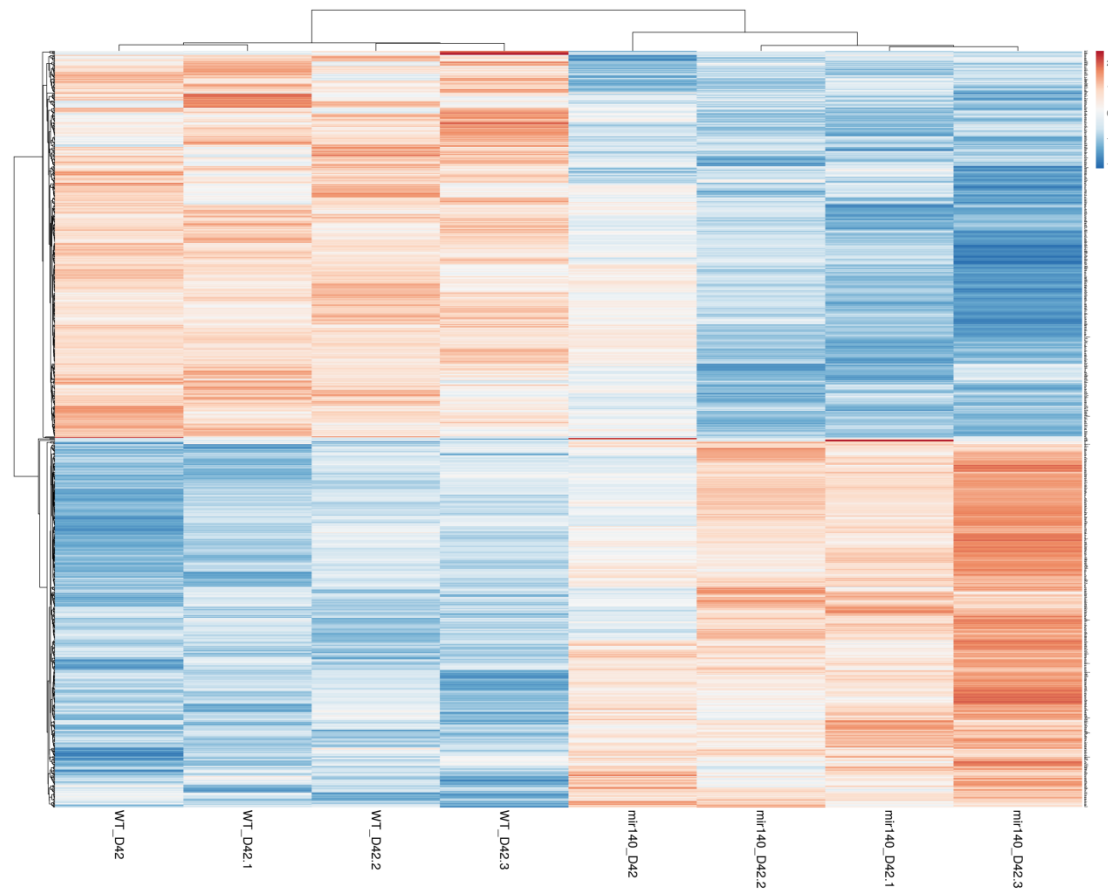
We found aggrecan staining loss in *Mir140*-null knee articular cartilage when compared to WT control mice, thus a time course of expression of genes involved in ECM proteoglycans pathway was generated (Fig. 5.29), which showed the expression of *Bgn*, *Matn4*, *Chst11*, and *ACAN* changed during the day before DMM surgery to 42-days post DMM surgery, with the expression level of these genes lower in *Mir140*-null knee cartilage when compared to WT knee cartilage, in agreement with DMM histological analysis.

Figure 5.26 The genes differentially expressed in *Mir140*-null murine knee cartilage with 42-days post-DMM treatment relative to control



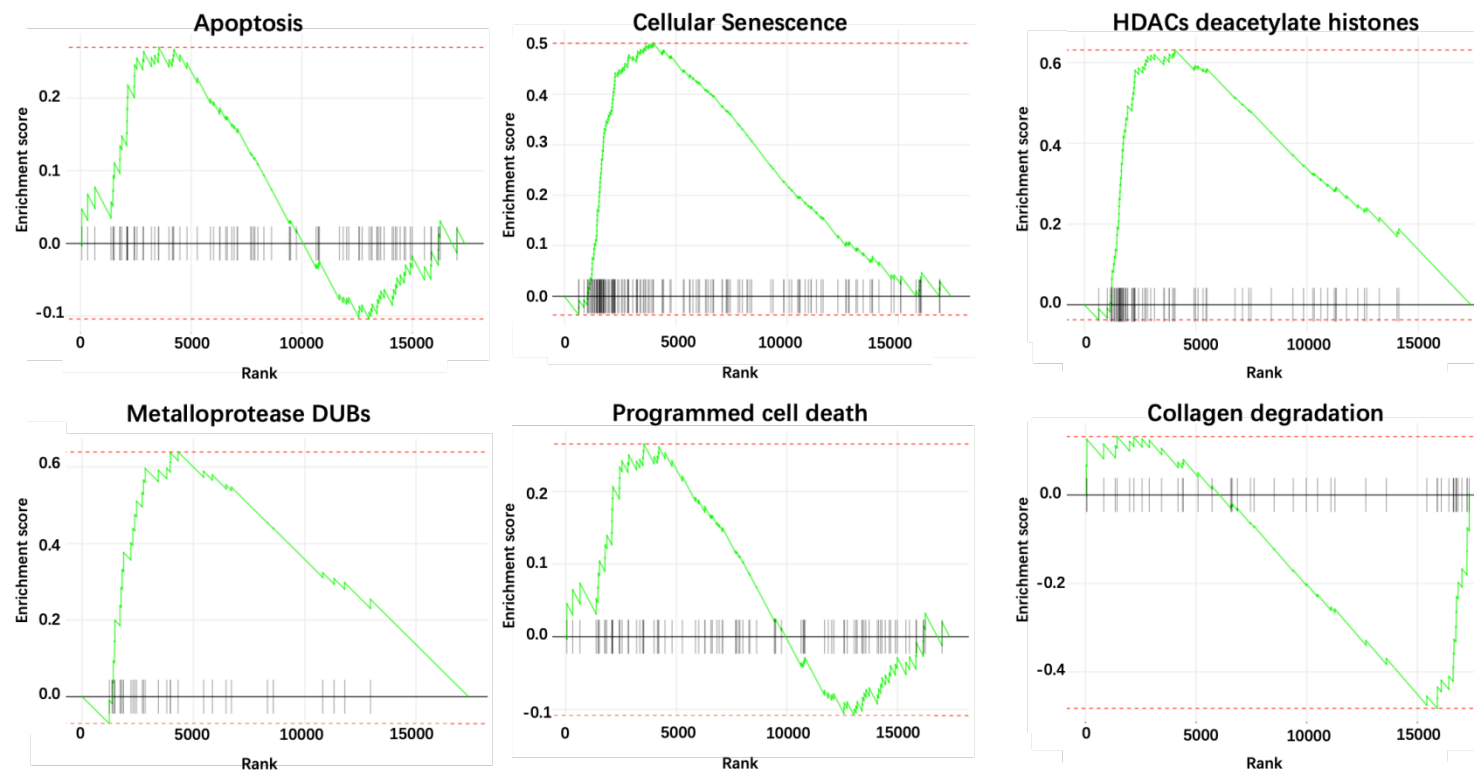
(A) A Volcano plot of gene fold-change (Log_2 , X axis) against $-\text{Log}_{10}$ FDR (false discovery rate, Y axis) between miR-140^{-/-} and WT, demonstrating the distribution of upregulated genes and downregulated genes. The vertical red lines correspond to $\pm 0.6 \text{ log}_2$ foldchange (equivalent to 1.5-fold change). The red horizontal line denotes an FDR of 0.05. Red points represent all significantly differentially expressed genes with an FDR p value ≤ 0.05 and fold change ≥ 1.5 . In total, 292 genes were found to be significantly downregulated and 308 genes to be significantly upregulated in miR-140^{-/-} mice. (B) Volcano plots demonstrating the significantly up-regulated and down-regulated predicted target genes of miR-140 (miR-140-5p (left), miR-140-3p.1 (centre), and miR-140-3p.2 (right)) in miR-140^{-/-} cartilage 42 days post-DMM surgery at 11-week-old. The volcano plots were generated in R studio.

Figure 5.27 Profile of significant differentially expressed genes in murine knee cartilage between WT and *Mir140*-null mice 42-days post-DMM surgery



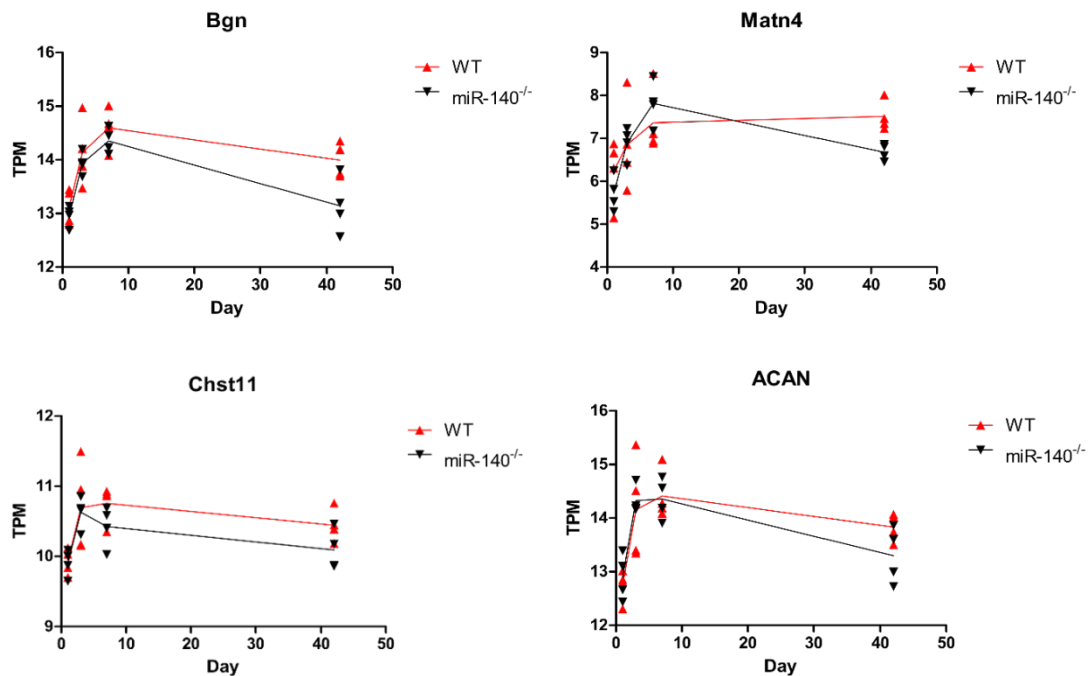
Heatmap of the relative expression of the top 462 differentially expressed genes (FDR ≤ 0.05) in WT versus *Mir140*-null knee cartilage 42 days post-DMM surgery (n=4/genotype). Heatmap was generated as previously described.

Figure 5.28 GSEA enrichment of pathways in miR-140^{-/-} mouse knee cartilage RNA-seq data 42 days post-DMM surgery



Enrichment analysis on GSEA results (FDR q-value < 0.05) showing affected cellular programs in *Mir140*-null knee cartilage 42 days post-DMM surgery. ‘Apoptosis’, ‘cellular senescence’, ‘HDACs deacetylate histones’, ‘metalloprotease DUBs’ and ‘programmed cell death’ pathways were significantly enriched in the up-regulated genes in miR-140^{-/-} mice when compared to WT mice. However, ‘collagen degradation’ pathway was significantly enriched in the down-regulated genes in miR-140^{-/-} mice.

Figure 5.29 ECM proteoglycan pathways gene expression time-course following DMM induction



Expression of genes involved in the ECM proteoglycans pathway time-course from 1-day pre-DMM surgery to 42 days post-DMM surgery.

5. 3. Discussion

Our previous data showed that the expression level of miR-140-5p and miR-455-3p were highly increased in adult human hip OA articular cartilage compared with human healthy articular cartilage (Swingler, Wheeler et al. 2012). In contrast, Miyaki et al. showed the reverse (Miyaki, Nakasa et al. 2009). Although contradictory, these results indicate miR-140 and miR-455 participate in human OA pathogenesis. Accelerated articular cartilage degeneration was observed recently in 12-mo-old *Mir455*-null mice (Mao, Kang et al. 2019), and although several years ago the loss of miR-140 in mice was reported to accelerate OA progression induced by surgery or ageing (Miyaki, Sato et al. 2010), the mechanisms of action of miR-140 and miR-455 in OA pathogenesis remain to be characterised in detail. The DMM mouse model (section 2.2.8) is considered to have a slow induction of OA progression and provide good reproducibility (Glasson, Blanchet et al. 2007). Thus, this model reflects human OA features and has become the most commonly selected approach to study OA (Miyaki, Sato et al. 2010, Lorenz and Grassel 2014, O'Brien, Philpott et al. 2017, Cornelis, de Roover et al. 2019, Wang, Zhao et al. 2019). Consequently, the aim of this chapter was to verify and compare the effect of miR-140 and/or miR-455 on OA pathogenesis using a DMM surgery-induced OA model, and to explore the potential underlying mechanisms.

5. 3. 1. Selection of optimal histological assessment

Currently, there are limited publications that describe histological assessment systems for either murine and or human knee OA damage. The Glasson assessment (system 1) is a semi-quantitative scoring system that is relatively easy to apply for both experienced and novice scorers due to its simple and clear scale of marks (grade range: 0-6) (Glasson, Chambers et al. 2010). This method provides a rapid evaluation of histological changes for murine knee articular cartilage. However, the narrow scoring range is unable to distinguish moderate articular damage (Fig. 5.1). Compared to system 1 (Glasson/OARSI scoring system), system 2 (OOCHAS) provides a more detailed standard for evaluation. A grade is assigned to articular cartilage damage in vertical depth (six grades) and abnormal articular cartilage area (four grades) or volume of abnormal articular cartilage (four grades) and combined to generate a final score (grade range: 0-25) for evaluation. Applied use of these systems has shown it is

suitable for evaluating damage of both the large knee joint (such as the human knee) and a small knee joint (i.e., mouse) (Pritzker, Gay et al. 2006). System 3 provides a comprehensive histological scoring system that is suitable for murine knee OA following either surgery-induced or spontaneously occurring damage. Similar to system 2, system 3 offers grading in articular cartilage structure and safranin-O staining, and also provides a more detailed scale of marks (12 grades for each). In addition, system 3 includes chondrocyte death as part of the evaluation which is not included in the other OA schemes.

Inter-scorer consistency is critical in creating valid and reliable results and allows multiple observers to evaluate the data to yield the most reproducible results. In this regard, system 3 (III B) showed the highest inter-scorer consistency amongst the scoring schemes at the MFC, although this was not significant. However, system 2 (II B) showed the highest inter-scorer consistency at the MFC and (II C) provided the highest inter-scorer consistency at the MTP. Furthermore, system 2 also gave the most extensive score range. Taken together, system 2 (OOCHAS) was selected for further histological assessment.

5. 3. 2. Evaluation of articular cartilage damage in the different genotypes

To evaluate the severity of OA in murine articular cartilage in the absence of either microRNA alone or combination, we applied DMM-induced OA model and the OOCHAS scheme. Our data showed that the loss of either miR-140 or miR-455 *in vivo* did not accelerates OA-like structural changes in the MFC or MTP. However, disruption of miR-140 and/or miR-455 induced a significant decrease in proteoglycan staining compared to WT control animals, which is reflected in higher scores (Fig. 5.5). Cartilage consists of two predominant cartilage-specific/selective extracellular matrix macromolecules, collagen (mainly Type II) and proteoglycans, predominately aggrecan. Disruption of miR-140 and/or miR-455 resulted in significantly less proteoglycan staining in the medial knee joint compared to WT animals, consistent with our costal chondrocyte RNA-seq results that showed that miR-140 and miR-455 were significantly involved in the regulation of GAG metabolism pathways (section 4.2.5.2 and section 4.2.7.1). Furthermore, *Mir455*-null mice showed less proteoglycan staining relative to *Mir140*-null mice. This is consistent with our previous histological staining finding that proteoglycan staining loss was observed in *Mir455*-null mice at P22 compared to other genotypes (section 3.2.1.4). Moreover, loss of

both miR-140 and miR-455 seem not to play a synergistic role to accelerate OA progression in surgical model. Since we performed the OOCHAS scheme in this experiment, the overall score (grade x stage) revealed that *Mir455*-null and DKO mice induced more severe OA-like damage in MFC than WT animals. *Mir140*-null mice showed a higher score than WT controls, but this was not significant, possibly due to the low animal numbers used in this research, particularly for the *Mir140*-null mice. These data suggest that miR-140 and miR-455, normally exert a protective effect in articular cartilage.

To address the mechanism of cartilage degradation in miRNA-null mice, we evaluated proteoglycan staining in the lateral knee joint of different genotypes (the opposite side to which structural damage is generally observed) and also found less proteoglycan staining in our miRNA-null mice. This suggests that miR-140 and miR-455 play critical roles in proteoglycan metabolism in articular cartilage, somewhat regardless of disease status. DMM-induced OA changes joint biomechanics and results in unbalanced forces. These forces could affect cell-to-cell and cell-to-ECM interactions (Martinez-Moreno, Jimenez et al. 2019). Lijima *et al.* identified less Safranin-O staining in regions covered by menisci in porcine knees relative to uncovered regions (Iijima, Aoyama et al. 2014), indicating cartilage covered by menisci receives more mechanical loading than uncovered regions. Taken together, mechanical loading alternation on articular cartilage of knee joint induces ECM changes, with lower mechanical loading limiting the formation of ECM including proteoglycans. The aggrecanase Adamts-5 is responsible for cartilage aggrecan degradation in murine OA (Stanton, Rogerson et al. 2005) and Miyaki *et al.* identified this gene is a direct target of miR-140 (Miyaki, Sato et al. 2010). There has been limited investigation into articular cartilage integrity in miR-455^{-/-} mice, which clearly warrants further investigation.

The Glasson/OARSI scoring scheme (Glasson, Chambers et al. 2010) is a widely used histological assessment to evaluate articular cartilage damage, even though it provides a limited score range for evaluation of cartilage damage. Here we also performed the OARSI scheme to examine the severity of OA in our four different genotypes. The results showed that microRNA-null mice exhibiting similar level of proteoglycan loss and fibrillation of articular cartilage in articular cartilage of the operated knee joints compared with WT mice, somewhat consistent with the result we obtained by using the OOCHAS scheme for Grade assessment. However, this differs from that reported previously for miR-140^{-/-} mice where

combined evaluation of cartilage damage (MFC+MTP) was significantly increased (Miyaki, Sato et al. 2010). There are several possible reasons for this discrepancy which include the low number of mice used in our research, that we sectioned samples on the recommended coronal as apposed sagittal plane, the mouse lines was generated by using different methodologies and a different genetic background (section 3.3.1), plus of course that histological scoring systems used were slightly different (Glasson, Askew et al. 2004). Like Miyaki *et al.*, we ended our DMM after 8 weeks, which is normally considered sufficient to identify histological differences between treatment groups (Miyaki, Sato et al. 2010). The choice of 8 weeks was pragmatic, based on experience, previous publications, and cost, however, more severe disease is generally observed at later time points and in general 16 weeks is recommended to observe chronic OA (Glasson, Blanchet et al. 2007). Taken together, although different histological assessments were used in our research, loss of miR-140 and/or miR-455 in surgical mouse model were found to play only a minor role in elevating the severity level of articular cartilage structural damage. However, we have further implicated these two miRNAs in the regulation of cartilage proteoglycan metabolism and showed a synergistical effect due to their loss.

5. 3. 3. Exploration of the role of miR-140 and/or miR-455 in murine articular chondrocytes

As we successfully identified miR-140 growth plate target genes from RNA-seq of costal chondrocyte and explored their roles in chondrocytes, we hoped to copy this success in articular cartilage. Additionally, though no miR-455 target genes were identified from growth plate chondrocytes, perhaps due to the mild phenotype of the null mice, we hoped to use RNA-seq to identify targets in articular cartilage, especially given the recently published work showing that the lack of miR-455 is positively correlated with age-related OA (Sun, Zhao et al. 2018, Hu, Zhao et al. 2019, Mao, Kang et al. 2019, Ito, Matsuzaki et al. 2021). Thus, we collected articular cartilage (medial side of knee joint, the more bearing side) from 11-week-old mice (the day before we normally perform DMM surgery), and performed RNA-seq on the RNA extracted from the ground tissue. Our histological analysis of the dissected tissue revealed the major caveat of the work, that the tissue was approximately 50% articular cartilage with a large, but variable, subchondral bone and

stromal tissue component. Similar to analysis we performed previously (Chapter 4) using Enrichr (Kuleshov, Jones et al. 2016) and the top 75 most abundantly expressed genes (on average across all our tissue samples) when overlapping with the ARCHS4 tissue database, ‘chondrocyte’ was identified as the most likely tissue source, with osteoblast ranked fifth (Table 5.6). However, when overlapped with Mouse Gene Atlas, ‘bone’, ‘osteoblast’, and ‘bone marrow’ were the first, third/fourth and fifth highest ranked terms returned, respectively (data not shown) – though it should be noted this category does not include ‘chondrocyte’ as an output option.

Table 5.6 Enrichr summary of overlapping expression ranked genes and ARCSH4 tissue database

Term	P-value	Adjusted P-value	Odds Ratio	Combined Score	Genes
CHONDROCYTE	3.11E-08	3.17E-06	4.334	74.92	<i>SPARC;AHNAK;LRP1;COL11A1;COL11A2;TNC;MKI67;SYNE1;COMP;ACAN;IBSP;HIST1H1C;BGN;FN1;PRG4;DCN;COL1A1;COL3A1;COL2A1;COL1A2;COL5A1;CILP;COL6A2;COL5A2;COL6A3;CREB5;PLEC</i>
PLACENTA (BULK)	1.34E-07	6.83E-06	4.086	64.67	<i>EIF4A1;MACF1;SPARC;AHNAK;LRP1;IQGAP1;IBSP;SPP1;BGN;FN1;RPSA;DCN;COL1A1;COL3A1;COL1A2;COL5A1;COL6A2;COL5A2;MYH9;COL6A3;TLN1;S100A9;S100A8;CREB5;LTF;PLEC</i>
FIBROBLAST	7.61E-06	2.59E-04	3.401	40.09	<i>SPARC;AHNAK;LRP1;COL11A1;TNC;BGN;FN1;MKI67;DCN;COMP;COL1A1;ACAN;COL3A1;COL1A2;COL5A1;COL6A2;COL5A2;MYH9;COL6A3;FLNA;VIM;TLN1;PLEC</i>
BLOOD DENDRITIC	2.60E-05	4.42E-04	3.191	33.69	<i>KLF10;EIF4A1;MTND4;DDX5;MTND5;AHNAK;RPL13A;RPSA;IQGAP1;MPO;ACTB;SYNE1;ACTG1;MTND1;MTATP6;EEF1A1;TMSB4X;PABPC1;VIM;S100A9;PTMA;S100A8</i>
OSTEOBLAST	2.60E-05	4.42E-04	3.191	33.69	<i>SPARC;AHNAK;LRP1;COL11A1;COL11A2;TNC;BGN;FN1;DCN;COMP;COL1A1;ACAN;COL3A1;COL1A2;IBSP;COL5A1;COL6A2;COL5A2;MYH9;COL6A3;FLNA;PLEC</i>

Top 75 ranked genes were used to overlap with ARCSH4 tissue database using an online tool (<https://maayanlab.cloud/Enrichr/enrich>). Details include *p*-value, adjusted *p*-value, odds ratio, combined score and confirmed genes that overlap with 'mouse chondrocyte genes'.

When analysing the pre-DMM RNA-seq expression data, only 41 genes (fold change > 1.5 and FDR threshold ≤ 0.05) were significantly up-regulated in *Mir140*-null chondrocytes when

compared to the WT chondrocytes, but none of these were predicted miR-140 -5p or miR-140-3p.2 target genes, with only one miR-140-3p.1 predicted gene (*Mboat2*) up-regulated.

For miR-455, even fewer genes (22) were significantly up-regulated in *Mir455*-null chondrocytes, and only one miR-455-5p predicted target gene (*Col8a1*) is upregulated. It was even more surprising that only 3 genes were significantly up-regulated in DKO mice when compared to the WT mice, but perhaps this again indicates that miR-140 and miR-455 play antagonistic roles in maintain homeostasis of articular chondrocytes, somewhat consistent with the results that we observed in growth plate chondrocytes (chapter 3.2.1.5). for both single miRNA-null genotypes the number of differentially expressed genes is far fewer than we identified in the costal chondrocytes. This could largely be due to experiment variability as a consequence of RNA quality, sequencing quality/depth, or the described variable inclusion of bone/marrow tissue. Our RNA-seq was performed at a reasonable depth (39.47 million reads/sample) for quantitative gene expression analysis however, the mapping rate to the mouse transcriptome was low (average 30.75%), meaning the average mapped reads were just 12.23 million/sample. In part, this was due to excessive non-coding transcript sequencing (including ribosomal RNA (rRNA), transfer RNAs (tRNA) and mitochondrial tRNA and rRNA) even though our samples were prepared using a ribosomal RNA depletion system. Such low mapping rates could affect the quality of the final data. Perhaps the adoption of only medial tibial cartilage for RNA-seq is a reason why there are no robust differentially expressed genes, when compared our costal chondrocyte RNA-seq datasets. The RNA-seq data would suggest miR-140 has only a modest function in articular cartilage compared to the growth plate, perhaps also supporting the limited structural differences observed following DMM-surgery. However, we remain confident that sampling the medial tibial cartilage is the best way to identify genes (and miR-140 targets) important during OA progression as other studies have suggested (Kung, Mullan et al. 2019).

We expected to see OA-liked changes occurring in our mutant mice when compared to the WT mice, however, both ‘collagen formation’ and ‘collagen degradation’ pathways were enriched in the down-regulated genes in *Mir140*-null mice 1 day before DMM surgery at 11-week-old. Furthermore, the ‘degradation of the extracellular matrix’ pathway was significantly enriched in the down-regulated genes in *Mir140*-null mice prior to DMM surgery at 11-weeks of age, and ‘ECM proteoglycans’ pathway was also enriched in the

down-regulated genes in *Mir140*-null mice. This indicates that the lack of miR-140 does not fully unbalance articular chondrocyte homeostasis, at least in 11-week-old murine knee articular chondrocytes in our study. Interestingly, ‘cellular senescence’ and ‘metalloprotease DUBs’ pathways are enriched in the up-regulated genes in *Mir140*-null mice without surgery. Cellular senescence refers to a signal transduction process that causes cells being a growth arrest state but remaining metabolic active (Toh, Brittberg et al. 2016, McCulloch, Litherland et al. 2017). Genetic and chemical removal of senescent cells has been shown to limit induced and age-dependent OA in mice (Jeon, Kim et al. 2017) but in human OA clinical trials the senolytic compound UBX1010 failed to meet the primary endpoint in terms of pain measurement (<https://www.clinicaltrialsarena.com/news/unity-ubx0101-osteoarthritis/>). Taken together, although our data is limited it adds to evidence that the lack of miR-140 may accelerate early-stage OA development in part by regulating chondrocyte senescence (Si, Yang et al. 2020).

Ubiquitination/ubiquitylation is an enzymatic post-translational modification in which a ubiquitin protein is covalently attached to a substrate. It is involved in many cellular processes. In chondrocytes, ubiquitination is negatively correlated with activity of matrix metalloproteinases in chondrocytes and subsequently attenuates extracellular matrix degradation (Wang, Chen et al. 2020). However, the global inhibition of ubiquitination in mice also limits DMM-induced OA (Radwan, Wilkinson et al. 2015). The removal of ubiquitin is catalyzed by metalloprotease deubiquitinating enzymes (metalloprotease DUBs), and some published work has identified a tight and positively correlated relationship between metalloprotease DUBs and activity of matrix metalloproteinases (Zhang, Yuan et al. 2016, Wang, Chen et al. 2020). MiR-140 is located in an intron of an E3 ligase, *WWp2*, one of many enzymes involved in the final third stage of the addition of ubiquitin to substrate proteins – the opposite process to which DUBs function. Our data showed that miR-140 deletion in our mice did not affect *WWp2* expression but we were unable to confirm no change in *WWp2* protein expression due to the lack of a functional antibody. MicroRNAs have been identified to function in the same pathways as their host genes (Liu, Shyr et al. 2018), therefore the identification of alterations in the expression of members of the metalloprotease DUB family warrants further investigation.

Given the limited histological effect of miR-455 removal on the joint we were surprised that 'degradation of the cellular matrix', 'activation of matrix metalloproteinases', and 'collagen degradation' pathways are all enriched in the up-regulated genes in *Mir455*-null mice, indicating lack of miR-455 accelerate the progress of OA. The cellular senescence and metalloprotease DUBs pathways were enriched in the down-regulated genes in *Mir455*-null mice, which is opposite to that of *Mir140*-null mice. Given these contrary findings between the individual miRNA-null mice, it is perhaps unsurprising that there were no significant pathway enriched in our DKO mice.

5. 3. 4. Identification of the role of miR-140 in murine articular cartilage after DMM

treatment

To explore the role of miR-140 in the development of OA, we performed DMM surgery on 11-week-old mice, and collected medial knee articular chondrocytes 3-days, 7-days, and 42-days post DMM surgery, respectively. RNA-seq was used to compare transcriptome changes in the articular chondrocytes post DMM surgery at the selected times. We had aimed to extend the detection time point to 56-days post DMM surgery, which is the same time point as our histological analysis (Chapter 5.2.2), but COVID-19 pandemic and laboratory closure made this untenable.

Compared to the data we obtained from prior to DMM surgery, more genes (281 genes) were significantly up-regulated in *Mir140*-null mice at 3-days post DMM, and consequently more predicted miR-140-5p (4 genes), miR-140-3p.1 (10 genes), and miR-140-3p.2 (5 genes) target genes identified. 'Cellular senescence' and 'metalloprotease DUBs' pathways are enriched in the up-regulated genes in *Mir140*-null mice, as observed prior to DMM surgery (Chapter 5.2.3). 'Degradation of the extracellular matrix' and 'collagen degradation' pathways were no longer significantly enriched in the down-regulated genes in *Mir140*-null mice. Taken together, this indicates that the lack of miR-140 has changed the homeostasis of articular chondrocytes during knee joint.

For the data at 7 days post DMM surgery, less genes (75) were significantly up-regulated in *Mir140*-null mice, and only 3 predicted miR-140-3p.1 target genes were increased. Interestingly, again 'degradation of the extracellular matrix' and 'collagen degradation'

pathways were significantly enriched in the down-regulated genes in *Mir140*-null mice. Miyaki *et al.* has showed that transfection of miR-140 repressed IL-1 induced ADAMTS5 expression in chondrocytes and rescued IL-1 dependent repression of ACAN expression (Miyaki, Nakasa *et al.* 2009). If miR-140 is involved in inflammatory signalling regulation, as proposed, our data could indicate that inflammatory/IL-1 signalling may be active 7-days post-DMM surgery.

At 42-days post DMM surgery, 292 genes are significant up-regulated in *Mir140*-null mice, and more predicted miR-140 target genes emerged when compared to the data that obtained from earlier days post DMM surgery. 'Apoptosis', 'cellular senescence', 'HDACs deacetylate histones', 'metalloprotease DUBs', and 'programmed cell death' pathways were all enriched in *Mir140*-null articular chondrocytes. Maintaining the homeostasis of extracellular matrix is a dynamic process via transduction of various chemical and physical signals to cells residing in the tissue (Daley, Peters *et al.* 2008). As the only cell that exist in articular cartilage, chondrocytes, coveys these signals to regulate the key cellular behaviour such as proliferation and differentiation. Cell death with molecular features of apoptosis has been detected in osteoarthritic cartilage, indicating a key role of chondrocyte death in the pathogenesis of OA (Musumeci, Castrogiovanni *et al.* 2015). Apoptosis is a highly-regulated process that causes cell death involved in development, homeostasis, and ageing, dysregulation of apoptosis in cells results in a pathological state, such as degenerative diseases, like OA (Hwang and Kim 2015). HDACs, are nuclear transcriptional regulatory proteins that regulate chromatin structure and the activity of transcriptional factors by removing acetyl group (Araki and Mimura 2017). Previously publications reported that HDACs are involved in chondrocyte development, cartilage and also osteoarthritis (Young, Lakey *et al.* 2005, Culley, Hui *et al.* 2013). Previous studies have also identified that relationships of HDACs and miRNAs in the pathogenesis of OA (Sondag and Haqqi 2016). Collectively, enriched apoptosis, cellular senescence, and programmed cell death pathways result in advanced chondrocyte death and subsequently affect homeostasis of extracellular matrix, which accelerates the development of osteoarthritis. In addition, we noticed that 'collagen formation' and 'collagen degradation' pathway were enriched in the down-regulated genes in *Mir140*-null articular chondrocytes before DMM surgery, and 7- and 42-

days post-DMM surgery, indicating that miR-140 plays roles to balance collagen homeostasis.

In our study, we found that lack of miR-140 reduced collagen degradation, combined with our histological analysis that proteoglycan staining loss in *Mir140*-null mice when compared to the WT mice, we hypothesized that lack of miR-140 accelerate proteoglycan degradation. Thus, we observed that the expression level of ECM proteoglycan pathway members *Bgn*, *Matn4*, *Chst11*, and *Acan* in *Mir140*-null articular cartilage are all lower than in WT articular cartilage, especially in mice at 42-days post DMM surgery. These genes are involved in the ECM proteoglycan pathway, which is consistent with our DMM histological analysis. Biglycan (Bgn) is a member of the small leucine-rich repeat proteoglycan family (SLRPs) and is highly expressed in bone, tendon, and cartilage (Ameye, Aria et al. 2002, Bi, Ehirchiou et al. 2007). Mice deficient in Biglycan and fibromodulin develop OA in multiple joints (Ameye, Aria et al. 2002, Wadhwa, Embree et al. 2005). Matrilins are proteins in the cartilage extracellular matrix, which function to connect collagen II and proteoglycans. Li *et al.* showed that *Matn4*^{-/-} mice developed severe spontaneous age-related OA suggesting *Matn4* plays a crucial role in maintaining the stability of articular cartilage (Li, Fleischhauer et al. 2020). *Chst11* encodes an enzyme that catalyses the transfer of sulfate groups to chondroitin to form chondroitin-4-sulfate, which is an important component in GAG chains that covalently bind to core proteins to form proteoglycan in the cartilage extracellular matrix (Kluppel 2010). Polymorphisms near/within *CHST11* are also genetically associated with OA (arc, arc et al. 2012). Collectively, the decrease of these genes in the articular chondrocyte could affect the metabolism of proteoglycan and might indeed accelerate the development of OA, but the mechanisms of the decrease of these genes in *Mir140* deficient articular chondrocyte remains unclear.

5. 3. 5. Summary

Both miR-140 and miR-455 were shown to be involved in OA pathogenesis of both human articular cartilage and mouse models. In this Chapter, we have demonstrated that miR-140 and miR-455 are potentially required for proteoglycan metabolism of articular cartilage and normally somewhat protect against OA pathogenesis, with the absence of miR-140 or miR-455 showing an effect on proteoglycan metabolism. Thus, we concluded that miR-140 and

miR-455 are regulators of articular cartilage homeostasis and a decrease in their expression level could cause diseases associated with cartilage destruction, including OA. The underlying mechanisms of the role of miR-140 and miR-455 in articular cartilage homeostasis has not yet been well elucidated, due in part to difficulty in determining the direct targets of each miRNA. Thus, we performed DMM+RNA-seq of articular cartilage to explore additional miR-140 and miR-455 target genes in (ideally) the articular chondrocytes, however we were unable to progress further due to the COVID-19 pandemic. Our bioinformatic analysis has led to several conclusions, include that mice that lack miR-455 are more susceptible to development of early-stage OA when compared to *Mir140*-null mice; the mechanisms of miR-140 and miR-455 in the development of OA are different; lack of miR-140 in articular chondrocytes accelerate pathogenesis of OA by activation of 'cellular senescence', 'apoptosis', 'programmed cell death', 'HDACs deacetylate histones', and 'metalloprotease DUBs pathways'; lack of miR-140 in the articular chondrocytes accelerates pathogenesis of OA in part through effect on ECM proteoglycans.

Chapter 6. Discussion

Epigenetic regulation plays multiple gene regulatory roles during essential biological processes, which is mediated by histone modification, DNA methylation and regulatory noncoding RNAs include miRNAs (Brazel and Vernimmen 2016, Shvedova and Kobayashi 2020). Dysregulation of miRNAs is involved in many human diseases include skeletal dysplasia and cartilage diseases like osteoarthritis (de Pontual, Yao et al. 2011, Piletic and Kunej 2016, Grigelioniene, Suzuki et al. 2019, Swingler, Niu et al. 2019). MiRNA expression varies between tissues and cell types. Many miRNAs were reported to play crucial roles in various aspects of cartilage development, physiology, and pathology (Mirzamohammadi, Papaioannou et al. 2014). The interaction of miRNA and its target RNA causes repression of translation of target RNA and subsequently induces its degradation (Bartel 2018). The molecular role of individual miRNA in chondrocytes has been widely studied, these findings increased our understanding of the role and function of miRNAs in cartilage development and OA, however, their physiological significances are still not fully appreciated due to limited identification and verification of their direct target genes.

Our laboratory's previous work has shown increased expression of miR-140 and miR-455 in human hip OA chondrocytes, and during human MSCs chondrogenesis (Swingler, Wheeler et al. 2012, Barter, Tselepi et al. 2015). To further explore the role of miR-140 and miR-455 in skeletal development and OA, we generated *Mir140*-null, *Mir455*-null and *Mir140:Mir455*-null mice using CRISPR/Cas9 system. Our miRNA-null mice are dwarf when compared to control animals, and the weight of mice is less than that of control mice. We started with measurement of the length of tibia, femur, and pelvis bones amongst our miRNA-null mice and control mice, with miRNA-null mice showing significantly shorter bone length in general. These phenotypes indicate that miR-140 and miR-455 are involved in mouse skeletal development. When comparing to previously published work about *Mir140*-null mice(Miyaki, Sato et al. 2010, Nakamura, Inloes et al. 2011), our *Mir140*-null mice have a similar skeletal phenotype including a domed-skull shape, dwarfism etc. However, our *Mir455*-null mice which showed delayed endochondral bone development, differs from identical mice from our lab partner Prof Ian Clark (UEA) and more recently from an independent *Mir455*-null mice published work by Ito *et al.* (Ito, Matsuzaki et al. 2021). We actually obtained the *Mir455*-null mice from Prof Ian Clark, but the offspring from these

mice were dwarf and weighed less, we suggest that different environmental conditions between the housing locations could contribute to this phenotype, but we are unable to confirm this due to the global pandemic. Our intention was to obtain a new colony of mice from UEA, which became untenable when the Covid-10 pandemic developed. The other possible explanation is that our WT animals were used are different from others, because they were from litters of crosses of DKO and miR-140^{+/−} mice, but the weight of our WT mice are within the well-established range for C57BL/6 mice (body weight information for C57BL/6J (000664), the Jackson laboratory).

When compared to control mice, our miRNA-null mice have abnormal tibial growth plate structure, delayed tibial secondary ossification centre, decreased numbers of proliferative chondrocytes and increased apoptotic chondrocytes. Taken together, these findings showed that lack of miR-140 and miR-455 normally play roles to enhance murine tibial skeletal development. This is consistent with an *in vitro* study by Zhang *et al.* that showed miR-455 functions as an activator of early chondrogenic differentiation (Zhang, Hou *et al.* 2015), and studies demonstrating that the lack of miR-140 attenuates murine, zebrafish and almost certainly human endochondral bone development (Eberhart, He *et al.* 2008, Miyaki, Sato *et al.* 2010, Nakamura, Inloes *et al.* 2011, Grigelioniene, Suzuki *et al.* 2019). To understand the underlying mechanism of miR-140 and miR-455 in skeletal development, we performed murine costal chondrocyte RNA-seq to screen direct target genes of miR-140 and miR-455. Our bioinformatic analysis showed a robust number of significantly differentially expressed genes in *Mir140*-null costal chondrocytes, in contrast, fewer significantly differentially expressed genes were observed in *Mir455*-null costal chondrocytes. In addition, our RNA-seq analysis revealed that the host genes of miR-140 and miR-455, *Wwp2* and *Col27a1*, respectively, were not disrupted by deletion of their intronic miRNA. However, we are unable to confirm no changes at the level respective due to the lack of efficient/available antibodies.

To reliably verify miR-140 growth plate target genes, we compared our costal chondrocyte RNA-seq dataset with a published murine costal chondrocyte RNA-seq dataset from Prof T. Kobayashi (Grigelioniene, Suzuki *et al.* 2019)(NCBI GEO – GSE98036). We screened several potential miR-140 target genes from both datasets (based on TargetScan 7.2) that were significantly differentially expressed in *Mir140*-null mice, and finally 10 potential miR-140-5p

target genes were selected for further verification due to described roles in bone or cartilage diseases. Luciferase assays were performed to verify these ten genes as direct miR-140-5p target genes, and we subsequently explored there (*Creb3l1*, *Nrf2*, and *Zeb1*) in murine costal chondrocytes. Increased expression of those miR-140 target genes attenuated the proliferative ability of chondrocytes *in vitro* using the WST-1 assay. Thus, we hypothesised that decreased expression of those miR-140-5p target genes subsequently delayed the murine endochondral development *in vivo*, which partially explains the short tibia, femur, and pelvis bone lengths of the mutant mice. Although the WST-1 assay we used to measure cell proliferation ability is highly sensitive and simple to perform *in vitro*, it is actually monitoring mitochondrial activity instead of cell proliferation. We were unable to detect changes chondrocyte proliferation *in vitro* using a BrdU assay or other method due to the COVID-19 pandemic. In contrast to miR-140-5p targets, we were unable to validate any miR-455 potential growth plate target genes probably due to the fewer identified initially as significantly up-regulated (when compared to miR-140 costal chondrocyte RNA-seq dataset). This again would reiterate that miR-140 is more important in mouse skeletal development than miR-455. We and others have observed that less GAG staining in knee articular cartilage of *Mir455*-null mice at different ages when compared to control mice (Hu, Zhao et al. 2019, Mao, Kang et al. 2019, Wen, Li et al. 2020, Ito, Matsuzaki et al. 2021). Thus, we hypothesised that miR-455 is involved in GAG metabolism, and subsequently selected *Acan* and *Chst11* as miR-455-3p.1 potential target genes, due to they function in proteoglycan metabolism and the fact that miR-455-3p.1 was implied to be the more functional isomiR of miR-455 (Crowe, Swingler et al. 2016). In addition, *Ppp1r10* was chosen as miR-455 potential target gene for further verification, because of its potential as a 'biomarker' for OA (Hellvard, Zeitlmann et al. 2016). Unfortunately, we failed to verify those genes as miR-455-3p.1 growth plate targets. In hindsight, we should have tested target genes of miR-455-3p.2 not for miR-455-3p.1, because our bioinformatic analysis of *Mir455*-null costal chondrocyte RNA-seq revealed that predicted target genes of miR-455-3p.2 had the highest overlapping with miR-455 predicted target genes (based on TargetScan 7.2, Chapter 4.2.6) and on average showed the most fold increase in expression.

Our costal chondrocyte GSEA analysis revealed that miR-140 was involved in the homeostasis of ECM proteins and miR-455 played a role in GAG metabolism. We had

explored the role of miR-140 target genes in proliferation of chondrocytes, thus we hypothesised that RNA-seq of tibial growth plate proliferative chondrocytes alone through laser microdissection (LMD) would identify more specific miR-140 target genes. (Belluoccio, Bernardo et al. 2008, Belluoccio, Etich et al. 2010, James, Stanton et al. 2010). We tried two different RNA isolation methods with the isolated RNA then subjected to low-input RNA-seq, finally selecting a partially optimised methodology. However, we again were unable to proceed to profile gene expression between the *Mir140*-null and WT proliferative chondrocytes because of the Covid-19 pandemic.

To visualise the role of miR-140 and miR-455 in articular cartilage and OA, we performed DMM surgery on our miRNA-null and control mice at 11-weeks of age. Knee joints were collected 8-weeks post-DMM surgery and histological analysis was followed to compare articular cartilage damage amongst the four genotypes. We used two different histological assessments to compare differences between genotypes, and *Mir140*-null mice showed more histological damage of the MFC than others, although this was not significant. However, we observed that our miRNA-null mice had more GAG staining loss at both the medial and lateral knee cartilage, again indicating that miR-140 and miR-455 are involved in GAG metabolism. For *Mir455*-null mice, this is consistent with published works (Hu, Zhao et al. 2019, Mao, Kang et al. 2019, Wen, Li et al. 2020, Ito, Matsuzaki et al. 2021). We collected joints 8-week post-DMM, because of pragmatic reasons and because previous publications have used this time point to assess cartilage damage in genetically mutant mice e.g. (Miyaki, Sato et al. 2010), however Mokuda *et al.* harvested knee joints at 10 weeks after DMM surgery (Mokuda, Nakamichi et al. 2019) and actually others recommended 12- to 16-weeks post-DMM is necessary to observe chronic OA (Zaki, Smith et al. 2021). This is because DMM surgery is less invasive than other surgical method such as anterior cruciate ligament transaction (ACLT) animal model thus causes slow cartilage lesion progression (Glasson, Blanchet et al. 2007). Of course, the relatively small number of animals that we included in our DMM analysis is likely a major reason for our failure to detect significant differences between the four four genotypes. A recent publication suggested 13 animals per group to be the optimised animal number for histological analysis for the DMM animal model (Mokuda, Nakamichi et al. 2019), though previous studies using *Mir140*-null used far fewer (Miyaki, Sato et al. 2010)

To reveal the targets and mechanisms of function of miR-140 and miR-455 in articular cartilage, we manually dissected medial tibial knee cartilage (the most weight bearing region) from *Mir140*-null, *Mir455*-null, DKO and control mice at 11-weeks of age, which was followed by RNA-seq to compare the role of miR-140 and miR-455 in articular chondrocytes. However, very limited significantly differentially expressed genes were up-regulated in miRNA-null mice, especially when compared to the numbers regulated in our costal chondrocyte RNA-seq data. In addition, we performed DMM-time course RNA-seq for *Mir140*-null and control mice at 3-, 7- and 42-days post-DMM surgery. Our bioinformatic analysis revealed that more significant differentially expressed genes were observed in *Mir140*-null mice at 42-days post-DMM. It was surprising that GSEA analysis showed 'collagen degradation' and 'degradation of the extracellular matrix' pathways as enriched in the down-regulated genes in *Mir140*-null articular chondrocytes at 7- and 42-days post-DMM. However, 'cellular senescence' and 'metalloprotease DUBs' pathways are enriched in the up-regulated genes in *Mir140*-null chondrocytes throughout the whole period. Furthermore, 'apoptosis' and 'programmed cell death' pathways were enriched in the up-regulated genes in *Mir140*-null chondrocytes. Taken together, these findings indicate that miR-140 is involved in OA pathology, probably through multiple mechanisms/pathways. Perhaps this is unsurprising given the number of predicted and validated targets of miR-140 that have been identified and the number of genes we found differentially expressed in our costal cartilage assessment. We hypothesised that worse cartilage damage would be observed as the disease progressed – similar to the discussion around DMM histological assessment. Since we saw more GAG staining loss in our *Mir140*-null mice when compared to control mice, consistently, we found genes that are involved in GAG synthesis were all expressed at lower levels during the DMM-time course than in WT mice, indicating that miR-140 play roles to affects GAG metabolism during OA pathology. It is interestingly that there is no synergistic role of miR-140 and miR-455 during OA development, a consistent finding we observed in tibial growth plate development, BrdU and TUNEL assays.

To conclude, we have successfully generated *Mir140*-null, *Mir455*-null and DKO mice. All our miRNA-null mice showed retarded skeletal development and more GAG staining loss in knee articular cartilage post-DMM surgery. Less proliferative chondrocytes and more apoptotic chondrocytes were observed in miRNA-null mice growth plates. Taken together, miR-140

and miR-455 function in endochondral bone development and OA progression. We had hypothesized that miR-140 and miR-455 would play synergistic roles during development of skeletal and OA, however, each miRNAs appears to function somewhat independently to affect skeletal development and OA pathogenesis, and in fact frequently displayed antagonistic effects. We have verified several miR-140 growth plate target genes, and explored their roles in chondrocytes, however, we failed to identify miR-455 growth plate target genes and cartilage target genes of both miRNAs, in part because of Covid-19 pandemic. Further work is clearly required in the identification of target genes of both miRNAs.

Reference

Agarwal, V., G. W. Bell, J. W. Nam and D. P. Bartel (2015). "Predicting effective microRNA target sites in mammalian mRNAs." *Elife* **4**.

Akhtar, N., Z. Rasheed, S. Ramamurthy, A. N. Anbazhagan, F. R. Voss and T. M. Haqqi (2010). "MicroRNA-27b regulates the expression of matrix metalloproteinase 13 in human osteoarthritis chondrocytes." *Arthritis Rheum* **62**(5): 1361-1371.

Ameye, L., D. Aria, K. Jepsen, A. Oldberg, T. Xu and M. F. Young (2002). "Abnormal collagen fibrils in tendons of biglycan/fibromodulin-deficient mice lead to gait impairment, ectopic ossification, and osteoarthritis." *FASEB J* **16**(7): 673-680.

Araki, Y. and T. Mimura (2017). "Matrix Metalloproteinase Gene Activation Resulting from Disordred Epigenetic Mechanisms in Rheumatoid Arthritis." *Int J Mol Sci* **18**(5).

Araldi, E., R. Khatri, A. J. Giaccia, M. C. Simon and E. Schipani (2011). "Lack of HIF-2alpha in limb bud mesenchyme causes a modest and transient delay of endochondral bone development." *Nat Med* **17**(1): 25-26; author reply 27-29.

Araldi, E. and E. Schipani (2010). "MicroRNA-140 and the silencing of osteoarthritis." *Genes Dev* **24**(11): 1075-1080.

arc, O. C., O. C. arc, E. Zeggini, K. Panoutsopoulou, L. Southam, N. W. Rayner, A. G. Day-Williams, M. C. Lopes, V. Boraska, T. Esko, E. Evangelou, A. Hoffman, J. J. Houwing-Duistermaat, T. Ingvarsson, I. Jonsdottir, H. Jonnson, H. J. Kerkhof, M. Kloppenburg, S. D. Bos, M. Mangino, S. Metrstry, P. E. Slagboom, G. Thorleifsson, E. V. Raine, M. Ratnayake, M. Ricketts, C. Beazley, H. Blackburn, S. Bumpstead, K. S. Elliott, S. E. Hunt, S. C. Potter, S. Y. Shin, V. K. Yadav, G. Zhai, K. Sherburn, K. Dixon, E. Arden, N. Aslam, P. K. Battley, I. Carluke, S. Doherty, A. Gordon, J. Joseph, R. Keen, N. C. Koller, S. Mitchell, F. O'Neill, E. Paling, M. R. Reed, F. Rivadeneira, D. Swift, K. Walker, B. Watkins, M. Wheeler, F. Birrell, J. P. Ioannidis, I. Meulenbelt, A. Metspalu, A. Rai, D. Salter, K. Stefansson, U. Stykarsdottir, A. G. Uitterlinden, J. B. van Meurs, K. Chapman, P. Deloukas, W. E. Ollier, G. A. Wallis, N. Arden, A. Carr, M. Doherty, A. McCaskie, J. M. Wilkinson, S. H. Ralston, A. M. Valdes, T. D. Spector and J. Loughlin (2012). "Identification of new susceptibility loci for osteoarthritis (arcOGEN): a genome-wide association study." *Lancet* **380**(9844): 815-823.

Arden, N. and M. C. Nevitt (2006). "Osteoarthritis: epidemiology." *Best Pract Res Clin Rheumatol* **20**(1): 3-25.

Bailey, D. and P. O'Hare (2007). "Transmembrane bZIP transcription factors in ER stress signaling and the unfolded protein response." *Antioxid Redox Signal* **9**(12): 2305-2321.

Ballock, R. T. and R. J. O'Keefe (2003). "The biology of the growth plate." *J Bone Joint Surg Am* **85**(4): 715-726.

Bandres, E., X. Agirre, N. Bitarte, N. Ramirez, R. Zarate, J. Roman-Gomez, F. Prosper and J. Garcia-Foncillas (2009). "Epigenetic regulation of microRNA expression in colorectal cancer." *Int J Cancer* **125**(11): 2737-2743.

Bartel, D. P. (2004). "MicroRNAs: genomics, biogenesis, mechanism, and function." *Cell* **116**(2): 281-297.

Bartel, D. P. (2009). "MicroRNAs: target recognition and regulatory functions." *Cell* **136**(2): 215-233.

Bartel, D. P. (2018). "Metazoan MicroRNAs." *Cell* **173**(1): 20-51.

Barter, M. J., M. Tselepi, R. Gomez, S. Woods, W. Hui, G. R. Smith, D. P. Shanley, I. M. Clark and D. A. Young (2015). "Genome-Wide MicroRNA and Gene Analysis of Mesenchymal Stem Cell Chondrogenesis Identifies an Essential Role and Multiple Targets for miR-140-5p." *Stem Cells* **33**(11): 3266-3280.

Belluoccio, D., B. C. Bernardo, L. Rowley and J. F. Bateman (2008). "A microarray approach for comparative expression profiling of the discrete maturation zones of mouse growth plate cartilage." *Biochim Biophys Acta* **1779**(5): 330-340.

Belluoccio, D., J. Etich, S. Rosenbaum, C. Frie, I. Grskovic, J. Stermann, H. Ehlen, S. Vogel, F. Zaucke, K. von der Mark, J. F. Bateman and B. Brachvogel (2010). "Sorting of growth plate chondrocytes allows the isolation and characterization of cells of a defined differentiation status." *J Bone Miner Res* **25**(6): 1267-1281.

Berendsen, A. D. and B. R. Olsen (2015). "Bone development." *Bone* **80**: 14-18.

Bernstein, E., S. Y. Kim, M. A. Carmell, E. P. Murchison, H. Alcorn, M. Z. Li, A. A. Mills, S. J. Elledge, K. V. Anderson and G. J. Hannon (2003). "Dicer is essential for mouse development." *Nat Genet* **35**(3): 215-217.

Bi, Y., D. Ehirchiou, T. M. Kilts, C. A. Inkson, M. C. Embree, W. Sonoyama, L. Li, A. I. Leet, B. M. Seo, L. Zhang, S. Shi and M. F. Young (2007). "Identification of tendon stem/progenitor cells and the role of the extracellular matrix in their niche." *Nat Med* **13**(10): 1219-1227.

Bijlsma, J. W., F. Berenbaum and F. P. Lafeber (2011). "Osteoarthritis: an update with relevance for clinical practice." *Lancet* **377**(9783): 2115-2126.

Blanco, F. J., I. Rego and C. Ruiz-Romero (2011). "The role of mitochondria in osteoarthritis." *Nat Rev Rheumatol* **7**(3): 161-169.

Bluhm, B., H. W. A. Ehlen, T. Holzer, V. S. Georgieva, J. Heilig, L. Pitzler, J. Etich, T. Bortecen, C. Frie, K. Probst, A. Niehoff, D. Belluoccio, J. Van den Bergen and B. Brachvogel (2017). "miR-322 stabilizes MEK1 expression to inhibit RAF/MEK/ERK pathway activation in cartilage." *Development* **144**(19): 3562-3577.

Boer, C. G., D. Radjabzadeh, C. Medina-Gomez, S. Garmaeva, D. Schiphof, P. Arp, T. Koet, A. Kurilshikov, J. Fu, M. A. Ikram, S. Bierma-Zeinstra, A. G. Uitterlinden, R. Kraaij, A. Zhernakova and J. B. J. van Meurs (2019). "Intestinal microbiome composition and its relation to joint pain and inflammation." *Nat Commun* **10**(1): 4881.

Bowen, M. E., U. M. Ayturk, K. C. Kurek, W. Yang and M. L. Warman (2014). "SHP2 regulates chondrocyte terminal differentiation, growth plate architecture and skeletal cell fates." *PLoS Genet* **10**(5): e1004364.

Brazel, A. J. and D. Vernimmen (2016). "The complexity of epigenetic diseases." *J Pathol* **238**(2): 333-344.

Burleigh, A., A. Chanalaris, M. D. Gardiner, C. Driscoll, O. Boruc, J. Saklatvala and T. L. Vincent (2012). "Joint immobilization prevents murine osteoarthritis and reveals the highly mechanosensitive nature of protease expression in vivo." *Arthritis Rheum* **64**(7): 2278-2288.

Burroughs, A. M., Y. Ando, M. J. de Hoon, Y. Tomaru, T. Nishibu, R. Ukekawa, T. Funakoshi, T. Kurokawa, H. Suzuki, Y. Hayashizaki and C. O. Daub (2010). "A comprehensive survey of 3' animal miRNA modification events and a possible role for 3' adenylation in modulating miRNA targeting effectiveness." *Genome Res* **20**(10): 1398-1410.

Butterfield, N. C., K. F. Curry, J. Steinberg, H. Dewhurst, D. Komla-Ebri, N. S. Mannan, A. T. Adoum, V. D. Leitch, J. G. Logan, J. A. Waung, E. Ghirardello, L. Southam, S. E. Youlten, J. M. Wilkinson, E. A. McAninch, V. E. Vancollie, F. Kussy, J. K. White, C. J. Lelliott, D. J. Adams, R. Jacques, A. C. Bianco, A. Boyde, E. Zeggini, P. I. Croucher, G. R. Williams and J. H. D. Bassett (2021). "Accelerating functional gene discovery in osteoarthritis." *Nat Commun* **12**(1): 467.

Cahill, K. M., Z. Huo, G. C. Tseng, R. W. Logan and M. L. Seney (2018). "Improved identification of concordant and discordant gene expression signatures using an updated rank-rank hypergeometric overlap approach." *Sci Rep* **8**(1): 9588.

Charles, J. F., J. Ermann and A. O. Aliprantis (2015). "The intestinal microbiome and skeletal fitness: Connecting bugs and bones." *Clin Immunol* **159**(2): 163-169.

Cheleschi, S., A. De Palma, A. Pecorelli, N. A. Pascarelli, G. Valacchi, G. Belmonte, S. Carta, M. Galeazzi and A. Fioravanti (2017). "Hydrostatic Pressure Regulates MicroRNA Expression Levels in Osteoarthritic Chondrocyte Cultures via the Wnt/beta-Catenin Pathway." *Int J Mol Sci* **18**(1).

Chen, H., F. Y. Ghori-Javed, H. Rashid, M. D. Adhami, R. Serra, S. E. Gutierrez and A. Javed (2014). "Runx2 regulates endochondral ossification through control of chondrocyte proliferation and differentiation." *J Bone Miner Res* **29**(12): 2653-2665.

Chen, H. and Y. Tian (2017). "MiR-15a-5p regulates viability and matrix degradation of human osteoarthritis chondrocytes via targeting VEGFA." *Biosci Trends* **10**(6): 482-488.

Chen, L. H., G. Y. Chiou, Y. W. Chen, H. Y. Li and S. H. Chiou (2010). "MicroRNA and aging: a novel modulator in regulating the aging network." *Ageing Res Rev* **9 Suppl 1**: S59-66.

Chen, Q. M. and A. J. Maltagliati (2018). "Nrf2 at the heart of oxidative stress and cardiac protection." *Physiol Genomics* **50**(2): 77-97.

Chen, W., L. Chen, Z. Zhang, F. Meng, G. Huang, P. Sheng, Z. Zhang and W. Liao (2016). "MicroRNA-455-3p modulates cartilage development and degeneration through modification of histone H3 acetylation." *Biochim Biophys Acta* **1863**(12): 2881-2891.

Chi, S. W., J. B. Zang, A. Mele and R. B. Darnell (2009). "Argonaute HITS-CLIP decodes microRNA-mRNA interaction maps." *Nature* **460**(7254): 479-486.

Chiang, H. R., L. W. Schoenfeld, J. G. Ruby, V. C. Auyeung, N. Spies, D. Baek, W. K. Johnston, C. Russ, S. Luo, J. E. Babiarz, R. Blelloch, G. P. Schroth, C. Nusbaum and D. P. Bartel (2010). "Mammalian microRNAs: experimental evaluation of novel and previously annotated genes." *Genes Dev* **24**(10): 992-1009.

Chiba, T., R. Kurimoto, T. Matsushima, Y. Ito, R. Nakamichi, M. Lotz and H. Asahara (2021). "MicroRNA Expression Profiling, Target Identification, and Validation in Chondrocytes." Methods Mol Biol **2245**: 151-166.

Cloonan, N., S. Wani, Q. Xu, J. Gu, K. Lea, S. Heater, C. Barbacioru, A. L. Steptoe, H. C. Martin, E. Nourbakhsh, K. Krishnan, B. Gardiner, X. Wang, K. Nones, J. A. Steen, N. A. Matigian, D. L. Wood, K. S. Kassahn, N. Waddell, J. Shepherd, C. Lee, J. Ichikawa, K. McKernan, K. Bramlett, S. Kuersten and S. M. Grimmond (2011). "MicroRNAs and their isomiRs function cooperatively to target common biological pathways." Genome Biol **12**(12): R126.

Colnot, C. (2005). "Cellular and molecular interactions regulating skeletogenesis." J Cell Biochem **95**(4): 688-697.

Colnot, C., C. Lu, D. Hu and J. A. Helms (2004). "Distinguishing the contributions of the perichondrium, cartilage, and vascular endothelium to skeletal development." Dev Biol **269**(1): 55-69.

Colnot, C. I. and J. A. Helms (2001). "A molecular analysis of matrix remodeling and angiogenesis during long bone development." Mech Dev **100**(2): 245-250.

Cornelis, F. M. F., A. de Roover, L. Storms, A. Hens, R. J. Lories and S. Monteagudo (2019). "Increased susceptibility to develop spontaneous and post-traumatic osteoarthritis in Dot1l-deficient mice." Osteoarthritis Cartilage **27**(3): 513-525.

Coryell, P. R., B. O. Diekman and R. F. Loeser (2021). "Mechanisms and therapeutic implications of cellular senescence in osteoarthritis." Nat Rev Rheumatol **17**(1): 47-57.

Coutinho de Almeida, R., Y. F. M. Ramos, A. Mahfouz, W. den Hollander, N. Lakenberg, E. Houtman, M. van Hoolwerff, H. E. D. Suchiman, A. Rodriguez Ruiz, P. E. Slagboom, H. Mei, S. M. Kielbasa, R. Nelissen, M. Reinders and I. Meulenhelt (2019). "RNA sequencing data integration reveals an miRNA interactome of osteoarthritis cartilage." Ann Rheum Dis **78**(2): 270-277.

Crowe, N., T. E. Swingler, L. T. Le, M. J. Barter, G. Wheeler, H. Pais, S. T. Donell, D. A. Young, T. Dalmay and I. M. Clark (2016). "Detecting new microRNAs in human osteoarthritic chondrocytes identifies miR-3085 as a human, chondrocyte-selective, microRNA." Osteoarthritis Cartilage **24**(3): 534-543.

Culley, K. L., W. Hui, M. J. Barter, R. K. Davidson, T. E. Swingler, A. P. Destreumat, J. L. Scott, S. T. Donell, S. Fenwick, A. D. Rowan, D. A. Young and I. M. Clark (2013). "Class I histone deacetylase inhibition modulates metalloproteinase expression and blocks cytokine-induced cartilage degradation." Arthritis Rheum **65**(7): 1822-1830.

Dai, L., X. Zhang, X. Hu, C. Zhou and Y. Ao (2012). "Silencing of microRNA-101 prevents IL-1beta-induced extracellular matrix degradation in chondrocytes." Arthritis Res Ther **14**(6): R268.

Daley, W. P., S. B. Peters and M. Larsen (2008). "Extracellular matrix dynamics in development and regenerative medicine." J Cell Sci **121**(Pt 3): 255-264.

de Pontual, L., E. Yao, P. Callier, L. Faivre, V. Drouin, S. Cariou, A. Van Haeringen, D. Genevieve, A. Goldenberg, M. Oufadem, S. Manouvrier, A. Munnich, J. A. Vidigal, M. Vekemans, S. Lyonnet, A. Henrion-Caude, A. Ventura and J. Amiel (2011). "Germline deletion of the miR-17 approximately 92 cluster causes skeletal and growth defects in humans." Nat Genet **43**(10): 1026-1030.

DeLise, A. M., L. Fischer and R. S. Tuan (2000). "Cellular interactions and signaling in cartilage development." *Osteoarthritis Cartilage* **8**(5): 309-334.

Denard, B., J. Seemann, Q. Chen, A. Gay, H. Huang, Y. Chen and J. Ye (2011). "The membrane-bound transcription factor CREB3L1 is activated in response to virus infection to inhibit proliferation of virus-infected cells." *Cell Host Microbe* **10**(1): 65-74.

Dunn, W., G. DuRaine and A. H. Reddi (2009). "Profiling microRNA expression in bovine articular cartilage and implications for mechanotransduction." *Arthritis Rheum* **60**(8): 2333-2339.

Eberhart, J. K., X. He, M. E. Swartz, Y. L. Yan, H. Song, T. C. Boling, A. K. Kunerth, M. B. Walker, C. B. Kimmel and J. H. Postlethwait (2008). "MicroRNA Mirn140 modulates Pdgf signaling during palatogenesis." *Nat Genet* **40**(3): 290-298.

Endisha, H., J. Rockel, I. Jurisica and M. Kapoor (2018). "The complex landscape of microRNAs in articular cartilage: biology, pathology, and therapeutic targets." *JCI Insight* **3**(17).

Enomoto, H., M. Enomoto-Iwamoto, M. Iwamoto, S. Nomura, M. Himeno, Y. Kitamura, T. Kishimoto and T. Komori (2000). "Cbfa1 is a positive regulatory factor in chondrocyte maturation." *J Biol Chem* **275**(12): 8695-8702.

Fabian, M. R. (2019). "Of seeds and supplements: structural insights into extended microRNA-target pairing." *EMBO J* **38**(13): e102477.

Favazzo, L. J., H. Hendesi, D. A. Villani, S. Soniwala, Q. A. Dar, E. M. Schott, S. R. Gill and M. J. Zuscik (2020). "The gut microbiome-joint connection: implications in osteoarthritis." *Curr Opin Rheumatol* **32**(1): 92-101.

Ferguson, C. M., T. Miclau, D. Hu, E. Alpern and J. A. Helms (1998). "Common molecular pathways in skeletal morphogenesis and repair." *Ann N Y Acad Sci* **857**: 33-42.

Friedman, R. C., K. K. Farh, C. B. Burge and D. P. Bartel (2009). "Most mammalian mRNAs are conserved targets of microRNAs." *Genome Res* **19**(1): 92-105.

Gabay, O. and K. A. Clouse (2016). "Epigenetics of cartilage diseases." *Joint Bone Spine* **83**(5): 491-494.

Gebhard, S., T. Hattori, E. Bauer, B. Schlund, M. R. Bosl, B. de Crombrugghe and K. von der Mark (2008). "Specific expression of Cre recombinase in hypertrophic cartilage under the control of a BAC-Col10a1 promoter." *Matrix Biol* **27**(8): 693-699.

Gentili, C., G. Tutolo, A. Pianezzi, R. Cancedda and F. Descalzi Cancedda (2005). "Cholesterol secretion and homeostasis in chondrocytes: a liver X receptor and retinoid X receptor heterodimer mediates apolipoprotein A1 expression." *Matrix Biol* **24**(1): 35-44.

Gerber, H. P., T. H. Vu, A. M. Ryan, J. Kowalski, Z. Werb and N. Ferrara (1999). "VEGF couples hypertrophic cartilage remodeling, ossification and angiogenesis during endochondral bone formation." *Nat Med* **5**(6): 623-628.

Gibson, G. and H. Asahara (2013). "microRNAs and cartilage." *J Orthop Res* **31**(9): 1333-1344.

Glasson, S. S., R. Askew, B. Sheppard, B. A. Carito, T. Blanchet, H. L. Ma, C. R. Flannery, K. Kanki, E. Wang, D. Peluso, Z. Yang, M. K. Majumdar and E. A. Morris (2004). "Characterization of and osteoarthritis susceptibility in ADAMTS-4-knockout mice." *Arthritis Rheum* **50**(8): 2547-2558.

Glasson, S. S., T. J. Blanchet and E. A. Morris (2007). "The surgical destabilization of the medial meniscus (DMM) model of osteoarthritis in the 129/SvEv mouse." *Osteoarthritis Cartilage* **15**(9): 1061-1069.

Glasson, S. S., M. G. Chambers, W. B. Van Den Berg and C. B. Little (2010). "The OARSI histopathology initiative - recommendations for histological assessments of osteoarthritis in the mouse." *Osteoarthritis Cartilage* **18 Suppl 3**: S17-23.

Goldring, M. B. and S. R. Goldring (2007). "Osteoarthritis." *J Cell Physiol* **213**(3): 626-634.

Goldring, M. B. and K. B. Marcu (2009). "Cartilage homeostasis in health and rheumatic diseases." *Arthritis Res Ther* **11**(3): 224.

Goldring, M. B., K. Tsuchimochi and K. Ijiri (2006). "The control of chondrogenesis." *Journal of Cellular Biochemistry* **97**(1): 33-44.

Goldring, S. R. (2012). "Alterations in periaricular bone and cross talk between subchondral bone and articular cartilage in osteoarthritis." *Ther Adv Musculoskelet Dis* **4**(4): 249-258.

Gonzaga-Jauregui, C., C. N. Gamble, B. Yuan, S. Penney, S. Jhangiani, D. M. Muzny, R. A. Gibbs, J. R. Lupski and J. T. Hecht (2015). "Mutations in COL27A1 cause Steel syndrome and suggest a founder mutation effect in the Puerto Rican population." *Eur J Hum Genet* **23**(3): 342-346.

Gress, C. J. and O. Jacenko (2000). "Growth plate compressions and altered hematopoiesis in collagen X null mice." *J Cell Biol* **149**(4): 983-993.

Griffiths-Jones, S., R. J. Grocock, S. van Dongen, A. Bateman and A. J. Enright (2006). "miRBase: microRNA sequences, targets and gene nomenclature." *Nucleic Acids Res* **34**(Database issue): D140-144.

Grigelioniene, G., H. I. Suzuki, F. Taylan, F. Mirzamohammadi, Z. U. Borochowitz, U. M. Ayturk, S. Tzur, E. Horemuzova, A. Lindstrand, M. A. Weis, G. Grigelionis, A. Hammarsjo, E. Marsk, A. Nordgren, M. Nordenskjold, D. R. Eyre, M. L. Warman, G. Nishimura, P. A. Sharp and T. Kobayashi (2019). "Gain-of-function mutation of microRNA-140 in human skeletal dysplasia." *Nat Med* **25**(4): 583-590.

Grigoriadis, A. E., K. Schellander, Z. Q. Wang and E. F. Wagner (1993). "Osteoblasts are target cells for transformation in c-fos transgenic mice." *J Cell Biol* **122**(3): 685-701.

Guan, Y. J., X. Yang, L. Wei and Q. Chen (2011). "MiR-365: a mechanosensitive microRNA stimulates chondrocyte differentiation through targeting histone deacetylase 4." *FASEB J* **25**(12): 4457-4466.

Guillemyn, B., H. Kayserili, L. Demuynck, P. Sips, A. De Paepe, D. Syx, P. J. Coucke, F. Malfait and S. Symoens (2019). "A homozygous pathogenic missense variant broadens the phenotypic and mutational spectrum of CREB3L1-related osteogenesis imperfecta." *Hum Mol Genet* **28**(11): 1801-1809.

Guo, L. and Z. Lu (2010). "The fate of miRNA* strand through evolutionary analysis: implication for degradation as merely carrier strand or potential regulatory molecule?" *PLoS One* **5**(6): e11387.

Hall, B. K. and T. Miyake (1992). "The membranous skeleton: the role of cell condensations in vertebrate skeletogenesis." *Anat Embryol (Berl)* **186**(2): 107-124.

Han, Y. C., J. A. Vidigal, P. Mu, E. Yao, I. Singh, A. J. Gonzalez, C. P. Concepcion, C. Bonetti, P. Ogorodowski, B. Carver, L. Selleri, D. Betel, C. Leslie and A. Ventura (2015). "An allelic series of miR-17 approximately 92-mutant mice uncovers functional specialization and cooperation among members of a microRNA polycistron." *Nat Genet* **47**(7): 766-775.

Harfe, B. D., M. T. McManus, J. H. Mansfield, E. Hornstein and C. J. Tabin (2005). "The RNaseIII enzyme Dicer is required for morphogenesis but not patterning of the vertebrate limb." *Proc Natl Acad Sci U S A* **102**(31): 10898-10903.

Hashimoto, M., T. Nakasa, T. Hikata and H. Asahara (2008). "Molecular network of cartilage homeostasis and osteoarthritis." *Med Res Rev* **28**(3): 464-481.

Hecht, N., B. Johnstone, P. Angele, T. Walker and W. Richter (2019). "Mechanosensitive MiRs regulated by anabolic and catabolic loading of human cartilage." *Osteoarthritis Cartilage* **27**(8): 1208-1218.

Hellemans, J., P. J. Coucke, A. Giedion, A. De Paepe, P. Kramer, F. Beemer and G. R. Mortier (2003). "Homozygous mutations in IHH cause acrocapitofemoral dysplasia, an autosomal recessive disorder with cone-shaped epiphyses in hands and hips." *Am J Hum Genet* **72**(4): 1040-1046.

Hellvard, A., L. Zeitlmann, U. Heiser, A. Kehlen, A. Niestroj, H. U. Demuth, J. Koziel, N. Delaleu, P. Jan and P. Mydel (2016). "Inhibition of CDK9 as a therapeutic strategy for inflammatory arthritis." *Sci Rep* **6**: 31441.

Hess, J., B. Hartenstein, S. Teurich, D. Schmidt, M. Schorpp-Kistner and P. Angel (2003). "Defective endochondral ossification in mice with strongly compromised expression of JunB." *J Cell Sci* **116**(Pt 22): 4587-4596.

Hinai, E., T. Takarada, S. Fujimori, L. Wang, M. Iemata, K. Uno and Y. Yoneda (2007). "Nuclear factor E2 p45-related factor 2 negatively regulates chondrogenesis." *Bone* **40**(2): 337-344.

Hirai, T., A. S. Chagin, T. Kobayashi, S. Mackem and H. M. Kronenberg (2011). "Parathyroid hormone/parathyroid hormone-related protein receptor signaling is required for maintenance of the growth plate in postnatal life." *Proc Natl Acad Sci U S A* **108**(1): 191-196.

Hornstein, E. and N. Shomron (2006). "Canalization of development by microRNAs." *Nat Genet* **38 Suppl**: S20-24.

Hu, S., X. Zhao, G. Mao, Z. Zhang, X. Wen, C. Zhang, W. Liao and Z. Zhang (2019). "MicroRNA-455-3p promotes TGF-beta signaling and inhibits osteoarthritis development by directly targeting PAK2." *Exp Mol Med* **51**(10): 1-13.

Huang, C. Y., K. Y. Lai, L. F. Hung, W. L. Wu, F. C. Liu and L. J. Ho (2011). "Advanced glycation end products cause collagen II reduction by activating Janus kinase/signal transducer and activator of transcription 3 pathway in porcine chondrocytes." *Rheumatology (Oxford)* **50**(8): 1379-1389.

Hwang, H. S. and H. A. Kim (2015). "Chondrocyte Apoptosis in the Pathogenesis of Osteoarthritis." *Int J Mol Sci* **16**(11): 26035-26054.

Hyde, G., S. Dover, A. Aszodi, G. A. Wallis and R. P. Boot-Handford (2007). "Lineage tracing using matrilin-1 gene expression reveals that articular chondrocytes exist as the joint interzone forms." *Dev Biol* **304**(2): 825-833.

Iijima, H., T. Aoyama, A. Ito, J. Tajino, M. Nagai, X. Zhang, S. Yamaguchi, H. Akiyama and H. Kuroki (2014). "Immature articular cartilage and subchondral bone covered by menisci are potentially susceptible to mechanical load." *BMC Musculoskelet Disord* **15**: 101.

Iliopoulos, D., K. N. Malizos, P. Oikonomou and A. Tsezou (2008). "Integrative microRNA and proteomic approaches identify novel osteoarthritis genes and their collaborative metabolic and inflammatory networks." *PLoS One* **3**(11): e3740.

Inada, M., Y. Wang, M. H. Byrne, M. U. Rahman, C. Miyaura, C. Lopez-Otin and S. M. Krane (2004). "Critical roles for collagenase-3 (Mmp13) in development of growth plate cartilage and in endochondral ossification." *Proc Natl Acad Sci U S A* **101**(49): 17192-17197.

Inui, M., S. Mokuda, T. Sato, M. Tamano, S. Takada and H. Asahara (2018). "Dissecting the roles of miR-140 and its host gene." *Nat Cell Biol* **20**(5): 516-518.

Ito, Y., T. Matsuzaki, F. Ayabe, S. Mokuda, R. Kurimoto, T. Matsushima, Y. Tabata, M. Inotsume, H. Tsutsumi, L. Liu, M. Shinohara, Y. Tanaka, R. Nakamichi, K. Nishida, M. K. Lotz and H. Asahara (2021). "Both microRNA-455-5p and -3p repress hypoxia-inducible factor-2alpha expression and coordinately regulate cartilage homeostasis." *Nat Commun* **12**(1): 4148.

Jacenko, O., D. Chan, A. Franklin, S. Ito, C. B. Underhill, J. F. Bateman and M. R. Campbell (2001). "A dominant interference collagen X mutation disrupts hypertrophic chondrocyte pericellular matrix and glycosaminoglycan and proteoglycan distribution in transgenic mice." *Am J Pathol* **159**(6): 2257-2269.

James, C. G., L. A. Stanton, H. Agoston, V. Ulici, T. M. Underhill and F. Beier (2010). "Genome-wide analyses of gene expression during mouse endochondral ossification." *PLoS One* **5**(1): e8693.

Janku, F., T. A. Yap and F. Meric-Bernstam (2018). "Targeting the PI3K pathway in cancer: are we making headway?" *Nat Rev Clin Oncol* **15**(5): 273-291.

Jenkins, E., J. B. Moss, J. M. Pace and L. C. Bridgewater (2005). "The new collagen gene COL27A1 contains SOX9-responsive enhancer elements." *Matrix Biol* **24**(3): 177-184.

Jeon, O. H., C. Kim, R. M. Laberge, M. Demaria, S. Rathod, A. P. Vasserot, J. W. Chung, D. H. Kim, Y. Poon, N. David, D. J. Baker, J. M. van Deursen, J. Campisi and J. H. Elisseeff (2017). "Local clearance of senescent cells attenuates the development of post-traumatic osteoarthritis and creates a pro-regenerative environment." *Nat Med* **23**(6): 775-781.

Ji, Q., X. Xu, Y. Xu, Z. Fan, L. Kang, L. Li, Y. Liang, J. Guo, T. Hong, Z. Li, Q. Zhang, Q. Ye and Y. Wang (2016). "miR-105/Runx2 axis mediates FGF2-induced ADAMTS expression in osteoarthritis cartilage." *J Mol Med (Berl)* **94**(6): 681-694.

Jiang, W., T. Li, J. Wang, R. Jiao, X. Shi, X. Huang and G. Ji (2019). "miR-140-3p Suppresses Cell Growth And Induces Apoptosis In Colorectal Cancer By Targeting PD-L1." *Onco Targets Ther* **12**: 10275-10285.

Jin, L., J. Zhao, W. Jing, S. Yan, X. Wang, C. Xiao and B. Ma (2014). "Role of miR-146a in human chondrocyte apoptosis in response to mechanical pressure injury in vitro." Int J Mol Med **34**(2): 451-463.

Jobert, A. S., P. Zhang, A. Couvineau, J. Bonaventure, J. Roume, M. Le Merrer and C. Silve (1998). "Absence of functional receptors for parathyroid hormone and parathyroid hormone-related peptide in Blomstrand chondrodysplasia." J Clin Invest **102**(1): 34-40.

Jochum, W., E. Passegue and E. F. Wagner (2001). "AP-1 in mouse development and tumorigenesis." Oncogene **20**(19): 2401-2412.

Jones, S. W., G. Watkins, N. Le Good, S. Roberts, C. L. Murphy, S. M. Brockbank, M. R. Needham, S. J. Read and P. Newham (2009). "The identification of differentially expressed microRNA in osteoarthritic tissue that modulate the production of TNF-alpha and MMP13." Osteoarthritis Cartilage **17**(4): 464-472.

Jones, T. L., M. S. Esa, K. H. C. Li, S. R. G. Krishnan, G. M. Elgallab, M. S. Pearce, D. A. Young and F. N. Birrell (2021). "Osteoporosis, fracture, osteoarthritis & sarcopenia: A systematic review of circulating microRNA association." Bone **152**: 116068.

Jude, J. A., M. Dileepan, S. Subramanian, J. Solway, R. A. Panettieri, Jr., T. F. Walseth and M. S. Kannan (2012). "miR-140-3p regulation of TNF-alpha-induced CD38 expression in human airway smooth muscle cells." Am J Physiol Lung Cell Mol Physiol **303**(5): L460-468.

Karaplis, A. C., B. He, M. T. Nguyen, I. D. Young, D. Semeraro, H. Ozawa and N. Amizuka (1998). "Inactivating mutation in the human parathyroid hormone receptor type 1 gene in Blomstrand chondrodysplasia." Endocrinology **139**(12): 5255-5258.

Karreth, F., A. Hoebertz, H. Scheuch, R. Eferl and E. F. Wagner (2004). "The AP1 transcription factor Fra2 is required for efficient cartilage development." Development **131**(22): 5717-5725.

Karsenty, G. and E. F. Wagner (2002). "Reaching a genetic and molecular understanding of skeletal development." Dev Cell **2**(4): 389-406.

Killion, C. H., E. H. Mitchell, C. G. Duke and R. Serra (2017). "Mechanical loading regulates organization of the actin cytoskeleton and column formation in postnatal growth plate." Mol Biol Cell **28**(14): 1862-1870.

Kim, H. K., G. S. Feng, D. Chen, P. D. King and N. Kamiya (2014). "Targeted disruption of Shp2 in chondrocytes leads to metachondromatosis with multiple cartilaginous protrusions." J Bone Miner Res **29**(3): 761-769.

Kim, I. S., F. Otto, B. Zabel and S. Mundlos (1999). "Regulation of chondrocyte differentiation by Cbfa1." Mech Dev **80**(2): 159-170.

Kluppel, M. (2010). "The roles of chondroitin-4-sulfotransferase-1 in development and disease." Prog Mol Biol Transl Sci **93**: 113-132.

Kluppel, M., T. N. Wight, C. Chan, A. Hinek and J. L. Wrana (2005). "Maintenance of chondroitin sulfation balance by chondroitin-4-sulfotransferase 1 is required for chondrocyte development and growth factor signaling during cartilage morphogenesis." Development **132**(17): 3989-4003.

Kobayashi, T., J. Lu, B. S. Cobb, S. J. Rodda, A. P. McMahon, E. Schipani, M. Merkenschlager and H. M. Kronenberg (2008). "Dicer-dependent pathways regulate chondrocyte proliferation and differentiation." Proceedings of the National Academy of Sciences of the United States of America **105**(6): 1949-1954.

Kobayashi, T., J. Lu, B. S. Cobb, S. J. Rodda, A. P. McMahon, E. Schipani, M. Merkenschlager and H. M. Kronenberg (2008). "Dicer-dependent pathways regulate chondrocyte proliferation and differentiation." Proc Natl Acad Sci U S A **105**(6): 1949-1954.

Kobayashi, T., G. Papaioannou, F. Mirzamohammadi, E. Kozhemyakina, M. Zhang, R. Blelloch and M. W. Chong (2015). "Early postnatal ablation of the microRNA-processing enzyme, Drosha, causes chondrocyte death and impairs the structural integrity of the articular cartilage." Osteoarthritis Cartilage **23**(7): 1214-1220.

Kobayashi, T., D. W. Soegiarto, Y. Yang, B. Lanske, E. Schipani, A. P. McMahon and H. M. Kronenberg (2005). "Indian hedgehog stimulates periarticular chondrocyte differentiation to regulate growth plate length independently of PTHrP." J Clin Invest **115**(7): 1734-1742.

Komori, T., H. Yagi, S. Nomura, A. Yamaguchi, K. Sasaki, K. Deguchi, Y. Shimizu, R. T. Bronson, Y. H. Gao, M. Inada, M. Sato, R. Okamoto, Y. Kitamura, S. Yoshiki and T. Kishimoto (1997). "Targeted disruption of Cbfa1 results in a complete lack of bone formation owing to maturational arrest of osteoblasts." Cell **89**(5): 755-764.

Kondo, S., S. I. Hino, A. Saito, S. Kanemoto, N. Kawasaki, R. Asada, S. Izumi, H. Iwamoto, M. Oki, H. Miyagi, M. Kaneko, Y. Nomura, F. Urano and K. Imaizumi (2012). "Activation of OASIS family, ER stress transducers, is dependent on its stabilization." Cell Death Differ **19**(12): 1939-1949.

Kotabagi, S., H. Shah, A. Shukla and K. M. Girisha (2017). "Second family provides further evidence for causation of Steel syndrome by biallelic mutations in COL27A1." Clin Genet **92**(3): 323-326.

Koyama, E., Y. Shibukawa, M. Nagayama, H. Sugito, B. Young, T. Yuasa, T. Okabe, T. Ochiai, N. Kamiya, R. B. Rountree, D. M. Kingsley, M. Iwamoto, M. Enomoto-Iwamoto and M. Pacifici (2008). "A distinct cohort of progenitor cells participates in synovial joint and articular cartilage formation during mouse limb skeletogenesis." Dev Biol **316**(1): 62-73.

Kozhemyakina, E., T. Cohen, T. P. Yao and A. B. Lassar (2009). "Parathyroid hormone-related peptide represses chondrocyte hypertrophy through a protein phosphatase 2A/histone deacetylase 4/MEF2 pathway." Mol Cell Biol **29**(21): 5751-5762.

Kozhemyakina, E., M. Zhang, A. Ionescu, U. M. Ayturk, N. Ono, A. Kobayashi, H. Kronenberg, M. L. Warman and A. B. Lassar (2015). "Identification of a Prg4-expressing articular cartilage progenitor cell population in mice." Arthritis Rheumatol **67**(5): 1261-1273.

Kronenberg, H. M. (2003). "Developmental regulation of the growth plate." Nature **423**(6937): 332-336.

Kronenberg, H. M. (2006). "PThrP and skeletal development." Ann N Y Acad Sci **1068**: 1-13.

Kuleshov, M. V., M. R. Jones, A. D. Rouillard, N. F. Fernandez, Q. Duan, Z. Wang, S. Koplev, S. L. Jenkins, K. M. Jagodnik, A. Lachmann, M. G. McDermott, C. D. Monteiro, G. W. Gundersen and A. Ma'ayan (2016). "Enrichr: a comprehensive gene set enrichment analysis web server 2016 update." Nucleic Acids Res **44**(W1): W90-97.

Kumar, A., A. K. Wong, M. L. Tizard, R. J. Moore and C. Lefevre (2012). "miRNA_Targets: a database for miRNA target predictions in coding and non-coding regions of mRNAs." *Genomics* **100**(6): 352-356.

Kung, L. H. W., L. Mullan, J. Soul, P. Wang, K. Mori, J. F. Bateman, M. D. Briggs and R. P. Boot-Handford (2019). "Cartilage endoplasmic reticulum stress may influence the onset but not the progression of experimental osteoarthritis." *Arthritis Res Ther* **21**(1): 206.

Kuuluvainen, E., E. Domenech-Moreno, E. H. Niemela and T. P. Makela (2018). "Depletion of Mediator Kinase Module Subunits Represses Superenhancer-Associated Genes in Colon Cancer Cells." *Mol Cell Biol* **38**(11).

Kwok, J., H. Onuma, M. Olmer, M. K. Lotz, S. P. Grogan and D. D. D'Lima (2016). "Histopathological analyses of murine menisci: implications for joint aging and osteoarthritis." *Osteoarthritis Cartilage* **24**(4): 709-718.

Lahiri, S., H. Kim, I. Garcia-Perez, M. M. Reza, K. A. Martin, P. Kundu, L. M. Cox, J. Selkirk, J. M. Posma, H. Zhang, P. Padmanabhan, C. Moret, B. Gulyas, M. J. Blaser, J. Auwerx, E. Holmes, J. Nicholson, W. Wahli and S. Pettersson (2019). "The gut microbiota influences skeletal muscle mass and function in mice." *Sci Transl Med* **11**(502).

Lalevee, S., O. Lapaire and M. Buhler (2014). "miR455 is linked to hypoxia signaling and is deregulated in preeclampsia." *Cell Death Dis* **5**: e1408.

Lamuedra, A., P. Gratal, L. Calatrava, V. L. Ruiz-Perez, R. Largo and G. Herrero-Beaumont (2020). "Disorganization of chondrocyte columns in the growth plate does not aggravate experimental osteoarthritis in mice." *Sci Rep* **10**(1): 10745.

Lanford, R. E., E. S. Hildebrandt-Eriksen, A. Petri, R. Persson, M. Lindow, M. E. Munk, S. Kauppinen and H. Orum (2010). "Therapeutic silencing of microRNA-122 in primates with chronic hepatitis C virus infection." *Science* **327**(5962): 198-201.

Lanske, B., A. C. Karaplis, K. Lee, A. Luz, A. Vortkamp, A. Pirro, M. Karperien, L. H. Defize, C. Ho, R. C. Mulligan, A. B. Abou-Samra, H. Juppner, G. V. Segre and H. M. Kronenberg (1996). "PTH/PTHRp receptor in early development and Indian hedgehog-regulated bone growth." *Science* **273**(5275): 663-666.

Le Rossignol, S., N. Ketheesan and N. Haleagrahara (2018). "Redox-sensitive transcription factors play a significant role in the development of rheumatoid arthritis." *Int Rev Immunol* **37**(3): 129-143.

Lee, I., S. S. Ajay, J. I. Yook, H. S. Kim, S. H. Hong, N. H. Kim, S. M. Dhanasekaran, A. M. Chinnaiyan and B. D. Athey (2009). "New class of microRNA targets containing simultaneous 5'-UTR and 3'-UTR interaction sites." *Genome Res* **19**(7): 1175-1183.

Lee, Y. R., M. Chen, J. D. Lee, J. Zhang, S. Y. Lin, T. M. Fu, H. Chen, T. Ishikawa, S. Y. Chiang, J. Katon, Y. Zhang, Y. V. Shulga, A. C. Bester, J. Fung, E. Monteleone, L. Wan, C. Shen, C. H. Hsu, A. Papa, J. G. Clohessy, J. Teruya-Feldstein, S. Jain, H. Wu, L. Matesic, R. H. Chen, W. Wei and P. P. Pandolfi (2019). "Reactivation of PTEN tumor suppressor for cancer treatment through inhibition of a MYC-WWP1 inhibitory pathway." *Science* **364**(6441).

Lefebvre, V., S. Garofalo, G. Zhou, M. Metsaranta, E. Vuorio and B. De Crombrugghe (1994). "Characterization of primary cultures of chondrocytes from type II collagen/beta-galactosidase transgenic mice." *Matrix Biol* **14**(4): 329-335.

Lewis, B. P., C. B. Burge and D. P. Bartel (2005). "Conserved seed pairing, often flanked by adenosines, indicates that thousands of human genes are microRNA targets." *Cell* **120**(1): 15-20.

Li, L., J. Jia, X. Liu, S. Yang, S. Ye, W. Yang and Y. Zhang (2015). "MicroRNA-16-5p Controls Development of Osteoarthritis by Targeting SMAD3 in Chondrocytes." *Curr Pharm Des* **21**(35): 5160-5167.

Li, M., C. Marin-Muller, U. Bharadwaj, K. H. Chow, Q. Yao and C. Chen (2009). "MicroRNAs: control and loss of control in human physiology and disease." *World J Surg* **33**(4): 667-684.

Li, P., L. Fleischhauer, C. Nicolae, C. Prein, Z. Farkas, M. M. Saller, W. C. Prall, R. Wagener, J. Heilig, A. Niehoff, H. Clausen-Schaumann, P. Alberton and A. Aszodi (2020). "Mice Lacking the Matrilin Family of Extracellular Matrix Proteins Develop Mild Skeletal Abnormalities and Are Susceptible to Age-Associated Osteoarthritis." *Int J Mol Sci* **21**(2).

Li, Y., X. Wei, J. Zhou and L. Wei (2013). "The age-related changes in cartilage and osteoarthritis." *Biomed Res Int* **2013**: 916530.

Liang, Z. J., H. Zhuang, G. X. Wang, Z. Li, H. T. Zhang, T. Q. Yu and B. D. Zhang (2012). "MiRNA-140 is a negative feedback regulator of MMP-13 in IL-1beta-stimulated human articular chondrocyte C28/I2 cells." *Inflamm Res* **61**(5): 503-509.

Lim, N. H., C. Wen and T. L. Vincent (2020). "Molecular and structural imaging in surgically induced murine osteoarthritis." *Osteoarthritis Cartilage* **28**(7): 874-884.

Liu, B., Y. Shyr, J. Cai and Q. Liu (2018). "Interplay between miRNAs and host genes and their role in cancer." *Brief Funct Genomics* **18**(4): 255-266.

Liu, W., X. Sun, A. Braut, Y. Mishina, R. R. Behringer, M. Mina and J. F. Martin (2005). "Distinct functions for Bmp signaling in lip and palate fusion in mice." *Development* **132**(6): 1453-1461.

Liu, X., X. Chen, X. Yu, Y. Tao, A. M. Bode, Z. Dong and Y. Cao (2013). "Regulation of microRNAs by epigenetics and their interplay involved in cancer." *J Exp Clin Cancer Res* **32**: 96.

Liu, Z., J. Xu, J. S. Colvin and D. M. Ornitz (2002). "Coordination of chondrogenesis and osteogenesis by fibroblast growth factor 18." *Genes Dev* **16**(7): 859-869.

Lorenz, J. and S. Grassel (2014). "Experimental osteoarthritis models in mice." *Methods Mol Biol* **1194**: 401-419.

Lotz, M. K. and V. B. Kraus (2010). "New developments in osteoarthritis. Posttraumatic osteoarthritis: pathogenesis and pharmacological treatment options." *Arthritis Res Ther* **12**(3): 211.

Lui, J. C., Y. H. Jee, P. Garrison, J. R. Iben, S. Yue, M. Ad, Q. Nguyen, B. Kikani, Y. Wakabayashi and J. Baron (2018). "Differential aging of growth plate cartilage underlies differences in bone length and thus helps determine skeletal proportions." *PLoS Biol* **16**(7): e2005263.

Lytle, J. R., T. A. Yario and J. A. Steitz (2007). "Target mRNAs are repressed as efficiently by microRNA-binding sites in the 5' UTR as in the 3' UTR." *Proc Natl Acad Sci U S A* **104**(23): 9667-9672.

Ma, F., C. Zhang, K. V. Prasad, G. J. Freeman and S. F. Schlossman (2001). "Molecular cloning of Porimin, a novel cell surface receptor mediating oncotic cell death." *Proc Natl Acad Sci U S A* **98**(17): 9778-9783.

MacLean, H. E., J. I. Kim, M. J. Glimcher, J. Wang, H. M. Kronenberg and L. H. Glimcher (2003). "Absence of transcription factor c-maf causes abnormal terminal differentiation of hypertrophic chondrocytes during endochondral bone development." *Dev Biol* **262**(1): 51-63.

Maeda, S., J. Nishida, T. Sato, Y. Inomata, T. Shimamura and S. Horiuchi (2005). "Changes in microstructure and gene expression of articular chondrocytes cultured in a tube under mechanical stress." *Osteoarthritis Cartilage* **13**(2): 154-161.

Maeda, Y., E. Nakamura, M. T. Nguyen, L. J. Suva, F. L. Swain, M. S. Razzaque, S. Mackem and B. Lanske (2007). "Indian Hedgehog produced by postnatal chondrocytes is essential for maintaining a growth plate and trabecular bone." *Proc Natl Acad Sci U S A* **104**(15): 6382-6387.

Maes, C., P. Carmeliet, K. Moermans, I. Stockmans, N. Smets, D. Collen, R. Bouillon and G. Carmeliet (2002). "Impaired angiogenesis and endochondral bone formation in mice lacking the vascular endothelial growth factor isoforms VEGF164 and VEGF188." *Mech Dev* **111**(1-2): 61-73.

Majoros, W. H., P. Lekprasert, N. Mukherjee, R. L. Skalsky, D. L. Corcoran, B. R. Cullen and U. Ohler (2013). "MicroRNA target site identification by integrating sequence and binding information." *Nat Methods* **10**(7): 630-633.

Mak, K. K., H. M. Kronenberg, P. T. Chuang, S. Mackem and Y. Yang (2008). "Indian hedgehog signals independently of PTHrP to promote chondrocyte hypertrophy." *Development* **135**(11): 1947-1956.

Manzano, M., E. Forte, A. N. Raja, M. J. Schipma and E. Gottwein (2015). "Divergent target recognition by coexpressed 5'-isomiRs of miR-142-3p and selective viral mimicry." *RNA* **21**(9): 1606-1620.

Mao, G., Y. Kang, R. Lin, S. Hu, Z. Zhang, H. Li, W. Liao and Z. Zhang (2019). "Long Non-coding RNA HOTTIP Promotes CCL3 Expression and Induces Cartilage Degradation by Sponging miR-455-3p." *Front Cell Dev Biol* **7**: 161.

Marco, A., J. H. Hui, M. Ronshaugen and S. Griffiths-Jones (2010). "Functional shifts in insect microRNA evolution." *Genome Biol Evol* **2**: 686-696.

Martinez-Moreno, D., G. Jimenez, P. Galvez-Martin, G. Rus and J. A. Marchal (2019). "Cartilage biomechanics: A key factor for osteoarthritis regenerative medicine." *Biochim Biophys Acta Mol Basis Dis* **1865**(6): 1067-1075.

Matsukawa, N., W. J. Grzesik, N. Takahashi, K. N. Pandey, S. Pang, M. Yamauchi and O. Smithies (1999). "The natriuretic peptide clearance receptor locally modulates the physiological effects of the natriuretic peptide system." *Proc Natl Acad Sci U S A* **96**(13): 7403-7408.

Matsukawa, T., T. Sakai, T. Yonezawa, H. Hiraiwa, T. Hamada, M. Nakashima, Y. Ono, S. Ishizuka, H. Nakahara, M. K. Lotz, H. Asahara and N. Ishiguro (2013). "MicroRNA-125b regulates the expression of aggrecanase-1 (ADAMTS-4) in human osteoarthritic chondrocytes." *Arthritis Res Ther* **15**(1): R28.

McCulloch, K., G. J. Litherland and T. S. Rai (2017). "Cellular senescence in osteoarthritis pathology." *Aging Cell* **16**(2): 210-218.

McNulty, M. A., R. F. Loeser, C. Davey, M. F. Callahan, C. M. Ferguson and C. S. Carlson (2011). "A Comprehensive Histological Assessment of Osteoarthritis Lesions in Mice." *Cartilage* **2**(4): 354-363.

Mengshol, J. A., M. P. Vincenti and C. E. Brinckerhoff (2001). "IL-1 induces collagenase-3 (MMP-13) promoter activity in stably transfected chondrocytic cells: requirement for Runx-2 and activation by p38 MAPK and JNK pathways." Nucleic Acids Res **29**(21): 4361-4372.

Min, Z., R. Zhang, J. Yao, C. Jiang, Y. Guo, F. Cong, W. Wang, J. Tian, N. Zhong, J. Sun, J. Ma and S. Lu (2015). "MicroRNAs associated with osteoarthritis differently expressed in bone matrix gelatin (BMG) rat model." Int J Clin Exp Med **8**(1): 1009-1017.

Minina, E., C. Kreschel, M. C. Naski, D. M. Ornitz and A. Vortkamp (2002). "Interaction of FGF, Ihh/Pthlh, and BMP signaling integrates chondrocyte proliferation and hypertrophic differentiation." Dev Cell **3**(3): 439-449.

Mirzamohammadi, F., A. Kozlova, G. Papaioannou, E. Paltrinieri, U. M. Ayturk and T. Kobayashi (2018). "Distinct molecular pathways mediate Mycn and Myc-regulated miR-17-92 microRNA action in Feingold syndrome mouse models." Nat Commun **9**(1): 1352.

Mirzamohammadi, F., G. Papaioannou and T. Kobayashi (2014). "MicroRNAs in cartilage development, homeostasis, and disease." Curr Osteoporos Rep **12**(4): 410-419.

Miyaki, S. and H. Asahara (2012). "Macro view of microRNA function in osteoarthritis." Nature Reviews Rheumatology **8**(9): 543-552.

Miyaki, S. and H. Asahara (2012). "Macro view of microRNA function in osteoarthritis." Nat Rev Rheumatol **8**(9): 543-552.

Miyaki, S., T. Nakasa, S. Otsuki, S. P. Grogan, R. Higashiyama, A. Inoue, Y. Kato, T. Sato, M. K. Lotz and H. Asahara (2009). "MicroRNA-140 is expressed in differentiated human articular chondrocytes and modulates interleukin-1 responses." Arthritis Rheum **60**(9): 2723-2730.

Miyaki, S., T. Sato, A. Inoue, S. Otsuki, Y. Ito, S. Yokoyama, Y. Kato, F. Takemoto, T. Nakasa, S. Yamashita, S. Takada, M. K. Lotz, H. Ueno-Kudo and H. Asahara (2010). "MicroRNA-140 plays dual roles in both cartilage development and homeostasis." Genes Dev **24**(11): 1173-1185.

Mokuda, S., R. Nakamichi, T. Matsuzaki, Y. Ito, T. Sato, K. Miyata, M. Inui, M. Olmer, E. Sugiyama, M. Lotz and H. Asahara (2019). "Wwp2 maintains cartilage homeostasis through regulation of Adamts5." Nat Commun **10**(1): 2429.

Moore, M. J., T. K. Scheel, J. M. Luna, C. Y. Park, J. J. Fak, E. Nishiuchi, C. M. Rice and R. B. Darnell (2015). "miRNA-target chimeras reveal miRNA 3'-end pairing as a major determinant of Argonaute target specificity." Nat Commun **6**: 8864.

Moore, M. J., C. Zhang, E. C. Gantman, A. Mele, J. C. Darnell and R. B. Darnell (2014). "Mapping Argonaute and conventional RNA-binding protein interactions with RNA at single-nucleotide resolution using HITS-CLIP and CIMS analysis." Nat Protoc **9**(2): 263-293.

Mootha, V. K., P. Lepage, K. Miller, J. Bunkenborg, M. Reich, M. Hjerrild, T. Delmonte, A. Villeneuve, R. Sladek, F. Xu, G. A. Mitchell, C. Morin, M. Mann, T. J. Hudson, B. Robinson, J. D. Rioux and E. S. Lander (2003). "Identification of a gene causing human cytochrome c oxidase deficiency by integrative genomics." Proc Natl Acad Sci U S A **100**(2): 605-610.

Moussavi-Harami, S. F., D. R. Pedersen, J. A. Martin, S. L. Hillis and T. D. Brown (2009). "Automated objective scoring of histologically apparent cartilage degeneration using a custom image analysis program." J Orthop Res **27**(4): 522-528.

Mundlos, S. (1994). "Expression patterns of matrix genes during human skeletal development." *Prog Histochem Cytochem* **28**(3): 1-47.

Murakami, T., S. Hino, R. Nishimura, T. Yoneda, A. Wanaka and K. Imaizumi (2011). "Distinct mechanisms are responsible for osteopenia and growth retardation in OASIS-deficient mice." *Bone* **48**(3): 514-523.

Murakami, T., S. Kondo, M. Ogata, S. Kanemoto, A. Saito, A. Wanaka and K. Imaizumi (2006). "Cleavage of the membrane-bound transcription factor OASIS in response to endoplasmic reticulum stress." *J Neurochem* **96**(4): 1090-1100.

Murray, D., P. Precht, R. Balakir and W. E. Horton, Jr. (2000). "The transcription factor deltaEF1 is inversely expressed with type II collagen mRNA and can repress Col2a1 promoter activity in transfected chondrocytes." *J Biol Chem* **275**(5): 3610-3618.

Musumeci, G., P. Castrogiovanni, F. M. Trovato, A. M. Weinberg, M. K. Al-Wasiyah, M. H. Alqahtani and A. Mobasher (2015). "Biomarkers of Chondrocyte Apoptosis and Autophagy in Osteoarthritis." *Int J Mol Sci* **16**(9): 20560-20575.

Nakamura, Y., X. He, T. Kobayashi, Y. L. Yan, J. H. Postlethwait and M. L. Warman (2008). "Unique roles of microRNA140 and its host gene WWP2 in cartilage biology." *J Musculoskelet Neuronal Interact* **8**(4): 321-322.

Nakamura, Y., J. B. Inloes, T. Katagiri and T. Kobayashi (2011). "Chondrocyte-specific microRNA-140 regulates endochondral bone development and targets Dnpep to modulate bone morphogenetic protein signaling." *Mol Cell Biol* **31**(14): 3019-3028.

Nicolas, F. E., H. Pais, F. Schwach, M. Lindow, S. Kauppinen, V. Moulton and T. Dalmay (2008). "Experimental identification of microRNA-140 targets by silencing and overexpressing miR-140." *RNA* **14**(12): 2513-2520.

Nie, Z. Y., X. J. Liu, Y. Zhan, M. H. Liu, X. Y. Zhang, Z. Y. Li, Y. Q. Lu, J. M. Luo and L. Yang (2019). "miR-140-5p induces cell apoptosis and decreases Warburg effect in chronic myeloid leukemia by targeting SIX1." *Biosci Rep* **39**(4).

Nishimori, S., F. Lai, M. Shiraishi, T. Kobayashi, E. Kozhemyakina, T. P. Yao, A. B. Lassar and H. M. Kronenberg (2019). "PTHRP targets HDAC4 and HDAC5 to repress chondrocyte hypertrophy." *JCI Insight* **4**(5).

Niswander, L. (2003). "Pattern formation: old models out on a limb." *Nat Rev Genet* **4**(2): 133-143.

Ntoumou, E., M. Tzetis, M. Braoudaki, G. Lambrou, M. Poulou, K. Malizos, N. Stefanou, L. Anastasopoulou and A. Tsezou (2017). "Serum microRNA array analysis identifies miR-140-3p, miR-33b-3p and miR-671-3p as potential osteoarthritis biomarkers involved in metabolic processes." *Clin Epigenetics* **9**: 127.

O'Brien, M., H. T. Philpott and J. J. McDougall (2017). "Understanding osteoarthritis pain through animal models." *Clin Exp Rheumatol* **35 Suppl 107**(5): 47-52.

Ohba, S. (2016). "Hedgehog Signaling in Endochondral Ossification." *J Dev Biol* **4**(2).

Olsen, B. R., A. M. Reginato and W. Wang (2000). "Bone development." *Annu Rev Cell Dev Biol* **16**: 191-220.

Ornitz, D. M. (2005). "FGF signaling in the developing endochondral skeleton." *Cytokine Growth Factor Rev* **16**(2): 205-213.

Ortega, N., D. J. Behonick and Z. Werb (2004). "Matrix remodeling during endochondral ossification." *Trends Cell Biol* **14**(2): 86-93.

Ostergaard, K., C. B. Andersen, J. Petersen, K. Bendtzen and D. M. Salter (1999). "Validity of histopathological grading of articular cartilage from osteoarthritic knee joints." *Ann Rheum Dis* **58**(4): 208-213.

Otto, F., A. P. Thornell, T. Crompton, A. Denzel, K. C. Gilmour, I. R. Rosewell, G. W. Stamp, R. S. Beddington, S. Mundlos, B. R. Olsen, P. B. Selby and M. J. Owen (1997). "Cbfa1, a candidate gene for cleidocranial dysplasia syndrome, is essential for osteoblast differentiation and bone development." *Cell* **89**(5): 765-771.

Pace, J. M., M. Corrado, C. Missero and P. H. Byers (2003). "Identification, characterization and expression analysis of a new fibrillar collagen gene, COL27A1." *Matrix Biol* **22**(1): 3-14.

Pais, H., F. E. Nicolas, S. M. Soond, T. E. Swingler, I. M. Clark, A. Chantry, V. Moulton and T. Dalmay (2010). "Analyzing mRNA expression identifies Smad3 as a microRNA-140 target regulated only at protein level." *RNA* **16**(3): 489-494.

Papaioannou, G., J. B. Inloes, Y. Nakamura, E. Paltrinieri and T. Kobayashi (2013). "let-7 and miR-140 microRNAs coordinately regulate skeletal development." *Proc Natl Acad Sci U S A* **110**(35): E3291-3300.

Papaioannou, G., F. Mirzamohammadi, T. S. Lisse, S. Nishimori, M. N. Wein and T. Kobayashi (2015). "MicroRNA-140 Provides Robustness to the Regulation of Hypertrophic Chondrocyte Differentiation by the PTHrP-HDAC4 Pathway." *J Bone Miner Res* **30**(6): 1044-1052.

Park, C. Y., Y. S. Choi and M. T. McManus (2010). "Analysis of microRNA knockouts in mice." *Human Molecular Genetics* **19**: R169-R175.

Paroni, G., N. Cernotta, C. Dello Russo, P. Gallinari, M. Pallaoro, C. Foti, F. Talamo, L. Orsatti, C. Steinkuhler and C. Brancolini (2008). "PP2A regulates HDAC4 nuclear import." *Mol Biol Cell* **19**(2): 655-667.

Peltomaki, T. and L. Hakkinen (1992). "Growth of the ribs at the costochondral junction in the rat." *J Anat* **181 (Pt 2)**: 259-264.

Peterson, S. M., J. A. Thompson, M. L. Ufkin, P. Sathyanarayana, L. Liaw and C. B. Congdon (2014). "Common features of microRNA target prediction tools." *Front Genet* **5**: 23.

Piletic, K. and T. Kunej (2016). "MicroRNA epigenetic signatures in human disease." *Arch Toxicol* **90**(10): 2405-2419.

Plaisier, S. B., R. Taschereau, J. A. Wong and T. G. Graeber (2010). "Rank-rank hypergeometric overlap: identification of statistically significant overlap between gene-expression signatures." *Nucleic Acids Res* **38**(17): e169.

Plumb, D. A., L. Ferrara, T. Torbica, L. Knowles, A. Mironov, Jr., K. E. Kadler, M. D. Briggs and R. P. Boot-Handford (2011). "Collagen XXVII organises the pericellular matrix in the growth plate." *PLoS One* **6**(12): e29422.

Prein, C., N. Warmbold, Z. Farkas, M. Schieker, A. Aszodi and H. Clausen-Schaumann (2016). "Structural and mechanical properties of the proliferative zone of the developing murine growth plate cartilage assessed by atomic force microscopy." *Matrix Biol* **50**: 1-15.

Pritzker, K. P., S. Gay, S. A. Jimenez, K. Ostergaard, J. P. Pelletier, P. A. Revell, D. Salter and W. B. van den Berg (2006). "Osteoarthritis cartilage histopathology: grading and staging." *Osteoarthritis Cartilage* **14**(1): 13-29.

Provot, S. and E. Schipani (2005). "Molecular mechanisms of endochondral bone development." *Biochem Biophys Res Commun* **328**(3): 658-665.

Radwan, M., D. J. Wilkinson, W. Hui, A. P. Destrument, S. H. Charlton, M. J. Barter, B. Gibson, J. Coulombe, D. A. Gray, A. D. Rowan and D. A. Young (2015). "Protection against murine osteoarthritis by inhibition of the 26S proteasome and lysine-48 linked ubiquitination." *Ann Rheum Dis* **74**(8): 1580-1587.

Reimold, A. M., M. J. Grusby, B. Kosaras, J. W. Fries, R. Mori, S. Maniwa, I. M. Clauss, T. Collins, R. L. Sidman, M. J. Glimcher and L. H. Glimcher (1996). "Chondrodysplasia and neurological abnormalities in ATF-2-deficient mice." *Nature* **379**(6562): 262-265.

Reynard, L. N. and J. Loughlin (2012). "Genetics and epigenetics of osteoarthritis." *Maturitas* **71**(3): 200-204.

Roach, H. I. and N. M. Clarke (2000). "Physiological cell death of chondrocytes in vivo is not confined to apoptosis. New observations on the mammalian growth plate." *J Bone Joint Surg Br* **82**(4): 601-613.

Sahni, M., D. C. Ambrosetti, A. Mansukhani, R. Gertner, D. Levy and C. Basilico (1999). "FGF signaling inhibits chondrocyte proliferation and regulates bone development through the STAT-1 pathway." *Genes Dev* **13**(11): 1361-1366.

Salomon, W. E., S. M. Jolly, M. J. Moore, P. D. Zamore and V. Serebrov (2015). "Single-Molecule Imaging Reveals that Argonaute Reshapes the Binding Properties of Its Nucleic Acid Guides." *Cell* **162**(1): 84-95.

Sandell, L. J., A. M. Nalin and R. A. Reife (1994). "Alternative splice form of type II procollagen mRNA (IIA) is predominant in skeletal precursors and non-cartilaginous tissues during early mouse development." *Dev Dyn* **199**(2): 129-140.

Sasagawa, S., H. Takemori, T. Uebi, D. Ikegami, K. Hiramatsu, S. Ikegawa, H. Yoshikawa and N. Tsumaki (2012). "SIK3 is essential for chondrocyte hypertrophy during skeletal development in mice." *Development* **139**(6): 1153-1163.

Schirle, N. T., J. Sheu-Gruttaduria and I. J. MacRae (2014). "Structural basis for microRNA targeting." *Science* **346**(6209): 608-613.

Shang, J., H. Liu and Y. Zhou (2013). "Roles of microRNAs in prenatal chondrogenesis, postnatal chondrogenesis and cartilage-related diseases." *J Cell Mol Med* **17**(12): 1515-1524.

Sherr, C. J. and J. M. Roberts (1999). "CDK inhibitors: positive and negative regulators of G1-phase progression." *Genes Dev* **13**(12): 1501-1512.

Shvedova, M. and T. Kobayashi (2020). "MicroRNAs in cartilage development and dysplasia." Bone **140**: 115564.

Si, H. B., T. M. Yang, L. Li, M. Tian, L. Zhou, D. P. Li, Q. Huang, P. D. Kang, J. Yang, Z. K. Zhou, J. Q. Cheng and B. Shen (2020). "miR-140 Attenuates the Progression of Early-Stage Osteoarthritis by Retarding Chondrocyte Senescence." Mol Ther Nucleic Acids **19**: 15-30.

Silberberg, M. and R. Silberberg (1962). "Osteoarthritis and osteoporosis in senile mice." Gerontologia **6**: 91-101.

Small, E. M. and E. N. Olson (2011). "Pervasive roles of microRNAs in cardiovascular biology." Nature **469**(7330): 336-342.

Sokoloff, L. (1956). "Natural history of degenerative joint disease in small laboratory animals. I. Pathological anatomy of degenerative joint disease in mice." AMA Arch Pathol **62**(2): 118-128.

Sondag, G. R. and T. M. Haqqi (2016). "The Role of MicroRNAs and Their Targets in Osteoarthritis." Curr Rheumatol Rep **18**(8): 56.

Stadnik, P. S., S. J. Gilbert, J. Tarn, S. Charlton, A. J. Skelton, M. J. Barter, V. C. Duance, D. A. Young and E. J. Blain (2021). "Regulation of microRNA-221, -222, -21 and -27 in articular cartilage subjected to abnormal compressive forces." J Physiol **599**(1): 143-155.

Stanton, H., F. M. Rogerson, C. J. East, S. B. Golub, K. E. Lawlor, C. T. Meeker, C. B. Little, K. Last, P. J. Farmer, I. K. Campbell, A. M. Fourie and A. J. Fosang (2005). "ADAMTS5 is the major aggrecanase in mouse cartilage in vivo and in vitro." Nature **434**(7033): 648-652.

Stefani, G. and F. J. Slack (2008). "Small non-coding RNAs in animal development." Nat Rev Mol Cell Biol **9**(3): 219-230.

Stickens, D., D. J. Behonick, N. Ortega, B. Heyer, B. Hartenstein, Y. Yu, A. J. Fosang, M. Schorpp-Kistner, P. Angel and Z. Werb (2004). "Altered endochondral bone development in matrix metalloproteinase 13-deficient mice." Development **131**(23): 5883-5895.

Subramanian, A., P. Tamayo, V. K. Mootha, S. Mukherjee, B. L. Ebert, M. A. Gillette, A. Paulovich, S. L. Pomeroy, T. R. Golub, E. S. Lander and J. P. Mesirov (2005). "Gene set enrichment analysis: a knowledge-based approach for interpreting genome-wide expression profiles." Proc Natl Acad Sci U S A **102**(43): 15545-15550.

Sun, H., X. Zhao, C. Zhang, Z. Zhang, J. Lun, W. Liao and Z. Zhang (2018). "MiR-455-3p inhibits the degenerate process of chondrogenic differentiation through modification of DNA methylation." Cell Death Dis **9**(5): 537.

Swingler, T. E., L. Niu, P. Smith, P. Paddy, L. Le, M. J. Barter, D. A. Young and I. M. Clark (2019). "The function of microRNAs in cartilage and osteoarthritis." Clin Exp Rheumatol **37 Suppl 120**(5): 40-47.

Swingler, T. E., G. Wheeler, V. Carmont, H. R. Elliott, M. J. Barter, M. Abu-Elmagd, S. T. Donell, R. P. Boot-Handford, M. K. Hajhosseini, A. Munsterberg, T. Dalmay, D. A. Young and I. M. Clark (2012). "The expression and function of microRNAs in chondrogenesis and osteoarthritis." Arthritis Rheum **64**(6): 1909-1919.

Takeda, S., J. P. Bonnamy, M. J. Owen, P. Ducy and G. Karsenty (2001). "Continuous expression of Cbfa1 in nonhypertrophic chondrocytes uncovers its ability to induce hypertrophic chondrocyte differentiation and partially rescues Cbfa1-deficient mice." *Genes Dev* **15**(4): 467-481.

Tardif, G., D. Hum, J. P. Pelletier, N. Duval and J. Martel-Pelletier (2009). "Regulation of the IGFBP-5 and MMP-13 genes by the microRNAs miR-140 and miR-27a in human osteoarthritic chondrocytes." *BMC Musculoskelet Disord* **10**: 148.

Tay, Y., J. Zhang, A. M. Thomson, B. Lim and I. Rigoutsos (2008). "MicroRNAs to Nanog, Oct4 and Sox2 coding regions modulate embryonic stem cell differentiation." *Nature* **455**(7216): 1124-1128.

Tian, Z., C. Tang and Z. Wang (2019). "Neuroprotective effect of ginkgetin in experimental cerebral ischemia/reperfusion via apoptosis inhibition and PI3K/Akt/mTOR signaling pathway activation." *J Cell Biochem* **120**(10): 18487-18495.

Tickle, C. (2003). "Patterning systems--from one end of the limb to the other." *Dev Cell* **4**(4): 449-458.

Tickle, C. and A. Munsterberg (2001). "Vertebrate limb development--the early stages in chick and mouse." *Curr Opin Genet Dev* **11**(4): 476-481.

Toh, W. S., M. Brittberg, J. Farr, C. B. Foldager, A. H. Gomoll, J. H. Hui, J. B. Richardson, S. Roberts and M. Spector (2016). "Cellular senescence in aging and osteoarthritis." *Acta Orthop* **87**(sup363): 6-14.

Torre, D., A. Lachmann and A. Ma'ayan (2018). "BioJupies: Automated Generation of Interactive Notebooks for RNA-Seq Data Analysis in the Cloud." *Cell Syst* **7**(5): 556-561 e553.

Tryfonidou, M. A., H. A. Hazewinkel, F. M. Riemers, B. Brinkhof, L. C. Penning and M. Karperien (2010). "Intraspecies disparity in growth rate is associated with differences in expression of local growth plate regulators." *Am J Physiol Endocrinol Metab* **299**(6): E1044-1052.

Tuddenham, L., G. Wheeler, S. Ntounia-Fousara, J. Waters, M. K. Hajihosseini, I. Clark and T. Dalmay (2006). "The cartilage specific microRNA-140 targets histone deacetylase 4 in mouse cells." *FEBS Lett* **580**(17): 4214-4217.

Ueta, C., M. Iwamoto, N. Kanatani, C. Yoshida, Y. Liu, M. Enomoto-Iwamoto, T. Ohmori, H. Enomoto, K. Nakata, K. Takada, K. Kurisu and T. Komori (2001). "Skeletal malformations caused by overexpression of Cbfa1 or its dominant negative form in chondrocytes." *J Cell Biol* **153**(1): 87-100.

van den Berg, W. B. (2011). "Osteoarthritis year 2010 in review: pathomechanisms." *Osteoarthritis Cartilage* **19**(4): 338-341.

van Dongen, S., C. Abreu-Goodger and A. J. Enright (2008). "Detecting microRNA binding and siRNA off-target effects from expression data." *Nat Methods* **5**(12): 1023-1025.

Vega, R. B., K. Matsuda, J. Oh, A. C. Barbosa, X. Yang, E. Meadows, J. McAnally, C. Pomajzl, J. M. Shelton, J. A. Richardson, G. Karsenty and E. N. Olson (2004). "Histone deacetylase 4 controls chondrocyte hypertrophy during skeletogenesis." *Cell* **119**(4): 555-566.

Vincent, T. L. (2020). "Of mice and men: converging on a common molecular understanding of osteoarthritis." *Lancet Rheumatol* **2**(10): e633-e645.

Volinia, S., G. A. Calin, C. G. Liu, S. Ambs, A. Cimmino, F. Petrocca, R. Visone, M. Iorio, C. Roldo, M. Ferracin, R. L. Prueitt, N. Yanaihara, G. Lanza, A. Scarpa, A. Vecchione, M. Negrini, C. C. Harris and C. M. Croce (2006). "A microRNA expression signature of human solid tumors defines cancer gene targets." *Proc Natl Acad Sci U S A* **103**(7): 2257-2261.

Vortkamp, A., K. Lee, B. Lanske, G. V. Segre, H. M. Kronenberg and C. J. Tabin (1996). "Regulation of rate of cartilage differentiation by Indian hedgehog and PTH-related protein." *Science* **273**(5275): 613-622.

Vu, T. H., J. M. Shipley, G. Bergers, J. E. Berger, J. A. Helms, D. Hanahan, S. D. Shapiro, R. M. Senior and Z. Werb (1998). "MMP-9/gelatinase B is a key regulator of growth plate angiogenesis and apoptosis of hypertrophic chondrocytes." *Cell* **93**(3): 411-422.

Wadhwa, S., M. C. Embree, T. Kilts, M. F. Young and L. G. Ameye (2005). "Accelerated osteoarthritis in the temporomandibular joint of biglycan/fibromodulin double-deficient mice." *Osteoarthritis Cartilage* **13**(9): 817-827.

Wang, G., S. Chen, Z. Xie, S. Shen, W. Xu, W. Chen, X. Li, Y. Wu, L. Li, B. Liu, X. Ding, A. Qin and S. Fan (2020). "TGFbeta attenuates cartilage extracellular matrix degradation via enhancing FBXO6-mediated MMP14 ubiquitination." *Ann Rheum Dis* **79**(8): 1111-1120.

Wang, W., B. Song, T. Anbarchian, A. Shirazy, J. E. Sadik and K. M. Lyons (2016). "Smad2 and Smad3 Regulate Chondrocyte Proliferation and Differentiation in the Growth Plate." *PLoS Genet* **12**(10): e1006352.

Wang, X., X. Wang, Y. Xu, M. Yan, W. Li, J. Chen and T. Chen (2020). "Effect of nicastrin on hepatocellular carcinoma proliferation and apoptosis through PI3K/AKT signalling pathway modulation." *Cancer Cell Int* **20**: 91.

Wang, X. B., F. C. Zhao, L. H. Yi, J. L. Tang, Z. Y. Zhu, Y. Pang, Y. S. Chen, D. Y. Li, K. J. Guo and X. Zheng (2019). "MicroRNA-21-5p as a novel therapeutic target for osteoarthritis." *Rheumatology (Oxford)*.

Wang, Y., S. Shen, Z. Li, W. Li and X. Weng (2020). "MIR-140-5p affects chondrocyte proliferation, apoptosis, and inflammation by targeting HMGB1 in osteoarthritis." *Inflamm Res* **69**(1): 63-73.

Wee, L. M., C. F. Flores-Jasso, W. E. Salomon and P. D. Zamore (2012). "Argonaute divides its RNA guide into domains with distinct functions and RNA-binding properties." *Cell* **151**(5): 1055-1067.

Wei, M., Q. Xie, J. Zhu, T. Wang, F. Zhang, Y. Cheng, D. Guo, Y. Wang, L. Mo and S. Wang (2016). "MicroRNA-33 suppresses CCL2 expression in chondrocytes." *Biosci Rep* **36**(3).

Wen, X., H. Li, H. Sun, A. Zeng, R. Lin, J. Zhao and Z. Zhang (2020). "MiR-455-3p reduces apoptosis and alleviates degeneration of chondrocyte through regulating PI3K/AKT pathway." *Life Sci* **253**: 117718.

Wienholds, E., W. P. Kloosterman, E. Miska, E. Alvarez-Saavedra, E. Berezikov, E. de Bruijn, H. R. Horvitz, S. Kauppinen and R. H. Plasterk (2005). "MicroRNA expression in zebrafish embryonic development." *Science* **309**(5732): 310-311.

Wienholds, E., M. J. Koudijs, F. J. van Eeden, E. Cuppen and R. H. Plasterk (2003). "The microRNA-producing enzyme Dicer1 is essential for zebrafish development." *Nat Genet* **35**(3): 217-218.

Wolter, J. M., K. Kotagama, A. C. Pierre-Bez, M. Firago and M. Mangone (2014). "3'LIFE: a functional assay to detect miRNA targets in high-throughput." *Nucleic Acids Res* **42**(17): e132.

Wong, N. and X. Wang (2015). "miRDB: an online resource for microRNA target prediction and functional annotations." *Nucleic Acids Res* **43**(Database issue): D146-152.

Woods, S., M. J. Barter, H. R. Elliott, C. M. McGillivray, M. A. Birch, I. M. Clark and D. A. Young (2019). "miR-324-5p is up regulated in end-stage osteoarthritis and regulates Indian Hedgehog signalling by differing mechanisms in human and mouse." *Matrix Biol* **77**: 87-100.

Woods, S., S. Charlton, K. Cheung, Y. Hao, J. Soul, L. N. Reynard, N. Crowe, T. E. Swingler, A. J. Skelton, K. A. Pirog, C. G. Miles, D. Tsompani, R. M. Jackson, T. Dalmay, I. M. Clark, M. J. Barter and D. A. Young (2020). "microRNA-seq of cartilage reveals an overabundance of miR-140-3p which contains functional isomiRs." *RNA* **26**(11): 1575-1588.

Wyman, S. K., E. C. Knouf, R. K. Parkin, B. R. Fritz, D. W. Lin, L. M. Dennis, M. A. Krouse, P. J. Webster and M. Tewari (2011). "Post-transcriptional generation of miRNA variants by multiple nucleotidyl transferases contributes to miRNA transcriptome complexity." *Genome Res* **21**(9): 1450-1461.

Xiao, C. and K. Rajewsky (2009). "MicroRNA control in the immune system: basic principles." *Cell* **136**(1): 26-36.

Xiao, X., Y. He, C. Li, X. Zhang, H. Xu and B. Wang (2016). "Nicastin mutations in familial acne inversa impact keratinocyte proliferation and differentiation through the Notch and phosphoinositide 3-kinase/AKT signalling pathways." *Br J Dermatol* **174**(3): 522-532.

Xie, M., P. Gol'din, A. N. Herdina, J. Estefa, E. V. Medvedeva, L. Li, P. T. Newton, S. Kotova, B. Shavkuta, A. Saxena, L. T. Shumate, B. D. Metscher, K. Grossschmidt, S. Nishimori, A. Akovantseva, A. P. Usanova, A. D. Kurenkova, A. Kumar, I. L. Arregui, P. Tafforeau, K. Fried, M. Carlstrom, A. Simon, C. Gasser, H. M. Kronenberg, M. Bastepe, K. L. Cooper, P. Timashev, S. Sanchez, I. Adameyko, A. Eriksson and A. S. Chagin (2020). "Secondary ossification center induces and protects growth plate structure." *Elife* **9**.

Xie, Z., A. Bailey, M. V. Kuleshov, D. J. B. Clarke, J. E. Evangelista, S. L. Jenkins, A. Lachmann, M. L. Wojciechowicz, E. Kropiwnicki, K. M. Jagodnik, M. Jeon and A. Ma'ayan (2021). "Gene Set Knowledge Discovery with Enrichr." *Curr Protoc* **1**(3): e90.

Xiong, Y., F. Cao, L. Hu, C. Yan, L. Chen, A. C. Panayi, Y. Sun, W. Zhou, P. Zhang, Q. Wu, H. Xue, M. Liu, Y. Liu, J. Liu, A. Abududilibaier, B. Mi and G. Liu (2019). "miRNA-26a-5p Accelerates Healing via Downregulation of PTEN in Fracture Patients with Traumatic Brain Injury." *Mol Ther Nucleic Acids* **17**: 223-234.

Yamasaki, K., T. Nakasa, S. Miyaki, M. Ishikawa, M. Deie, N. Adachi, Y. Yasunaga, H. Asahara and M. Ochi (2009). "Expression of MicroRNA-146a in osteoarthritis cartilage." *Arthritis Rheum* **60**(4): 1035-1041.

Yamashita, S., S. Miyaki, Y. Kato, S. Yokoyama, T. Sato, F. Barrionuevo, H. Akiyama, G. Scherer, S. Takada and H. Asahara (2012). "L-Sox5 and Sox6 proteins enhance chondrogenic miR-140 microRNA expression by strengthening dimeric Sox9 activity." *J Biol Chem* **287**(26): 22206-22215.

Yan, S., C. Jiang, H. Li, D. Li and W. Dong (2019). "FAM3A protects chondrocytes against interleukin-1beta-induced apoptosis through regulating PI3K/Akt/mTOR pathway." *Biochem Biophys Res Commun* **516**(1): 209-214.

Yang, J., S. Qin, C. Yi, G. Ma, H. Zhu, W. Zhou, Y. Xiong, X. Zhu, Y. Wang, L. He and X. Guo (2011). "MiR-140 is co-expressed with Wwp2-C transcript and activated by Sox9 to target Sp1 in maintaining the chondrocyte proliferation." FEBS Lett **585**(19): 2992-2997.

Yang, L., K. Y. Tsang, H. C. Tang, D. Chan and K. S. E. Cheah (2014). "Hypertrophic chondrocytes can become osteoblasts and osteocytes in endochondral bone formation." Proceedings of the National Academy of Sciences of the United States of America **111**(33): 12097-12102.

Yang, X., L. Chen, X. Xu, C. Li, C. Huang and C. X. Deng (2001). "TGF-beta/Smad3 signals repress chondrocyte hypertrophic differentiation and are required for maintaining articular cartilage." J Cell Biol **153**(1): 35-46.

Yin, H., Y. Jiang, Y. Zhang, H. Ge and Z. Yang (2019). "The inhibition of BDNF/TrkB/PI3K/Akt signal mediated by AG1601 promotes apoptosis in malignant glioma." J Cell Biochem **120**(11): 18771-18781.

Yoshida, C. A., H. Yamamoto, T. Fujita, T. Furuichi, K. Ito, K. Inoue, K. Yamana, A. Zanma, K. Takada, Y. Ito and T. Komori (2004). "Runx2 and Runx3 are essential for chondrocyte maturation, and Runx2 regulates limb growth through induction of Indian hedgehog." Genes Dev **18**(8): 952-963.

Young, D. A., R. L. Lakey, C. J. Pennington, D. Jones, L. Kevorkian, D. R. Edwards, T. E. Cawston and I. M. Clark (2005). "Histone deacetylase inhibitors modulate metalloproteinase gene expression in chondrocytes and block cartilage resorption." Arthritis Res Ther **7**(3): R503-512.

Yuan, Y., G. Q. Zhang, W. Chai, M. Ni, C. Xu and J. Y. Chen (2016). "Silencing of microRNA-138-5p promotes IL-1beta-induced cartilage degradation in human chondrocytes by targeting FOXC1: miR-138 promotes cartilage degradation." Bone Joint Res **5**(10): 523-530.

Zaki, S., M. M. Smith and C. B. Little (2021). "Pathology-pain relationships in different osteoarthritis animal model phenotypes: it matters what you measure, when you measure, and how you got there." Osteoarthritis Cartilage.

Zhang, P., A. S. Jobert, A. Couvineau and C. Silve (1998). "A homozygous inactivating mutation in the parathyroid hormone/parathyroid hormone-related peptide receptor causing Blomstrand chondrodysplasia." J Clin Endocrinol Metab **83**(9): 3365-3368.

Zhang, R., J. Ma and J. Yao (2013). "Molecular mechanisms of the cartilage-specific microRNA-140 in osteoarthritis." Inflamm Res **62**(10): 871-877.

Zhang, S., J. Yuan and R. Zheng (2016). "Suppression of Ubiquitin-Specific Peptidase 17 (USP17) Inhibits Tumorigenesis and Invasion in Non-Small Cell Lung Cancer Cells." Oncol Res **24**(4): 263-269.

Zhang, Z., C. Hou, F. Meng, X. Zhao, Z. Zhang, G. Huang, W. Chen, M. Fu and W. Liao (2015). "MiR-455-3p regulates early chondrogenic differentiation via inhibiting Runx2." FEBS Lett **589**(23): 3671-3678.

Zhang, Z., Y. Kang, Z. Zhang, H. Zhang, X. Duan, J. Liu, X. Li and W. Liao (2012). "Expression of microRNAs during chondrogenesis of human adipose-derived stem cells." Osteoarthritis Cartilage **20**(12): 1638-1646.

Zhao, S., W. P. Fung-Leung, A. Bittner, K. Ngo and X. Liu (2014). "Comparison of RNA-Seq and microarray in transcriptome profiling of activated T cells." PLoS One **9**(1): e78644.

Zhao, Y., M. Yan, Y. Yun, J. Zhang, R. Zhang, Y. Li, X. Wu, Q. Liu, W. Miao and H. Jiang (2017). "MicroRNA-455-3p functions as a tumor suppressor by targeting eIF4E in prostate cancer." Oncol Rep **37**(4): 2449-2458.

Zhou, S., Y. Xie, J. Tang, J. Huang, Q. Huang, W. Xu, Z. Wang, F. Luo, Q. Wang, H. Chen, X. Du, Y. Shen, D. Chen and L. Chen (2015). "FGFR3 Deficiency Causes Multiple Chondroma-like Lesions by Upregulating Hedgehog Signaling." PLoS Genet **11**(6): e1005214.

Zhou, Z., S. S. Apte, R. Soininen, R. Cao, G. Y. Baaklini, R. W. Rauser, J. Wang, Y. Cao and K. Tryggvason (2000). "Impaired endochondral ossification and angiogenesis in mice deficient in membrane-type matrix metalloproteinase I." Proc Natl Acad Sci U S A **97**(8): 4052-4057.

Zou, W., X. Chen, J. H. Shim, Z. Huang, N. Brady, D. Hu, R. Drapp, K. Sigrist, L. H. Glimcher and D. Jones (2011). "The E3 ubiquitin ligase Wwp2 regulates craniofacial development through mono-ubiquitylation of Goosecoid." Nat Cell Biol **13**(1): 59-65.